NEWCASTLE UNIVERSITY

DOCTORAL THESIS

Exciton Dynamics in Organic Light Emitting Diodes

Author:
Shawana AHMAD

Supervisor:
Dr. Thomas PENFOLD

A thesis submitted in fulfillment of the requirements
for the degree of Doctor of Philosophy

May 27, 2025

Declaration of Authorship

I, Shawana AHMAD, declare that this thesis titled, "Exciton Dynamics in Organic Light Emitting Diodes" and the work presented in it are my own. I confirm that:

- This work was completed entirely during my candidature for a research degree at this University.
- Where any part of this thesis has previously been submitted for a degree or any other qualification at this University or any other institution, this has been clearly stated.
- Where I have consulted the published work of others, this is always clearly attributed.
- Where I have quoted from the work of others, the source is always given. With the exception of such quotations, this thesis is entirely my own work.
- I have acknowledged all main sources of help.
- Where the thesis is based on work done by myself jointly with others, I have made clear exactly what was done by others and what I have contributed myself.

Signed:

Date: 26/07/2024

NEWCASTLE UNIVERSITY

Abstract

Faculty Name
Department or School Name

Doctor of Philosophy

Exciton Dynamics in Organic Light Emitting Diodes

by Shawana AHMAD

Organic light emitting diode (OLED) technology has gained significant attention over the past few decades due to its self-emissive displays, high contrast ratios, and energy efficiency compared to traditional lighting sources. However, substantial challenges remain in achieving OLED emitters with long lifetimes and high efficiency while also having narrowband emissions. Current high-performance thermally activated delayed fluorescence (TADF) emitters, which can achieve 100% internal quantum efficiency (IQE), predominantly utilise charge-transfer (CT) excited states that exhibit inherently broad emissions, typically with a full-width half maximum (FWHM) of 70-120 nm. This broad emission necessitates the use of filters or optical microcavities to enhance colour purity, which often introduces trade-offs in efficiency and lifespan. To address this, multi-resonant (MR) emitters have been developed, offering narrow emissions but large singlet-triplet gaps, resulting in less TADF. Additionally, advancements in computational methods are needed to study these molecules effectively. This thesis is structured into three key parts that aim to tackle these challenges by investigating the optimisation of compounds used in OLED devices, focusing on the interplay between structural and electronic properties, thoroughly understanding the mechanisms involved, benchmarking computational methods, and designing novel organic molecules for OLEDs, thereby contributing to the broader goal of making OLED technology a superior alternative to current display technologies.

The first part of the thesis explores the conformational control of TADF emitters using non-covalent interactions. TADF emitters typically require a specific Donor-Acceptor (D-A) framework, where the highest and lowest energy states have minimal spatial overlap, achieved by maintaining a near 90-degree angle between the D and A units. However, overly rigid D-A bonds can hinder TADF efficiency by limiting molecular movement necessary for vibrational coupling, while excessive flexibility can lead to dispersed TADF rates, broader emissions, and increased non-radiative decay rates. Introducing explicit chemical bonds to increase rigidity often excessively alters the electronic structure of these emitters, hindering their ability to exhibit TADF. One strategy is introducing steric hindrance between D-A groups, such as methylation; however, this can lead to enforcing orthogonal dispositions between D-A groups. We've demonstrated by examining a series of D-A molecules with a B-N bond that the introduction of non-covalent interactions via oxygen and sulphur atoms significantly stabilises the twisted conformer necessary for efficient TADF. This stabilisation enhances spin-orbit coupling, thus improving intersystem crossing (ISC) and reverse intersystem crossing (rISC) rates. The study highlighted the importance of methoxy groups at donor in enhancing conformational control, leading to more stable and efficient TADF properties, particularly in solid-state applications.

The second part of thesis addresses the challenge of achieving narrowband emission in luminescent materials for high-resolution and energy-efficient

OLED displays. Calculations of emission spectra typically require ground and excited state geometries and Hessians, making them challenging for large molecule due to the high computational costs involved. The DHO model was employed in this study to predict the emission FWHM for various organic molecules including π-π^*, charge transfer (CT), and multiple-resonance (MR) without extensive excited state optimisations, making it a valuable tool for high-throughput screening. In addition, it can also be extended to include off-diagonal coupling between excited states, accounting for non-Condon and non-Born-Oppenheimer effects, which are crucial for functional organic molecules, especially those exhibiting TADF. Furthermore, by combining quantum chemistry at both TDDFT and CC2 levels of theory with rate calculations within the semi-classical Marcus formalism, we demonstrate that incorporating heteroatoms like oxygen and sulphur into the B-N framework slightly increases emission FWHM but significantly enhances the ISC pathway compared to the spin-vibronic mechanism, simplifying triplet harvesting mechanisms. This, along with the DHO model, offers new avenues for designing high-efficiency MR-TADF emitters and improving high-throughput screening procedures.

The third part of thesis focuses on multi-resonance TADF (MR-TADF) materials, which offer high colour purity and photoluminescence quantum yield but suffer from slow rISC rates, resulting in long-delayed fluorescence lifetimes. Previous studies have highlighted the importance of double excitations, not accounted for within the framework of Linear Response Time-Dependent Density Functional Theory (LR-TDDFT). This study employs Mixed-Reference Spin-Flip Time-Dependent Density Functional Theory (MRSF-TDDFT) to overcome these limitations, providing accurate excited state energetics, including the crucial $\Delta E_S T$, and outperforming traditional LR-TDDFT methods. By increasing the density of states to enhance coupling between singlet and triplet states, this method was used to explore the excited state properties of these materials. The results in this work set the foundation for computationally efficient in silico development of high-performing MR-TADF materials within the framework of MRSF-TDDFT. Despite progress in developing MR-TADF, narrow blue MR-TADF emitters face significant challenges due to the high energy required for blue emission, leading to energy losses and efficiency roll-off. Inverse design and high-throughput computational screening offer powerful, resource-efficient approaches to discover new deep blue MR-TADF emitters compared to traditional methodologies. However, the scarcity of documented MR-TADF emitters complicates this process. To address this, we have used the stoned algorithm with SELFIES molecular representation to generate a diverse candidate dataset, followed by high-throughput computational screening. This multi-stage funnel approach systematically narrowed the candidate pool, but the structures at the end showed minimal variations from the initial hypothesis. Nevertheless, the SF-TDDFT and MRSF-TDDFT approach proves promising for studying the excited state properties of MR-TADF emitters.

In summary, this thesis presents significant advancements in the optimisation of compounds for OLED devices, enhancing the understanding of structural and electronic properties, and developing computational methods for designing novel organic molecules.

Acknowledgements

I would like to take this opportunity to acknowledge the individuals whose support and contributions made this thesis possible.

First and foremost, I extend my deepest gratitude to my respected supervisor, Professor Thomas Penfold for providing me with the opportunity to pursue this PhD and learn how to conduct research without losing interest. His unwavering support, boundless kindness, and invaluable guidance throughout my PhD journey have been instrumental in sustaining my enthusiasm for research. I consider myself incredibly fortunate to have had a supervisor so deeply invested in this project from its inception/beginning to its conclusion.

I am profoundly grateful to Dr. Andrew Beniston and Dr. Marina Freitag for their expert insights and guidance during our progress meetings. My heartfelt thanks go out to the members of the Penfold group, past and present, whose fellowships have enriched this experience: Julien Eng, Thomas Pope, Tudur David, Sneha Verma, Yvelin Giret, Conor Rankine, Miriam Fasadni, Clelia Middleton, Luke Watson, Marwah Madkahli, Yang Cao, and Josh Littlefair. My sincere gratitude goes to Julien for all his work during our collaboration, answering my questions and helping at various stages during the analysis.

Heartiest thanks are due to Nosheen for being such a terrific friend through the years, whose unwavering support and concern have been a source of comfort during stressful times. Her emotional support and care for me and my family has been invaluable. My cordial thanks also go to my dearest oldest friends Afshan, Fakhra, and Farwa, whose warm companionship has been always kept me uplifted.

I can never thank enough my parents, siblings, and in-laws for their unconditional love, contribution, support, and constant encouragement. Their belief in me has kept me grounded and focused.

Finally, my deepest appreciation goes to my two sons, Khizar Ahmad and Mughees Ahmad, for being a constant source of love, strength, and joy. Last but not least, to my beloved husband, Ayaz Ahmad, You have helped me immensely throughout my PhD. In addition your endless love, emotional support, and belief in me have carried me through the hardest times and kept my vision clear. You mean more to me than words can express.

Thank you all for being an integral part of this journey

PUBLICATIONS

1. S. A. Ahmad , J. Eng and T. J. Penfold , "Rapid predictions of the colour purity of luminescent organic molecules", J. Mater. Chem. C, 2022, 10, 4785-4794
2. S. A. Ahmad , J. Eng and T. J. Penfold , "Conformational Control of Donor-Accepted Molecules using Non-Covalent Interactions", J. Phys. Chem. A, 2024, 128, 8035–8044
3. S. A. Ahmad , J. Eng and T. J. Penfold , "Towars the Accurate Simulation of Multi-Resonance Emitters using Mixed-Reference Spin-Flip Time-Dependent Density Functional Theory", Org. Electron., 2024, 135, 107138

Contents

3 Quantum Chemistry Methodologies

List of Figures

List of Tables

List of Abbreviations

AO	**A**tomic **O**rbital
AM1	**A**ustin **M**odel **1**
AIMD	**A**b **I**nitio **M**olecular **D**ynamics
A	**A**cceptor
AMOLED	**A**ctive **M**atrix **O**rganic **L**ight **E**mitting **D**iode
BS	**B**asis **S**et
B3LYP	**B**ecke **3**-parameter **L**ee-Yang-Parr
CT	**C**harge **T**ransfer
CC	**C**oupled **C**luster
CC2	**S**econd **O**rder **C**oupled **C**luster
CGTOs	**C**ontracted **G**aussian **T**ype **O**rbital
CASSCF	**C**omplete **A**ctive **S**pace **S**elf **C**onsistent **F**ield
D–A	**D**onor-**A**cceptor
D	**D**onor
D–A–D	**D**onor-**A**cceptor-**D**onor
DFT	**D**ensity **F**unctional **T**heory
DHO	**D**isplaced **H**armonic **O**scillator
DZ	**D**ouble **Z**eta
EML	**E**mission **L**ayer
EQE	**E**xternal **Q**uantum **E**fficiency
FWHM	**F**ull **W**idth **H**alf **M**aximum
GGA	**G**eneralised **G**radient **A**pproximation
GTO	**G**aussian **T**ype **O**rbital
GS	**G**round **S**tate
HOMO	**H**ighest **O**ccupied **M**olecular **O**rbital
HF	**H**artree **F**ock
HTVS	**H**igh–**T**hroughput **V**irtual **S**creening
ISC	**I**ntersystem **C**rossing
IQE	**I**nternal **Q**uantum **E**fficiency
IC	**I**nternal **C**onversion
LCD	**L**iquid **C**rystal **D**isplay
LED	**L**ight **E**mitting **D**iode
LR–TDDFT	**L**ong-**R**ange **T**ime-**D**ependent **D**ensity **F**unctional **T**heory
LRC–BLYP	**L**ong-**R**ange **C**orrected **B**ecke–Lee–Yang–Parr
LCAO	**L**inear **C**ombination of **A**tomic **O**rbitals
LUMO	**L**owest **U**noccupied **M**olecular **O**rbital
LDA	**L**ocal **D**ensity **A**pproximation

MRSF–TDDFT	**M**ixed-**R**eference **S**pin-**F**lip **T**ime-**D**ependent **D**ensity **F**unctional **T**heory
MR	**M**ulti-**R**esonance
MR–TADF	**M**ulti-**R**esonance **T**hermally **A**ctivated **D**elayed **F**luorescence
MO	**M**olecular **O**rbital
OLED	**O**rganic **L**ight **E**mitting **D**iode
PES	**P**otential **E**nergy **S**urface
PMOLED	**P**assive **M**atrix **O**rganic **L**ight **E**mitting **D**iode
PM3	**P**arametric **M**ethod **3**
QZ	**Q**uadruple **Z**eta
rISC	**R**everse **I**ntersystem **C**rossing
RHF	**R**estricted **H**artree-**F**ock
ROHF	**R**estricted **O**pen-shell **H**artree-**F**ock
SOC	**S**pin-**O**rbit **C**oupling
SF–TDDFT	**S**pin-**F**lip **T**ime-**D**ependent **D**ensity **F**unctional **T**heory
SCF	**S**elf **C**onsistent **F**ield
STO	**S**later **T**ype **O**rbital
SOCME	**S**pin **O**rbit **C**oupling **M**atrix **E**lements
SELFIES	**S**elf-**R**eferencing **E**mbedded **S**trings
SCS–CC2	**S**pin-**C**omponent **S**caling **S**econd-**O**rder **C**oupled **C**luster
TDDFT	**T**ime **D**ependent **D**ensity **F**unctional **T**heory
TADF	**T**hermally **A**ctivated **D**elayed **F**luorescence
TDA	**T**amm–**D**ancoff **A**pproximation
TZ	**T**riple **Z**eta
UHF	**U**nrestricted **H**artree **F**ock
xtb	**E**xtended **T**ight **B**inding

Chapter 1

Introduction

1.1 Motivation: Let there be light!

Artificial lighting is a very important part of our daily lives which have provided comfort in various ways: at work, at home, at leisure, and everywhere else. Thomas Edison has been credited for developing the first incandescent light bulb (which featured a carbon filament enclosed in a high-quality vacuum to prolong the filament's lifespan) which was both practical and affordable at that time and revolutionise the way energy was used. Since then, engineers and scientists have been constantly trying to improve the way we light our homes and offices. This has led to the development of liquid crystal displays (LCDs) and light-emitting diodes (LEDs).

Another technology that has gained considerable interest over the past three decades is the use of organic light-emitting diodes (OLEDs) also known as organic electroluminescence diodes. In conventional LEDs, the light-emitting layer consists of inorganic crystalline semiconductors. In contrast, OLEDs use organic semiconductors, typically aromatic small molecules, as their electroluminescent layer. OLEDs are considered more environmentally friendly than conventional LEDs and fluorescent lights because of the less hazardous materials and milder processing conditions involved. In addition to their eco-friendly nature, OLEDs offer several other advantages:

- OLEDs have self-emissive displays (unlike LCDs in which light comes from a back-lighting unit), hence having the higher contrast ratios with true blacks Fig. 1.1, along with wider viewing angles.
- The fabrication of OLEDs on flexible and transparent substrates opens the door to future technologies such as rollable, foldable, and even transparent OLED displays.
- They have faster response time typically in the microsecond to nanosecond range, which enables them to produce sharp and clear moving images.
- OLED lighting is up to 80% more efficient than traditional lighting sources (LCDs), so consuming less energy over its lifetime

- OLED panels can be easily recyclable because they are made of nearly 100% glass and toxic-free substances
- They have a simple design and can be printed using simple ink-jet processes; in future this will result in a reduction of cost

FIGURE 1.1: Comparison of OLEDs with LEDs

Fig. 1.2 depicts the evolution of OLED technology, highlighting significant milestones from the 1950s to date [1]. Light emission utilising organic material was first reported by Bernanonse et al. in the 1950s [2]. However, it largely remained the theoretical field for the next three decades as devices suffered from low luminance/efficiency and required large electric fields (typically 100v). A breakthrough achievement was reported by Tang et al. in 1987 [3] who first demonstrated the practical OLED called fluorescent OLEDs using Alq_3 and observed bright light emission from as low as about 2.5 V and achieved high luminance (>1000 cd/m^2). Although the obtained external quantum efficiency (EQE *i.e.* photons emitted per electron injected) and power efficiency were still low (1% EQE and 1.5 lm/W), this report sparked interest in further developing OLED. In 1996, Pioneer Corporation produced the world's first commercial PMOLED (Passive-Matrix OLED) [4]. PMOLEDs are simpler and cheaper to manufacture than AMOLEDs (Active-Matrix OLEDs) but are generally used in smaller displays due to their line-by-line and column-by-column pixel control, which limits resolution and increases power consumption. After that, construction of the first high-efficiency phosphorescent OLED was achieved in 1998 [5], which significantly improved the technology's efficiency. By the year 2000, major companies like Motorola and LG began developing various OLED displays. This period marked the beginning of commercial applications of the OLED technology in mobile phones, digital cameras, and other consumer electronics. In 2001, Sony developed the world's largest full-colour OLED, demonstrating the scalability of OLED technology for larger displays such as televisions and computer monitors. The production of the first OLED TV in 2007 marked a significant milestone in the technology's commercial application [6]. The subsequent years saw the introduction of AMOLED displays [7] by many companies in 2010, which offered several advantages over PMOLED. By using a grid of thin-film transistors (TFTs) and capacitors to directly control each pixel's brightness, AMOLEDs enabled higher resolution, faster response times, and lower power consumption. This made them ideal for better performance in larger and more complex displays, such as those in smartphones and tablets. A crucial development occurred in 2012 with the creation of purely organic TADF (Thermally Activated Delayed Fluorescence) OLED emitters, which provided higher efficiencies, enhancing overall performance by harvesting triplet excitons, which were previously lost in traditional OLEDs. By 2015, the European Commission began a project named Phebe, with the goal of commercialising TADF emitters [8], further improving efficiency and reducing power consumption of OLED displays. The most efficient fluorescent blue OLED emitter to date was launched in 2020 [9], addressing one of the major challenges in OLED technology by improving the efficiency and lifespan of blue emitters.

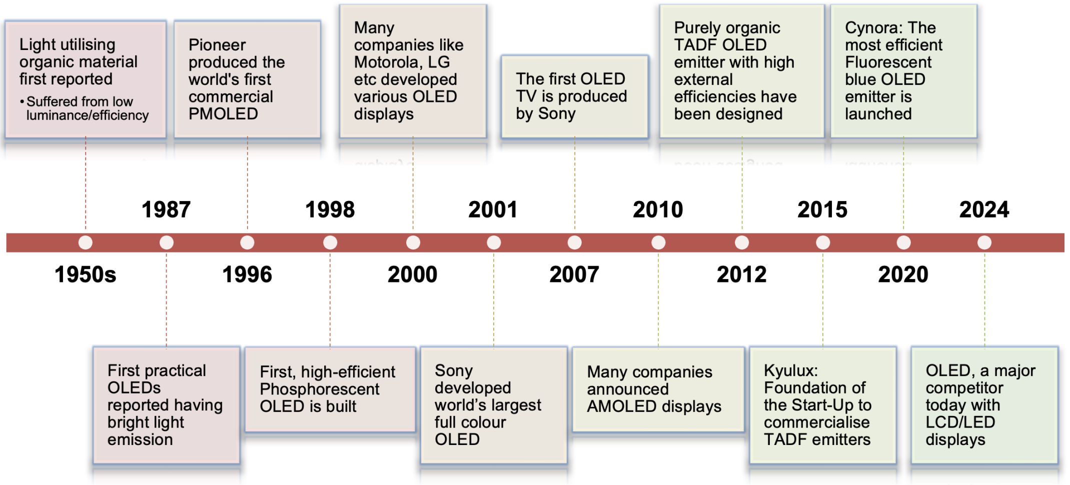

FIGURE 1.2: Key milestones in the development of OLED

Today, OLED technology has established itself as a major competitor compared to other display technologies *e.g*; LCD and LED displays. It is anticipated that OLEDs will replace the entire LCD/LED technology in the near future [10], [11]. Making this replacement presents significant challenges that must be addressed through focused research and development. This thesis aims to tackle these challenges by investigating the optimisation of compounds used in OLED devices, thoroughly understanding all mechanisms involved in optimising compounds and designing suitable novel organic molecules, thereby contributing to the broader goal of making OLED technology a viable and superior alternative to current display technologies.

1.2 Organic Light-Emitting Diodes (OLEDs): Basics

The organic materials used in OLEDs are organic semiconductors. Many organic semiconductor materials are π-conjugated, which means they have alternating single and double bonds. Each carbon atom has three valence electrons to form covalent σ-bonds with adjacent carbons, but the last electron, whose p-orbitals overlap, forms a delocalised π-bond. Due to the delocalisation of charges along the conjugated backbone of the molecule, electrons and holes are able to travel. Depending on their configuration, these π orbitals can either form bonding orbitals (constructive orbital overlap) or antibonding orbitals (destructive orbital overlap). (see Fig. 1.3).

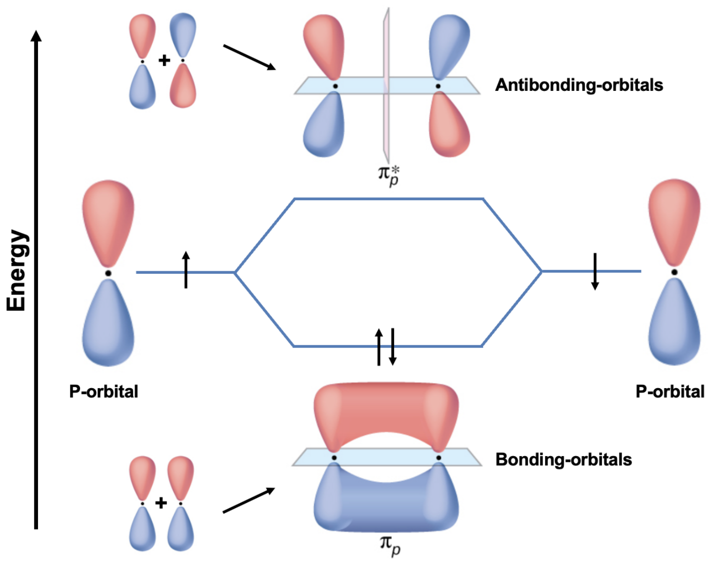

FIGURE 1.3: p-orbitals, which can overlap in a conjugated molecule to form bonding and antibonding orbitals.

These bonding and antibonding orbitals have different energies. Consequently, the overlap of many p-orbitals can form two energetic bands - the lowest unoccupied molecular orbital (LUMO) and the highest occupied molecular orbital (HOMO). These HOMO and LUMO orbitals are often referred to as the frontier orbitals, play a crucial role in the electronic properties of the material. Analogously to inorganic semiconductors, organic semiconductors also exhibit a band gap, which results from the difference in energy levels between LUMO and HOMO called HOMO-LUMO energy gap which is critical for the material's semiconductor behaviour and its ability to emit light. In short, the charges can travel due to the delocalisation of electrons in the overlapping orbitals of a single molecule along the conjugation length.

1.2.1 Working Principle of OLEDs:

The working principle of an OLED is illustrated in Fig. 1.4. An OLED is an electroluminescent device composed of stacked organic layers sandwiched between two electrodes, an anode and a cathode.

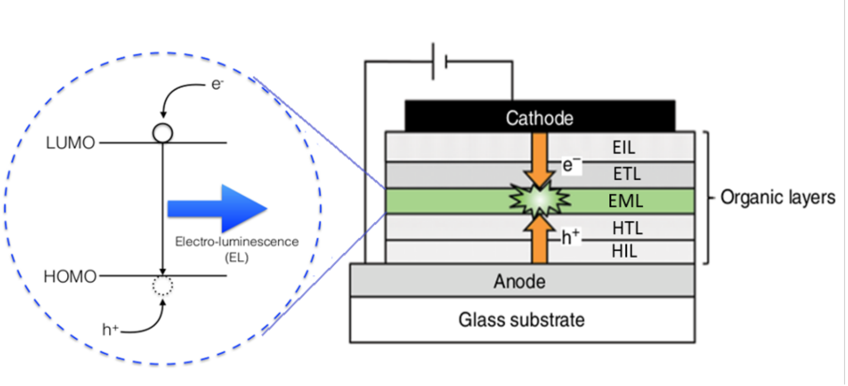

FIGURE 1.4: Schematic illustration of a typical OLED device structure and the emission mechanism; EIL - electron injection layer; ETL - electron transport layer; EML - electron emissive layer; HTL - hole transport layer, HIL - hole injection layer

By applying voltage to an OLED device, an electron is injected from the cathode into a LUMO and another electron is extracted from the HOMO by the anode, resulting in the formation of a hole (or a hole is injected from the anode into a HOMO). Due to the energetic landscape of the stacks, the charged particles (electrons and holes) start travelling via transporting layers to an emission layer (EML) which is composed of organic compounds where they form a strong Coulombic bound state of an electron and hole called an exciton (Fig. 1.5). This exciton is treated as a neutral quasi-particle with zero net charge. The main purpose of a multilayer device is to ensure efficient hole-electron recombination within the EML.

Electrons and holes are fermions having half-integer spins, so the total spin of exciton can either one (S = 1) called triplet exciton or zero (S = 0) called a singlet exciton. The specific spin state depends on the relative orientation of the electron and hole spins. As shown in Fig. 1.5, there is only one spin configuration that leads to S = 0, whereas three possible spin alignments give rise to S = 1 (hence the names singlet and triplet exciton). This means that when organic molecules in the EML are excited, creating 25% singlet excitons and 75% triplet excitons electronically. When these excitons decay back into

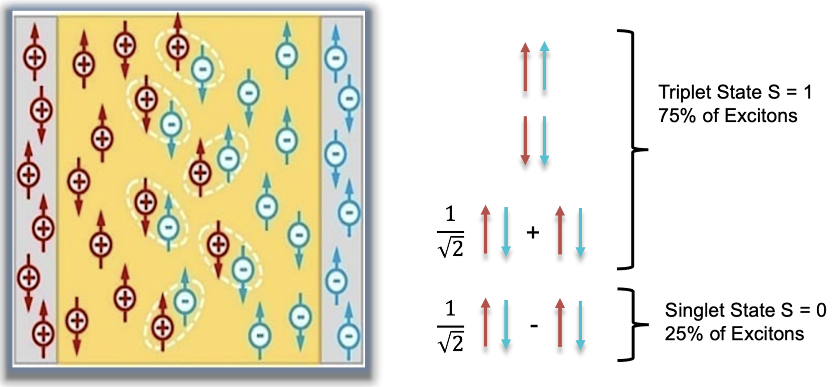

FIGURE 1.5: 75% triplet exciton formation and 25% singlet exciton formation due to spin statistics

the electronic ground state, then emission occurs. (Fig. 1.4). Unlike photoexcitation, where the spin is preserved and only singlet exciton is generated, electrical excitation of organic semiconductors generates both singlet and triplet excited states in a statistical ratio of 1:3. The ground state is typically a singlet state usually denoted as S_0, while the first excited singlet state above S_0 is denoted as S_1 and the first triplet state above S_0 is denoted as T_1. T_1 state generally lies at an energy lower than that of the S_1 state.

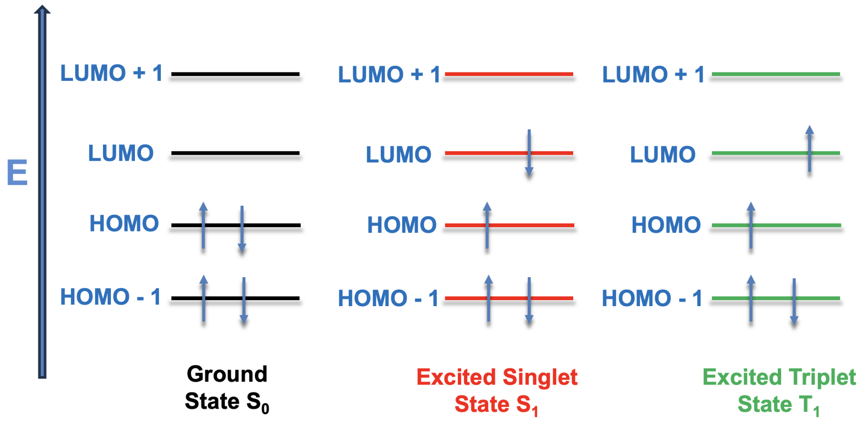

FIGURE 1.6: Spin conditions of the ground state (S_0), the singlet excited state (S_1), and the triplet excited state (T_1)

The spin conditions of the resulting (S_0), the (S_1), and the (T_1) states created in EML have been shown in Fig. 1.6. The ground state of organic molecules containing two electrons occupying a single orbital and their spins are antiparallel paired while in the excited state, each electron is in a different orbital, i.e., one is in the highest occupied molecular orbitals (HOMO), and another one in the lowest unoccupied molecular orbital (LUMO), and they can either have electron spin parallel (↑↑, triplet) or antiparallel (↑↓, singlet).

1.2.2 Generations of OLEDs:

On the basis of the light emission mechanism, OLEDs have three generations. These generations reflect significant advancements in efficiency, brightness, and colour purity. First-generation OLEDs utilised fluorescence, where only singlet excitons can emit radiatively while triplet excitons are non-emissive as they are spin forbidden (ΔS should be equal to 0) arising from the weak spin-orbit coupling (SOC) in purely organic materials. As excitons are formed in 1:3 singlet: triplet ratio, so, 75% of the electrons and holes injected into the device are lost as heat and these first-generation OLEDs can have a maximum theoretical internal quantum efficiency of only 25% (Fig. 1.7).

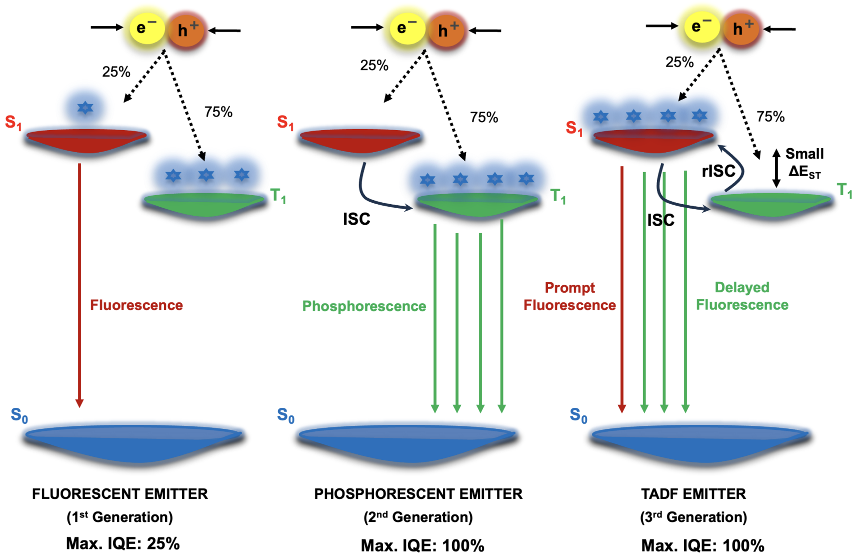

FIGURE 1.7: Comparison of emission mechanism in Fluorescent, Phosphorescent and TADF emitter, ISC-intersystem crossing; rISC-reverse intersystem crossing; ΔE_{ST}-first excited singlet-triplet energy gap

To overcome the limitations of fluorescent OLED materials, 2^{nd} generation phosphorescent OLEDs (Fig. 1.7) were reported by T. Tsutsui *et al.* [12]. These exploit the large SOC arising from heavy metals [13] to mix the character of singlet and triplet states. This makes the singlet exciton decays into triplet exciton non-radiatively *via* intersystem crossing (ISC) and the triplet exciton to become emissive in the form of phosphorescence. Thus, achieving the internal quantum efficiency of nearly 100% and overcoming a major limitation of first generation devices. However, there remain challenges and one of the most significant problems associated with these 2^{nd} generation OLEDs is the long-living triplet states which can cause chemical degradations and inclusion of metals such as iridium and platinum which are both rare and expensive.

These disadvantages motivated the development of 3^{rd} generation OLED materials (Fig. 1.7) which achieve 100% internal quantum efficiency without the use of heavy metals. These types of materials display thermally activated delayed fluorescence, [14] [15]. The concept of TADF is not a recent development; it was first introduced by Perrin *et al.* in 1929 [16] and later explored by several researchers throughout the 20^{th} century [17] [18]. However, in 2012 Chihaya Adachi and co-workers used the TADF mechanism for the first time to create an efficient OLED using only organic molecules [19]. This work attracted widespread interest and has since been the focus of extensive research by groups around the world in developing new emitters and understanding the photophysics of the TADF process [19] [20]. TADF achieves emission initially through singlet excitons, resulting in prompt fluorescence. For triplet excitons, TADF requires that both radiative and non-radiative decay rates of the triplet state should be slow and the energy difference between the singlet and triplet state excitons needs to be much smaller than in typical organic molecules (< 0.1 eV) [21]. This singlet-triplet gap reduction is made possible by giving thermal energy (~25.85 meV at room temperature) which raise the triplet state to a vibronic sub-level iso-energetic with the singlet states, resulting in highly efficient spin up-conversion from the non-radiative triplet states to the radiative singlet states which is process called reverse intersystem crossing (rISC) (Fig. 1.7) [22]. Once in the singlet state the excitons can decay back to the ground state, giving delayed fluorescence [23]. Hence, TADF materials harness both prompt fluorescence and delayed fluorescence to achieve 100% internal quantum efficiency, significantly improving the overall performance of OLED devices.

1.3 Industry Requirement & Challenges for OLEDs:

1.3.1 Industry requirement for OLEDs

Commercially, good OLED emitters rely on these factors: colour purity, high efficiency, long lifetime of device and low in cost.

Colour Purity/Tuning:

OLED should have excellent colour purity to avoid usage of colour filters, which reduces the external quantum efficiency. Emission width (Full width at half maximum, *i.e.* FWHM) contributes to the colour purity. Therefore, to attain a pure emission, spectrum must be narrow (FWHM < 50 nm) which can be achieved by designing rigid molecules because molecular flexibility causes broadening in emission spectra which results in the reduction of colour purity. The critical aspect of colour tuning involves the S_1 energy of the substance (or T_1 for phosphorescence). The lower the energy of the excited state, the more the emission shifts toward the red spectrum. Currently, the industry is still looking for highly efficient blue emitters.

High Efficiency:

In addition to colour purity, OLED emissions should be highly efficient. To achieve high efficiency, number of photons emitted should be equal to the no of electrons passing through the device which can be measured as an external quantum efficiency and can be expressed as,

$$EQE(external\ quantum\ efficiency) = IE \times IQE \times EE \tag{1.1}$$

where IE is the injection efficiency, IQE is the internal quantum efficiency and EE is the extraction efficiency. IQE can further be expressed as,

$$\text{IQE} = \gamma \times \phi_{PL} \times \phi_r \tag{1.2}$$

where γ, is the hole-electron recombination factor, which is assumed to be unity, relates to the likelihood of holes and electrons recombining to form excitons; ϕ_{PL} represents the fraction of excitons that undergo radiative decay resulting in the emission of light. The final term, ϕ_r, represents the number of emissive excitons generated per hole-electron recombination. The IQE can be maximised by designing emission materials that optimise the molecular structure to enhance radiative decay rates and minimise non-radiative pathways.

long lifetime:

Another requirement for OLEDs is the good lifetime of the organic materials, i.e. OLEDs should maintain their brightness and performance for an extended period of time. For that purpose organic materials used in OLED device must be stable and shouldn't degrade over time from thermal stress, chemical breakdown, and environmental factors.

Low in cost:

OLEDs must be manufactured at low cost to be commercialised on a large scale. To meet this requirement, high-performance and low-cost materials should be used instead of expensive metal elements (e.g. Iridium, Platinum), which not only increases fabrication costs but also raises concerns regarding biological applications.

1.3.2 Challenges in OLEDs:

Although OLEDs have been successfully commercialised, there are still some important research areas remaining for their improvement. This includes high power efficiency at brightness levels typically reaching several thousand candelas per square meter, along with a long operational lifetime. The internal quantum efficiency of OLEDs can be high at low brightness, but falls significantly at high brightness. This drop is due to excitonic interactions leading to efficiency loss. Additionally, these interactions can lead to degradation events, which shorten their operational lifetime.

In OLED displays, each pixel is made up of three separate OLEDs, red, green and blue. Red and green emitters are indeed more efficient and pure compared to blue emitters. The main challenges with blue emitters lie in achieving high efficiency and maintaining colour purity and stability. This is due to the higher energy required to produce blue light, which often results in higher rates of non-radiative decay and thus lower efficiency. In addition, the materials often have broader emission spectra, and maintaining stability and colour purity over time can be difficult. This limits the applicability of blue OLEDs. However, the ongoing research still aims to address these issues to make better blue emitters, which involves developing new materials and improving the existing ones to match the performance levels of red and green.

As TADF materials hold great potential and will allow to make a stable and highly efficient blue emitter, mainly due to their high efficiency and low cost which is the most active and rapidly evolving area of OLEDs research today. The drawback to such OLEDs is that the mechanism involved here is more complicated compared to the previous two generations, so a more detailed understanding of mechanisms involved particularly rISC (a crucial step in TADF mechanism), exciton formation and excitonic interactions will be needed. This area of interest will be explored in this thesis. The understanding from theoretical studies will lead to new perspectives for the design of novel molecules in OLEDs to be able to improve the efficiency and operational lifetime of OLEDs at high brightness, particularly in designing a narrow deep blue TADF emitter with good efficiency and long lifetime which is a major challenge to date.

1.4 Thesis Summary

This thesis aims to address the challenges in designing TADF emitters through focused research and development. It involves optimising compounds used in OLED devices, thoroughly understanding the mechanisms involved, uncover the molecular properties and design novel organic molecules thereby contributing to the broader goal of making OLED technology a viable and superior alternative to current display technologies.

In the preceding sections, we highlighted the significant ongoing interest in OLED emitter development. We covered the introduction, working principles, and various generations of OLED emitters, emphasizing the potential of third-generation TADF emitters in the OLED industry. Additionally, we addressed the industry's requirements and challenges associated with OLED technology.

Chapter 2 details the essential background theory needed to study OLED emitters and the fundamental concepts for designing TADF molecules. In chapter 3 the quantum chemistry methodologies have been employed to investigate chemical phenomena and calculate the electronic properties of molecules.

In Chapter 4, we tackled the challenges of improving conformational control of TADF emitters and tried to achieve better conformational control using non-covalent interactions. Orthogonality between donor (D) and acceptor (A) units is vital for TADF but overly rigid dihedral constraints can hinder vibrational coupling, leading to room temperature phosphorescence and reduced rISC rates. Conversely, excessive flexibility around the D-A bond results in variable TADF rates, broader emissions, and higher non-radiative decay. Adding chemical bonds for rigidity often disrupts the electronic structure, preventing TADF. Steric hindrance, like methylation, can destabilise the D-A orthogonal arrangement. Instead, non-covalent interactions, such as hydrogen bonding and $\pi - \pi^*$ interactions, offer a solution but still have shown limited efficiency. We computationally investigated three sets of molecules based on a donor-acceptor and donor-acceptor-donor framework with a B-N connecting bond to compare how steric hindrance and non-covalent interactions (using oxygen···boron and sulphur···boron interactions) affect the conformational control and excited state properties of TADF emitters, highlighting the potential of oxygen-boron and sulphur-boron interactions in controlling conformational dynamics without compromising TADF.

Our study of the first set of molecules identified three main conformers; planar, bent, and twisted differing around the D-A bond. Both unhindered and sterically hindered molecules favoured planar or bent conformers in the ground state, increasing the singlet-triplet energy gap and making TADF less favorable. In contrast, non-covalent interactions, especially involving oxygen and sulphur, stabilised the twisted conformer, enhancing TADF properties. These interactions increased spin-orbit coupling, improving ISC/rISC rates and offering control over the energy gap and emission energy. This stabilisation reduced dynamic dispersion in D-A molecules, especially with methoxy derivatives, resulting in narrowed emission and better suitability for OLED applications. The study of the second set of molecules also confirmed that methoxy groups enhance conformational control in TADF materials via non-covalent interactions. Adding methoxy groups decreased the energy gap and reduced the delayed lifetime by altering the dihedral angle and its rigidity, lowering oscillator strength and shortening the prompt lifetime. While large spin-orbit couplings occurred between the S2-T1 states, the significant energy gap made the S1-T2 interaction more relevant. In the third set of molecules, the one with the methoxy group emerged as the most promising TADF emitter due to its structural rigidity, large dihedral angles, favorable singlet-triplet energy gaps, and enhanced spin-orbit coupling, facilitating efficient rISC and TADF performance. The molecule with B···S interaction, despite a narrow singlet-triplet energy gap, was less efficient due to high flexibility and longer B-S bond lengths, reducing charge transfer efficiency. The molecule with steric effects lacked the necessary dihedral angle variations and had a higher singlet-triplet gap, making it less suitable for TADF. Overall, the methoxy group's compact, twisted conformation and higher oscillator strengths made it the best candidate for TADF applications.

In Chapter 5, we discussed that colour purity is crucial for designing high-resolution, energy-efficient OLEDs. In this chapter, we demonstrated the use of the DHO model to predict the emission FWHM for various organic molecules with different emitting states, including π-π^*, CT, and MR without time-consuming excited state optimisations. It provides a framework for understanding excited state structural changes through normal modes and facilitates incorporating emission FWHM considerations into molecular design and high-throughput screening. The DHO can also be extended to incorporate off-diagonal coupling between excited states, addressing non-Condon and non-Born-Oppenheimer effects, which are crucial for functional organic molecules, especially TADF emitters. Moreover, using quantum chemistry techniques like TDDFT and CC2 theories combined with the semi-classical Marcus formalism, we investigated the intersystem crossing (ISC) mechanisms in MR-type emitters containing O and S atoms in the B-N framework. Although the inclusion of these heteroatoms slightly increased the emission FWHM, it also enhanced the ISC rate due to increased spin-orbit coupling (SOC). This enhancement favoured a direct ISC pathway over the spin-vibronic mechanism, due to the small reorganization energy and valid energy gap law. This smaller energy gap, combined with higher SOC, facilitates triplet harvesting and reduces environmental effects, aiding in developing high-throughput design rules for OLED materials.

In Chapter 6, we benchmarked MRSF-TDDFT for MR-Emitters and used it to study MR-emitters and tried to discover narrow blue MR-TADF emitters through data generation and analysis. The MR molecular framework holds great promise due to its high colour purity and photoluminescence quantum yield, but it faces challenges like long-delayed lifetimes from slow reverse intersystem crossing (rISC) rates and consequently developing novel high-performing materials using in silico method is an important step in the design process. In this study, we addressed the limitations of LR-TDDFT in accurately modelling the excited state properties of MR molecules by employing MRSF-TDDFT, MRSF-TDDFT, which accounts for double excitations. Our study of 50 MR-emitters shows that MRSF-TDDFT provides accurate energetics comparable to more computationally intensive methods like SCS-CC2 with a strong, but slightly shifted, correlation between experimental and computational absorption and emission spectra. NEVPT2 simulations revealed that for the prototypical emitter DABNA, the observed shift stems from electron correlation captured by higher-order excitations. As the size of the active space increases, the excited state properties and radiative rates align more closely with experimental values, particularly for predicting radiative rates where no correlation was found between experimental results and MRSF-TDDFT calculations for the 50 MR-emitters studied. Therefore, during in silico design, calculated oscillator strengths should be interpreted carefully. In addition, the MRSF-TDDFT framework has been utilised to investigate the excited state properties of systems designed to improve the coupling between singlet and triplet states by increasing the density of states. Moreover, to address the lack of data on MR emitters, we used a sophisticated algorithm STONED ALGORITHM to generate a diverse dataset of these emitters, aiming to find new narrow blue TADF MR emitters through high-throughput virtual screening. However, the algorithm did not perform as expected, producing similar structures rather than a diverse range, thus limiting the effectiveness of our screening efforts. In summary, the findings of this study underscore the potential of MRSF-TDDFT for achieving accurate and computationally efficient in silico development of high-performance MR-TADF emitters.

The final chapter 7 offers concluding remarks and a forward-looking perspective on future research of TADF emitters. It begins by integrating the main findings from the previous chapters, creating a comprehensive summary of the entire thesis. Additionally, it outlines future research directions aimed at deepening and broadening the analysis of TADF emitters.

Chapter 2

Background Theory

2.1 The Schrödinger Equation

Newtonian mechanics predicts and describes the behaviour of classical systems. However, to understand the properties of matter on the molecular scale, it is necessary to consider both particle-like and wave-like properties. These dual characteristics are described using quantum mechanics, with the Schrödinger equation. This fundamental equation, formulated by the Austrian physicist Erwin Schrödinger in 1925, describes evolution of the quantum state with respect to time. This quantum state is represented by the wavefunction, having all the information about the quantum state. By solving the Schrödinger Equation, the electronic structure and properties of molecules can be predicted.

The Schrödinger equation is commonly solved in two main forms: the time-dependent Schrödinger equation and the time-independent Schrödinger equation.

- **Time-Dependent Schrödinger Equation:** The time-dependent Schrödinger equation describes how a quantum state evolves over time. It is usually written as,

  $$\hat{H}\psi(\mathbf{R},\mathbf{r},t) = i\hbar\frac{\partial}{\partial t}\psi(\mathbf{R},\mathbf{r},t) \tag{2.1}$$

  In this equation, i is the imaginary unit. $\hbar$ is the reduced Planck constant, which relates the energy of a quantum system to its frequency. $\psi(\mathbf{R},\mathbf{r},t)$ is the wavefunction of the quantum system. Its squared magnitude $|\psi(\mathbf{R},\mathbf{r},t)|^2$ is a mathematical function that encodes information about the probability amplitude of finding a particle at a particular position $\mathbf{R},\mathbf{r}$ and time t. $\mathbf{R}$ are a collective variable for the nuclear coordinates, while $\mathbf{r}$ is a collective variable for the electronic coordinates. This probabilistic interpretation is a cornerstone of quantum mechanics, differing fundamentally with the deterministic nature of classical mechanics. $\hat{H}$ is the Hamiltonian operator, which represents the total energy (sum of kinetic and potential energy) of the system.

For a single non-relativistic particle moving in a potential $V(\mathbf{r}, t)$, the Hamiltonian is,

$$\hat{H} = -\frac{\hbar^2}{2m}\nabla^2 + V(\mathbf{r}, t) \tag{2.2}$$

where m is the mass of the particle and ∇^2 is the Laplacian operator representing the kinetic energy.

- **Time-Independent Schrödinger Equation:** When the potential V does not depend upon on time, the Schrö-dinger equation can be separated into spatial and temporal parts. This leads to time-independent Schrödinger equation which deals with stationary states, where the energy of a system remains constant. It is written as,

  $$\hat{H}\psi(\mathbf{r};\mathbf{R}) = E\psi(\mathbf{r};\mathbf{R}) \tag{2.3}$$

  where $\psi(\mathbf{r};\mathbf{R})$ is the spatial part of wavefunction of the stationary state depending only on the nuclear coordinates $\mathbf{R}$ and the electronic coordinates $\mathbf{r}$. $\hat{H}$ represents the Hamiltonian operator again correspond to the total energy of the system, while E is the corresponding eigenvalue for a given stationary quantum state.

Although the time independent Schrödinger equation is often introduced as the main equation in quantum mechanics, it is actually the time dependent Schrödinger equation that forms the foundational framework for understanding non-relativistic quantum mechanics. This is particularly important because many chemical systems are inherently dynamic and not in a state of rest. Using the time-independent equation alone would be inadequate to account for important changes over time.

2.2 Molecular Electronic States

Molecular electronic states are quantum states that emerge from specific electron configurations within molecular orbitals. Unlike in classical mechanics, these quantum states correspond to discrete energy levels, meaning the system can only occupy certain well-defined energies. Molecular ground states are the most preferred electronic states for molecules, because these are the states with the lowest energy. Therefore, all energy levels up to and including the highest occupied molecular orbital (HOMO) are filled with electrons, while the energy levels above and including the lowest unoccupied molecular orbital (LUMO) remain vacant. Basically, it follows that electrons occupy the lowest available energy orbitals first prior to occupying higher energy orbitals based on the Aufbau principle. However, in an excited state, at least one electron has been promoted to a higher energy orbital, leaving behind a vacancy in a lower energy level. This makes the molecule a thermodynamically unstable since a free electron is excited by gaining sufficient energy to remain in the LUMO. As a result, the system uses excitation decay processes to reduce its energy in order to bring the electron back to lower level of energy.

Each electron possesses a unique angular momentum called "spin" which can be either up or down. Specifically, 2S+1 determines the spin multiplicity of the molecular state, where S is the total spin. Molecular electronic states in which the net spin of all the electrons is zero (anti-parallel spin) are referred to as singlet states S_n, with n denoting the nth excited state. Therefore, the lowest singlet excited state is S_1 and S_0 corresponds to the ground state. In contrast, the molecular electronic states with a net spin of one arising from one pair of electrons having parallel spins are called triplet states T_n. T_1 is the lowest possible triplet state as T_0 cannot exist because if two electrons sharing the same spin in the same orbital, their electronic wavefunction vanishes because of the Pauli exclusion principle.

2.2.1 Graphical Representation of Molecular Electronic States

The symbols S_n and T_n represent electronic states, conveying essential quantum mechanical information. However, graphical representations like potential energy curves and Jablonski diagrams provide a more intuitive and comprehensive understanding of potential molecular behaviour. These visual tools illustrate energy levels, transition pathways, and the potential energy landscape, simplifying the analysis of spectroscopic transitions, reaction dynamics, and molecular physics. Commonly used in photophysics and photochemistry, they effectively illustrate processes like fluorescence, phosphorescence, internal conversion, and intersystem crossing.

The Jablonski Diagram

Electronic states and electronic transitions between these states after excitation in a molecular system can also be shown by the Jablonski Diagram (Fig. 2.1), depicts energy levels, without showing the effect of nuclear coordinates on the relative energy of the states. It is mostly used to schematically represent the processes of light absorption, emission, and energy transfer. By visualising these energy states and transitions, helps understand the mechanisms underlying various molecular interactions with light. On the vertical axis the diagram shows the energy levels of different electronic states with each state displayed as a column, and states with the same spin multiplicity are positioned adjacent to one another.

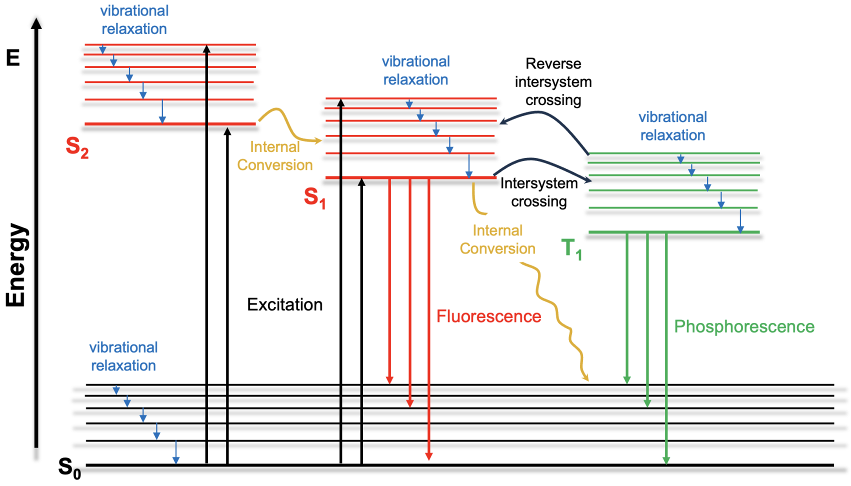

FIGURE 2.1: Jablonski Diagram for processes following photoexcitation, S_0-ground state; S_2-second singlet state; S_1-first singlet state; T_1-first triplet state; with vibrational states, and pathways of the excited state dynamics.

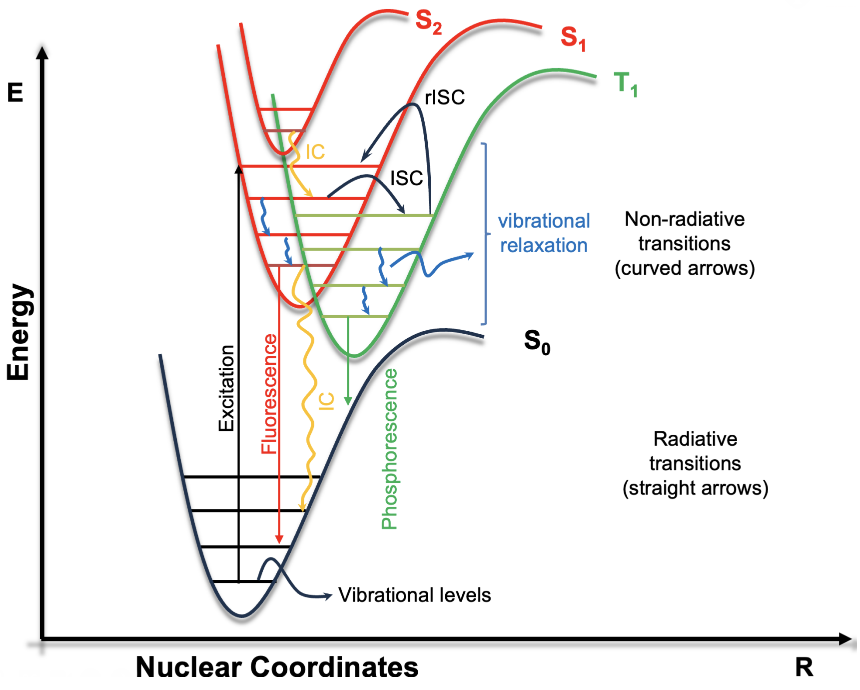

FIGURE 2.2: Potential energy curve, showing the electronic states and electronic transitions; S_0-ground state; S_2-second singlet state; S_1-first singlet state; T_1-first triplet state; ISC-Intersystem crosisng ; rISC-reverse intersystem crossing ; IC-Internal conversion

Potential Energy Curves

Potential energy curves (Fig. 2.2) graphically represent the potential energy of a molecule as a function of its nuclear coordinates, describing how the energy levels E of the states vary with the molecular geometry R, providing critical information on the potential dynamics of chemical reactions. In simple cases, such as a diatomic molecule, the minimum point on a potential energy curve corresponds to the equilibrium bond length, where the molecule is most stable, while the depth of the well indicates the bond dissociation energy. In more complex systems, analysing potential energy curves helps to understand vibrational energy levels, electronic transitions, reaction pathways, and the energy barriers as functions of multiple bond lengths and angles, offering a comprehensive view of of molecular behaviour under different conditions.

In both of the above representation, radiative processes like fluorescence and phosphorescence are illustrated with straight arrows, whereas non-radiative process such as internal conversion and intersystem crossing are marked by curved arrows. Electronic states are indicated by thick lines while vibrational states are represented by thinner lines. The Jablonski diagram is more focused on discrete states and transitions, whereas potential energy curves provide a continuous perspective on how molecular energy varies with atomic positions. Both are complementary and crucial for a comprehensive understanding of molecular behaviour.

2.3 Radiative and non-radiative transitions

Following excitation, electrons or excitons can follow a number of different transition pathways. These electronic transition pathways differ in two ways: radiative transitions and non-radiative transitions (see Fig. 2.2, 2.1). In radiative transitions, a photon is absorbed or emitted as a result of transition to a higher or lower electronic state of a molecule. So, emission, which is a two-step process, is radiative transition involves an initial absorption from the electronic ground state with specific energy, which creates an electronically excited state with different energy and then decays radiatively back into the electronic ground state (Fig. 2.3). The emission can be represented by the following equation,

$$hv = E_m - E_n = \Delta E \tag{2.4}$$

where h is the Planck constant, v is the frequency of the emission, E_m is the energy of the ground state, E_n is the energy of the excited state and ΔE is the energy gap between both ground and excited states. Radiative transitions from the first excited singlet state S_1 to the ground state S_0 are known as fluorescence, while those from the first triplet state T_1 to the ground state S_0 are known as phosphorescence.

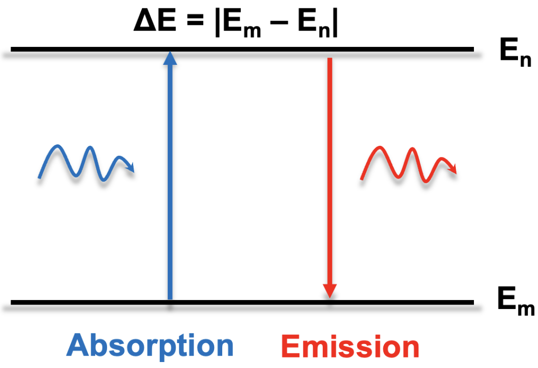

FIGURE 2.3: Schematic illustration of absorption and emission from the ground E_m and excited state E_n

On the other hand, non-radiative transitions occur without photon absorption or emission, as a result of transition to a lower electronic state. These non-radiative transitions occur between absorption and emission process. These processes include:

- **Internal conversion (IC):** radiationless deexcitation between electronic states where the spin state remains same.
- **Intersystem crossings (ISC):** non-radiative transition between the two states of different spin multiplicity. It involves a change in the spin state of the molecule and typically occurs via spin-orbit coupling.
- **Reverse intersystem crossing (rISC):** a process in which a triplet exciton is converted back into a singlet exciton. Since the singlet exciton state lies at a higher energy than the triplet state, the energy gap between them ΔE_{ST} must be overcome with the help of thermal energy.
- **Vibrational Relaxation:** involves dissipation of vibrational energy to the environment by interacting with other molecules (e.g. collisions).
- **Intramolecular vibrational redistribution (IVR):** involves redistribution of vibrational energy between different quantum states of a vibrationally excited molecule. In other words, we can say that energy transfer between different vibrational modes within the same molecule.

2.4 Excited state transition probability

The transition probability between two electronic states of an atom or molecule is a critical concept in quantum mechanics. Mathematically, the transition probability $P_{i \to f}$ for a transition from an initial state $|\psi_i\rangle$ to a final state $|\psi_f\rangle$ can be determined using the appropriate coupling operators $\hat{H}_{if}$. In the case of radiative transition, this is usually the transition dipole operator, $\hat{\mu}$, given by

$$\mu_{fi} = \langle \psi_f | \hat{\mu} | \psi_i \rangle = \int \psi_i \hat{\mu} \psi_f^* \, d\tau \tag{2.5}$$

If μ_{fi} is non-zero, the transition is considered allowed, whereas a zero value indicates a forbidden transition. The oscillator strength, f is a dimensionless quantity that provides a measure of the transition probability's strength and is defined as:

$$f_{if} = \frac{2m_e}{3\hbar^2 e^2}(E_f - E_i)|\mu_{fi}|^2 \tag{2.6}$$

where m_e is the electron mass, $\hbar$ is the reduced Planck constant, e is the electron charge, and E_f and E_i are the energies of the final and initial states, respectively. The oscillator strength incorporates both the energy difference and the transition dipole moment, offering a comprehensive measure of the likelihood and intensity of the transition. If $f = 0$, the transition is forbidden, as it depends on μ_{fi}. In addition, if an emissive state has a small oscillator strength, non-radiative decay is more likely to occur more rapidly than radiative decay. Conversely, "bright" transitions have large oscillator strengths, meaning that radiative decay is more prominent than non-radiative decay.

2.5 Born-Oppenheimer Approximation in Excited state dynamics

As electrons are much lighter than the nuclei, the motion of the electrons can be considered much faster compared to the nuclear motion. So, the nuclei can be assumed to be fixed in place and only the electron's motion will be considered. This is called the Born-Oppenheimer approximation. It treats the nuclei as moving on a potential energy surface (PES) determined by electronic energies, which adjusts instantaneously to nuclear positions. In excited state dynamics, this approximation enables the treatment of electronic transitions independently of nuclear movements.

When a molecule absorbs energy and transitions to an excited state, the electronic configuration shifts quickly compared to nuclear positions, creating a new PES for the nuclei. As a result, the electronic and nuclear motions on this new PES can be treated separately in molecules. This approximation is mostly used in molecular dynamics where it helps to speed up the computation of molecular wavefunctions and other properties for large molecules.

According to Born-Oppenheimer approximation, the molecular wavefunction can be expressed as a product of the nuclear wavefunction ($\phi(\mathbf{R})$), which depends on the nuclear coordinate R and the electronic wavefunction (ψ (**r;R**)) which is a function of the electronic coordinates r, and has a parametric dependence on the nuclear positions R.

$$\psi(\mathbf{r}, \mathbf{R}) = \phi(\mathbf{R})\psi(\mathbf{r}; \mathbf{R}) \tag{2.7}$$

This allows us to treat the nuclear and electronic terms separately while cross-terms between them can be ignored; hence the two simple and decoupled systems can be solved more efficiently even in complex interactions.

However, this approximation can break down near conical intersection, where non-adiabatic coupling between electronic and nuclear motions becomes significant. The reason behind is that for excited states even a very small amount of energy would be enough to push electrons between states with very close energies as a result potential energy surfaces of different electronic states approach each other, or even cross. In this case the nuclear motion cannot be really ignored, and one must fall back to the coupled system (i.e. coupling between nuclear and electronic motion cannot be neglected) to accurately describe the excited state dynamics.

2.6 Spin-orbit coupling

Spin-orbit coupling (SOC) in a molecule involves a relativistic interaction of a particle’s "spin" motion with its "orbital" motion. This interaction arises because an electron moving through a nucleus’s electric field experiences a magnetic field in its rest frame, which interacts with the electron’s magnetic moment associated with its spin. As a result, it mixes the electronic states of different multiplicities (fine-structure, energy splitting). According to the non-relativistic spin rule, the transitions between states with changes in the spin multiplicity are forbidden ($\Delta S = 0$), but due to SOC, spin flip transitions can occur and these forbidden transitions, such as ISC and phosphorescence, can become allowed. SOC is particularly significant in heavier atoms due to their larger nuclear charge, which allows electrons to move at speeds approaching the speed of light, enhancing relativistic effects.

Spin–orbit coupling represents a relativistic effect that modifies the non-relativistic electron Hamiltonian within a molecular system. This spin-orbit coupling term in the Hamiltonian of an electron can be expressed as:

$$\hat{H}_{SOC} = \xi(r)\, \hat{\mathbf{L}} \cdot \hat{\mathbf{S}} \tag{2.8}$$

where $\xi(r)$ is the spin-orbit coupling constant, which varies with the radial distance r from the nucleus, **L** is the orbital angular momentum operator and **S** signifies the spin angular momentum operator. The coupling between two physical quantities angular momentum eigenvector **L** and spin eigenvector **S** can be viewed as the vector sum of their eigenvectors called total angular momentum **J** (Fig. 2.4). The relationship must satisfy the following equations:

$$\mathbf{J} = \mathbf{L} + \mathbf{S} \tag{2.9}$$

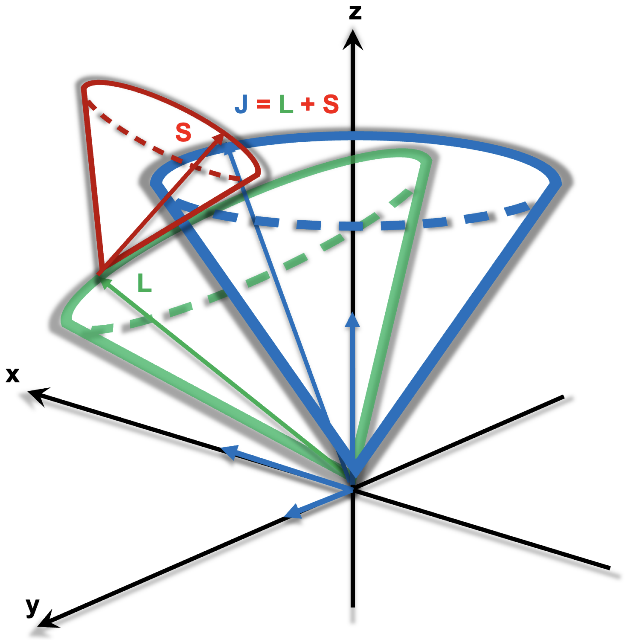

FIGURE 2.4: A visual representation of the spin–orbit coupling using a vector cone. L-Orbital angular momentum; S-Spin angular momentum; J-Total angular momentum

2.6.1 El-Sayed's rules

For spin-orbit coupling to occur, an orbital angular momentum must accompany the change in spin to conserve total angular momentum (orbital plus spin), Fig. 2.4. Thus, a transition between different spin states can be facilitated by a simultaneous change in orbital angular momentum (e.g. from a p orbital of an angular momentum 1 to a p orbital of angular momentum 0, i.e. $p_x \rightarrow p_y$ transition). This principle is known as El-Sayed's rule, which states that transitions between electronic states are more likely and faster if they involve a change in the type of orbital (e.g., from a singlet state to a triplet state) and spin-forbidden. In other words, we can say that the probability of ISC is higher when there is a change in the orbital type between the initial and final states. For instance, transitions from a singlet state ($^1\pi\pi^*$) to a triplet state ($^3n\pi^*$) are more probable than transitions between singlet and triplet states having the same orbital type ($^1\pi\pi^* \rightarrow {}^3\pi\pi^*$). Another example is ($^1n\pi^*$) $\rightarrow$ ($^3\pi\pi^*$) is faster than ($^1n\pi^* \rightarrow {}^3n\pi^*$).

2.7 Vibronic Coupling

Vibronic coupling reveals the interaction between "motion of nuclei (vibrations)" and "electronic motion" when a molecule is an electronically excited state (Fig. 2.5), breaking down the Born-Oppenheimer approximation.

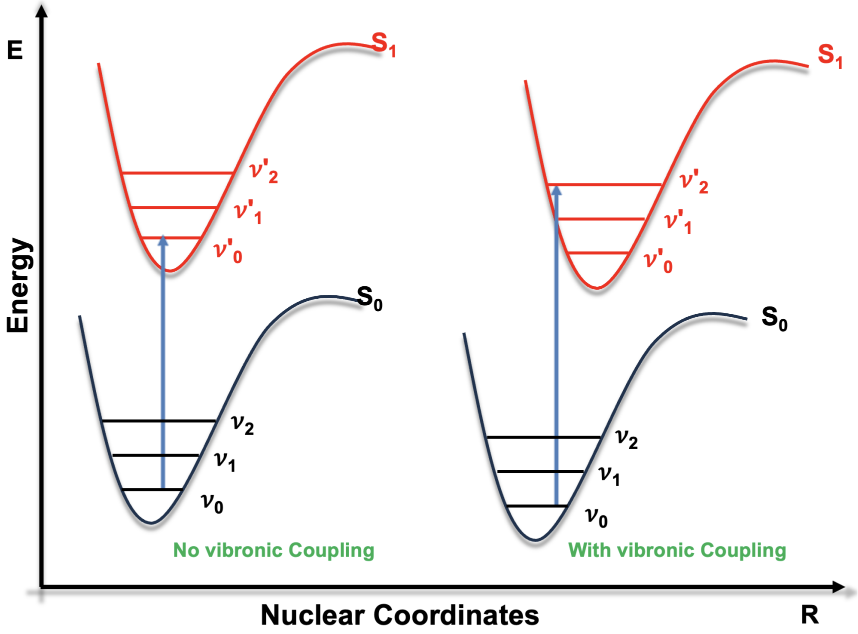

FIGURE 2.5: (a) Pure electronic transition (b) electronic transition coupled with vibrational transition, i.e. vibronic transition

This coupling arises because the electronic energy levels depend on nuclear positions, which are influenced by vibrational motions. As a result, electronic transitions are often accompanied by changes in vibrational states. Consequently, vibronic coupling permits the mixing of different electronically excited states due to small vibrations called vibronic states, facilitating different non-radiative decays such as rISC (an important factor in thermally activated delayed fluorescence (TADF)). In short, vibronic coupling involves electronic transitions accompanied by changes in the vibrational state of the nuclei, leading to mixed vibronic states. Understanding vibronic coupling is essential for optimising light extraction from molecules used in organic light-emitting diodes (OLEDs).

Mathematically, the Hamiltonian considering vibronic coupling can be written as,

$$H = \hat{H}_{\text{elec}} + \hat{H}_{\text{vib}} + \hat{H}_{\text{vc}} \tag{2.10}$$

where $\hat{H}_{\text{elec}}$ is the electronic Hamiltonian, $\hat{H}_{\text{vib}}$ is the vibrational Hamiltonian, and $\hat{H}_{\text{vc}}$ represents the vibronic coupling term.

2.8 Franck Condon Principle

The Franck–Condon principle explains the intensities of vibronic transitions, which involve the absorption or emission of a photon accompanied by changes in vibrational energy levels. This principle is based on the Born-Oppenheimer approximation and states that as the time scale of electronic transition is so fast as compared to nuclear motion, so nucleus can be considered static during the transition. Thus, electronic transition is assumed to be likely to occur when the nucleus is in its extreme position on the potential energy curve. So, atomic nuclei do not have time to readjust their positions. Instead, the nuclei move after the transition, initiating vibrational motion (energy loss without light emission) and resulting in a change in the molecule's vibrational state. These combined electronic and vibrational transitions, known as vibronic transitions, give rise to the vibrational structure observed in electronic spectra. The resulting excited state immediately after photon absorption is referred to as a Franck–Condon state where the nuclei are assumed to remain "fixed" during the transition. Consequently, electronic transitions are represented as vertical transitions on a potential energy diagram (Fig. 2.6), reflecting no change in nuclear coordinates at the moment of excitation and these vertical transitions are more likely to happen if ground and excited states are largely overlapped. The intensity of the vibrational peak in an electronically allowed transitions is proportional to the absolute square of the overlap integral between the vibrational wavefunctions of the initial and final states involved in the transition.

$$I \propto < \nu_i | \nu_f > \tag{2.11}$$

This overlap integral between vibrational state (ν) in the initial (i) and final (f) states is called Franck-Condon factor. Hence, strong vibronic coupling is often associated with high Franck-Condon factors, indicating significant overlap between vibrational states. So, this factor can successfully help to understand the reason why we get sometimes strong peaks in a spectrum and sometimes very weak (or even not observed) in absorption spectroscopy. This principle is crucial for understanding and interpreting absorption and emission spectra in molecular systems.

2.9 Herzberg-Teller Effect

The Herzberg-Teller effect is a specific manifestation of vibronic coupling. It describes how vibrational motion can cause normally forbidden electronic transitions to become partially allowed. This effect arises because the

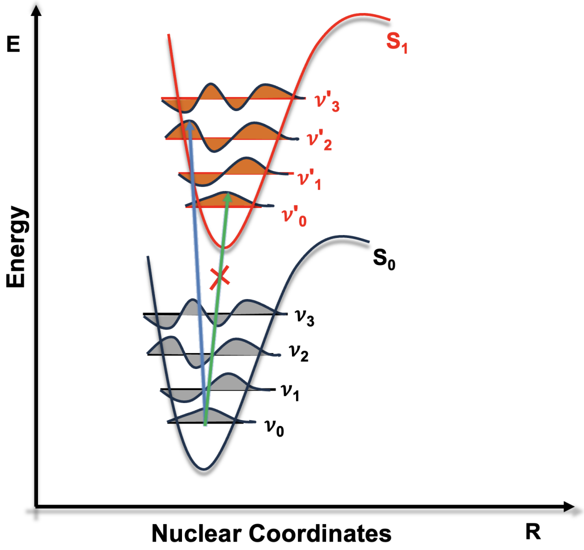

FIGURE 2.6: Franck-Condon principle energy diagram; Blue line- vertical transition. The electronic eigenstates favor the vibrational transition v_0 in the ground electronic state to v_2' in the excited electronic state, while peak intensity of v_0 to v_0' transition is expected to be low because the overlap between their wavefunctions is very low.

transition dipole moment depends on nuclear coordinates. As a result, transitions that are forbidden by symmetry can gain intensity by borrowing from allowed transitions through the coupling of electronic states with vibrational modes. Essentially, vibrational motion can mix electronic states, making electronic transitions partially allowed by providing a pathway through vibrational states. This effect is crucial for understanding vibronic coupling in molecules.

The transition dipole moment μ_{if} for a transition between initial state i and final state f can be expanded in a Taylor series around the equilibrium nuclear configuration Q_0:

$$\mu_{if} = \mu_{if}^0 + \sum_i \left(\frac{\partial \mu_{if}}{\partial Q_i} \right)_{Q_0} Q_i + \cdots \tag{2.12}$$

where:

- μ_{if}^0 is the transition dipole moment at the equilibrium position.
- $\left(\frac{\partial \mu_{if}}{\partial Q_i} \right)_{Q_0}$ is the first-order derivative of the transition dipole moment with respect to the nuclear coordinate Q_i at equilibrium.
- Q_i represents the normal coordinates of the vibrational modes.

The zero-order term μ_{if}^0 corresponds to Franck-Condon component where the transition dipole moment assuming no nuclear displacement. After this, all terms mediates Herzberg-Teller component. The first-order term $\left(\frac{\partial \mu_{if}}{\partial Q_i}\right)_{Q_0} Q_i$ accounts for the linear dependence on nuclear displacements. Higher-order terms can be included for more accurate descriptions, but are often less significant.

This expansion allows for the inclusion of vibrational contributions to electronic transitions, leading to vibronic transitions where electronic and vibrational states are coupled. The Herzberg-Teller effect thus enables the analysis of transitions that involve changes in both electronic and vibrational states, contributing to the fine structure observed in molecular spectra. When a transition is very intense, like in strong fluorescence, using the Franck-Condon approximation is usually sufficient. However, if the transition is weak, like in weak fluorescence, we need to go beyond the Franck-Condon approximation and consider the Herzberg-Teller effect to provide a more complete and accurate explanation for the observed spectral features.

2.10 Mixing Singlet and Triplet States in TADF

Energy splitting between singlet and triplet states ($E_S - E_T$) has an important role in the degree and efficiency of TADF as k_{rISC} can only occur if the state mixing between triplet and singlet states is possible. First and second order perturbation theory offer ways to mix different states.

1st order

To a first approximation, first-order mixing is the interaction that occurs directly between the S_1 and T_1 states. The degree of state mixing between S_1 and T_1 can be quantified using the first-order mixing coefficient, λ [24]:

$$\lambda \approx \frac{\mathrm{SOC}_{S_1-T_1}}{\Delta E_{\mathrm{ST}}} \tag{2.13}$$

Here, λ is directly proportional to the magnitude of SOC and inversely proportional to the energy difference between the singlet and triplet states, ΔE_{ST}. The magnitude of SOC is primarily influenced by the presence of heavy atoms. However, the majority of TADF emitters possess the lowest energy singlet and triplet excited states that are both of charge-transfer nature, which often results in a relatively small SOC between these states [25]. Since most TADF emitters are composed of light elements, the heavy atom effect on SOC is minimal.

The rate of ISC and rISC also depends on energy splitting can be described using Arrhenius equation,

$$k_{rISC} \approx k_{ISC}\, exp[(-\Delta E_{ST})/(K_B T)] \tag{2.14}$$

where k_{ISC} and k_{rISC} describe the rate constants for intersystem crossing (from singlet to triplet) and reverse intersystem crossing (from triplet back to singlet respectively; K_B is the Boltzmann constant and T is temperature. The threshold value of ΔE_{ST} where we observe non-negligible rISC is often presented as < 0.2 eV [26]. Greater energy splitting between singlet and triplet states increases the rISC. This splitting is proportional to the exchange interaction integral J as shown below:

$$E_S - E_T = \Delta E_{ST} = 2J \tag{2.15}$$

which further depends on to the excited and ground state wavefunction overlap, i.e., the overlap between the HOMO and the LUMO:

$$J = \int\int \phi(r_1)\psi(r_2)(\frac{e^2}{r_1 - r_2})\phi(r_2)\psi(r_1)dr_1 dr_2 \tag{2.16}$$

where $\phi(r_1)$ and $\psi(r_2)$ represent the HOMO and LUMO wavefunctions, respectively, r_1 and r_2 are position vectors and e is the electron charge. So, for fast rISC, overlapping of HOMO and LUMO should be reduced. This is the primary design criteria for TADF materials.

It is generally observed that a smaller energy gap ΔE_{ST} between the singlet and triplet states leads to faster rISC. However, this relationship is not always linear. Some materials with a relatively large ΔE_{ST} can also have fast rISC rates [27]. Therefore, the efficiency of TADF emitters cannot be fully explained by the first order mixing of states. Spin-vibronic coupling, which involves interactions beyond first-order mixing, may also play a significant role.

2nd order

Reverse intersystem crossing in TADF emitters doesn't always happen directly from the T_1 to the S_1 but may involve intermediate excited states, which can be accessed due to spin-vibrational coupling (Fig. 2.7). In this second-order perspective, the Born-Oppenheimer approximation breaks down, requiring the consideration of both electronic and vibrational degrees of freedom. Consequently, the up-conversion from T_1 to the S_1 happens through higher triplet states T_{1+n} because of strong vibrational coupling between T_1 and T_{1+n}. This process, called reverse internal conversion, allows energy to move from T1 to higher triplet states T_{1+n} efficiently. If one of these higher triplet states T_{1+n} has a different electronic nature compared to S_1, the SOC is stronger, allowing rISC to proceed. To facilitate efficient reverse internal conversion

(RIC), T_1 and T_{1+n} states should close in energy to maximise the vibrational coupling [25], [28]. Furthermore, a negative energy gap between the triplet state with localized electronic excitation ^3LE and the singlet state with charge transfer ^1CT also speeds up rISC [29]. In short, the process of rISC can be more complex than a direct T_1 to S_1transition and involves additional excited states and strong vibrational interactions, which enhance the efficiency of TADF emitters.

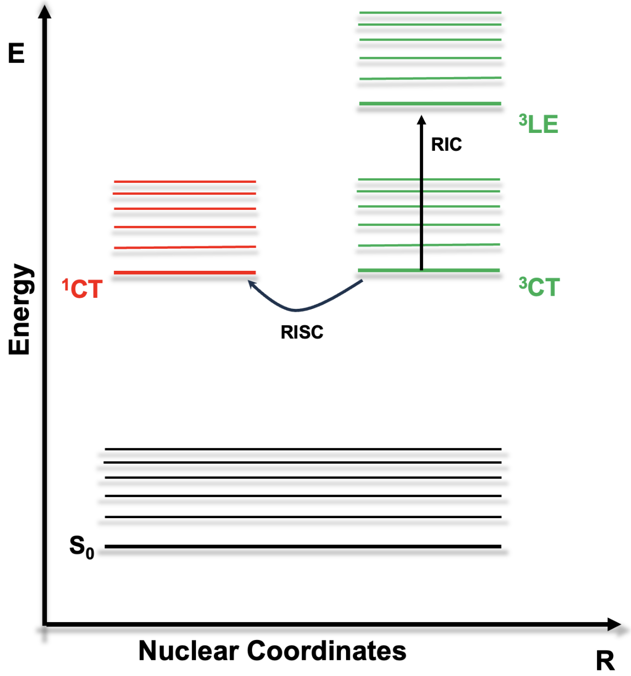

FIGURE 2.7: Jablonski diagram of TADF via intermediate ^3LE triplet state

2.11 Fundamental Concepts for TADF Molecular Design

The designing of TADF molecules involves understanding of all these factors described below in detail:

- For the TADF process , radiative and non-radiative decay of triplet state should be slow and the energy gap between the singlet and triplet states (ΔE_{ST}) must be less than 0.1 eV for rISC to occur [30] . This can be done by spatially separating the HOMO and LUMO orbitals. (eq. 2.15)
- TADF emitters usually gives broad emission spectra > 100 nm which is due to some specific molecular vibrations results in reduction of the

colour purity (needed < 50 nm). Hence, it is necessary to understand which molecular vibrations contribute in TADF and which ones in broadening of spectra to reduce the flexibility of the molecule. That means by enhancing the rigidity of a molecule, a narrow spectrum at the desired colour coordinate can be obtained. So, it is worth aiming to design molecular structures having intrinsically smaller FWHM.

- To achieve high efficiency in TADF materials requires large radiative rate and small ΔE_{ST}. As discussed before ΔE_{ST} could be small by the good separation of the HOMO and LUMO, but it also reduces fluorescence rate (k_F) while molecules significant HOMO–LUMO overlap typically exhibit higher fluorescence rate (k_F), but at the cost of a larger ΔE_{ST}, which limits their TADF contribution. As, these two requirements conflict with each other, a compatibility of a smaller ΔE_{ST} and a sufficiently long radiative decay time requires overcoming competing non-radiative decay pathways [19] which can be achieved via careful balance between the overlap of HOMO and LUMO.

2.12 TADF emitter Design

By keeping all factors described in previous section in mind, this thesis will explore following two approaches to design an efficient OLED molecule:

2.12.1 Donor-Acceptor Structure

The most popular approach to design TADF emitter is donor-acceptor (D-A) architecture in which D-A moities are in poor electronic communication with each other. In this setup, the HOMO is mainly located on the donor, while the LUMO is on the acceptor. This setup promotes the formation of intramolecular charge transfer (CT) states between the donor and acceptor units with localised HOMO and LUMO orbitals and leads to a decrease in electronic exchange energy and, so the singlet-triplet gap will also reduce (needs to be < 0.1 eV). This reduction increased rISC and hence TADF. These D-A, or donor-acceptor-donor (D-A-D) structure showed a well description of a second-order vibronic-coupled spin-orbit coupling mechanism with the spin flip mediated between and CT states by a local triplet state either from a D or A [31], [32]. The strength of the donor and acceptor units influences the localisation of electron density on the HOMO and LUMO, respectively. Stronger donor and acceptor units lead to more localised electron densities, further reducing ΔE_{ST}. Apart from localisation of

HOMO and LUMO, still a minimal overlap between orbitals is necessary for rISC to take place which can be favoured by increasing the twist angle (D-A moieties are not in the same plane) between the donor and acceptor moiety called dihedral angle. This also increased the oscillator strength f. It means the conformation of the donor and acceptor units affects the spatial separation of these frontier orbitals in the way that more twisted conformations result in more HOMO-LUMO overlap, results in larger oscillator strength. But this twisting angle will also increase vibrational motion giving broad emission which deteriorates the colour purity. In short, twist angle is needed for efficient TADF, and rigidness needed for narrow emitter. Hence, a compromise between small ΔE_{ST} and overlap has to be found. To achieve this, many factors such as molecular geometry, the dielectric medium, the presence of low energy triplet excited states, localised in the D or A units will have to be analysed.

From a design perspective, achieving this can be done by using substituents near the D-A bond, such as adding methyl groups. Incorporating multiple donor or acceptor groups, which force the molecule into a twisted geometry (non-planar structure) to alleviate steric congestion. These twisted geometries decrease the interaction between groups. Despite the thousands of reported donor-acceptor TADF emitters, they are typically made from a relatively small set of components. Adjusting the nature of the donor and acceptor groups allows for colour tuning in D-A systems by changing the band gap ΔE_{ST} and the energies of the excited states. D-A systems have achieved remarkable efficiencies, comparable to established phosphorescent materials

2.12.2 Multiple Resonance Structure

Although D-A emitters can produce all visible colours, their emission is often broad, indicating emission from CT states with significant reorganization between ground and excited states. Broad emission spectra reduce colour purity, which is important for OLEDs. The broadness is measured by the FWHM. Aromatic compounds are primarily localised between atoms, thus forming π-bonds. This bonding/antibonding character enhances the vibronic coupling between S_0 and S_1 as well as vibrational relaxation at S_1 state giving broad emission. To suppress emission band broadening, in 2016 Hatakeyama et al. introduced a new strategy to design structures using p- and n-doped fragments called multiple resonance structure [33]. This approach uses complementary multiple resonance effects to localise the electron density of the HOMO and LUMO on neighboring atoms compared to between atoms. This localisation not only reduces the singlet-triplet gap, promoting rISC but also minimizes their bonding/antibonding character. Consequently, reduced vibronic coupling and limited vibrational relaxation result in a narrower emission bandwidth [34].

Hence, MR-TADF emitters designed to be rigid and functional group/atoms should have greater push-pull effect, causing minimal geometry changes between the ground and excited states. This leads to small Stokes shifts and narrowband emission, characterized by a small FWHM.

Chapter 3

Quantum Chemistry Methodologies

Quantum chemistry methodologies are essential tools in computational chemistry, which combine the power of computation and the foundation of physics to unravel chemical phenomena and calculate the electronic properties of molecules [35]. It offers significant advantages over traditional experimental methods by avoiding typical laboratory constraints, such as long reaction times and the use of hazardous materials [35, 36]. This allows for the exploration of molecules that have not yet been synthesised in the lab, speeding up scientific research. The challenge in quantum chemistry is to simplify the calculation sufficiently to be solvable within a reasonable timescale, but still sufficiently accurate enough to predict the desired physical quantity. Despite these challenges, selecting an appropriate theoretical framework is crucial to ensure that the electronic representation of the molecules is both physically meaningful and computationally feasible. This chapter offers a comprehensive overview of the quantum chemistry methods employed in this thesis. ORCA quantum chemistry package is predominantly used throughout for computations [37]. However, for specific sections, electronic properties have been calculated with TURBOMOLE [38]. The geometries of all molecules were optimised using density functional theory (DFT), time-dependent density functional theory (TDDFT), linear response time-dependent density functional theory (LR-TDDFT), or spin-flip time-dependent density functional theory (SF-TDDFT). *Ab initio* Molecular dynamics (AIMD) have been used to probe the conformational dynamics of designed molecules. The B3LYP (Becke, 3-parameter, Lee–Yang–Parr) and LRC-BLYP (Long range corrected Becke-Lee–Yang–Parr)functionals were applied with the def2-SVP and def2-TZVP basis sets.

3.1 Energy of a Many-Electron System

The total energy of a many-electron system is a fundamental quantity in quantum chemistry, obtained as the expectation value of the Hamiltonian operator, which encapsulates all contributions to the system's energy:

$$E = \langle \psi | \hat{H} | \psi \rangle \tag{3.1}$$

where ψ is the many-body wavefunction representing the system's quantum state, and $\hat{H}$ is the Hamiltonian operator, expressed in the non-relativistic context for many-body system as,

$$\hat{H} = -\frac{1}{2}\sum_{i=1}^{n}\nabla_i^2 - \frac{1}{2}\sum_{A=1}^{N}\frac{1}{M_A}\nabla_A^2 - \sum_{i=1}^{n}\sum_{A=1}^{N}\frac{Z_A}{r_{iA}} + \sum_{i=1}^{n}\sum_{j>i}^{n}\frac{1}{r_{ij}} + \sum_{A=1}^{N}\sum_{B>A}^{N}\frac{Z_A Z_B}{r_{AB}} \tag{3.2}$$

where N denotes the total number of nuclei and n denotes the total number of electrons. M_A represents mass of nucleus A expressed in units of the electron mass m_e and Z_A is its atomic number. The symbol r_{iA} represents the distance between electron i and nucleus A, r_{ij} the separation between electron i and j, and r_{AB} the distance between nucleus A and nucleus B. The Laplacian operator ∇^2 in Cartesian coordinates is given by:

$$\nabla^2 = \frac{\partial^2}{\partial x^2} + \frac{\partial^2}{\partial y^2} + \frac{\partial^2}{\partial z^2} \tag{3.3}$$

In Equation (3.2) the first two terms account for the kinetic energies of the electrons and the nuclei. The third term corresponds to the Coulomb interaction between electrons and nuclei. The fourth term represents repulsion among the electrons, whereas the fifth term describes the repulsive interaction between the nuclei.

Assuming the clamped nuclear representation (*i.e.* removing the kinetic energy of the nuclei), the time-independent Schrödinger equation for the electrons can be employed to find the total energy (E_e) of a molecular system:

$$\hat{H}_e \psi_e = E_e \psi_e \tag{3.4}$$

where the electronic Hamiltonian operator ($\hat{H}_e$) takes the form

$$\hat{H}_e = -\frac{1}{2}\sum_{i=1}^{n}\nabla_i^2 - \sum_{i=1}^{n}\sum_{A=1}^{N}\frac{Z_A}{r_{iA}} + \sum_{i=1}^{n}\sum_{j>i}^{n}\frac{1}{r_{ij}} \tag{3.5}$$

and ψ_e is the electronic wavefunction.

However, the above equation (3.4) is only analytically solvable for systems containing a single electron. In many-electron systems, the computational complexity and high dimensionality make exact solutions infeasible, requiring the adoption of approximate methods.

To get the total energy of the system, one must find two unknowns, *i.e.* the energy and wavefunction. To solve this, the variational theorem plays a crucial role. We choose a trial wavefunction and then compute its expected energy, which helps to assess its quality. A poor trial wavefunction leads to an energy higher than the actual value and inaccurate predictions. Therefore, among all approximate wavefunctions, the optimal choice is the one that minimises the calculated energy, bringing it as close as possible to the exact value:

$$E_{\text{trial}} = \frac{\langle \psi_{\text{trial}} | \hat{H} | \psi_{\text{trial}} \rangle}{\langle \psi_{\text{trial}} | \psi_{\text{trial}} \rangle} \leq E_{\text{exact}} \tag{3.6}$$

The denominator in Equation (3.6) is required only if the trial wavefunction has not been normalized beforehand. Improving the trial wavefunction can be achieved through linear combinations of wavefunctions or expanding the basis set.

3.2 Electronic Wavefunction and Slater determinant

In studying molecular systems, one examines the complete electronic wavefunction by taking into account both the spatial and spin degrees of freedom of the electrons. Since electrons are fermions, they must obey the Pauli exclusion principle, which forbids two identical particles from occupying the same quantum state. This leads to orthonormal electronic wavefunctions, and if two electrons were assigned identical quantum numbers, the overall wavefunction would vanish. Furthermore, when two electrons have the same spatial coordinates, their spins must be opposite.

Moving to a system of two electrons, labeled i and j, each residing in a different quantum state, the combined wavefunction in this case can first be expressed as:

$$|\psi(\mathbf{r}_1, \mathbf{r}_2)\rangle = \phi_i(\mathbf{r}_1)\phi_j(\mathbf{r}_2) \tag{3.7}$$

where $\phi_i(\mathbf{r_1})$ and $\phi_j(\mathbf{r_2})$ denote the single-electron wavefunctions for electrons i and j, respectively. However, this representation fails to address the indistinguishability of the electrons and cannot be possible to label an electron to one particular quantum state. Thus, a linear combination of the wavefunctions is introduced to yield a normalized wavefunction, which accounts for electron indistinguishability. This is denoted by:

$$|\psi(\mathbf{r}_1, \mathbf{r}_2)\rangle = \frac{1}{\sqrt{2}} \left[\phi_i(\mathbf{r}_1)\phi_j(\mathbf{r}_2) - \phi_i(\mathbf{r}_2)\phi_j(\mathbf{r}_1)\right] \tag{3.8}$$

Alternatively, in matrix determinant form:

$$|\psi(\mathbf{r}_1, \mathbf{r}_2)\rangle = \frac{1}{\sqrt{2}} \begin{vmatrix} \phi_i(\mathbf{r}_1) & \phi_i(\mathbf{r}_2) \\ \phi_j(\mathbf{r}_1) & \phi_j(\mathbf{r}_2) \end{vmatrix} \tag{3.9}$$

Note the negative sign in this linear combination, indicating the antisymmetric character of the single-electron wavefunction. This means that interchanging particles results in a sign change of the wavefunction, i.e.

$$\psi(\mathbf{r}_1, \mathbf{r}_2) = -\psi(\mathbf{r}_2, \mathbf{r}_1) \tag{3.10}$$

One can extend this form to multi-electron systems by using an analogous determinant construction, known as a Slater determinant, which is the determinant of a matrix composed of one-electron orbitals that builds the overall many-electron wavefunction. This approach ensures that the wavefunction changes sign upon the exchange of two electrons, maintaining the Pauli exclusion principle. An N-electron system is described by a wavefunction of the form:

$$|\psi(\mathbf{r}_1, \mathbf{r}_2, ..., \mathbf{r}_N)\rangle = \frac{1}{\sqrt{N!}} \begin{vmatrix} \phi_i(\mathbf{r}_1) & \phi_i(\mathbf{r}_2) & \cdots & \phi_i(\mathbf{r}_N) \\ \phi_j(\mathbf{r}_1) & \phi_j(\mathbf{r}_2) & \cdots & \phi_j(\mathbf{r}_N) \\ \vdots & \vdots & \ddots & \vdots \\ \phi_N(\mathbf{r}_1) & \phi_n(\mathbf{r}_2) & \cdots & \phi_N(\mathbf{r}_N) \end{vmatrix} \tag{3.11}$$

where each row represents different electron in the multi-electron wavefunction. The number of rows corresponds to the total number of electrons in the system. Each column represents a specific spatial or spin orbital that the electrons can occupy. The number of columns corresponds to the total number of orbitals being considered in the wavefunction. Thus, a Slater determinant is a matrix in which the element at the i-th row and j-th column corresponds to the value of the i-th electron's wavefunction evaluated in the j-th orbital. In compact notation, the above Slater determinant takes the form:

$$|\psi(\mathbf{r}_1, \mathbf{r}_2, ..., \mathbf{r}_N)\rangle = |\phi_i\phi_j\phi_k...\phi_N\rangle \tag{3.12}$$

This determinant form guarantees that the electrons remain indistinguishable, with each electron effectively linked to every orbital. Swapping any two rows or columns, which corresponds to exchanging two electrons, flips the sign of the wavefunction. Furthermore, if two rows become identical (i.e., two electrons occupy the same quantum state), the determinant vanishes, upholding the Pauli exclusion principle.

3.3 Wavefunction Theory

Wavefunction theory is a framework within quantum chemistry in which the quantum state of a system is fully described by its wavefunction ψ, a mathematical entity that encodes all quantum mechanical details of the particles and their interactions, and can be derived by solving the Schrödinger equation. *ab initio* methods, which are grounded in first principles and do not rely on empirical data and computations depends only on the quantum mechanics, form the foundation of wave function theory. It is derived directly from theoretical principles. It explains how electrons behave within a molecule. It solves Schrödinger equation, providing both the system's energy and its corresponding wavefunction. In this section, we will outline some of the methods used in this thesis.

3.3.1 Hartree–Fock Approximation

The Hartree-Fock (HF) method is one of the simplest *ab initio* approaches developed to tackle the complexities of many-body systems. This method approximates the true wavefunction of a multi-electron system by using a single Slater determinant built from chosen spin-orbitals. This determinant represents the arrangement of electrons in a system while inherently enforcing the antisymmetry required by the Pauli exclusion principle. This assumption implies that the correlation effects between electrons are neglected, and the wavefunction is represented as a product of single-electron wavefunctions, each occupying a molecular orbital (MO) which is formed by a linear combination of atomic orbitals (LCAO). In addition to the Born–Oppenheimer approximation, this theory introduces an additional approximation to lessen more the computational cost of solving the Schrödinger equation. To understand the formulation of HF theory, we start from the single-electron Hamiltonian in equation (3.5) and split it into two components:

$$\hat{H}_e = \sum_{i=1}^{n} \hat{h}_i + \sum_{i=1}^{n} \sum_{j>i}^{n} \frac{1}{r_{ij}} \tag{3.13}$$

In above equation, the operator $\hat{h}_i$ is a one-electron Hamiltonian for electron i, comprising its kinetic energy and the Coulomb attraction between that electron and the nuclei:

$$\hat{h}_i = -\frac{1}{2}\sum_{i=1}^{n} \nabla_i^2 - \sum_{i=1}^{n}\sum_{A=1}^{N} \frac{Z_A}{r_{iA}} \tag{3.14}$$

The remaining term is a two-electron operator representing how two electrons interact due to their electric charges which cannot be easily separable for each electron, requiring the positions of both electrons. To avoid the prohibitive cost of computing every pairwise interaction directly, Hartree–Fock employs a mean-field approximation in which each electron moves in an effective potential generated by the averaged charge distribution of all other electrons. Consequently, complex two-electron operator can be reformulated as an effective one-electron term in the equation. Adding this to the one-electron Hamiltonian $\hat{h}_i$ produces the Fock operator ($\hat{f}_i$), which governs the motion of an individual electron in its spin-orbital. The Fock operator is determined as

$$\hat{f}_i = \hat{h}_i + \hat{v}_i^{HF} \tag{3.15}$$

where the operator $\hat{v}_i^{HF}$ is the Hartree-Fock potential represents the mean-field electrostatic potential generated by all other electrons acting on electron i:

$$\hat{v}_i^{HF} = \sum_{j=1}^{n} (\hat{J}_j - \hat{K}_j) \tag{3.16}$$

where, $\hat{J}$ and $\hat{K}$ denote the Coulomb and exchange operators, respectively. The Coulomb operator$\hat{J}$ represents the classical electrostatic potential created by electron j at position $\mathbf{r}_2$, acting on electron i at position $\mathbf{r}_1$ is described by:

$$\hat{J}_j(\mathbf{r}_1) = \int \frac{1}{r_{12}} \phi_j^\star(\mathbf{r}_2)\phi_j(\mathbf{r}_2) d\mathbf{r}_2 \tag{3.17}$$

The exchange operator $\hat{K}_j$ has no classical counterpart; it embodies the energy change due to exchanging two electrons. When $\hat{K}_j$ acts on an electron's spin-orbital, it effectively swaps that orbital with electron $j's$, reflecting the antisymmetric requirement of the many-electron wavefunction:

$$\hat{K}_j(\mathbf{r}_1)\phi_i(\mathbf{r}_1) = \left[\int \frac{1}{r_{12}} \phi_j^\star(\mathbf{r}_2)\phi_i(\mathbf{r}_2) d\mathbf{r}_2\right] \phi_j(\mathbf{r}_1) \tag{3.18}$$

Hence, the Fock operatore can be expressed as:

$$\hat{f}_i = \hat{h}_i + \sum_{j=1}^{n}(\hat{J}_j - \hat{K}_j) \tag{3.19}$$

Hence, by solving the Schrödinger equation for electron i, one arrives at the HF equation that determines its eigenvalue ϵ_i. This HF equation is expressed as:

$$\hat{f}|\phi_i\rangle = \epsilon_i|\phi_i\rangle \tag{3.20}$$

By projecting the HF equation onto the orbital $\phi_i|$, multiplying on the left by $\langle\phi_i|$ and then integrating over all coordinates, one obtains the expression for the energy ϵ_i of electron i:

$$\langle\phi_i|\hat{f}_i|\phi_i\rangle = \epsilon_i\langle\phi_i|\phi_i\rangle \tag{3.21}$$

As we got normalised wavfunctions, $\langle\phi_i|\phi_i\rangle = 1$. By substituting equation (3.19) into the left-hand side of above equation, yields the expression for the eigenvalue ϵ_i:

$$\epsilon_i = h_{ii} + \sum_{j=1}^{n}(J_{ij} - K_{ij}) \tag{3.22}$$

The above first term represents the energy of electron i as it moves within the potential created by the nuclei:

$$h_{ii} = \langle\phi_i|\hat{h}_i|\phi_i\rangle = \int \phi_i^*(\mathbf{r_1})\left(-\frac{1}{2}\sum_{i=1}^{n}\nabla_i^2 - \sum_{i=1}^{n}\sum_{A=1}^{N}\frac{Z_A}{r_{iA}}\right)\phi_i(\mathbf{r}_1)\,d\mathbf{r}_1 \tag{3.23}$$

While the second and third terms represents electron-electron coulomb repulsion and electron-electron exchange interaction respectively, arising from anti-symmetry principle Consequently, the approximate two-electron repulsion energy can be expressed as,

$$J_{ij} = \langle\phi_i\phi_i|\hat{J}_{ij}|\phi_j\phi_j\rangle = \iint \phi_i^*(\mathbf{r}_1)\phi_i(\mathbf{r}_1)\frac{1}{r_{ij}}\phi_j^*(\mathbf{r}_2)\phi_j(\mathbf{r}_2)d\mathbf{r}_1 d\mathbf{r}_2 \tag{3.24}$$

$$K_{ij} = \langle\phi_i\phi_j|\hat{K}_{ij}|\phi_j\phi_i\rangle = \iint \phi_i^*(\mathbf{r}_1)\phi_j(\mathbf{r}_1)\frac{1}{r_{ij}}\phi_j^*(\mathbf{r}_2)\phi_i(\mathbf{r}_2)d\mathbf{r}_1 d\mathbf{r}_2 \tag{3.25}$$

Within the HF scheme, the electronic energy is obtained by substituting the exact two-electron operator in equation 3.13 with its mean-field counterpart, yielding,

$$\sum_{i=1}^{n}\sum_{j>i}^{n} = \frac{1}{2}\sum_{i=1}^{n}\sum_{j=1}^{n} \tag{3.26}$$

The HF energy becomes,

$$E_{HF} = \langle\psi|\hat{H}_e|\psi\rangle = \sum_{i=1}^{n}\hat{h}_{ii} + \sum_{i=1}^{n}\sum_{j>i}^{n}(J_{ij} - K_{ij}) \tag{3.27}$$

$$= \sum_{i=1}^{n} h_{ii} + \frac{1}{2}\sum_{i=1}^{n}\sum_{j=i}^{n}(J_{ij} - K_{ij}) \tag{3.28}$$

If we compare the above equation with eq. (3.22) shows that HF total energy E_{HF} doesn't equal the straightforward sum of the individual electron's energies. To express HF energy in terms of the ϵ_i, the above equation must be reorganised accordingly,

$$\begin{aligned} E_{HF} &= \left[\sum_{i=1}^{n}\hat{h}_{ii} + \sum_{i=1}^{n}\sum_{j=1}^{n}(J_{ij} - K_{ij})\right] - \frac{1}{2}\sum_{i=1}^{n}\sum_{j=1}^{n}(J_{ij} - K_{ij}) \\ &= \sum_{i=1}^{n}\epsilon_i - \frac{1}{2}\sum_{i=1}^{n}\sum_{j=i}^{n}(J_{ij} - K_{ij}) \end{aligned} \tag{3.29}$$

Total energy of the system can be obtained by adding simply the nuclear repulsion term:

$$E = \sum_{i=1}^{n}\epsilon_i - \frac{1}{2}\sum_{i=1}^{n}\sum_{j=i}^{n}(J_{ij} - K_{ij}) + \sum_{A=1}^{N}\sum_{B>A}^{N}\frac{Z_A Z_B}{r_{AB}} \tag{3.30}$$

In a closed-shell system, such as the electronic ground state of organic molecules, there is an even number of electrons. Each molecular orbital is occupied by two electrons with opposite spins, sharing the same spatial wavefunction (Fig. 3.1). Consequently, the Slater determinant for the system is expressed as follows:

$$|\psi(\mathbf{r}_1, \mathbf{r}_2, \ldots, \mathbf{r}_N)\rangle = |\phi_i\bar{\phi}_i\phi_j\bar{\phi}_j\ldots\phi_N\bar{\phi}_N\rangle \tag{3.31}$$

In this notation, a bar above an individual electronic wavefunction denotes the opposite spin. This approach, where each orbital is associated with two electronic wavefunctions that share the same spatial component but have different spin components, is known as the Restricted Hartree–Fock (RHF) method.

An open-shell system refers to a system whose net spin is non-zero meaning there are one or more unpaired electrons, such as in the first triplet excited state. Two variations of HF theory are used to describe an open-shell system: restricted open-shell Hartree–Fock (ROHF) theory and unrestricted Hartree–Fock (UHF) theory. In ROHF theory, the system is assigned two types of orbitals (Fig. 3.1). First, doubly occupied orbitals are used as much as possible for all paired electrons. Then, the remaining unpaired electrons occupy singly occupied orbitals. The Slater determinant representing an ROHF wavefunction is given by:

$$|\psi(\mathbf{r}_1, \mathbf{r}_2, \ldots, \mathbf{r}_N)\rangle = |\phi_i\bar{\phi}_i\phi_j\bar{\phi}_j \ldots \phi_{N_D}\bar{\phi}_{N_D}\phi_{N_D+1}\phi_{N_D+1} \ldots \phi_{N_D+N_S}\rangle \tag{3.32}$$

where N_D denotes the number of doubly occupied orbitals and N_S the number of singly occupied orbitals. Two electrons in a doubly occupied orbital share the same spatial wavefunction but have different spin wavefunctions.

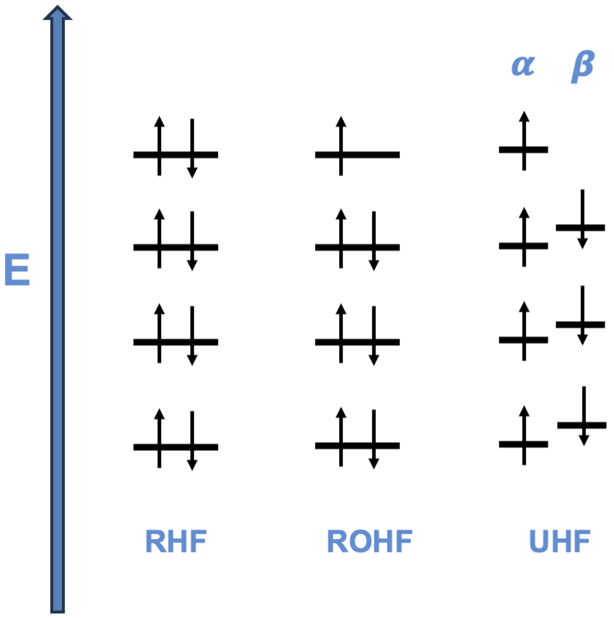

FIGURE 3.1: Schematic Representation of the orbitals in RHF, ROHF and UHF.

On the other hand, the UHF method is the more commonly used method to describe an open-shell system. UHF also employs two types of orbitals similar to ROHF, but it uses different sets of orbitals for each spin (Fig. 3.1). The Slater determinant representing the UHF wavefunction is given by:

$$|\psi(\mathbf{r}_1, \mathbf{r}_2, \ldots, \mathbf{r}_N)\rangle = |\phi_i^{\alpha}\phi_j^{\alpha} \ldots \phi_{N_\alpha}^{\alpha}\phi_i^{\beta}\phi_j^{\beta} \ldots \phi_{N_\beta}^{\beta}\rangle \tag{3.33}$$

where ϕ^{α} and ϕ^{β} refer to wavefunctions of spin-α and spin-β electrons respectively, N_α denotes the number of spin-α electrons, and N_β the number of spin-β electrons. However, α and β electrons are treated differently, as if no given electron pairs ever share the same orbital. This results in spin contamination, which is the artificial mixing of higher-energy spin eigenstates (e.g., a doublet wavefunction exhibiting characteristics of quartet, sextet, etc., or a triplet wavefunction exhibiting characteristics of quintet, septet, etc. [39].

In summary, the HF theory approximates the many-body wavefunction as a single Slater determinant, and introduces the HF potential to simplify the solution of the electronic Schrödinger equation, making it computationally feasible for many-electron systems.

3.3.2 Roothaan–Hall equation and self-consistent field (SCF) method

The Self-Consistent Field (SCF) method is the basis for solving the HF equations. It is implemented numerically using iterative algorithms such as the Roothaan-Hall equations or the density matrix formulation. This approach transforms the problem of determining the wavefunction (due to dependence of the Fock matrix elements on spatial wavefunctions) into one of calculating coefficients. By expressing molecular orbitals as a combination of basis functions multiplied by coefficients, the SCF method allows for the determination of these coefficients (arising from the diagonalization of the Fock matrix) iteratively. This iterative process involves making initial guesses for the coefficients and iteratively solving these equations until a predefined convergence criterion is met (a consistent field (or set of orbitals) is obtained that does not change with further iterations). So, energy of a molecular orbital can be obtained from the modified version of the HF equation called Roothaan-Hall equation. [40]

$$\mathbf{F}C = \mathbf{S}C\epsilon \tag{3.34}$$

where **F** is the Fock matrix, C is the coefficient matrix, **S** is the overlap matrix (representing the overlap between atomic orbitals) and and ϵ represents the matrix of orbital energies. The eq. 3.34 has a non-trivial solution only if the following equation is satisfied :

$$\det|\mathbf{F} - \epsilon_a \mathbf{S}| = 0 \tag{3.35}$$

This equation cannot be solved directly due to the dependence of the Fock matrix elements on spatial wavefunctions. Thus, the SCF process involves making an initial guess of the orbitals, solving the S.E to obtain a more accurate set of orbitals, and iteratively refining this guess to minimise energy until the results converge to a stable threshold. It involves (Fig. 3.2),

- Initialization: Begin with an initial guess for the MOs or spin-orbitals.
- Build Fock Matrix: Construct the Fock matrix using the current set of MOs. The Fock matrix represents the one-electron Hamiltonian operator modified by the electron-electron interaction.
- Diagonalisation: Diagonalise the Fock matrix to obtain a new set of MO coefficients.
- Update: Update the MO coefficients and repeat steps 2 and 3 until convergence criteria are met.
- Convergence Criteria: Typically, convergence is achieved when the change in the total energy and/or MO coefficients between successive iterations falls below a predefined threshold.
- Calculate Total Energy: Once convergence is achieved, calculate the total electronic energy using the final set of MO coefficients.

In conclusion, the SCF method provides a robust and efficient approach for solving the electronic structure problem in quantum chemistry. By iteratively optimising the molecular orbitals to minimise the total energy of the system, the SCF method lays the groundwork for understanding and predicting the behavior of molecules at the quantum level. However, Hartree-Fock calculations are limited by their inability to fully capture electron correlation effects. Specifically, the method considers electron exchange but overlooks dynamic correlations due to its mean-field approach, which does not account for real-time electron-electron interactions. Additionally, relying on a single Slater determinant to describe the wavefunction can be inadequate when the ground state of a system is more accurately represented by multiple quasi-degenerate determinants, highlighting issues with static correlation. To account for electron correlation, which makes up the remaining of the energy, involves advanced post-Hartree-Fock methods such as Møller-Plesset perturbation theory (MP2), Configuration Interaction (CI), and Coupled Cluster (CC) theory calculating electron correlation beyond the HF approximation to improve the accuracy of the wavefunction.

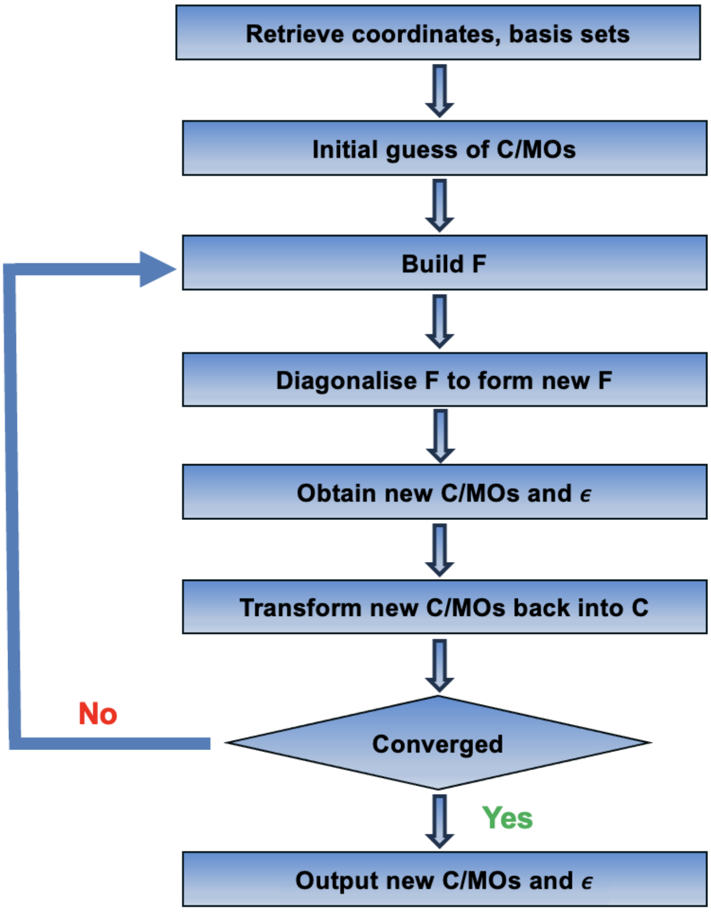

FIGURE 3.2: A schematic workflow of the SCF procedure

3.3.3 Coupled Cluster Theory

The HF method is unable to adequately address electron-electron correlation. Despite this limitation, its close approximation to the full wavefunction makes it a common starting point for electron correlation methods, so called post Hartree-Fock methods. One effective method to include electron correlation effects is CC theory. In these methods, the wave function is expressed as:

$$\psi = a_0\phi_0 + \sum_{i=1} a_i\phi_i \tag{3.36}$$

where $a_0\phi_0$ represents the weighted contribution from the HF method, and the summation accounts for the correlation correction to Hartree-Fock, capturing the total electron energy. This correction incorporates all possible excitations (relative to the HF ground state) that might occur within the molecular system, extending to infinity. Approaching the limit of an infinite basis set would theoretically yield an exact result. However, calculations that closely approximate this limit are exceedingly computationally demanding and often exceed the memory capacities of most computers. Therefore, approximations to the exact solution are necessary. These approximations balance accuracy and computational cost, making the correlation method practical for everyday computational science. This theory utilises a series of excitation operators T known as cluster operator acting on the HF reference state to generate excitations and can be described as,

$$T = T_1 + T_2 + T_3 + \cdots + T_\mathrm{n} \tag{3.37}$$

where T_1, T_2, etc., represent single, double, and higher excitations, respectively, up to the fully excited state with no electrons remaining in the ground state.

The coupled-cluster wavefunction ψ_{CC} can be represented as an exponential of cluster operator T applied to a reference wavefunction ϕ_{HF},

$$\psi_{CC} = e^T\phi_{HF} \tag{3.38}$$

The coupled clustor energy E_{CC} can be calculated by solving the Schrödinger equation ,

$$E_{CC} = \langle\phi_{HF}|e^{-T}\hat{H}e^T|\phi_{HF}\rangle \tag{3.39}$$

Specifically, T_1 and T_2 are defined as:

$$T_1 = \sum_{ia} t_i^a a_a^\dagger a_i, \quad T_2 = \frac{1}{4}\sum_{ijab} t_{ij}^{ab} a_a^\dagger a_b^\dagger a_j a_i \tag{3.40}$$

where t_i^a and t_{ij}^{ab} are the amplitudes for single and double excitations, respectively,ab and ij are occupied and unoccupied orbitals, and $a^\dagger$, a denote creation and annihilation operators. The strength of the coupled cluster method lies in its inclusion of higher-level correlations (double, triple, etc.), making it reliable for many chemical systems. So, accuracy of the calculation can be improved by increasing the number of cluster operators. The methods of Coupled Cluster Single (CCS), Coupled Cluster Single Double (CCSD), and Coupled Cluster Single Double Triple (CCSDT) incorporate contributions to the cluster operator up to first, second, and third orders, respectively

$$\psi_{CCS} = e^{T_1}\phi_{HF} \tag{3.41}$$

$$\psi_{CCSD} = e^{T_1+T_2}\phi_{HF} \tag{3.42}$$

$$\psi_{CCSDT} = e^{T_1+T_2+T_3}\phi_{HF} \tag{3.43}$$

The exponential function is expanded using the Taylor series:

$$e^T = 1 + T + \frac{T^2}{2!} + \frac{T^3}{3!} + \cdots + \sum_{k=0}^{\infty} \frac{1}{k!}T^k \tag{3.44}$$

Expressing in terms of component excitations of the T operator,

$$e^T = 1 + T_1 + (T_2 + \frac{1}{2}T_1^2) + (T_3 + T_2T_1 + \frac{1}{6}T_1^3) + \cdots \tag{3.45}$$

For clarity, all singlet, doublet, triplet excitations, and beyond have been categorized together. They are classified as either "connected" or "true" excitations, resulting from the simultaneous interaction of electrons, or as unconnected excitations, which arise from a combination of non-interacting excitations, such as a triplet formed from three singlet excitations or a combination of a singlet and a doublet. Due to computational limits, coupled-cluster calculations are often limited or truncated to balance computational cost and accuracy. For example, in the CCSDT method, the T operator is limited to:

$$T = T_1 + T_2 \tag{3.46}$$

It includes singlet and doublet contributions. Incorporating excitations beyond this order involves higher computational expenses.

The CC2 Approximation

The second-order coupled cluster CC2 approximation simplifies the coupled cluster approach by focusing primarily on single and a subset of double excitations, making it significantly faster and reducing computational costs compared to full CCSD:

$$T \approx T_1 + T_2^{CC2} \tag{3.47}$$

$$e^{T_1+T_2^{CC2}} \approx 1 + (T_1 + T_2^{CC2}) \tag{3.48}$$

In CC2, the T_2^{CC2} operator is modified from the full T_2 used in CCSD, and the amplitude equations are simplified. The CC2 amplitude equations, derived from projecting the Schrödinger equation onto singly and doubly excited states, are:

$$\begin{aligned} \text{Singles equation (for } t_i^a\text{):} \quad & \langle \phi_i^a | (\hat{H}_N e^{\hat{T}_1+\hat{T}_2^{CC2}})_c | \phi_{HF} \rangle = 0 \\ \text{Doubles equation (for } t_{ij}^{ab}\text{):} \quad & \langle \phi_{ij}^{ab} | (\hat{H}_N e^{\hat{T}_1+\hat{T}_2^{CC2}})_c | \phi_{HF} \rangle = 0 \end{aligned}$$

where H_N is the normal-ordered Hamiltonian, ϕ_i^a and ϕ_{ij}^{ab} corresponds to singly and doubly excited determinants. The subscript c indicates that only connected terms are included. TURBOMOLE is used in this thesis to handle efficiently coupled-cluster calculations, ricc2 which Implements approximate Coupled-Cluster methods and second-order Møller-Plesset perturbation theory.

3.4 Semi-Empirical Methods

Semi-empirical methods combine theoretical models with empirical data to parameterise and therefore simplify calculations to reduce computational costs. These calculations are structured similarly to HF calculations, featuring a Hamiltonian and a wave function but unlike *ab initio* methods, which are based solely on first principles (solving the Schrödinger equation from fundamental principles) without empirical input, semi-empirical methods modify the Schrödinger equation to include parameters derived from experimental data or higher-level calculations, allowing for faster computations at the expense of some accuracy. While *ab initio* methods provide more accurate and reliable results, semi-empirical methods offer a practical alternative for studying complex systems where full ab initio calculations would be computationally prohibitive. In this framework, certain aspects, like core electrons, are typically not considered, and only a minimal basis set is employed. Additionally, more approximations are applied e.g. Neglect of Differential Diatomic Overlap (NDDO) approximation is applied which assumes that overlap integrals between non-bonded atoms are zero in solving the Schrödinger equation, and the very complicated integrals that must be calculated in *ab initio* method are not actually evaluated. To address the inaccuracies introduced by these omissions, the semi-empirical methods are parameterized which means they draws on a kind of library of integrals that was compiled by finding the best fit of some calculated entity like geometry or energy to the experimental values. This plugging of experimental values into mathematical procedure to get the best calculated values is called parameterisation like ionization potentials and electron affinities. In short, semi-empirical methods are a compromise between fully empirical methods and first-principles approaches.

The main advantage of semi-empirical methods is their speed compared to ab initio calculations as they are much faster than ab initio, so these methods are particularly valuable when dealing with large systems where full quantum mechanical calculations would be computationally prohibitive. But they often produce less consistent results and can reliably predict fewer properties. The accuracy of the results depends significantly on the similarity between the molecule under study and those in the database used for parameterisation and may not predict properties accurately outside the parameterized range. For example, molecules like cyclopropane and cubane, which have unusual bond angles, might not be well predicted unless specifically included in the parameterization database.

Common semi-empirical methods include MNDO which simplifies the calculation of two-electron integrals and excludes certain overlap integrals, AM1 (Austin Model 1) predicts energies and geometries better than MNDO and PM3 (Parametric Method 3). The semi-empirical method PM3 (Parametric Method 3) is used in this thesis. It is developed by James J. P. Stewart in 1989, and is an improvement over its predecessors, MNDO and AM1. It uses nearly the same equations as the AM1, but with an improved set of parameters. For instance, in AM1 and PM3, the core Hamiltonian might be calculated as:

$$H_{ij}^{\text{core}} = K_{ij}(\text{IP}_i + \text{IP}_j) \tag{3.49}$$

where K_{ij} is a scaling factor, and IP_i and IP_j are the ionization potentials of atoms i and j. The method modifies core parameters and includes additional parameters specific to certain elements, aiming to enhance the accuracy of thermochemical calculations, geometries, and other properties compared to previous both. It is particularly noted for its ability to handle larger molecules than can typically be managed by ab initio methods due to its reduced computational demands. While PM3 is computationally efficient, it is important to note that it can sometimes yield less accurate results compared to more computationally intensive methods. The accuracy of PM3 calculations can be particularly limited for molecules containing elements not well-parametrized in the method or for those involving transition metal complexes. xtb is also used in this study for high-throughput screening. PM3 and xtb are both computational methods used in quantum chemistry, but they differ significantly in their approach and applications. PM3, or Parametric Method 3, is a type of semi-empirical molecular orbital method. It simplifies the calculation of molecular electronic structure by using empirical parameters derived from experimental data, focusing primarily on the valence electrons and their interactions. PM3 is specifically designed to handle organic molecules and is commonly used for studying molecular geometries, reaction pathways, and spectroscopic properties in relatively small systems. On the other hand, xtb (extended tight-binding) is a more recent approach that extends the tight-binding approximation, which is also a semi-empirical method but generally provides faster computations with a broader applicability including both organic and inorganic systems. Unlike PM3, xtb can efficiently handle larger molecular systems and is better suited for high-throughput screenings and large-scale material simulations due to its computational efficiency and reasonable accuracy. xtb's ability to quickly evaluate molecular properties and potential energy surfaces makes it particularly useful in materials science and large biomolecular systems, areas where PM3 might be less effective due to its computational demands and the specificity of its parametrisation for smaller organic molecules.

3.5 Density Functional Theory (DFT)

Density Functional Theory (DFT) is the most popular and efficient quantum chemical method and is based upon computing the electronic energy of a molecule based on the electronic density [41], $\rho(\mathbf{r})$. The post-HF methods typically involve high computational demands and can face difficulties with convergence. DFT, on the other hand, provides a formally exact framework that efficiently addresses electron correlation and provides accurate and efficient solutions for ground-state properties, such as molecular geometry, electronic energies, and molecular orbitals.

Instead of directly computing the wavefunction from the Schrödinger equation, which is the approach taken by semi-empirical and ab initio methods, DFT calculates the system's charge density. From this density, it's possible to derive the wavefunctions. It reduces the problem of many interacting electrons to a problem of non-interacting electrons moving in an effective potential. The connection between the wavefunction and $\rho(\mathbf{r})$ is established via the equation:

$$\rho(\mathbf{r}) = N \int \cdots \int |\phi(\mathbf{x}_1, \mathbf{x}_2, \ldots, \mathbf{x}_N)|^2 \, d\mathbf{x}_2 \cdots d\mathbf{x}_N \tag{3.50}$$

3.5.1 Hohenberg and Kohn Theorems

DFT is grounded on two pivotal theorems by Hohenberg and Kohn. The first theorem asserts that for any ground state density $\rho_0(\mathbf{r})$, total energy of the ground state can be calculated when the external potential $V_{\text{ext}}(\mathbf{r})$ is determined. The second theorem declares that for any density ρ different from the ground state density ρ_0, the total energy calculated for any other density will be higher than that of the ground-state density ρ_0:

$$E[\rho] \geq E_0[\rho_0] \tag{3.51}$$

This is a modification of the variational principle previously described in HF, now in terms of electronic density. The electronic energy of ground state depending on ρ_0 can be expressed as:

$$E_0[\rho_0] = T[\rho_0] + E_{ee}[\rho_0] + E_{en}[\rho_0] \tag{3.52}$$

where $T[\rho_0]$ represents the kinetic energy of electrons, $E_{ee}[\rho_0]$ is the electron-electron repulsion, and $E_{en}[\rho_0]$ is the electron-nuclei attraction, expressed as:

$$E_{en}[\rho_0] = \int \rho_0(\mathbf{r}) V_{\text{ext}}(\mathbf{r}) \, d\mathbf{r} \tag{3.53}$$

The first two terms of $E_0[\rho_0]$, namely $T[\rho_0]$ and $E_{ee}[\rho_0]$, are universal and combined into the Hohenberg and Kohn functional $F_{HK}[\rho_0]$:

$$F_{HK}[\rho_0] = T[\rho_0] + E_{ee}[\rho_0] \tag{3.54}$$

The term $E_{ee}[\rho_0]$ is subdivided into a Coulomb term $J[\rho_0]$ which is classical term and $E_{nn}[\rho_0]$ which is a non-classical term :

$$E_{ee}[\rho_0] = J[\rho_0] + E_{nn}[\rho_0] = \frac{1}{2} \int \int \frac{\rho_0(r_1)\rho_0(r_2)}{r_{12}} \, d\mathbf{r_1} \, d\mathbf{r_2} + E_{nn}[\rho_0] \tag{3.55}$$

$E_{nn}[\rho_0]$ includes self-interaction error, exchange correlation, and Coulomb correlation.

3.5.2 Kohn-Sham Approach

The calculation of the kinetic energy term $T[\rho_0]$ in a system of interacting electrons is impractical. To address this infeasibility of directly calculating $T[\rho_0]$, Kohn and Sham proposed a system of non-interacting electrons where $E_s[\rho_0]$ comprises the total kinetic energy of non-interacting electrons T_s and a local effective external potential $V_{\text{eff}}(\mathbf{r})$:

$$V_{\text{eff}}[\rho_0(\mathbf{r})] = \sum_i V_s^i[\rho_0(\mathbf{r})] \tag{3.56}$$

where V_s^i represents the one-electron operator corresponding to the external potential. This leads to a series of one-electron Kohn-Sham equations for non-interacting electrons:

$$f_i^{KS}\phi_i = \epsilon_i\phi_i \tag{3.57}$$

where ϕ_i are the Kohn-Sham orbitals and f_i^{KS} is the Kohn-Sham operator for electron i:

$$f_i^{KS} = -\frac{1}{2}\Delta + V_s^i \tag{3.58}$$

The total wavefunction of the non-interacting system can be represented as a Slater determinant ψ_s expressed in terms of ϕ_i. The kinetic energy of an interacting electronic system, denoted by $T[\rho]$, can be expressed in terms of the kinetic energy of a corresponding non-interacting system. This relationship is formulated as:

$$T[\rho_0] = T_s[\rho_0] + T_c[\rho_0] \tag{3.59}$$

where $T_s[\rho_0]$ represents the kinetic energy of the non-interacting system, and $T_c[\rho_0]$ is the correction term that accounts for correlations among electron motions due to interactions. Finally, the Hohenberg and Kohn functional is expanded to include both kinetic and potential energy contributions:

$$F_{HK}[\rho_0] = T_s[\rho_0] + T_c[\rho_0] + J[\rho_0] + E_{nn}[\rho_0] \tag{3.60}$$

where $T_c[\rho_0]$ and $E_{nn}[\rho_0]$ are unknown and are expressed as a combination under the exchange-correlation energy $E_{XC}[\rho_0]$,

$$F_{HK}[\rho_0] = T_s[\rho(\mathbf{r})] + J[\rho(\mathbf{r})] + E_{xc}[\rho(\mathbf{r})] \tag{3.61}$$

Here, $J[\rho(\mathbf{r})]$ represents the classical Coulomb interaction energy, and $E_{xc}[\rho(\mathbf{r})]$ encompasses the exchange-correlation energy, capturing additional electron-electron interaction effects not described by $J[\rho(\mathbf{r})]$.

Kohn and Sham proposed that the electron density ρ_0 in both interacting and non-interacting systems should be identical. According to the first Hohenberg and Kohn theorem, this equivalence in density suggests that there is a correspondence between the external potential V_{ext} in the interacting system and the potential V_s in the non-interacting system. Following the application of the second Hohenberg and Kohn theorem, which employs the variational principle, where the functional derivatives of the energy with respect to the density are set to zero for both systems, i.e., $\frac{\partial E_0[\rho_0]}{\partial \rho_0} = \frac{\partial E_s[\rho_0]}{\partial \rho_0} = 0$, the potential V_s for the non-interacting system is derived as:

$$V_s(\mathbf{r}) = \int \frac{\rho(r_2)}{r_{12}} d\mathbf{r_2} + V_{XC} - \sum_{A}^{M} \frac{Z_A}{r_{1A}} \tag{3.62}$$

Here, V_{XC} is the exchange-correlation potential, derived from the derivative of the exchange-correlation energy with respect to ρ, is:

$$V_{xc} = \frac{\delta E_{xc}}{\delta \rho} \tag{3.63}$$

Similar as in HF theory, Kohn-Sham equations are solved typically using the LCAO method for a molecular system and a SCF procedure. The progress in the field of DFT is concentrated on deriving accurate formulations for the exchange-correlation potential V_{xc}. The objective is to enhance DFT calculations so that they align closely with experimental observations or with results obtained from wavefunction-based computational techniques. [41]

3.5.3 Different Density Functionals

Different density functionals means, we are often specifically talking about different exchange-correlation (XC) functionals. These exchange-correlation functionals are key components in DFT calculations, as they account for the complex many-body electron interactions that are not captured by the other terms in the total energy functional. Its exact form is unknown and must be approximated. Various types of these functions have been developed, each with different level of approximation and unique characteristics. The choice of the density functional affects the accuracy of the calculations. Commonly used functional include:

- Local Density Approximations (LDA)
- Generalised Gradient Approximations (GGA)
- Global Hybrid functionals
- Range separated hybrid functionals
- Tuned range separated functionals

Local density approximation

The Local Density Approximation (LDA) is a foundational approach for calculating the energy E_{XC} in electronic structure calculations. It treats the system as a uniform electron gas by assuming that the exchange-correlation potential V_{xc}^{LDA} depends only on the local electron density. Under this approximation, the potential experienced by each electron is considered uniform across the system. The functional form for the energy within LDA is represented as:

$$E_{xc}^{LDA}[\rho] = \int \rho(\mathbf{r}) V_{xc}^{LDA}[\rho(\mathbf{r})] \, d\mathbf{r} \tag{3.64}$$

where $\rho(\mathbf{r})$ denotes the local electron density at position $\mathbf{r}$. Despite its utility, this approximation is overly simplistic for complex systems, such as molecular structures, where electron density variations are significant.

Generalised Gradient Approximation

In the Generalised Gradient Approximation (GGA), the exchange-correlation potential V_{xc} is a function not only of the local electron density, $\rho(\mathbf{r})$, but also of its gradient, $\nabla\rho(\mathbf{r})$. This approach modifies the Local Density Approximation by incorporating the density gradient, which helps address the non-uniformity in electron distributions. The GGA expression for the energy E is given by:

$$E_{xc}^{GGA}[\rho] = \int f[\rho(\mathbf{r})\nabla\rho(\mathbf{r})] \, d\mathbf{r} \tag{3.65}$$

where f is a functional that depends on both the electron density and its gradient. There are various forms of f available in the literature [42], which can be derived from first principles or calibrated against experimental data to enhance accuracy in describing electronic systems. GGA functionals significantly enhance the precision of calculations compared to the Local Density Approximation (LDA), yet they remain computationally affordable. Notably, the Perdew-Burke-Ernzerhof (PBE) and Becke-Lee-Yang-Parr (BLYP) functionals are among the most recognized examples of GGA functionals. [43] [44]

Global Hybrid Functionals

An alternative strategy to enhance the description of E_{XC} and particularly to address the issue of electron-electron self-interaction involves the partial inclusion of HF exchange, denoted as K. The exchange-correlation energy is then reformulated as:

$$E_{XC} = aK + (1-a)E_x^{DFT} + E_c^{DFT} \tag{3.66}$$

where a is the fraction of HF exchange, E_{xc}^{DFT} represents the DFT exchange energy computed using methods such as LDA, or GGA,, and E_c^{DFT} is the correlation energy at the DFT level, which could also be derived using LDA, GGA, or a combination of both.

Hybrid functionals, which are prevalent in computational chemistry, typically contain a fixed proportion of exact HF exchange. For instance, the B3LYP [45] and PBE0 [46] functionals include 20% and 25% HF exchange, respectively. The PBE0 functional is specifically formulated as follows:

$$E_{xc}^{PBE0} = \frac{3}{4}E_x^{PBE} + \frac{1}{4}E_x^{HF} + E_c^{PBE} \tag{3.67}$$

Here, E_x^{PBE} and E_c^{PBE} are the exchange and correlation energies computed using the PBE functional.

Range-separated hybrid functionals

Range-separated functionals represent a subclass of hybrid functionals in which the contribution of exact exchange is determined by the distance between interacting electrons, distinguishing between short-range and long-range regimes. [47] In these functionals, long-range interactions are treated using HF exchange, while the short-range interactions rely more on DFT-like exchange mechanisms. The inter-electron Coulomb potential can be formally expressed as:

$$\frac{1}{r_{12}} = \frac{1-[\alpha+\beta erf(\omega r_{12})]}{R_{12}} + \frac{\alpha+\beta erf(\omega r_{12})}{R_{12}} \tag{3.68}$$

where erf is the error function that connects short-range (first-term) and long-range (second-term) components of the e-e (electron-electron) interaction. The parameter ω is the range separation constant that dictates the switch from short- to long-range interactions at a certain inter-electronic distance r_{12} and it changes from functional to functional. Typical values for ω are 0.400 Bohr^{-1} for LC-ωPBE [48] and 0.330 Bohr^{-1}

[49] for CAM-B3LYP functional. The coefficients α and β modulate the degree of HF-like exchange within the short- and long-range interactions, respectively. The parameter α describes the magnitude of the Hartree-Fock-like exchange incorporated in the short-range interaction. The sum $\alpha + \beta$ indicates the amount of Hartree-Fock-like exchange involved in the long-range interaction. For example, in the LC-ωPBE functional, $\alpha = 0.0$ and $\alpha + \beta = 1.0$, indicating that short-range interactions are treated entirely within the DFT framework while long-range interactions are governed entirely by HF exchange [48]. In contrast, the CAM-B3LYP functional uses $\alpha = 0.19$ and $\alpha + \beta = 0.65$, allowing for some amount of exact exchange in both interaction ranges.

Range-separated functionals are particularly useful in addressing deficiencies in traditional DFT approaches, such as the underestimation of long-range charge transfer effects, ionization potentials, and excitation energies.

Tuned range separated functionals

In context of the range-separated functionals previously discussed, both the contributions from HF and DFT for short- and long-range interactions along the range separation parameter ω, are typically fixed. However, research has demonstrated that the optimal value of ω can vary significantly depending on the system being studied. This approach [50], [51, 52] is based on the principle that, in the limit of an exact exchange-correlation functional, DFT satisfies the Koopmans' theorem for the HOMO energy. Consequently:

$$IP^{(0)} + \epsilon_{HOMO}^{(0)} = 0. \tag{3.69}$$

Using the same methodology for the anionic system:

$$IP^{(-)} + \epsilon_{HOMO}^{(-)} = 0. \tag{3.70}$$

where $\epsilon_{HOMO}^{(-)}$ is the HOMO energy of the anionic species and $IP^{(-)}$ refers to its ionisation potential, so the expression becomes

$$IP^{(-)} = E^{(0)} - E^{(-)} = -EA^{(0)} \tag{3.71}$$

where $EA^{(0)}$ represents electronic affinity of the neutral species. Accordingly, the expression can be reformulated as

$$-EA^{(0)} + \epsilon_{HOMO}^{(-)} = 0. \tag{3.72}$$

The optimal tuning method involves optimising the range-separation parameter ω, which controls how the long-range corrected (LRC) functional transitions between short- and long-range interactions, in order to better replicate the behaviour of the exact exchange-correlation functional, *i.e.* minimising the optimal tuning (OT) function $J^2_{OT}(\omega)$

$$J^2_{OT}(\omega) = J^2_{IP}(\omega) + J^2_{EA}(\omega) \tag{3.73}$$

where

$$J^2_{IP}(\omega) = \left[IP^{(0)} + \epsilon^{(0)}_{HOMO}\right]^2 \tag{3.74}$$

and

$$J^2_{EA}(\omega) = \left[-EA^{(0)} + \epsilon^{(-)}_{HOMO}\right]^2. \tag{3.75}$$

Past studies have shown that optimally tuned functionals significantly enhance the description of various molecular properties, such as ionization potentials, optical gaps, and charge transfer and Rydberg transition energies.

.

3.6 Time Dependent DFT (TDDFT)

DFT serves as a foundational theory primarily focused on describing the ground-state behaviour of a system. However, when exploring excited states and phenomena involving time-dependent potentials like those governed by electric or magnetic perturbations, or optical processes like absorption and emission, a more suitable framework is needed. This is where Time-Dependent Density Functional Theory (TDDFT) comes into play within the realm of quantum molecular modeling, where potentials dynamically evolve over time to consider time-dependent quantum mechanics. So, we can say that TDDFT extends standard DFT to describe systems influenced by external, time-dependent fields which is ideal for studying dynamic processes and excited states.

3.6.1 The Runge-Gross theorem

The 1984 Runge–Gross theorem by Erich Runge and Eberhard K. U. Gross underpins the formalism of TDDFT, serves a role analogous to the first Hohenberg and Kohn theorem in the ground-state DFT. It deals with a system under the influence of a time-dependent potential which takes $\rho_{GS}(\mathbf{r})$ from DFT and obtains the excited states by the addition of a time-dependent perturbation by an external potential [53]. This theorem demonstrates that when a system originates from an initial state, there exists a corresponding time-dependent external potential that influences the system's density at any given time. To describe such systems, the time-dependent Schrödinger equation is employed, which accounts for both electronic and nuclear coordinates as well as time :

$$i\hbar\frac{\partial}{\partial t}|\psi(\mathbf{r},t)\rangle = \hat{H}|\psi(\mathbf{r},t)\rangle = [\hat{T} + \hat{V_{ext}}(\mathbf{r},t) + \hat{E}]|\psi(\mathbf{r},t)\rangle \tag{3.76}$$

where $\hat{T}$ denotes the kinetic energy operator and $\hat{E}$ the electron-electron interaction. The term $\hat{V_{ext}}(\mathbf{r},t)$ is the external potential with explicit time dependence. In DFT, this external potential includes only the static electron–nuclear Coulomb term, whereas in TDDFT it is supplemented by an additional time-varying field.

3.6.2 Van Leeuwen Theorem and Time-dependent Kohn-Sham

The van Leeuwen theorem extends the foundational ideas of the Runge-Gross theorem. It shows that if one starts with a given initial many-body wavefunction and a specific time-dependent electron density $\rho(\mathbf{r},t)$, there exists a unique time-dependent external potential $V_{\text{ext}}(\mathbf{r},t)$ (up to an additive purely time-dependent function) that will produce the same time-dependent density via the solution of the time-dependent Schrödinger equation. It means there is 1-1 relationship exists between the time-dependent external potential and the time-dependent density [54] . In other words we can say that two different time-dependent potentials applied to the same initial state will always result in different time-dependent densities. Consequently, the density at any given time uniquely determines the external potential.

This one-to-one correspondence between density and external potential enables the formulation of a time-dependent Kohn–Sham framework, wherein non-interacting electrons move in an effective potential that generates the exact time-dependent density as the fully interacting system. This time-dependent Kohn-Sham equation is derived [55] as,

$$i\hbar\frac{\partial}{\partial t}|\psi(\mathbf{r},t)\rangle = \hat{H}|\psi(\mathbf{r},t)\rangle = [\hat{T} + \hat{V_{KS}}(\mathbf{r},t)]|\psi(\mathbf{r},t)\rangle \tag{3.77}$$

where $\psi(\mathbf{r},t)$ denotes the time-dependent Kohn-Sham orbitals and $V_{KS}(\mathbf{r},t)$ denotes the Kohn-Sham potential which can be decomposed similarly to ground state DFT as,

$$\hat{V}_{KS}(\mathbf{r},t) = \hat{V}_{ext}(\mathbf{r},t) + \hat{V}_{Hartree}(\mathbf{r},t) + \hat{V}_{xc}(\mathbf{r},t) \tag{3.78}$$

where, $\hat{V}_{\text{Hartree}}(\mathbf{r},t)$ represents the Coulomb interactions, and $\hat{V}_{\text{xc}}(\mathbf{r},t)$ includes exchange-correlation term which is unlike in DFT, is time-dependent. The density can be obtained from the time-dependent Kohn-Sham orbitals as follows:

$$\rho(\mathbf{r},t) = \sum_{i}^{n} |\psi_i(\mathbf{r},t)|^2 \tag{3.79}$$

Just as in DFT, the exchange-correlation potential in TDDFT is unknown and is critical for its accuracy. However, the time-dependent nature of TDDFT suggests that entirely new exchange-correlation functionals would need to be developed. Despite this, in most applications of TDDFT, the time-dependence of the exchange-correlation functional is ignored, using what is known as the adiabatic approximation. This approximation states that the time-dependent V_{xc} is replaced by a time-independent one equivalent to the ground state potential:

$$V_{\text{xc}}(\mathbf{r},t) = V_{\text{xc}}(\mathbf{r})\big|_{\rho_0(\mathbf{r})=\rho(\mathbf{r},t)} \tag{3.80}$$

This assumes that changes in density are slow, with the electron density remaining in its eigenstate when perturbed [54].

In summary, TDDFT is necessary for studying molecular systems undergoing time-dependent changes and transitions between different electronic states, providing insights into phenomena such as electromagnetic absorption/emission and vibrational relaxation.

3.6.3 LR-TDDFT

While conceptually appealing, solving the time-dependent (TD) Kohn-Sham equations is computationally intensive, even for small molecules. Therefore, it is not universally applicable. To mitigate the computational burden when addressing the effects of an external field on quantum systems, one can approximate the interaction as a linear response called Linear Response TDDFT (LR-TDDFT). So, linear response theory is used which is an alternative to direct resolution of the TD-Kohn-Sham equations by characterising a system's reaction to small perturbations, providing a way to study the excited states energies and dynamic properties within the DFT framework:

$$\delta\rho(\omega) = \chi(\omega)\delta v(\omega) \tag{3.81}$$

Here $\delta\rho(\omega)$ represents the electron density's variation induced by a perturbation oscillating at a frequency ω and $\chi(\omega)$ is the corresponding frequency-dependent response function of the system. It characterizes how the system responds to external perturbations at different frequencies. Essentially, it acts as a mediator between the perturbing potential and the resulting change in electron density. $\delta v(\omega)$ denotes the external perturbing potential at frequency ω. ω represents the small perturbation applied to the system, such as an external electric field. In short, above equation describes that the change in the electron density $\delta\rho(\omega)$ is proportional to the applied perturbation $\delta v(\omega)$, with the proportionality factor being the response function $\chi(\omega)$.

Assuming the perturbation induced by the time-dependent field is minor—which is typical for many fields in chemistry, such as those used in measuring absorption spectra—this assumption is valid. The response within this approximation can be expressed using a Taylor expansion:

$$\rho(\mathbf{r},t) - \rho_0(\mathbf{r},t) = \rho_1(\mathbf{r},t) + \rho_2(\mathbf{r},t) + \rho_3(\mathbf{r},t) \tag{3.82}$$

Here, $\rho_0(\mathbf{r},t)$ is the initial density, and the subscripts denote the order of the perturbation. The first order linear electron density response, $\rho_1(\mathbf{r},t)$, is given by:

$$\rho_1(\mathbf{r},t) = \int\int \chi(\mathbf{r},t,\mathbf{r}',t') v_{1_{KS}}(\mathbf{r}',t')\, d^3\mathbf{r}'\, dt' \tag{3.83}$$

where $v_{1_{KS}}(\mathbf{r}',t')$ is the first-order perturbed potential and $\chi(\mathbf{r},t,\mathbf{r}',t')$ is the first-order density response function of the interacting system.

Until this point, the discussion has been framed within the time-domain. However, it is often more practical to apply these equations in the frequency space, especially when using them within quantum chemistry codes. Consequently, a Fourier transform is typically performed to convert data from the time domain into the frequency domain:

$$\rho_1(\mathbf{r},\omega) = \int \chi(\omega,\mathbf{r},\mathbf{r}') v_{1_{KS}}(\mathbf{r}',\omega) d^3\mathbf{r}' dt' \tag{3.84}$$

where $\chi(\omega,\mathbf{r},\mathbf{r}')$ is expressed as,

$$\chi(\omega, \mathbf{r}, \mathbf{r}') = \sum_{i,a} \left[\frac{\psi_i^*(\mathbf{r})\psi_a(\mathbf{r})\psi_i(\mathbf{r}')\psi_a^*(\mathbf{r}')}{\omega - (\epsilon_a - \epsilon_i)} - \frac{\psi_i(\mathbf{r})\psi_a^*(\mathbf{r})\psi_i^*(\mathbf{r}')\psi_a(\mathbf{r}')}{\omega + (\epsilon_a - \epsilon_i)} \right] \tag{3.85}$$

where i and a represents occupied and unoccupied energy levels, and ϵ_a and ϵ_i are their respective energies. The poles of the response function which correspond to excitation energies. To evaluate them, the problem can be reformulated in a eigenmatrix form known as TD-DFT equation [54] ,

$$\begin{bmatrix} A & B \\ B^* & A^* \end{bmatrix} \begin{bmatrix} X \\ Y \end{bmatrix} = \omega \begin{bmatrix} 1 & 0 \\ 0 & -1 \end{bmatrix} \begin{bmatrix} X \\ Y \end{bmatrix} \tag{3.86}$$

With ω representing the excitation energy, and X, Y denoting the excitation and deexcitation amplitudes, respectively, the solution of this non-Hermitian eigenvalue problem yields the excited state energies. In Mulliken (chemist's) notation, the A and B matrix elements are expressed as follows:

$$A_{ia,jb}(\omega) = \delta_{ij}\delta_{ab}(\epsilon_a - \epsilon_i) + (ia|jb) + (ia|f_{xc}|jb) \tag{3.87}$$

$$B_{ia,jb}(\omega) = (ia|bj) + (ia|f_{xc}|bj) \tag{3.88}$$

Here, f_{xc} denotes exchange-correlation kernel expressed by:

$$f_{xc}(\mathbf{r}, t, \mathbf{r}', t') = \frac{\delta V_{xc}[\rho](\mathbf{r}, t)}{\delta\rho(\mathbf{r}', t')}|_{\rho=\rho_0} \tag{3.89}$$

The Tamm-Dancoff approximation (TDA) simplifies the TD-DFT equations by setting the B matrix to zero, thereby excluding de-excitation contributions from the TD-DFT calculation of excited-state energies. Under TDA, the TD-DFT equations reduce to:

$$AX = \omega X \tag{3.90}$$

This approximation is particularly relevant for excited states with significant charge transfer characteristics, where elements of the B matrix tend toward zero [54]. Implementing TDA is also beneficial in addressing the triplet instability problem, which can lead to an overestimation of triplet state stability at the TD-DFT level [55].

3.7 Basis Sets

Besides the functional aspect, another crucial parameter that needs attention when conducting quantum chemistry calculations is the choice of a basis set (BS) as they define the quality of results. They serve as building blocks for representing the molecular orbitals, which describe the spatial distributions of electrons in a molecule. A basis set is defined as a collection of mathematical functions used to describe the electronic wavefunction that can be combined to construct an MO. These basis functions are often atom-centered in molecular calculations, such as atomic orbital (AO) basis functions, but they do not have to be. For example, plane-wave basis sets, commonly used in solid-state calculations, are delocalised and do not centered on atoms. Within the realm of TADF research, the focus typically lies on atom-centered AO basis functions, wherein all AOs combine to form MO through a process termed LCAO. The molecular orbital ϕ_i comprising n atomic orbitals can be represented linearly as:

$$\phi_i = c_{1i}\chi_1 + c_{2i}\chi_2 + c_{3i}\chi_3 + \cdots + c_{ni}\chi_n = \sum_{k=1}^{n} c_{ki}\chi_k \tag{3.91}$$

Here, c_{ki} are the coefficients that represent the contribution weight of the ith AO, while χ_k denotes the basis function for an individual AO.

Types of Basis sets

The choice of BS can significantly impact the accuracy and convergence of electronic structure calculations, and several strategies exist for selecting appropriate BS for a given molecular system. In quantum chemistry packages, two primary types of BS are commonly employed. The earlier variant is known as a Slater-type orbital (STO), devised by physicist John C. Slater in 1930 used for describing atomic orbitals. STOs in the Cartesian coordinate system can be shown as:

$$\chi^{\text{STO}}(x,y,z) = Nx^a y^b z^c e^{-\zeta r} \tag{3.92}$$

Here, N represents a normalization constant, while parameter ζ dictating the orbital's spatial extent; smaller ζ results in a more diffuse orbital, while larger ζ creates a tighter orbital. The combination of three quantum numbers (a, b, c) determines the angular momentum of the orbital. For instance, combinations like $(1,0,0)$, $(0,1,0)$, and $(0,0,1)$ correspond to p-orbitals, while combinations like $(2,0,0)$, $(0,2,0)$, $(0,0,2)$, as well as $(1,1,0)$, $(1,0,1)$, and $(0,1,1)$ are associated with d-orbitals.

Consequently, an s-type atomic orbital is represented by a single basis function, a p-type by three, and a d-type by six, continuing in this pattern for higher orbitals. STOs offer accurate physical AO representations but face challenges in evaluating integrals, making them less practical for polyatomic molecular calculations. In 1950, an alternative called Gaussian-type orbital (GTO), which is similar in form to the STOs, was introduced by Boys.

$$\chi^{\mathrm{GTO}}(x,y,z) = Nx^a y^b z^c e^{-\zeta r^2} \tag{3.93}$$

The key difference lies in exponent of the function, which simplifying the integration which involve two Gaussian function products. The product of these functions are expressed as,

$$e^{-\zeta_a(\mathbf{r}-\mathbf{R}_a)^2} e^{-\zeta_b(\mathbf{r}-\mathbf{R}_b)^2} = e^{-(\zeta_a+\zeta_b)(\mathbf{r}-\mathbf{R'})^2} e^{-\zeta'(\mathbf{R}_a-\mathbf{R}_b)^2}$$

Here R' and ζ' can be represented as:

$$\mathbf{R'} = \frac{\zeta_a \mathbf{R}_a + \zeta_b \mathbf{R}_b}{\zeta_a + \zeta_b}$$

$$\zeta' = \frac{\zeta_a \zeta_b}{\zeta_a + \zeta_b}$$

which results a new single Gaussian basis function that is centered at a point between the original two centers. This streamlined form significantly reduces computational demands.

However, due to gaussian shape of equation GTO in case of GTOs don't offer as precise AO descriptions as STOs do. At the nucleus, GTOs have a zero slope, unlike STOs which exhibit a sharp cusp due to a discontinuous derivative. This characteristic causes GTOs to inaccurately represent the behavior close to the nucleus. Additionally, GTOs decline too quickly at distances far from the nucleus compared to STOs, leading to a less accurate depiction of the wavefunction's outer regions. Although they have these limitations, GTOs are predominantly used in modern computations because they have the ability to accelerate the evaluation of 1- and 2-electron integrals compared to STOs. Consequently, to reach the same accuracy as STOs to accurately model the sharp increase in electron density at the nucleus while maintaining computational efficiency, a linear combination of GTOs is employed, known as CGTOs (Contracted Gaussian type orbitals) . These CGTOs, represented as STO-nG, where n corresponds to the number of primitive Gaussian functions. For instance, STO-3G approximates an STO by combining three Gaussian basis functions, each scaled by a specific coefficient:

$$\chi^{\mathrm{STO-3}G} = c_1\chi_1^{\mathrm{GTO}} + c_2\chi_2^{\mathrm{GTO}} + c_3\chi_3^{\mathrm{GTO}} \tag{3.94}$$

As the main purpose of using BS is to approximate the system's electronic wavefunction, thereby enabling computers to solve BS, including an infinite number of functions, would provide an exact representation of the wavefunction. But, in practical scenarios, we use a finite number of functions to approximate the electronic wavefunction. The effectiveness of a BS depends upon several factors. Smaller BS generally results in less accurate representations, whereas larger sets can more closely mimic atomic orbitals by imposing fewer constraints on the wavefunction, albeit with a substantially higher computational cost. The specific types of basis functions selected also significantly affect the performance, influencing both the accuracy of integral computations and the speed of these computations.

Minimal and Extended Basis sets

The precision of a basis set is primarily dependent on the number of basis functions it contains. For each type of occupied atomic orbital, it must include at minimum one basis function. Each contracted Gaussian function corresponds to a single atomic orbital. The most basic representation of atomic orbitals is referred to as a minimal basis set, which contains just enough functions to represent all the electrons in a neutral atom. For instance:

- Hydrogen & Helium require only one function (1s)
- 1st row elements need five functions (1s, 2s, 2px, 2py, 2pz)
- 2nd row elements need nine functions (1s, 2s, 2px, 2py, 2pz, 3s, 3px, 3py, 3pz)

One of the most commonly used minimal basis sets is STO-3G. However, minimal basis sets typically lack the precision required for accurate modeling, particularly in capturing anisotropic effects in bonding. This limitation arises because the exponent values remain fixed, meaning the orbitals cannot adjust in size (neither expand nor contract) to reflect bonding environments. For example, in case of Carbon ($1s^2, 2s^2, 2p^2$), a minimal basis set would include three contracted Gaussian functions, one for each occupied orbital type. A single-zeta basis set is an example of this minimal approach, using only one contracted Gaussian function for each type of occupied orbital on an atom.

To improve accuracy, extended basis sets are employed, which increase the number of functions beyond the minimal requirement. These include multiple-zeta basis sets, where each occupied orbital type is described by more than one contracted Gaussian function. Each of these functions is assigned its own variational coefficient in the construction of molecular orbitals, allowing for greater flexibility in achieving a lower energy wavefunction.

The inclusion of more basis functions enhances the ability to describe bonding interactions more precisely. For example, a double-zeta (DZ) BS for hydrogen includes two s-type functions. For elements in the first row, it typically includes four s-functions and two sets of p-functions. In this basis set, two orbitals of identical type are combined through a linear combination, sharing the same mathematical expression. However, they differ in their exponential parameters ζ-values. Consequently, now a single atomic orbital is depicted by two atomic orbitals of varying sizes. This concept is extended further in triple-zeta (TZ) and quadruple-zeta (QZ) basis sets, follow a similar pattern which use 3 STOs and 4 STOs per atomic orbital, respectively. These expanded sets offer greater accuracy, albeit with increased computational cost.

Another widely used extended basis set, split-valence basis sets, pioneered by Nobel Laureate John Pople, focuses on outer electron shells because it operates on the premise that chemical bonding primarily involves the outer (valence) electron shells, while the inner (core) electrons shells remain remain largely uninvolved. Hence, describing core orbitals with single STOs whereas each valence orbital is expanded into two or more CGTOs of differing exponents. This added flexibility allows the valence region to adapt to changes in bonding environments. John Pople introduced a notation system for this basis set, commonly represented as X-YZG. In this notation, X denotes the number of GTOs combined to form a single STOs for inner orbitals, while Y and Z indicate the GTO counts for the first and second STOs in the double-zeta set, respectively. To specify a triple-zeta valence orbital, an additional letter is appended: X-YZWG. In this basis set, often only the valence orbitals are expanded, converting standard double, triple, and quadruple zeta (DZ, TZ, QZ) sets into their split-valence forms (VDZ, VTZ, VQZ). In these split-valence basis sets, each valence orbital is described by two or more contracted Gaussian functions with different exponents, providing the flexibility needed to accommodate changes in bonding environments. Common double-zeta split-valence examples are 3-21G and 6-31G, while 6-311G is a widely used triple-zeta split-valence set.

Electron-electron repulsion representation is not smooth with Gaussian function. So, further modifications to Pople basis sets to improve AO descriptions can be made by adding polarizing functions, which significantly enhance the description of chemical bonding. When atoms approach closely, the distribution of charge changes, inducing polarization in the atoms. Consequently, orbital shapes become distorted, with s-orbitals may begin to show features similar to p-orbitals, and p-orbitals may take on characteristics of d-orbitals. To accurately model such bonding behavior between atoms, it is often necessary to add polarization functions, which are typically denoted by an asterisk. A single asterisk indicates the inclusion of d-type functions for elements ranging from lithium to calcium, while a double asterisk signifies the addition of p-type functions for hydrogen and helium. For example, adding p-type orbitals for hydrogen or d-type orbitals for p-block elements enhances bonding descriptions. When one set of polarization functions is added to a double-zeta (DZ) basis set, it forms a Double Zeta plus Polarization (DZP) set. Similarly, incorporating two sets of polarization functions into a triple-zeta (TZ) basis set yields a Triple Zeta plus Double Polarization (TZ2P) set. Polarization functions possess higher angular momentum and enable the modeling of directional (anisotropic) variations in electron distribution that occur during bonding. They also help to more accurately represent features like the inter-electronic cusp. For example, basis sets such as 6-31G(d) or 6-31G^* include d-type functions on heavier atoms, while 6-31G(d,p) or 6-31G^{**} extend this by also adding p-type functions to hydrogen atoms.

Furthermore, the inclusion of diffuse functions characterised by very small exponential coefficients ζ is beneficial for accurately describing systems with weakly bound electrons, such as anions, excited states, and soft or extended molecular systems. These functions typically consist of a diffuse s orbital along with a set of diffuse p orbitals sharing the same exponent. A single plus sign (+) indicates that diffuse functions are added to heavy atoms, while a double plus sign (++) means they are also included for hydrogen and helium. For instance, 6-31+G includes diffuse functions on heavier atoms, whereas 6-31++G extends this to the hydrogen atom as well.

In this thesis, the R. Ahlrich basis sets, specifically the double-zeta (def2-SVP) and triple-zeta (def2-TZVP) [56] were used. These basis sets are of the contracted split-valence type and include polarization functions on s-, p-, and d-type orbitals. Compared to traditional Pople-style split-valence basis sets, the def2 series generally offers improved reliability and accuracy for DFT calculations [56].

3.8 Geometry optimisation

Geometry optimisation is a fundamental technique in molecular modeling and quantum chemistry involves identifying stationary points such as energy minima or saddle points (transition states) on a molecule's potential energy surface (PES). A single point energy calculation is typically conducted to to evaluate the system's properties at the optimised geometry (the most stable structure). This process, often referred to as energy minimisation, aims to achieve a molecular structure that closely mirrors experimental observations.

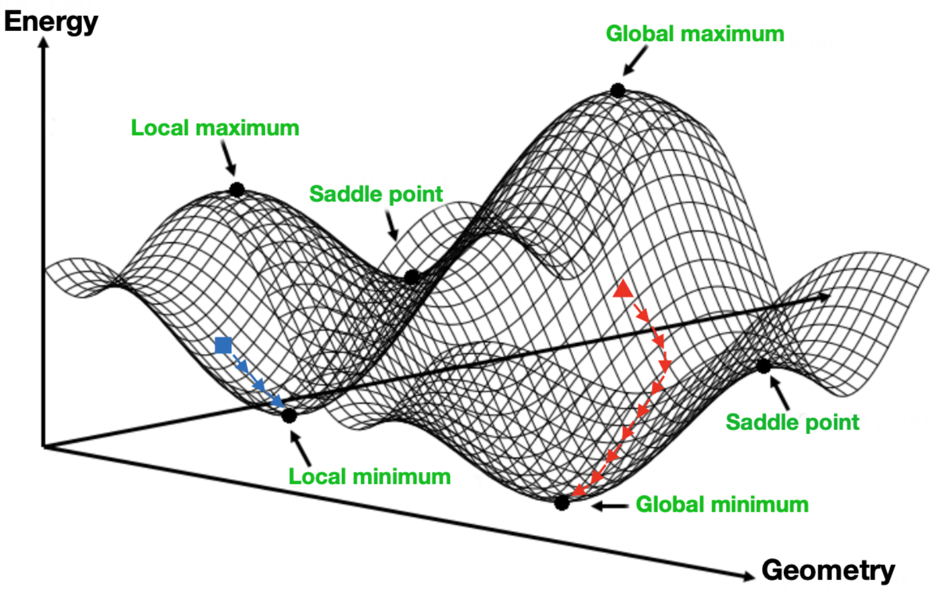

FIGURE 3.3: A three-dimensional visualization of a two-dimensional Potential Energy Surface (PES) depicting a molecule's potential energy as a function of its geometry.

Fig. 3.3 presents a 3D visualisation of a 2D potential energy surface depicting how the potential energy of the molecule varies with changes in its geometry. At global maximum, the molecule assumes its highest energy and least stable configuration. A local maximum refers to a region where the energy is higher than that of nearby geometries but not the highest overall. Saddle points represent transition states, positions that are energy maxima along one coordinate while being minima along the remaining directions. The global minimum corresponds to the point yielding the lowest energy structure on the PES. However, during energy minimisation, the geometry converges only to the closest minimum, typically a local one. Consequently, one molecule may have multiple optimised structures depending on the initial geometry. For example, in Fig. 3.3, starting geometry at the red triangle leads the system to the global minimum, while starting from the blue square result towards a local minimum.

To obtain the equilibrium geometry of a molecule where the system has minimum energy, the forces acting on each atom should nearly zero. It involves the idea of adjusting atomic positions e.g. vary bond length, bond angle, etc until lowest energy configuration of molecules is attained. Software varies nuclear positions and find electron position around it and then find energy if it is getting low or not and repeats that until more energy doesn't reduce. This is called variational process. This process involves computing the forces exerted on atoms and make iterative changes to their positions, aiming to locate the point on potential energy surface where the gradient of energy with respect to atomic coordinates becomes zero. At this point, the second derivative represented by the Hessian matrix is positive definite, indicating a stable minimum. The molecule's potential energy E is expressed as a function of its atomic coordinates:

$$E = E(x_1, x_2, \ldots, x_N) \tag{3.95}$$

where x_i are the coordinates of the atoms. The atomic forces are derived from gradient of this potential energy E with respect to the positions of the atoms:

$$F = \nabla E = \left(\frac{\partial E}{\partial x_1}, \frac{\partial E}{\partial x_2}, \ldots, \frac{\partial E}{\partial x_N} \right) \tag{3.96}$$

For an optimised geometry, the condition $\nabla E = 0$ must be satisfied, indicating that the net force on each atom is zero. However, satisfying this condition alone does not guarantee that the structure is at a minimum. To distinguish between minima, maxima, and saddle points, a second derivative test is applied using the Hessian matrix, which consists of the second partial derivatives of the energy and is defined as:

$$H = \left[\frac{\partial^2 E}{\partial x_i \partial x_j} \right] \tag{3.97}$$

where Hessian hepls to understand the curvature of the PES around the minimum, which is further important for assessing the stability of the optimised structure. This can be done by determining the signs of the eigenvalues of the Hessian matrix. A point on the potential energy surface (PES) is a minimum if all Hessian eigenvalues are positive, while all negative eigenvalues indicate a maximum. If the eigenvalues include both positive and negative values, the point corresponds to a saddle point or transition state, despite the gradient being zero.

In practice, since the PES can be highly complex, geometry optimisation is carried out iteratively in cycles until the changes in atomic positions fall within a predefined convergence threshold. The geometry optimisation process involves the following cyclical steps (Fig. 3.4):

- **Initialization**: Start with an initial guess of the molecule's geometry, typically by manually inputting atomic coordinates or by using experimentally obtained crystal structures.
- **Energy and Gradient Calculation**: Compute the energy and the gradient of the energy w.r.t. atomic positions.
- **Update Geometry**: Adjust the atomic positions by changing nuclear coordinates using optimisation algorithms and calculates again electron's position and energy
- **Convergence Check**: Assess by comparing this calculated energy with the previous one. If the changes in energy and positions are below predefined thresholds/ get minimum energy(by changing nuclear coordinates , energy is not changing), we say we got stationary point (lowest point/minimum point) and SCF is converged. If not, the cycle repeats from step 2.

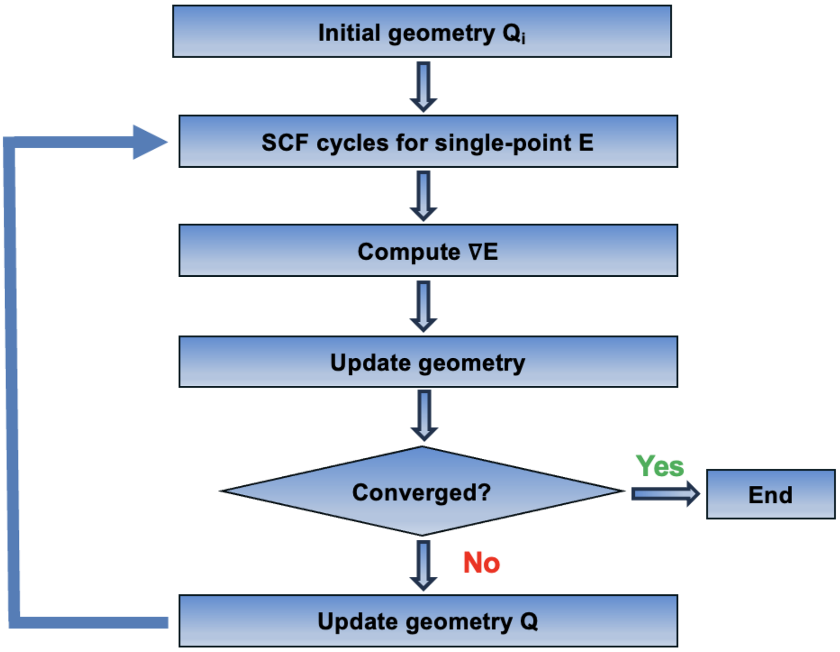

FIGURE 3.4: The Geometry Optimisation Cycle

The closer the initial guess to the true minimum, the faster the convergence. Different systems and potential energy surfaces may require different optimisation algorithms for efficient convergence. Potential Energy Surface features like multiple minima and flat regions can complicate the optimisation process. Convergence is typically determined by several criteria, including:

- Maximum force on any atom below a threshold.

- Maximum displacement of any atom is small between iterations.
- Energy change between successive iterations is below a certain limit.

Geometry optimisation is crucial for accurately predicting molecular properties and behaviors, facilitating advances in fields like drug design and materials science.

3.9 Ab Initio Molecular Dynamics (AIMD):

Ab initio molecular dynamics (AIMD) is a powerful simulation technique that combines molecular dynamics simulations with ab initio methods for studying the dynamic behavior of molecules and materials from first principles to calculate forces on atoms dynamically. It integrates quantum mechanics with classical mechanics to explore the behaviour of atoms and molecules in materials at finite temperatures. In this study, AIMD will be employed to explore the conformational changes and structural dynamics of the designed molecules and provides insights into their behavior. Unlike classical Molecular Dynamics (MD) where the gradients of the potential energy V are utilised to determine the positions and velocities of the system's particles at subsequent time steps, the AIMD integrates DFT or wavefunction-based methods to solve the electronic Schrödinger equation, thereby obtaining the electronic structure of the system. The forces between atoms are determined by quantum mechanical methods, where the electronic structure of system is computed at each time step involves the minimisation of energy of the system with respect to wavefunction, and from this minimisation, interaction energies are derived.

The Hellmann-Feynman theorem provides a fundamental principle to calculate the forces in AIMD simulations.. It provides a method to directly calculate the forces acting on atoms based on electronic structure of the system. According to the theorem the forces exerted on the nuclei are given by taking the negative gradient of the total energy with respect to the positions of the nuclei, under the condition that the electronic wavefunction remains an eigenstate of the Hamiltonian as the nuclei move. The theorem can be mathematically expressed as follows:

$$\mathbf{F} = -\nabla_{\mathbf{R}} E_{\text{total}} \tag{3.98}$$

where $\mathbf{F}$ is the force vector on the nuclei, $\mathbf{R}$ represents the nuclear coordinates, and E_{total} is the system's total energy, which is the function of the nuclear coordinates.

The theorem also states the derivative of an energy eigenvalue with respect to the forces acting on the atoms can be formulated as the expectation value of the Hamiltonian's derivative with respect to that same parameter

$$\frac{\partial E}{\partial \lambda} = \langle \psi | \frac{\partial \hat{H}}{\partial \lambda} | \psi \rangle \tag{3.99}$$

where λ represents a parameter on which the Hamiltonian depends (such as the positions of the nuclei), $\hat{H}$ represents Hamiltonian, and ψ represents electronic wavefunction of the system. In AIMD, this relation is employed to approximate the forces on the atoms. To ensure energy conservation throughout the simulation, the wavefunction needs to be tightly converged at each time step.

The atomic positions and velocities are updated using the Velocity Verlet algorithm:

$$\mathbf{R}(t + \Delta t) = \mathbf{R}(t) + \mathbf{V}(t)\Delta t + \frac{1}{2m}\mathbf{F}(t)\Delta t^2 \tag{3.100}$$

$$\mathbf{V}(t + \Delta t) = \mathbf{V}(t) + \frac{1}{2m}(\mathbf{F}(t) + \mathbf{F}(t + \Delta t))\Delta t. \tag{3.101}$$

The trajectory obtained from AIMD simulations will be analysed to investigate the conformational changes and dynamic behavior of the molecules. Although the primary challenges in AIMD include significantly more computationally intensive than classical MD, which limits its application to smaller systems and shorter time scales, it offers superior accuracy, making it particularly valuable for simulating molecular conformational changes over time.

.

Chapter 4

Conformational Control of TADF Emitters using Non-Covalent Interactions

4.1 Introduction

Thermally activated delayed fluorescence (TADF) from fully organic chromophores has seen increasingly being used into diverse technologies ranging from organic light-emitting diodes (OLEDs) [57, 58] and chemical sensors [59, 60] to photocatalysts [61, 62], bioimaging agents [63, 64], and fluorescent tags [65, 66]. Designing efficient TADF emitters generally requires, with a few exceptions [67, 68], the use of orthogonally orientated donor (D) and acceptor (A) moieties (Fig. 4.1) [23, 69].

This perpendicular orientation minimizes the spatial overlap between the highest-occupied molecular orbital (HOMO) and the lowest-unoccupied molecular orbital (LUMO), thereby reducing the energetic gap between the lowest singlet and triplet states and enabling thermal up-conversion of nonradiative triplet states into emissive singlet states [70, 71].

While orthogonality between the D and A units is critical, constraining this dihedral bond too rigidly is detrimental to TADF due to a lack of rotational/breathing freedom which is important for the vibrational coupling mechanism, [72–75] and tends to yield room temperature phosphorescence instead, *i.e.* the reversed intersystem crossing (rISC) rate is quenched [76, 77]. In contrast, unrestricted rotation about the donor–acceptor bond generates a wide dispersion of TADF rate [78–80], broadens the emission width [81–86] and leads to an increase in the non-radiative decay rates [87, 88].

Embedding rigidifying covalent linkages tends to perturb the electronic structure of emitters severely, preventing TADF and consequently other

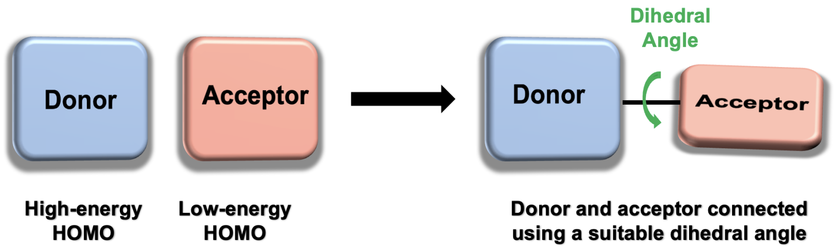

FIGURE 4.1: D-A structure; Donor and acceptor connected using suitable dihedral angle for HOMO-LUMO separation

approaches to control the conformation dynamics of donor-acceptor molecules are required. One strategy is to introduce steric bulk such as adding methyl groups [89–93] to hinder rotation between donor and acceptor groups to hinder rotation. However, this can inadvertently alter their relative geometry, breaking the desired orthogonality between the D and A [77, 94]. A different tactic exploits non-covalent forces, as these are strong enough to dampen conformational flexibility without abolishing TADF. Towards this goal, Rajamalli et al. [95] have proposed a design that takes advantage of hydrogen bonding. Subsequently, Chen *et al.* [96], He *et al.* [97] and Shimoda *et al.* [98] invoked donor-aaceptor hydrogen bonding schemes to develop planar TADF molecules. However, these derivatives show large (>0.43 eV) ΔE_{ST} making TADF at best inefficient. In addition, recent theoretical studies supported by experimental time-resolved spectroscopy in various intramolecular H-bonded donor–acceptor models [99, 100] indicate that these D–A hydrogen bonds are unlikely to play a significant role in the TADF mechanism. Consequently, the role of intramolecular interactions in controlling the excited state properties of TADF molecules remains an open question.

While the strength of a hydrogen bond is only approximately 5% that of an average covalent bond, incorporating these and similar non-covalent interactions, such as $\pi - \pi^*$ interactions [83, 101, 102], can have to a significant effect on both electronic ground and excited state properties. Indeed, recently oxygen$\cdots$boron heteroatom interactions have recently been employed to control the conformation of linear conjugated molecules and polymers [103, 104]. Inspired by these previous works, herein we computationally investigate 8 molecules (**1a-1d** & **2a-2d**) (Fig. 4.2) in the beginning to compare the effect of steric hindrance and non-covalent interactions (achieved using oxygen$\cdots$boron and sulphur$\cdots$boron heteroatom interactions) in exerting fine conformational control of the excited state dynamics of potential TADF emitters.

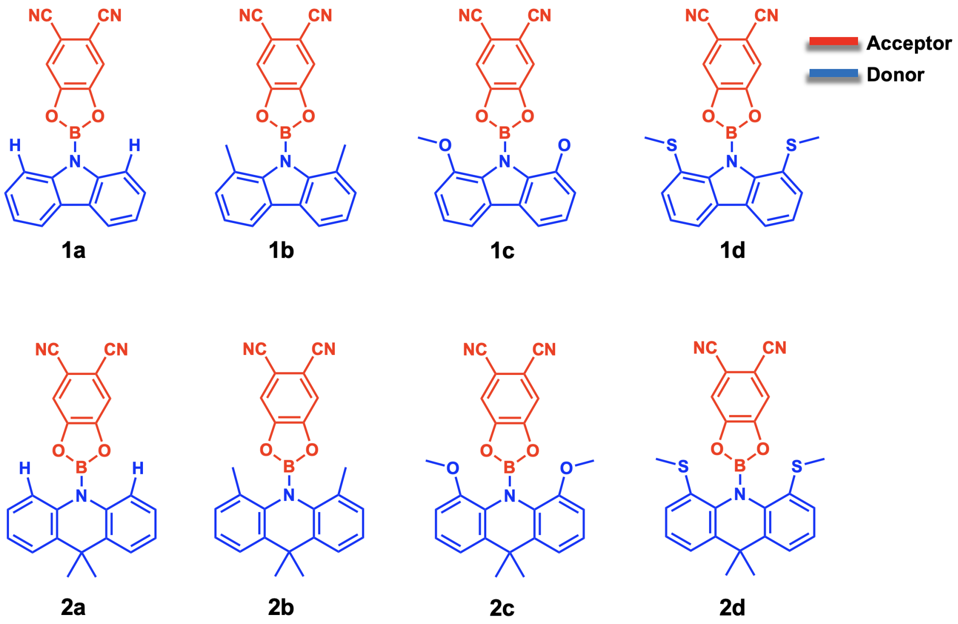

FIGURE 4.2: Donor-Acceptor structures

In molecules **1a**-**1d** (Fig. 4.2) carbazole moiety is a donor whilst aryl nitrile acts as an acceptor. Inclusion of pyrazine in these molecules further makes the ring more electron deficient and hence would allow better charge transfer. The lone pair on the methoxy group in **1c** will interact with the empty p orbital of the boron group and hence this interaction will allow conformational control. The methyl group in **1b** is not expected to form any non-covalent interactions, steric clash will be the major force in controlling the dihedral angle. While in **1a**, methyl group is replaced by a hydrogen atom to establish a robust baseline for comparison. This hydrogen-substituted compound functions as a control, enabling us to isolate and understand the specific effects of other substituent on donor. Thioether in **1d** is also expected to form the same interactions as methoxy but these interactions are expected to be weaker. By just replacing carbazole donor with another promising acridone donor in all the above molecules we have another set of molecules **2a**-**2d** (Fig. 4.2). Our molecular design is in part motivated by the work of Wu *et al.* [105] and related 3-coordinate boron systems that have demonstrated promising TADF behaviour [106–108].

We subsequently studied an additional series of molecules, i.e. **JC** molecules (Fig. 4.3). These molecules have been synthesised by the Skabara group at Glasgow university and characterised by the Monkman group at Durham University. They are also based on the D-A framework, that incorporate a carbazole unit as the donor and diphenyl boron as the acceptor. Within this set of molecules, **JC274** and

JC257 features a methoxy group on side and methoxy group on the both sides of donor respectively, another variant **JC324** possesses a methyl group on both sides of donor. Finally, in **JC258**, the methyl group is replaced with a hydrogen atom again to establish a reliable reference point for comparison. The examination of these molecules contributes to a more comprehensive understanding of the influence of weak B...O interactions in conformational control between the donor and acceptor groups.

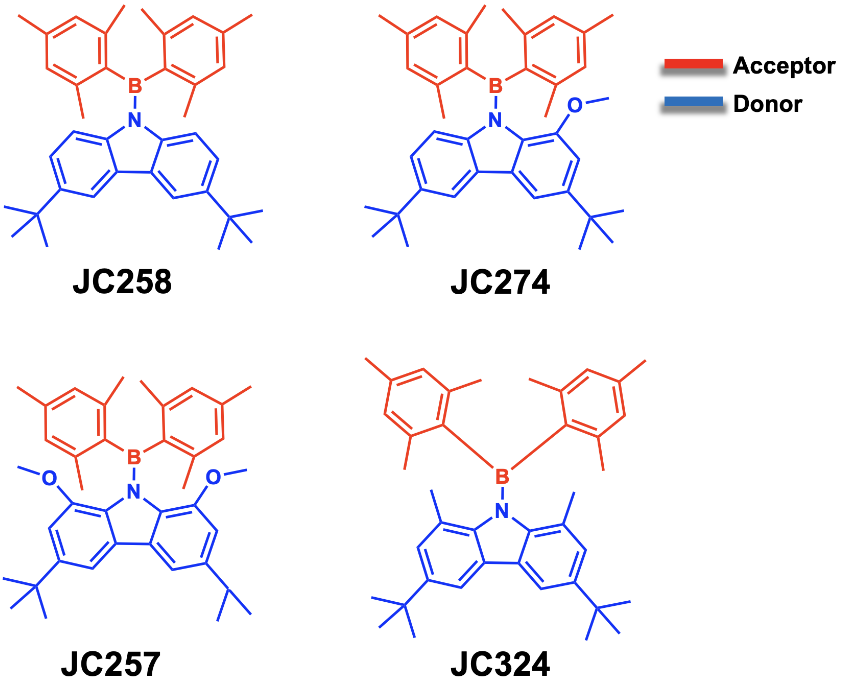

FIGURE 4.3: Donor-Acceptor JC molecules

Furthermore, we expanded our study by investigating a D-A-D system (Fig. 4.4), based upon the emitter designed in [105]. However, we replaced the central methyl substitutes with methoxy and methylthio groups, so we can control the motion around the donor-acceptor bond, building upon our previous D-A framework. This study further seeks to exploit weak B...O and B...S interactions between donor-acceptor groups compared to steric clash for conformational control of TADF emitter.

This work, combining quantum chemistry and *ab intio* molecular dynamics, demonstrates the potential for non-covalent interactions to control both the conformational preference of the molecules studied and the dispersion of dihedral angles around the D-A bond. Unlike covalent bond in which electrons are shared, non-covalent interactions involve more dispersed variation in electromagnetic interactions between molecules or within molecules which makes them comparatively weaker.

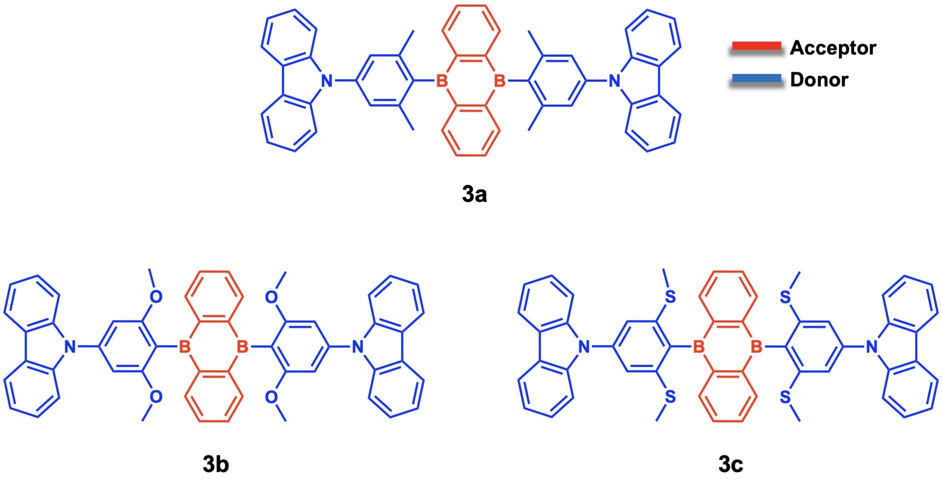

FIGURE 4.4: Donor-Acceptor-Donor structures

These are driven by induced electrical interactions between two or more atoms or molecules that are very close to each other and so are distance-dependent interactions which quickly vanishes at longer distances. Taking advantage of these weak interactions allows for a fine conformational control between donor and acceptor, keeping them rigid but still permit some vibrational flexibility in the conformation, which is necessary for triplet harvesting. In contrast to steric interactions, the molecules studied in this work exhibiting oxygen$\cdots$boron non-covalent interactions are locked slighter close to orthogonal, a property which promotes favourable TADF characteristics.

4.2 Computational Details

All computations were carried out with the ORCA quantum chemistry package. [109]. Geometries were optimised in the electronic ground state, as well as in the first singlet and triplet excited states, employing density functional theory (DFT) and linear-response time-dependent DFT (LR-TDDFT) within the Tamm–Dancoff approximation (TDA) [110], respectively. The LRC-BLYP which is exchange-correlation functional [111] was used and to address the challenge of charge transfer excitations [52] the optimal tuning methodology was used to refine the range-separation parameter, ω [112]. Throughout this work, $\omega_{OT}^{*} = 0.2a_0^{-1}$ was found to be optimal for each molecule, assessed at the electronic ground state geometry. A def2-TZVP basis set [113] was utilised and all energies recorded describe the solvent effect via the conductor-like polarisable continuum medium (CPCM) [114].

Using the PBE0 functional within density functional theory [115, 116] and def2-SVP basis set [117], we carried out *Ab initio* molecular dynamics (AIMD) simulations for both the ground state and the first excited singlet state using the ORCA quantum chemistry software [109]. Each simulation was initiated from either the ground or first singlet excited state optimised geometry. The temperature was maintained to 300 K for the 20 ps of dynamics. 100 geometries were selected at random from the last 15 ps of the dynamics and the excited state properties calculated using the LRC-BLYP exchange and correlation functional and def2-TZVP basis set described above.

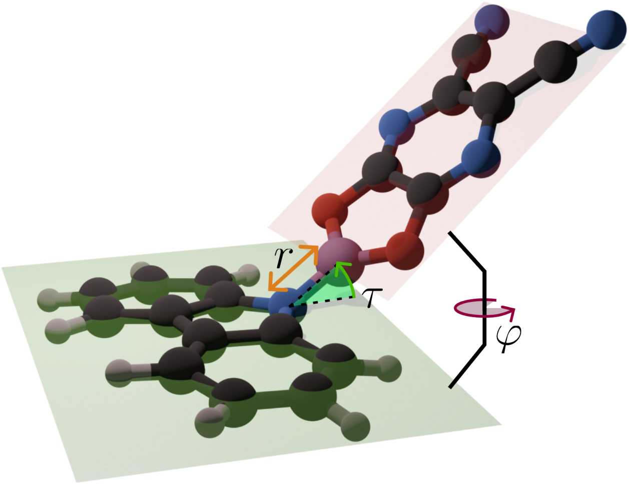

FIGURE 4.5: Schematic showing the coordinates used to describe the geometry of the molecules studied in this work. r represents the distance between the donor and acceptor, φ represents the relative orientation between the D and A and τ represents the angle between the plane of the D and the plane of the A.

Fig. 4.5 shows a schematic of the structural parameters used to describe the molecular structures throughout this work. r represents the distance between the D and A, φ (twist angle) represents the spatial orientation between the donor and acceptor planes and τ (bend angle) represents the angle between the donor and acceptor planes. The two angles can be used to define 3 conformers found in this work: planar (φ=0°, τ=0°), twisted (φ=90°, τ=0°) and bent (φ=0°, $\tau >$15°).

4.3 Results

4.3.1 Donor-Acceptor Molecules

Quantum Chemistry Calculations of Critical Points

Table 6.1 and 4.2 show key structural parameters and associated excited state properties of both the carbazole and acridone-based molecules in their energy minimised electronic ground and excited S_1 and T_1 states.

Structure	State	Conformer	r / Å	B-X / Å	$\angle_\varphi$ / °	$\angle_\tau$ / °	E_{S1}	f_{S1}	E_{T1}	ΔE_{S1-T1}	E_{SOC}
1a	GS	Twisted	1.43	–	89.2	0.1	3.58	0.00002	3.42	0.16	0.15
	GS	Planar*	1.40	–	0.2	0.1	4.04	0.47984	3.28	0.76	0.05
	T_1	Twisted	1.49	–	79.2	0.1	3.01	0.01419	3.00	0.01	0.08
	T_1	Planar*	1.40	–	0.8	0.5	3.85	0.00007	2.41	1.44	0.38
	S_1	Twisted	1.50	–	89.7	0.1	2.85	0.00001	2.84	0.01	0.00
	S_1	Planar*	1.49	–	0.5	0.0	3.11	0.15901	2.86	0.25	0.00
1b	GS	Twisted	1.43	3.00	0.5	0.2	3.44	0.00005	3.40	0.04	0.16
	GS	Bent*	1.41	3.31	49.4	37.4	4.05	0.37769	3.27	0.78	0.05
	T_1	Twisted	1.49	2.95	90.1	0.1	2.67	0.00001	2.67	0.00	0.01
	T_1	Bent*	1.40	3.31	0.0	37.5	3.83	0.01514	2.40	1.43	0.75
	S_1	Twisted*	1.49	3.00	89.7	0.2	2.65	0.00001	2.64	0.01	0.01
	S_1	Bent	1.40	3.32	1.2	35.5	3.25	0.00349	2.59	0.72	1.21
1c	GS	Twisted*	1.44	2.69	89.9	0.0	3.44	0.00007	3.37	0.07	0.15
	GS	Bent	1.41	3.08	0.2	31.2	3.77	0.27690	3.25	0.52	0.05
	T_1	Twisted	1.50	2.73	88.4	0.4	2.50	0.00001	2.50	0.00	0.01
	T_1	Bent*	1.42	2.81	50.8	10.1	3.21	0.03689	2.19	1.02	1.40
	S_1	Twisted*	1.50	2.75	1.2	89.9	2.47	0.00001	2.46	0.01	0.01
1d	GS	Twisted*	1.48	2.83	81.5	0.6	3.62	0.00301	3.15	0.47	0.06
	GS	Bent	1.41	3.34	3.22	41.2	3.69	0.14269	3.27	0.42	0.32
	T_1	Twisted*	1.49	2.90	88.9	5.2	2.45	0.00124	2.44	0.01	0.18
	S_1	Twisted*	1.49	2.91	89.5	6.9	2.37	0.00001	2.35	0.02	0.02

TABLE 4.1: Key structural parameters and associated excited state properties of molecules **1a**, **1b**, **1c** and **1d**. Only the stable conformers are shown and the lowest energy conformer for each state is marked with *. The bond distance r and angles angles φ and τ are defined in Fig. 4.5.

In the electronic ground state, **1a** exhibits two conformers, twisted and planar, with the latter being strongly preferred due to it being 0.6 eV lower in energy (Tables A.1 and A.2). The planar structure exhibits a D-A bond distance of 1.40 Å, which increases to 1.43 Å in the twisted structure due to the reduced overlap between the D and A orbitals arising from orthogonality. Upon excitation into the S_1 state, the same conformers remain present, but their relative energy gap decreases to 0.18 eV (Tables A.1 and A.2). This increases the probability to form the twisted conformer, which is more favourable for TADF due to its smaller ΔE_{S1-T1} (Table 6.1), However as the planar conformer is dominant in the electronic ground state, this would require a large conformational change which may be challenging in the solid state media, native for

OLED devices [118]. Both S_1 optimised structures are accompanied by a $\sim$0.08 Å elongation of the D-A bond distance, which leads to a large predicted Stokes shift ($\sim$0.7 eV) and a reduction in oscillator strength, spin orbit coupling and lowest singlet-triplet energy gap. In contrast, the lowest triplet state exhibits a single stable planar conformer, associated with a local exciton on the acceptor (See A.2). Consequently, the molecular structure exhibits comparatively small changes compared to the electronic GS, but a significantly larger $\Delta E_{S_1-T_1}$ making TADF impossible.

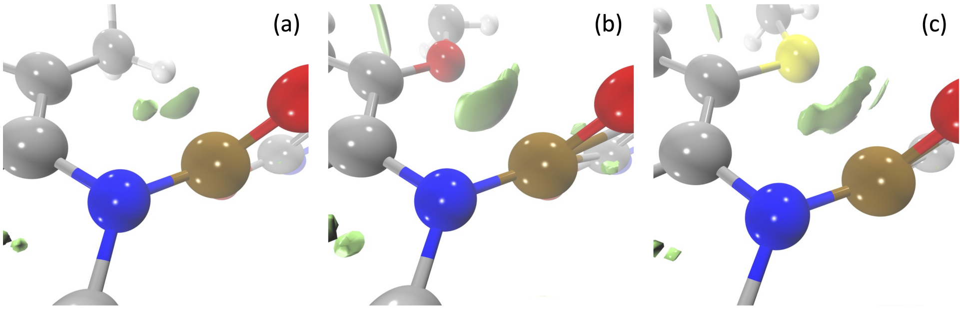

FIGURE 4.6: 3D isosurface of the reduced density gradient (s) isosurface (s = 0.3 a.u.) for molecules **1b** (a), **1c** (b) and **1d** (c).

Upon addition of the methyl (**1b**), methoxy (**1c**) and methylthio (**1d**) groups, the bulky side groups prevent the formation of the planar conformer meaning that the bent and twisted conformers become dominant. In addition, the relative energy gap between the twisted and bent conformers decreases. For molecule **1b**, this arises from the steric clash between the D and A. In contrast, for methoxy (**1c**) and methylthio (**1d**) this occurs due to the non-covalent bond between the B-N bond and the oxygen (sulphur), arising from the 3-centre-2-electrons interaction between the oxygen (sulphur) lone pair and low-lying antibonding orbitals of the B-N bond [119]. Indeed, this electron donation from the lone pair into the B-N bond gives rise to an increase in the D-A bond length in the electronic GS of the twisted conformers of **1c** and **1d** and makes the twisted conformers of these molecules the lowest energy conformer even in the electronic GS. This interaction can be seen using the reduced density gradient (s):[120–122]:

$$s(r) = \frac{1}{2(3\pi^2)^{1/3}} \frac{\nabla\rho}{\rho} \tag{4.1}$$

shown in Fig. 4.6. These highlight stronger contributions between the B-N bond and the oxygen (sulphur) as discussed above.

In the excited S_1 state, the twisted conformer is the lowest energy conformer for the methyl (**1b**), methoxy (**1c**) and methylthio (**1d**) emitters. This creates the desired orthogonality between the HOMO and LUMO based on the Donor and Acceptor groups, respectively (Fig.s A.1 - A.24). With the exception of **1d**, the lowest energy conformer for the excited T_1 state remains bent and the excited state in the case exhibits a ^{3}LE focused upon the A. Importantly, for the methoxy substitutes (**1c**) emitter, the energy difference among the twisted and bent conformers in triplet state is small and the mix of excited state character, *i.e.* CT and LE is expected to promote TADF [71].

Overall, the simulations of the carbazole emitters demonstrates that the twisted conformers are the only ones likely to exhibit efficient TADF as both the bent and planar conformers exhibit a larger $\Delta E_{S_1-T_1}$. While the steric hindrance of methyl group somewhat promotes the formation of the twisted conformer, it is only upon the inclusion of non-covalent interactions, that the structure is sufficiently controlled to promote the twisted conformer in the ground state. This is observed for both the methoxy (**1c**) and methylthio (**1d**) groups, while the latter increase the SOC slightly due to heavy atom effect [123].

Structure	State	Conformer	r / Å	B-X / Å	$\angle_\varphi$ / °	$\angle_\tau$ / °	E_{S1}	f_{S1}	E_{T1}	ΔE_{S1-T1}	E_{SOC}
2a	GS	Bent*	1.40	–	0.1	35.5	4.00	0.44949	3.23	0.77	0.07
	T_1	Twisted	1.50	–	79.1	0.5	2.41	0.04050	2.36	0.05	0.05
	T_1	Bent*	1.39	–	2.3	33.4	3.64	0.10686	2.18	1.36	1.45
	S_1	Twisted*	1.50	–	89.8	0.0	2.30	0.00001	2.29	0.01	0.02
	S_1	Bent	1.50	–	1.5	24.2	2.82	0.14981	2.61	0.21	0.14
2b	GS	Bent*	1.39	3.19	0.1	39.9	4.13	0.40272	3.24	0.89	0.05
	T_1	Bent*	1.39	2.94	2.1	51.6	3.66	0.13260	2.13	1.53	2.54
	S_1	Twisted*	1.51	2.98	81.7	61.2	2.46	0.00421	2.45	0.01	0.11
	S_1	Bent	1.50	3.05	26.2	51.2	2.84	0.11183	2.65	0.19	0.45
2c	GS	Twisted*	1.49	2.15	86.7	24.4	3.65	0.00002	3.12	0.53	0.25
	GS	Bent	1.40	2.91	0.2	45.6	3.93	0.23901	3.22	0.71	0.04
	T_1	Twisted	1.52	2.30	86.6	0.5	2.24	0.00008	2.23	0.01	0.03
	T_1	Bent*	1.39	2.90	1.3	42.4	3.59	0.07999	2.16	1.43	0.54
	S_1	Twisted*	1.52	2.31	87.7	1.1	2.21	0.00006	2.20	0.01	0.01
2d	GS	Bent*	1.40	3.23	2.1	51.9	3.78	0.01218	3.24	0.54	0.11
	T_1	Bent*	1.43	3.08	1.0	43.8	2.32	0.00499	2.16	0.16	0.31
	S_1	Bent*	1.47	3.013	32.6	48.34	2.31	0.00308	2.29	0.02	0.31

TABLE 4.2: Key structural parameters and associated excited state properties of molecules **2a**, **2b**, **2c** and **2d**. Only the stable conformers are shown and the lowest energy conformer for each state is marked with *. The bond distance r and angles φ and τ are defined in Fig. 4.5.

Table 4.2 shows the structural parameters and excited state properties of molecules **2a-2d**. In contrast to the carbazole donor, the acridone donor promotes the bent conformer for the unsubstituted conformer (**2a**). For both the unsubstituted and methyl substituted molecule, the lowest energy conformer in the electronic GS is the bent structure, which owing to the absence of orthogonality between the D and A, gives rise to a large $\Delta E_{S_1-T_1}$. Indeed, for the unsubstituted molecule (**2a**), there is no stable twisted conformer making TADF very unlikely for this particular example. However, as observed for molecules **1a**-**1d**, the addition of the non-covalent interactions *via* the methoxy group promotes the twisted conformer exhibits a small $\Delta E_{S_1-T_1}$ required for TADF. However, in contrast to the carbozole donor (**1d**), addition of the methylthio groups (**2d**) leads to only the bent conformer in the electronic ground state, suggesting that only the methoxy substituted systems will be favourable for TADF.

As observed for the carbazole donors, the acridone donor molecules favour the bent conformer in the triplet state, which predominantly exhibits a ^{3}LE centrered on the A. However, for **2c**, the non-covalent interactions between the B-N and the lone pair oxygen stabilises the twisted conformer making this comparable (0.1 eV higher in energy, See Table A.13 and A.14), which is highly favourable for TADF due to the mixed character of the states. Besides this, the primary difference for the acridone donors is an increase in the excited state energies, associated with the weakening of the donor strength. However, this also generates a larger Stokes shift ($\sim$ 1.7 eV), which is likely to be problematic in devices as it will likely to lead large radiative rate.

Importantly, these properties are static, *i.e.* performed at a single optimised geometry. Extensive research has shown that both the dynamic behaviour of molecular emitters [70], and their conformation are critical in the TADF emitters performance. Consequently, in the following section we will integerate molecular dynamics with excited state calculations to understand the dynamics.

Molecular Dynamics of the Conformational Disorder

In this section we seek to understand the impact of the molecular dynamics on properties of the 8 studied emitters, with a particular focus on the influence of the steric (methyl) and non-covalent (methoxy and methylthio) interactions on the structural freedom around the D-A bond. Fig. 4.7 shows the absorption spectrum calculated from 100 snapshots obtained from the ground state *ab initio* molecular dynamics trajectories of molecules **1a**-**1d**, further analysis of these trajectories is shown in the appendix B. The absorption spectrum of **1a** shows a single strong band at ~4.0 eV, associated with transitions into the S_1 state. As shown in the density differences plot in the supporting information (Fig. A.1), this corresponds to a state which is largely charge transfer (CT) in character, but the planar structure leads, as usually expected [124], to enhance the electron–hole overlap, increasing the oscillator strength and creating a larger (0.90 eV) singlet-triplet splitting.

Upon addition of the methyl groups (**1b**), the calculated absorption spectrum exhibits 3 bands below 4.5 eV. The first (~3.5 eV) is weakest

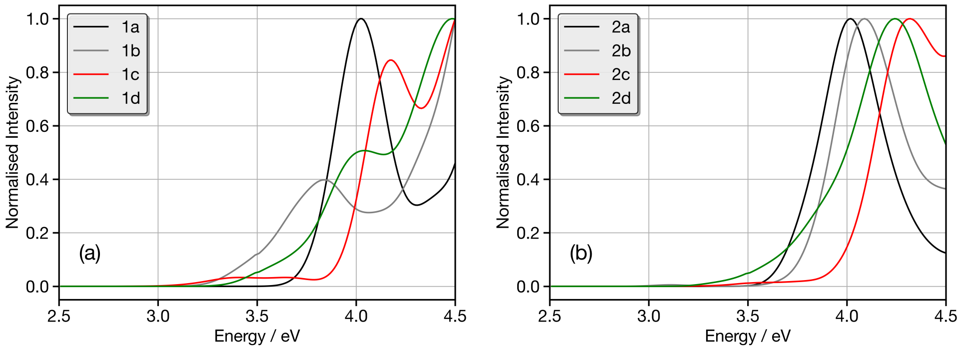

FIGURE 4.7: The calculated absorption spectrum of (a) **1a** (black), **1b** (grey), **1c** (red) and **1d** (green) and (b) **2a** (black), **2b** (grey), **2c** (red) and **2d** (green). Each spectrum is calculated by averaging the 100 spectra simulated from structures sampled at random from the ground state *ab initio* molecular dynamics. Each individual spectrum has been broadened using the Gaussian with a full-width at half-maximum of 0.1 eV.

and associated with the orthogonal CT band, with a long tail to lower energy reflecting a dispersion of CT states arising from a large variation and flexibility around the D-A dihedral angle (110±30°Table 4.3). The second band (∼3.9 eV) is associated with the S_1(CT) state in the planar arrangement, with a distorted donor and acceptor, similar to **1a**. The presence of both bands reflects the increased presence of the twisted isomer compared to **1a**. The band just visible at 4.5 eV corresponds to transitions into the S_2 states of both the bent and twisted isomers.

Addition of the methoxy groups (**1c**), which promotes the twisted isomer, significantly changes the shape of the spectrum. The two low lying bands remain, but due to the significantly stronger CT character substantially decreases the oscillator strength of these transitions. This arises due to closer to orthogonal arrangements and much smaller dispersion of dihedral angles around the D-A bond (91.6±10°, Table 4.3). There are two bands above 4.0 eV, which correspond to higher lying CT states and LE state on the D (Tables A.5 and A.6).

Finally, the absorption spectrum for **1d** exhibits a shape similar to **1c**, although the intensities are slightly modulated due to the increased dispersion of dihedral distances (Table 4.3) which permits increased mixing between the D and A, increasing orbital overlaps and therefore intensity of the low lying bands. In this case, clearly the 3 centre-2 electron interaction between the B-N bond and sulphur lone pair is not as effective at controlling the D-A motion as the methoxy group.

Fig. 4.7b shows the calculated absorption spectrum for **2a**-**2d**. These spectra appear to exhibit much less variation in contrast to Fig. 4.7a.

	S_0 State								
Structure	B-N / Å	B-X / Å	$\angle_\phi$ / °	$\angle_\tau$ / °	E_{S_1} / eV	E_{T_1} / eV	ΔE / eV	f_{S1}	SOC / cm^{-1}
1a	1.41±0.03	–	92.8±78.9	0.4±11.3	4.00±0.09	3.10±0.10	0.90±0.12	0.43±0.13	0.58±0.52
1b	1.42±0.03	3.19±0.17	110.7±30.1	11.7±23.1	3.70±0.20	3.11±0.13	0.59±0.25	0.23±0.13	0.56±0.39
1c	1.44±0.03	2.73±0.14	91.6±7.2	0.6±6.6	3.38±0.16	3.14±0.11	0.24±0.18	0.02±0.03	1.07±0.64
1d	1.46±0.03	2.97±0.23	90.1±14.7	14.0±10.1	3.64±0.17	3.05±0.11	0.60±0.20	0.06±0.07	2.48±1.99
2a	1.40±0.02	–	89.5±45.6	18.7±38.3	3.83±0.50	3.02±0.25	0.90±0.14	0.36±0.15	0.53±0.40
2b	1.42±0.03	2.97±0.23	99.4±20.4	42.5±25.5	3.99±0.23	3.04±0.12	0.96±0.25	0.28±0.14	0.96±0.61
2c	1.49±0.03	2.23±0.43	91.0±10.7	1.7±11.4	3.58±0.18	3..03±0.12	0.56±0.22	0.009±0.01	1.90±1.30
2d	1.50±0.03	2.67±0.40	87.9±18.6	0.1±7.0	3.56±0.15	2.94±0.12	0.61±0.19	0.035±0.038	3.06±2.37

	S_1 State								
Structure	B-N / Å	B-X / Å	$\angle_\phi$ / °	$\angle_\tau$ / °	E_{S_1} / eV	E_{T_1} / eV	ΔE / eV	f_{S1}	SOC / cm^{-1}
1a	1.50±0.03	–	91.1±60.7	1.6±8.7	3.11±0.17	2.71±0.16	0.40±0.20	0.07±0.05	0.36±0.19
1b	1.51±0.03	3.02±0.11	85.1±6.8	0.2±4.6	2.61±0.13	2.60±0.12	0.02±0.01	0.004±0.005	0.08±0.09
1c	1.52±0.03	2.78±0.15	93.6±6.8	0.8±5.0	2.40±0.17	2.39±0.17	0.01±0.01	0.004±0.004	0.15±0.27
1d	1.52±0.04	3.02±0.28	97.0±12.3	7.8±6.6	2.44±0.18	2.41±0.17	0.03±0.06	0.003±0.03	0.75±1.07
2a	1.53±0.03	–	0.3±8.8	4.5±14.5	2.30±0.13	2.29±0.12	0.02±0.02	0.005±0.007	0.05±0.06
2b	1.53±0.03	2.97±0.23	86.1±5.6	26.9±22.4	2.46±0.19	2.40±0.15	0.06±0.06	0.015±0.015	0.21±0.18
2c	1.55±0.04	2.34±0.13	91.6±9.5	1.6±6.2	2.23±0.17	2.22±0.16	0.01±0.02	0.003±0.002	0.27±0.48
2d	1.55±0.04	2.73±0.25	92.6±23.7	0.4±8.0	2.22±0.25	2.18±0.22	0.04±0.05	0.0069±0.01	0.88±0.99

TABLE 4.3: Analysis of the geometric and electronic structure properties obtained from 15 ps of *ab initio* molecular dynamics in the electronic ground (S_0) and first singlet excited state (S_1).

Indeed, the strong band which exists above 4 eV for all molecules arises from transitions into the S_1 state of the bent conformer, which has a larger oscillator strength due to the orbital overlap. However, as observed for **1c** and **1d**, the absorption spectra of molecules **2c** and **2d** exhibit weak low lying CT bands between 3.5 - 3.8 eV. This is weakest for the methoxy substituted **2c** as the D-A arrangement is closest to orthongonal and exhibits the smallest dispersion. For **2d**, these low lying CT bands of the twisted conformer gain intensity and appear as a long tail on the low energy side of the higher lying band.

Overall, these absorption spectra clearly show that for these molecules the non-covalent interactions clearly promote the formation of low lying twisted CT bands more than the steric non-covalent interaction. In addition, the methoxy clearly controls the dispersion giving rise to bands with strongest CT character. It is also importantly to note, that the addition of the methoxy and methylthio groups substantially increases the SOC between the lowest lying excited states which will also promote the ISC/rISC required for TADF.

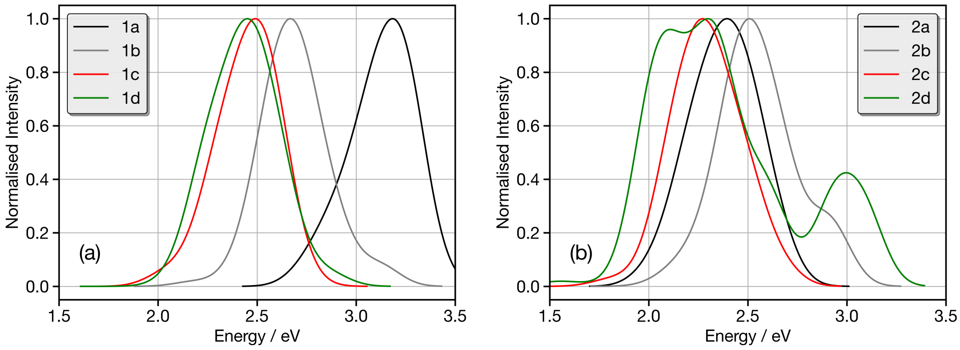

FIGURE 4.8: The calculated emission spectrum of (a) **1a** (black), **1b** (grey), **1c** (red) and **1d** (green) and (b) **2a** (black), **2b** (grey), **2c** (red) and **2d** (green). Each spectrum is calculated by average the 100 spectra simulated from structures sampled at random from the excited S_1 *ab initio* molecular dynamics. Each individual spectrum has been broadened using the Gaussian with a full-width at half-maximum of 0.1 eV.

Fig. 4.8a shows the emission spectra of molecules **1a**-**1d** calculated from the S_1 excited state *ab initio* molecular dynamics trajectories. Molecule 1a shows a band centred a 3.1 eV, which corresponds to emission from the low lying CT state associated with the planar structure. This band exhibits a distinct asymmetry (∼2.6 eV) which arises from a weaker contribution of the twisted conformers. Upon addition of the methyl groups, the two same bands (∼2.6 eV and 3.1 eV) remain present, but the relative intensity of the two bands is completely switched due to the increased prevalence of the twisted conformer in the excited state.

The emission for **1c** and **1d** shows a single broad band in both cases centred just below 2.5 eV. This arises from the emission of the twisted conformer's lowest-energy singlet excited state, which is dominant in these non-covalently controlled structures.

The emission spectra for molecules **2a**-**2d** exhibit quite a different trend. **2a** exhibits a single band at ∼2.3 eV, which corresponds to the bent conformer which dominates the *ab initio* molecular dynamics. The addition of the methyl groups (**2b**) generates two bands at 2.5 and 2.9 eV arising from the twisted and bent conformers which both appear for this system. A similar structure for emission is also observed for **2d** which also exhibits both conformers. Finally, the emission of **2c**, exhibits a single band, associated with the twisted conformer which is preferred due to the non-covalent interactions.

Overall, the emission properties of **1c** and **2c** are clearly preferred. The emission is both the narrowest and the strong CT character favourable for TADF. We note that the emission spectra in Fig. 4.8 have all been normalised to the largest intensity peak. Figure A.16 shows the average oscillator strength and as expect, this is weakest for molecules **1c** and **2c** due to the strong CT character.

4.3.2 JC Molecules

Quantum Chemistry Calculations of Critical Points

Table 4.4 summarises the *static* structures of the second set of 4 D-A molecules **JC258**, **JC274**, **JC257** and **JC324** at their ground, T_1 and S_1 optimised structures. From these we can see that in the electronic ground state, the B-N bond increases upon the addition of methoxy groups due to electron donation into the bond. The same is observed for the excited state, but the effect is much weaker as the bond is already expanded compared to the electronic ground state. $B\cdots O$ interaction is strong in the dimethoxy than the monomethoxy complex. In the monomethoxy the $B\cdots O$ interaction gets stronger in the S_1 state, but slightly weaker in the dimethoxy. The system is planar in the ground state in **JC258** and **JC274**, but the two methoxy and methyl groups make it perpendicular in both its ground and excited states.

Table 4.5 summarises the energies of the low-lying singlet and triplet excited states for these 4 molecules at their ground, T_1 and S_1 optimised structures. From these we can see that the S_1 energies computed at the ground state geometry, correspond to the first absorption peak fall at 3.98 eV (311 nm), 3.81 eV (325 nm), 3.41 eV (364 nm) and 3.42 eV (363 nm) for **JC258**, **JC274**, **JC257** and **JC324**. This is in reasonable agreement with the 323, 340, 364 and 371 nm observed experimentally. At the optimised

Structure	State (E / eV)	B-N / Å	B-X / Å	$\angle_{D-A}$ / °
JC258	GS	1.40	2.94	0.0
	S_1	1.49	2.88	0.0
	T_1	1.40	2.94	4.0
JC274	GS	1.41	3.31	0.0
	S_1	1.49	2.94	84.0
	T_1	1.40	3.30	0.0
JC257	GS	1.44	2.70	89.2
	S_1	1.50	2.75	88.0
	T_1	1.50	2.72	87.6
JC324	GS	1.49	2.25/3.21	91.1
	S_1	1.49	2.80/2.93	81.0
	T_1	1.49	2.14/3.26	94.5

TABLE 4.4: Summary of the ground, S_1 and T_1 structures for the **JC258**, **JC274**, **JC257** and **JC324**.

S_1 geometry, the first excited singlet-state energies that correspond to the observed emission are 2.56, 2.55, 2.62, and 2.38 eV. These are in good agreement and follow the trend to those recorded experimentally 2.61 eV, 2.61 eV, 2.69 eV and 2.47 eV. These shows that the adiabatic energy gap is 0.15, 0.17, 0.15 and 0.15 eV for **JC258**, **JC274**, **JC257** and **JC324**.

Table 4.6 summarises the SOC linking the low-energy singlet and triplet excited states. of the 4 molecules considered in this work at their ground, T_1 and S_1 optimised structures. From these we can see that the SOC is small between the S_1-T_1 states because they are the same character. The SOC is generally largest between the S_1-T_2 state. Large spin orbit couplings do appear between the S_2-T_1 state, but as the energy gap between these states is generally large, this will not be as significant as the S_1-T_2 state.

Structure	State	GS	S_1	T_1
JC258	GS	0.00	0.55	0.40
	S_1	3.98	3.11	3.24
	S_2	4.29	4.06	4.14
	S_3	4.37	4.29	4.21
	S_4	4.37	4.46	4.39
	T_1	3.43	3.04	2.96
	T_2	3.51	3.61	3.54
	T_3	3.67	3.85	3.69
	T_4	3.70	3.88	3.79
JC274	GS	0.00	0.51	0.40
	S_1	3.81	3.06	3.11
	S_2	4.25	4.16	4.16
	S_3	4.29	4.31	4.23
	S_4	4.34	4.43	4.33
	T_1	3.32	2.94	2.89
	T_2	3.51	3.63	3.56
	T_3	3.60	3.69	3.50
	T_4	3.61	3.81	3.73
JC257	GS	0.00	0.33	0.27
	S_1	3.41	2.95	2.98
	S_2	4.06	4.17	4.10
	S_3	4.23	4.19	4.21
	S_4	4.27	4.41	4.37
	T_1	3.04	2.84	2.80
	T_2	3.41	3.50	3.42
	T_3	3.49	3.51	3.47
	T_4	3.52	3.68	3.64
JC324	GS	0.00	0.46	0.30
	S_1	3.42	2.84	2.89
	S_2	3.92	3.95	3.88
	S_3	4.11	4.17	4.07
	S_4	4.21	4.35	4.34
	T_1	3.01	2.74	2.69
	T_2	3.36	3.50	3.40
	T_3	3.42	3.60	3.51
	T_4	3.52	3.75	3.62

TABLE 4.5: Summary of the excited state energies of the **JC258**, **JC274**, **JC257** and **JC324**. at their ground, T_1 and S_1 optimised structures.

Structure	States	GS	S_1	T_1
JC258	S_1-T_1	0.10	0.20	0.20
	S_1-T_2	0.12	2.83	1.89
	S_2-T_1	0.49	0.42	0.76
	S_2-T_2	0.18	0.13	0.05
JC274	S_1-T_1	0.24	0.22	0.24
	S_1-T_2	0.52	3.20	0.52
	S_2-T_1	3.20	1.03	3.20
	S_2-T_2	0.31	0.24	0.31
JC257	S_1-T_1	0.24	0.13	0.16
	S_1-T_2	2.62	1.02	0.87
	S_2-T_1	2.69	2.26	3.08
	S_2-T_2	0.54	0.39	0.12
JC324	S_1-T_1	0.33	0.19	0.26
	S_1-T_2	0.85	2.94	2.81
	S_2-T_1	0.30	0.45	0.46
	S_2-T_2	0.34	0.12	0.13

TABLE 4.6: Summary of the spin orbit couplings between the low lying states of the **JC258**, **JC274**, **JC257** and **JC324** at their ground, T_1 and S_1 optimised structures.

Molecular Dynamics and the Influence of Disorder

Table 4.7 shows a summary of the results obtained from the molecular dynamics simulations, which provides an insight into the disorder and the conformational flexibility for the JC molecules considered. The average structures obtained agree well with the optimised geometries described above and the trends (in terms of B-N and B-X bond lengths) remain the same.

	S_0 State						
Structure	B-N / Å	B-X / Å	∠ D-A / °	E_{S_1} / eV	E_{T_1} / eV	$\Delta E_{S_1-T_1}$ / eV	f_{S1}
JC258	1.45±0.03	–	26.4±10.0	3.76±0.26	3.19±0.13	0.57±0.12	0.26±0.05
JC274	1.46±0.03	3.09±0.14	36.5±12.7	3.63±0.23	3.15±0.15	0.48±0.11	0.19±0.06
JC257	1.49±0.04	3.01±0.12	118.0±5.6	3.26±0.16	2.94±0.10	0.32±0.08	0.14±0.05
JC324	1.48±0.03	3.36±0.20	46.3±16.4	3.57±0.24	3.09±0.12	0.48±0.11	0.17±0.04
	S_1 State						
Structure	B-N / Å	B-X / Å	∠ D-A / °	E_{S_1} / eV	E_{T_1} / eV	$\Delta E_{S_1-T_1}$ / eV	f_{S1}
JC258	1.58±0.04	–	53.5±9.2	2.58±0.16	2.41±0.10	0.16±0.08	0.05±0.04
JC274	1.59±0.04	3.04±0.12	60.3±10.5	2.47±0.17	2.33±0.13	0.14±0.06	0.04±0.03
JC257	1.63±0.06	3.10±0.14	97.5±3.7	2.29±0.21	2.20±0.18	0.09±0.05	0.02±0.02
JC324	1.60±0.04	3.21±0.21	72.1±7.7	2.40±0.14	2.28±0.12	0.12±0.04	0.03±0.02

TABLE 4.7: Structure and energetics of **JC258**, **JC274**, **JC257** and **JC324** from MD.

4.3.3 Donor-Acceptor-Donor Molecules

Quantum Chemistry Calculations of Critical Points

The table 4.8 presents a comprehensive overview of the primary structural parameters of three D-A-D molecules **3a**, **3b** and **3c** studied at their optimised electronic ground, excited S_1 and T_1 states, offering insights into the geometric configurations of these molecules and their potential for TADF. In the ground state, the B-C bond lengths are quite consistent across all three structures, with **3a** and **3b** both at 1.57 Å, and **3c** slightly longer at 1.58 Å. The B-X bond lengths vary, with **3b** having the shortest at 2.79 Å, suggesting a stronger interaction or possibly less steric hindrance/more rigid in this configuration while **3c** has the longest at 3.00 Å, indicating a more extended structure. Dihedral angles show significant variation, with **3b** at 109.30°, indicating a more twisted conformation compared to **3a** (97.45°) and **3c** (95.30°). Upon excitation to the singlet state, B-C bond lengths in **3a** and **3c** slightly change, while **3b** remains at 1.57 Å. The B-X bond lengths exhibit minor changes; **3b** remains the shortest at 2.80 Å. The dihedral angles highlight conformational adjustments, with **3b** and **3c** showing substantial changes. Structure **3a** has two distinct dihedral angles

(94.66° and 98.30°), suggesting flexibility, while **3b**'s angle reduces to 104.45°,indicating substantial structural relaxation upon excitation and **3c** shows a range from 103.40° to 87.01°, indicating a dynamic structural behavior. In the triplet state (T1), B-C bond lengths are stable with slight variations. B-X bond lengths shows variation with **3b** still as the shortest at 2.81 Å while **3c** shows significant elongation in the T1 state. Molecule **3a** and **3b** shows moderate changes in the dihedral angle while molecule **3c** exhibits the most dramatic changes in the dihedral angle in the T1 state where the angle increases to 126.98°, suggesting significant structural reorganization in the triplet state.

Structure	State (E / eV)	B-C / Å	B-X / Å	$\angle_{D-A}$ / °
3a	GS	1.57	2.95	97.45
	S_1	1.56/1.58	2.96	94.66/98.30
	T_1	1.57	2.94/2.99	96.46/101.82
3b	GS	1.57	2.79	109.30
	S_1	1.57	2.80	104.45
	T_1	1.58	2.81	96.46/101.82
3c	GS	1.58	3.00	95.30
	S_1	1.57/1.59	2.95/3.01	103.40/87.01
	T_1	1.59	2.79/3.22	126.98/99.71

TABLE 4.8: Summary of the ground, S_1 and T_1 structures for **3a**, **3b** and **3c**

In short, molecule **3a** exhibits relatively stable structural parameters across states, potentially beneficial for maintaining the energy gap required for TADF. However, less twisted in S1, potentially limit the spin-orbit coupling efficiency and less efficient charge transfer dynamics compared to **3b** and **3c** (see Fig. A.27). Molecule **3b** shows consistent B-C and B-X bond lengths with shortest B-X bond lengths and largest dihedral angles in the ground state (GS) which decreases from 109.30° in the GS to 104.45° in the S_1 state indicating significant conformational changes upon excitation. This shows **3b** is a rigid and flexible structure, which is favorable for enhanced spin-orbit coupling, efficient charge transfer and TADF (see Fig. A.28). Molecule **3c** with longest B-X bond lengths and wide range of dihedral angles, particularly in T_1 state suggests a high degree of structural reorganization which lead to less efficient charge transfer (see Fig. A.29). Overall, **3b** appears superior due to its balanced structural parameters and moderate reorganization.

The table 4.9 provides a corresponding excited state characteristics of D-A-D molecules **3a**, **3b** and **3c** at their electronic ground, excited S_1 and T_1 optimised structures. Molecule **3c** shows the smaller ΔE_{ST} (0.082 eV at GS and 0.084 eV at S1), indicating the highest potential for efficient rISC, crucial for TADF. However, its f_{OSC} is the lowest (0.0005) at ground state, suggesting weak light-harvesting. Molecule **3b** has a moderate ΔE_{ST} (0.116 eV at GS and 0.064 eV at S1) and a higher f_{OSC} 0.0218 at ground state and moderate at S_1, balancing between rISC efficiency and radiative strength. Molecule **3a**, while having the highest f_{OSC} (0.1425) at GS, exhibits a larger ΔE_{ST} (0.178 eV at ground state and 0.133 eV at S_1), which might hinder rISC. Therefore, molecule **3b** presents a better balance between ΔE_{ST} and f_{OSC}, making it a most promising candidate for TADF applications.

Structure	**Geometry**	S_1	S_2 **/eV**	S_3 **/eV**	T_1 **/eV**	T_2 **/eV**	T_3 **/eV**	ΔE_{ST} **/eV**	f_{OSC}
3a	GS	3.027	3.203	3.475	2.849	2.860	3.027	0.178	0.1425
	S_1	2.792	2.964	3.331	2.659	2.692	2.853	0.133	0.0886
	T_1	2.861	2.995	3.014	2.345	2.688	2.841	0.516	0.166
3b	GS	2.977	3.141	3.492	2.861	2.862	3.085	0.116	0.022
	S_1	2.549	3.005	3.305	2.485	2.664	2.929	0.064	0.009
	T_1	2.707	2.965	3.020	2.262	2.755	2.901	0.445	0.018
3c	GS	2.602	2.681	2.877	2.520	2.621	2.641	0.082	0.0005
	S_1	2.287	2.535	2.685	2.203	2.437	2.479	0.084	0.01
	T_1	2.081	2.530	2.738	1.736	2.449	2.499	0.345	0.05

TABLE 4.9: Summary of excited state energies of molecules **3a**, **3b** and **3c** at their ground, S_1 and T_1 optimised structures.

Molecular Dynamics of Conformational Disorder

Here, we aim to explore the properties of 2 D-A-D **3a** and **3b** emitters through molecular dynamics. The table 4.10 provides a detailed comparison of structural parameters and energetics of these molecules derived from molecular dynamics simulations in both the ground state and the singlet excited state. Overall, the molecular dynamics results agree well with the results calculated at optimised geometries. Molecule **3a**, compared to **3b** shows a comparative extended structure with slightly longer B-X bond lengths and smaller dihedral angles in both GS and S1 states. In contrast, molecule **3b** has shorter B-X bond lengths and larger dihedral angles, indicating a more twisted and compact conformation. Energetically, **3b** has higher singlet excited state energies in the ground state but lower in the S1 state compared to **3a**. The triplet excited state energies are very similar for both molecules, with slight reductions upon excitation. The singlet-triplet energy gaps indicate that **3b** has a larger gap in the ground state but a smaller gap in the S_1 state, suggesting better potential for TADF due to easier rISC. Therefore, molecule **3b** is giving a better conformational control due to B...O interaction and appears to be a better candidate for TADF applications.

	S_0 State							
Structure	r Å	B-X / Å	∠ D-A / °	E_{S_1} / eV	E_{T_1} / eV	$\Delta E_{S_1-T_1}$ / eV	f_{S1}	SOC / cm^{-1}
3a	1.58±0.03	3.01±0.09	90.71±7.65	3.04±0.096	2.78±0.09	0.26±0.08	0.02±0.026	0.82±0.39
3b	1.59±0.04	2.88±0.17	110.85±5.98	3.05±0.09	2.77±0.09	0.27±0.07	0.0457±0.03	0.98±0.50
	S_1 State							
Structure	r Å	B-X / Å	∠ D-A / °	E_{S_1} / eV	E_{T_1} / eV	$\Delta E_{S_1-T_1}$ / eV	f_{S1}	SOC / cm^{-1}
3a	1.60 ±0.04	2.97±0.09	91.93±8.94	2.88 ±0.10	2.56±0.09	0.31±0.12	0.01±0.01	0.39±0.23
3b	1.61 ±0.05	2.93±0.16	99.92±14.36	2.67±0.15	2.49±0.11	0.16±0.10	0.02±0.03	0.55±0.36

TABLE 4.10: Structure and energetic of molecules **3a** and **3b** from MD

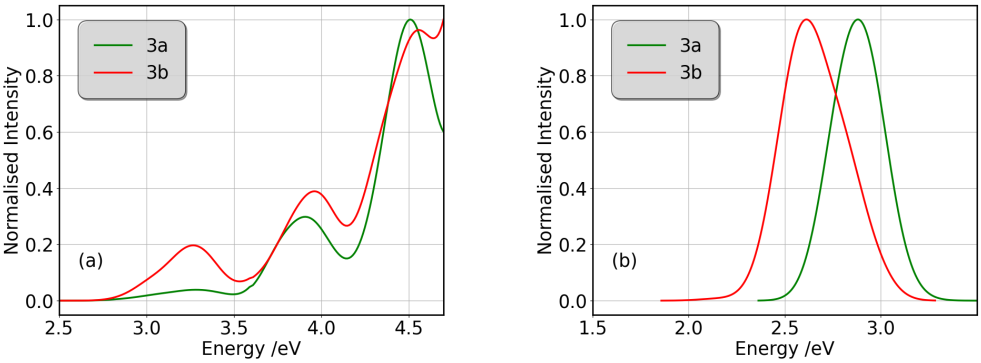

FIGURE 4.9: Fig. (a) shows calculated absorption spectrum of **3a** (green) and **3b** (red) and (b) shows calculated emission spectrum of **3a** (green) and **3b** (red). Each spectrum is calculated by average the 100 spectra simulated from structures sampled at random from the excited S_1 *ab initio* molecular dynamics. Each individual spectrum has been broadened using the Gaussian with a full-width at half-maximum of 0.1 eV.

Fig. 4.9 presents the calculated absorption and emission spectra for two D-A-D molecules, labeled as **3a** (green) and **3b** (red). The Fig. 4.9 (a) displays the absorption spectra, while the right Fig. 4.9(b) shows the emission spectra for these molecules. The spectra were generated by averaging 100 simulations of spectra obtained from structures sampled randomly from the excited S_1 state using ab initio molecular dynamics. Each spectrum was broadened using a Gaussian function with a full-width at half-maximum (FWHM) of 0.1 eV. In the absorption spectrum (Fig. 4.9a), both molecules exhibit multiple peaks, with **3a** showing its most significant absorption peaks around 3.9 eV and 4.5 eV with weak absorption around 3.3eV, and **3b** exhibiting peaks around 3.25 eV, 3.96 eV and 4.56 eV. Molecule **3b** better absorb at low energy compared to **3a**. The differences in the absorption profiles of **3a** and **3b**, likely due to different degrees of charge transfer between the donor and acceptor units within each molecule (Fig. A.27, A.28). In the emission spectrum (Fig. 4.9b), both molecules show a similar pattern. While molecule **3a** exhibits its emission peak around 2.88 eV, while molecule **3b** shows its emission peak around 2.62 eV.

4.4 Discussion and Conclusions

We have investigated a series of donor-acceptor molecules, exhibiting a B-N bond between the donor and acceptor with the objective of understanding the interplay of steric hindrance and non-covalent interactions in exerting fine conformational control on the excited state properties.

In the first set of molecules, our results show that for these molecules there are 3 major conformers, namely planar, bent and twisted, which differ in the structure around the D-A bond. In the electronic ground state, both the unhindered (**1a** and **2a**) and sterically methyl hindered (**1b** and **2b**) molecules favour the planar or bent conformers. This increases the communication between the D and A, and therefore increases the energy gap between the singlet and triplet states making TADF unfavourable. While the electronically excited states decrease the energy gap between the planar/bent and twisted conformers, generate the favourable twisted conformer in the excited state will require a significant structural rearrangements. While such changes are possible in the unconstrained environment of solution, the probability of it occurring in the restricted solid state medium of an OLED. The addition of non-covalent interactions (**1c**, **1d**, **2c** and **2d**) arising from the 3-centre-2-electron interaction between the oxygen (sulphur) lone pair and low-lying anti-bonding orbitals of the B-N bond [119] gives rise to a somewhat different picture. Indeed, these interactions strongly stabilise the twisted conformer required for these emitters to exhibit favourable TADF properties. In addition, the presence of oxygen and sulphur increase the spin orbit coupling increasing the rate of ISC/rISC. This class of non-covalent controlled TADF emitters not only offers the opportunity to fine-tune excited state functional properties such as energy gap and emission energy, but also control important dynamic properties which are detrimental to TADF materials. Indeed, unconstrained D-A molecules tend to exhibit CT emission which dynamically shifts in time arising from energy dispersion cause by dihedral angle inhomogeneity in most twisted D-A molecule [125]. The narrowing of the distribution around the D-A bond, especially for the methoxy derivatives arising from the non-covalent interactions offers the opportunity to reduce this dynamical dispersive behaviour and ultimately narrow the emission achieving molecules more suitable for OLED application.

The study of second set of molecules shows that the energy gap gradually decreases upon the inclusion of methoxy groups, consistent with the reduction of the delayed lifetime. This is associated with the clear change in the dihedral angle and its rigidity, as indicated by the standard deviation. The oscillator strength also decreases, consistent with the reduction of the prompt lifetime. Large spin orbit couplings do appear between the S_2-T_1 state, but as the energy gap between these states is generally large, this will not be as significant as the S_1-T_2 state. The S_1 energies (at the ground state geometry), corresponding to the first absorption peak fall at 3.76 eV (329 nm), 3.63 eV (341 nm), 3.26 eV (380 nm) and 3.57 eV (347 nm) for **JC258**, **JC274**, **JC257** and **JC324**. This is in very good agreement with the 323, 340, 364 and 371 nm observed experimentally. The S_1 energies (at the S_1 state geometry), corresponding to the emission energies are at 2.58, 2.47, 2.29, 2.40 eV. These are in good agreement and follow the trend to those 2.61 eV, 2.61 eV, 2.69 eV and 2.47 eV recorded experimentally. Hence, above study indicates that adding methoxy groups can improve conformational control in TADF materials due to the influence of non-covalent interactions.

In third set of molecules **3a** and **3b**. The detailed analysis highlights among the three structures, molecule **3b** appears to be the most promising candidate for TADF applications. Its structural rigidity, large dihedral angles and significant conformational changes upon excitation enhance spin-orbit coupling, can efficiently facilitate the rISC process, making it suitable for TADF applications. In addition favorable singlet-triplet energy gaps in the S_1 state in case of **3b** suggest enhanced rISC and efficient TADF performance. Structure **3c** also shows potential due to its very narrow singlet-triplet energy gap, but shows less efficient charge transfer due to its high flexibility and wide range of dihedral angles and longer B-X bond lengths, might limit its practical efficiency. Structure **3a**, while stable, lacks the necessary dihedral angle variations to significantly enhance TADF properties and also with higher ΔE_{ST} is less favorable for TADF compared to **3b** and **3c**. The above study reveal that molecule **3b** has the shortest B-X bond lengths and the largest dihedral angles, indicating a more twisted and compact conformation compared to **3a** and **3c**. This structural rigidity in **3b** is complemented by its higher oscillator strengths, suggesting stronger transition probabilities.

Chapter 5

Narrow Emitters using DHO Model

5.1 Introduction

Luminescent materials that exhibit narrowband emission represent an important challenge in the development of high resolution and energy efficient displays and are becoming increasingly important with the stringent requirements associated with high definition (HD) and ultra-high definition (UHD) displays. Light-emitting diodes (LEDs) based upon gallium nitride [126] or quantum dot LEDs [127, 128] have achieved emission profiles with full-width at half-maximum (FWHM) of <20 nm, however delivering equally high colour purity in organic light emitting diodes (OLEDs) remains a significant challenge [71].

This is because high performing phosphorescence [129] and thermally activated delayed fluorescence (TADF) [130] emitters which can achieve 100% internal quantum efficiency (IQE), predominantly use charge-transfer (CT) excited states which usually exhibit an inherently broad emission, with a typical FWHM ∼70-120 nm [83]. Consequently, commercial devices often use filters or optical microcavities [131] to enhance the colour purity of the electroluminescence (EL). However, this filtering significantly reduces the external quantum efficiency (EQE) leading to increased power consumption and shorter operational lifetime because the pixels need to run at higher brightness to compensate for this loss. With the ever increasing commercial requirements for high-resolution OLED displays, new emitters achieving both 100% IQE and narrowband emission, obviating the use of colour filters and their associated energy loss, are urgently required [132].

Emission broadening is caused by coupling between the electronic and vibrational degrees of freedom, *i.e.* vibronic coupling [123]. Electronic changes occurring upon excitation drive structural changes that modulate the energy gap between the S_0 and S_1 states, increasing the emission FWHM. A particular challenge is for systems that exhibit excited state electron density changes that are delocalised over multiple atoms. In such cases, as observed in the $\pi - \pi^*$ excitations in perylene, even small structural changes can give rise to a broad vibronic structure on top of the emission spectrum [133]. To overcome this, Hatakeyama *et al.* [134] developed the multi-resonance (MR) concepted, based upon on p- and n-doped polycyclic aromatic hydrocarbons. This exploits spatial symmetry (resonance) to separate the frontier orbitals involved in the low-lying excited states and minimise their bonding/antibonding character. The resulting non-bonding molecular orbitals (MOs) minimise the vibronic coupling, leading to narrow luminescence. The multi-resonance effect also reduces the exchange interaction making these materials suitable for application in TADF and the success of this approach has led to a significant number of experimental [133, 135–143] and theoretical [144–146] investigations into these systems, which have achieved high-performing 3^{rd}-generation [133] and Hyper-fluorescence OLEDs [147].

Despite the importance of the emission FWHM, there are few computatio-nal studies computing and/or predicting the emission FWHM of luminescent organic materials [133, 148, 149]. This is likely, at least in part, associated with the computational expense of calculating emission spectra from first principles which usually requires computation of ground and excited state geometries and Hessians [150, 151], although recent methods have been proposed that avoid the need for full excited state geometry optimisations [152]. Indeed, even with the huge progress in the speed of quantum chemistry methods, it remains a significant challenge to perform such calculations on a large set of molecules as would be required to incorporate the consideration of emission FWHM into high-throughput screening approaches [153, 154]. Recently, Ansari *et al.* [155] used a combination of experiment and theory to study the origin of the broad emission in TADF emitters. They concluded, based upon careful characterisation of donor-acceptor (D-A) based TADF emitters that the dominant factor was the charge transfer character of the molecule measured by the overlap between the HOMO and LUMO orbitals involved in the lowest excited states.

While, the authors demonstrated a strong correlation for 5 D-A TADF molecules, this approach does not take into account vibronic coupling and is therefore unlikely to be widely applicable beyond D-A type materials. Consequently, in this work we have studied 27 organic molecules exhibiting emitting states of different characteristics, including π-π^*, charge transfer (CT) and multiple-resonance (MR) to establish the key aspects responsible for emission FWHM. We have demonstrated that the emission width can be interpreted/predicted using the displaced harmonic oscillator model (DHO). Subsequently, we use quantum chemistry and rate calculations of three of the narrow MR-type thermally activated delayed fluorescence (MR-TADF) emitters to provide insight into into the balance between direct and spin-vibronic [69, 72, 73, 156] intersystem crossing (ISC) pathways, with the relative contribution of the former increased when sulphur is used within the B-N framework to increase the spin-orbit coupling and reduce the energy gap between the coupled S_1 and T_1 states. This, along the DHO model offers new perspectives for improving rational molecular design and/or high-throughput screening procedures for developing high efficiency MR-TADF emitters.

5.2 Theory and Computational Details

5.2.1 Molecular structures

Figures 5.1, 5.2 and 5.3 shows the 27 molecules considered in this work.

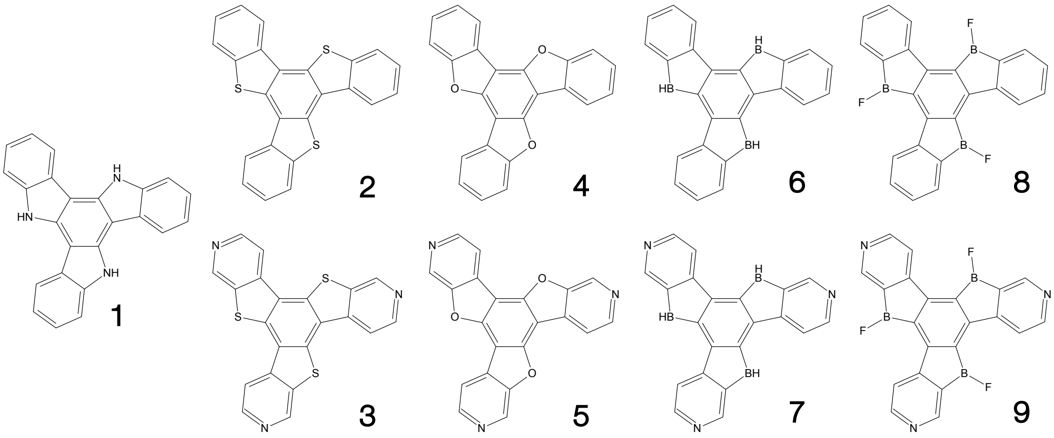

FIGURE 5.1: Truxene-type structures considered in this work.

Molecules **1** − **9** are based upon 10,15-Dihydro-5H-dindeno[1,2-a;1', 2'-c]fluorene-c]fluorene, commonly known as truxene [157]. This planar heptacyclic polyarene structure, obtained by trimerization of indan-1-one, has recently attracted a lot of attention in organic electronics due to its high thermal stability and ease of modification[158–164]. Molecules **10** − **18** are based upon the MR concept, which incorporates nitrogen atoms substituted in the para-position relative to a central boron atom, to exploit the opposite resonance effect of the two atoms to localised the electronic structure onto atomic sites reducing vibronic coupling and minimising the energy gap between singlet and triplet states [133, 134]. Molecules **19** − **24** are D-A type materials whose which exhibit CT

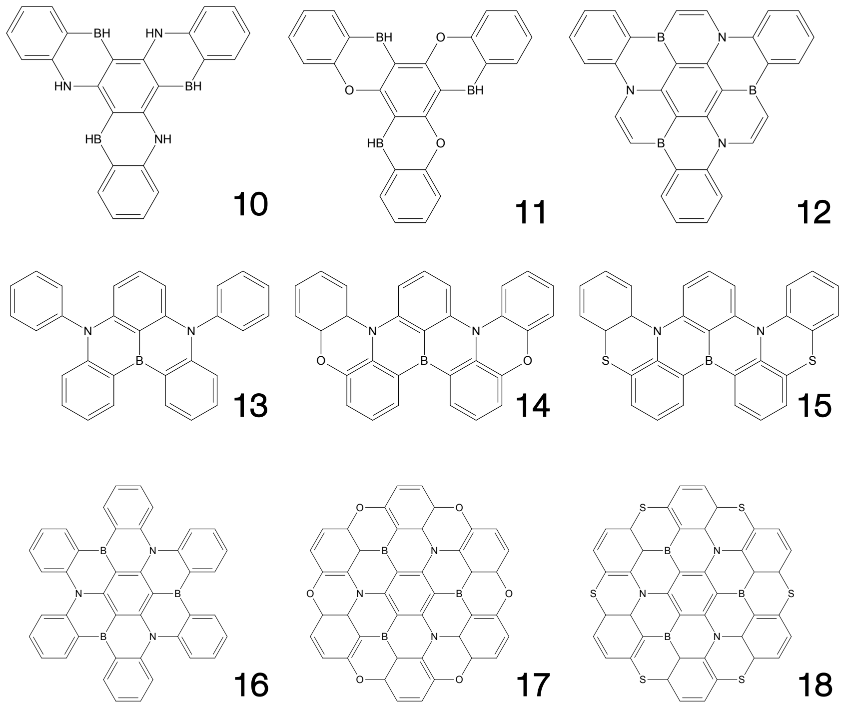

FIGURE 5.2: Multi-resonance type structures considered in this work.

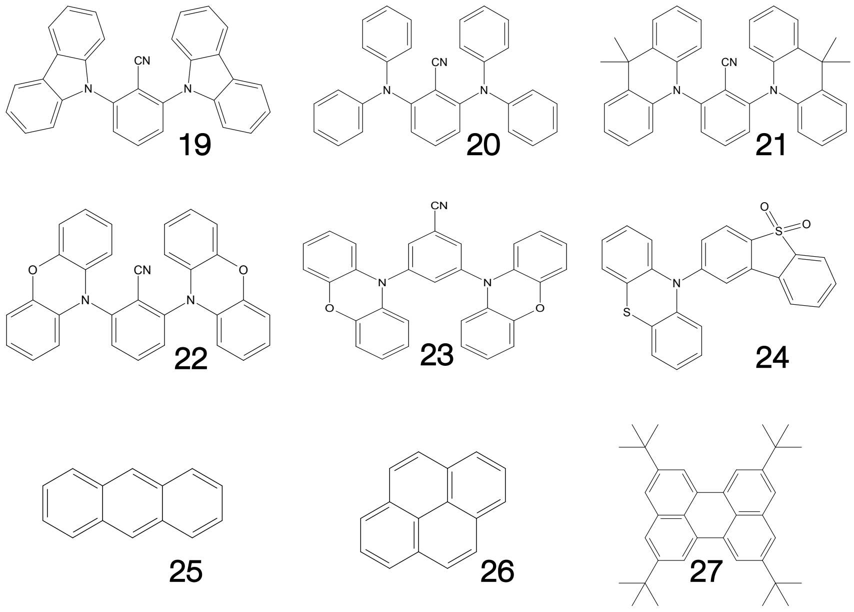

FIGURE 5.3: Charge transfer (**19-24**) and polycyclic aromatic (**25-27**) type structures considered in this work.

type emission [76, 155] and molecules **25** $-$ **27** are polycyclic aromatic hydrocarbons exhibiting low-lying $\pi - \pi^*$ states.

5.2.2 Quantum Chemistry and Fluorescence Spectra Simulations

Density functional theory (DFT) and linear-response time-dependent density functional theory (LR-TDDFT) simulations were performed within the approximation of the B3LYP exchange and correlation functional [165–168] as implemented within the ORCA quantum chemistry package [109]. A def2-SVP basis set was used throughout [117]. Frequency calculations were used verify that optimised geometries were true minima and not saddle points. CC2 simulations, simulated using the Turbomole quantum chemistry package [169]. These were performed at the TDDFT optimise S_1 geometry using a def2-TZVP basis set [117].

The absolute overlap between the HOMO and LUMO orbitals were calculated as:

$$\mathcal{O} = \langle |\phi_i||\phi_a| \rangle = \int |\phi_i||\phi_a| d\mathbf{r} \tag{5.1}$$

where ϕ_i and ϕ_a refer to the Kohn-Sham HOMO and LUMO orbitals respectively. It should be noted that the lowest excited state is not always a pure HOMO-LUMO transition and therefore we have also calculated Tozer's Λ diagnostic [170] defined:

$$\Lambda = \frac{\sum_{i,a} c_{ia}^2 \mathcal{O}_{ia}}{\sum_{i,a} c_{ia}^2} \tag{5.2}$$

where i refers to occupied molecular orbitals and a refers to unoccupied molecular orbitals and the absolute overlap between all the orbitals involved in the excited state are calculated and then weighted (c_{ia}) according to the occupied-unoccupied pair contribution to that excited state. This method has been widely used to characterised charge-transfer states within the framework of TDDFT [170].

The fluorescence spectra were calculated using the first principles path integral approach [152] implemented within the ORCA quantum chemistry package [109]. Here, the initial (S_1 optimised geometry) and final (ground state optimised geometry) states and their respective Hessian matrices are computed. This is used to compute the Duschinsky rotation matrix and displacement vector. Subsequently, the derivatives for the transition dipoles are computed. The spectrum is calculated as a Discrete Fourier Transform of the transition dipole correlation function, including both the well-known Franck-Condon and so-called Herzberg-Teller (HT) effects [123]. Throughout the temperature was set to 300 K and the stick spectrum was broadened using a Voigt function with line widths are Lorentzian component of width 50 cm^{-1} and a Gaussian component of width 250 cm^{-1}.

5.2.3 The Displaced Harmonic Oscillator Model

The method described in the previous section provides a first principles approach to computing fluorescence spectra, but can be time-consuming for larger molecules. The focus of this chapter is to develop an approach to speed up the prediction of emission bandwidth which will be achieved within the framework of the displaced harmonic oscillator (DHO), shown schematically in Fig. 5.4.

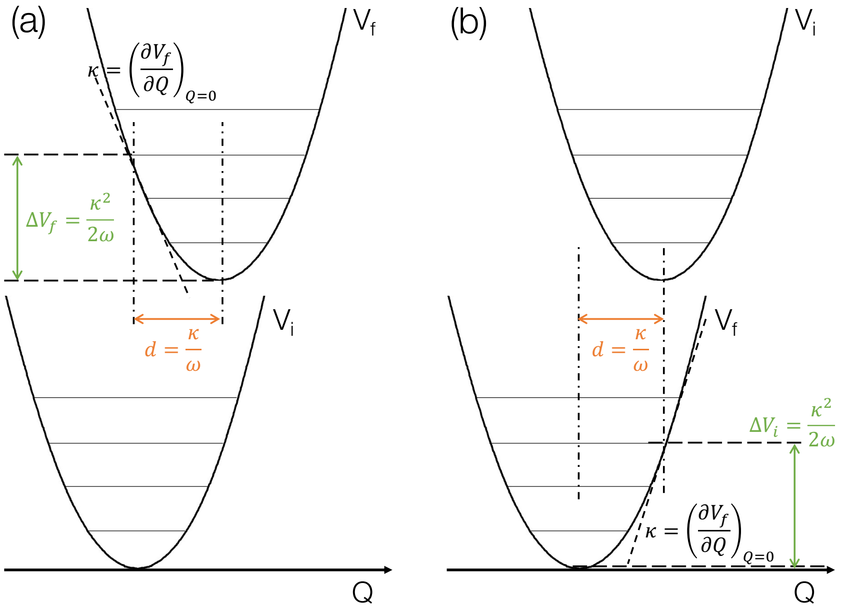

FIGURE 5.4: A potential schematic representation of the displaced harmonic oscillator model including the key insights that can be obtained and the components required to estimate the FWHM for the lowest (a) absorption and (b) emission bands.

Within the DHO model, shown schematically in Fig. 5.4, the magnitude of the displacement of the excited state with respect to the ground state for a particular normal mode, ω_α is expressed $d_\alpha = \kappa_\alpha/\omega_\alpha$, where κ_α is the gradient of the potential at the Franck-Condon geometry:

$$\kappa_\alpha^{(i)} = \left.\frac{\partial V_f}{\partial Q_\alpha}\right|_{\mathbf{Q}_0} \tag{5.3}$$

The Stokes shift can be estimated as $\Delta V_f + \Delta V_i = \kappa^2/\omega$. The displacement, d, which can be related to the Huang-Rhys parameter as d^2=D, corresponds roughly to the mean number of vibrational quanta excited from Q_0 in the ground state. This is the Franck-Condon principle, *i.e.* the transition intensities are dictated by the vertical overlap between nuclear wavefunctions in the two electronic surfaces. This can be written [171]:

$$|\langle\psi_g^{n=0}|\psi_e^n\rangle|^2 = \exp^{-D}\frac{D^n}{n!} \tag{5.4}$$

Consequently, as d influences the vibrational states excited, it will also influence the width of the absorption/emission spectrum. Within the Condon approximation, the spectrum can be written:

$$\sigma(\omega) = |\mu_{if}|^2 \sum_{n=0}^{\infty} e^{-D}\frac{D^n}{n!}\delta(\omega - \omega_{if} - n\omega_\alpha) \tag{5.5}$$

This spectrum is a progression of peaks deriving from ω_{if}, separated the frequency of the displaced normal mode, ω_α and a Poisson distribution of intensities. The intensities of these peaks are dependent on D, which is a measure of the coupling strength between nuclear and electronic degrees of freedom. The relationship between the distribution of intensities and the displacements motivated us to explore the correlation between FWHM and the DHO and throughout this work we relate the spectral width to κ^2.

The above discussion illustrates how the DHO model can be used to predict the FWHM of an absorption/emission band and the key aspects are shown in Fig. 5.4. We note that Fig. 5.4a corresponds to the lowest absorption band, in which the gradient of the S_1 state at the ground state optimised geometry in performed. For emission, the gradient of the S_0 state at the S_1 state optimised geometry needs to be performed, as shown in Fig. 5.4b. In the present work we perform both and discuss the correlations with the emission FWHM below.

5.3 Results

5.3.1 Calculated Emission Spectra

Fig. 5.5 shows the calculated emission spectra for **1**, **13**, **14** and **15** plotted against experimental spectra [134, 142, 161].

The remaining computed spectra are all shown in the Figures In each case, with the exception of the low energy vibronic structure observed for **15** (Fig. 5.5d) the calculated spectral shape is in good agreement with

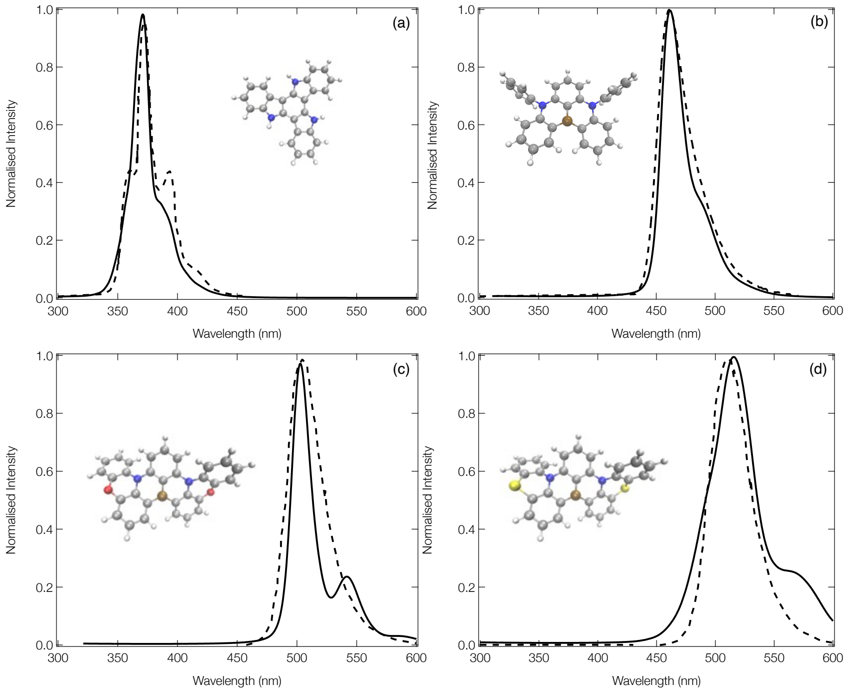

FIGURE 5.5: The experimental (dashed) and computed (solid) emission spectra of **1** (a), **13** (b), **14** (c) and **15** (d). In order to facilitate a more direct comparison between experiment and theory, the computed spectra of **1**, **13** and **15** have been shifted down by 20, 20 and 50 nm, respectively. The experimental spectra have been reproduced from refs. [134, 142, 161].

their experimental counterpart providing confidence in the theoretical approach used.

The emission spectrum of **1** has the smallest FWHM, with the side bands forming the vibrational progression separated by ~0.17 eV. This is driven by the normal mode exhibiting the largest displacement between the ground and excited state (ν_{81}, see Fig. B.1), which is dominated by a hydrogen wagging and slight breathing motion of the carbon-carbon bonds in the main structure. For **13**, commonly known as DABNA-1 [134], the vibronic progression has a separation of ~0.16 eV which arises from 2 dominant normal modes (ν_{112} and ν_{123}, the former is shown in Fig. B.13) which corresponds to breathing and stretching motions of the central B,N-core. Molecules **14** and **15** aim at rigidifying the DABNA-1 skeleton by incorporating oxygen or sulphur atoms, respectively. However, both of these molecules exhibit a slightly broader emission spectra which is because, as shown in Fig. B.14 and B.15, the non-planar structure associated with **14** and **15** means that the density change in the excited state is more delocalised compared to the atom site centred density change of **13**. In addition, although the dominant vibrational modes contributing to this emission FWHM remains primarily breathing and stretching of the central B,N-core, the fusing of the oxygen and sulphur atoms into the B-N based framework means these normal modes become delocalised over the whole structure.

5.3.2 Charge Transfer as a Metric for Emission Width

As outlined in the introduction, Ansari *et al.* [155] recently demonstrated for a series of CT emitters correlation between emission FWHM and HOMO-LUMO overlap ($\mathcal{O}$). Fig. 5.6a shows a plot of FWHM against $\mathcal{O}$ with the corresponding numerical data available in Table 5.1 for all 27 molecules. Although a correlation is observed it is not strong as indicated by the R^2=0.34 obtained from the line of the best fit (dashed line). While a transition between HOMO and LUMO orbitals is often a good approximation to describe low-lying CT state, not all of the molecules studied herein can be described using a pure HOMO-LUMO basis, which contributes to the low correlation seen in Fig. 5.6a.

Consequently, Fig. 5.6b (corresponding numerical data in Table 5.1) shows the correlation between emission FWHM and Λ (eq. 5.1). This slightly improves the correlation, as shown by the R^2=0.49. This improvement occurs primarily due to a better description of molecules whose excited states are not well approximated by a HOMO-LUMO transition and therefore poorly described using $\mathcal{O}$, for example molecule **26** as shown by the difference between $\mathcal{O}$ and Λ in Table 5.1. The excited state energy of CT states exhibit a $1/R$ dependence, where R is the

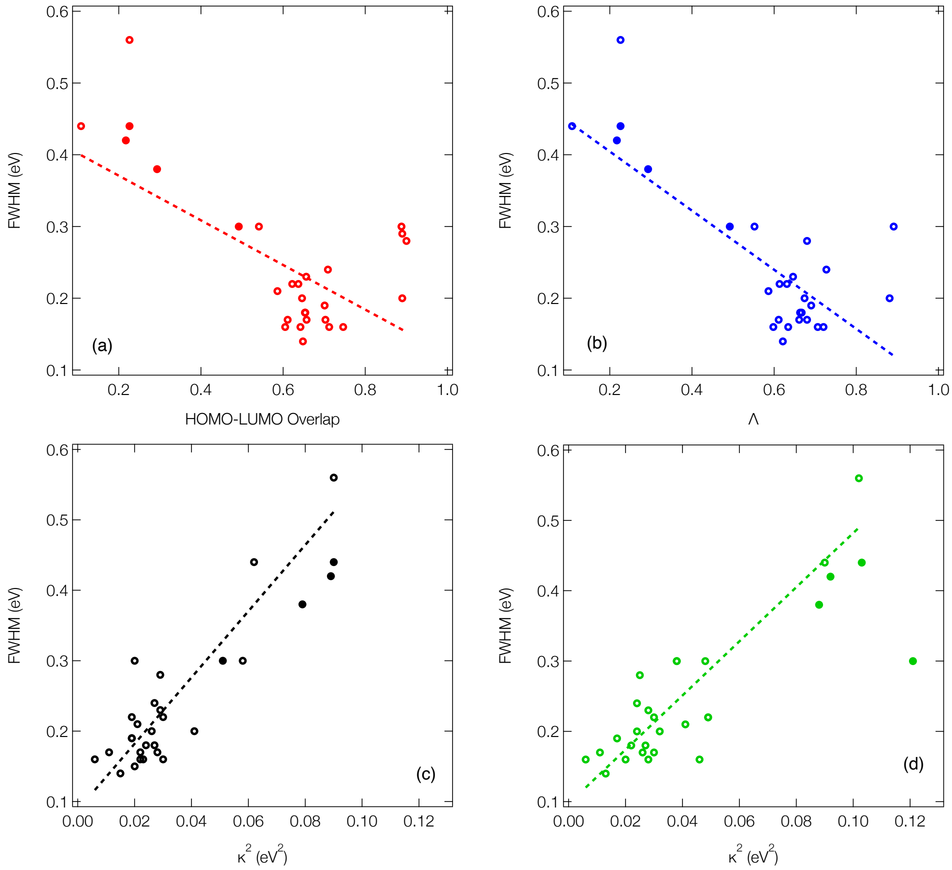

FIGURE 5.6: The correlation between emission FWHM and (a) HOMO-LUMO overlap, (b) Λ diagnostic, (c) κ^2 analysed using the S_1 gradient at the ground state geometry and (d) κ^2 analysed using the ground state gradient at the S_1 geometry. The open circles correspond to molecules where the calculated FWHM has been used. The filled circles correspond to molecules where we were unable to compute the spectra and so the experimental FWHM have been used. The dashed lined shows a linear fit to the data, excluding the data points based upon experimental FWHM.

	$\mathcal{O}$	Λ	κ^2_{GS} / eV^2	κ^2_{S1} / eV^2	FWHM / eV	
					Theo.	Expt.
1	0.712	0.720	0.023	0.020	0.16	0.14 [161]
2	0.709	0.727	0.027	0.024	0.24	–
3	0.653	0.663	0.024	0.022	0.18	–
4	0.746	0.706	0.030	0.028	0.16	–
5	0.657	0.680	0.028	0.026	0.17	–
6	0.646	0.674	0.026	0.024	0.20	–
7	0.654	0.667	0.027	0.027	0.18	–
8	0.656	0.646	0.029	0.028	0.23	–
9	0.637	0.631	0.030	0.030	0.22	–
10	0.701	0.690	0.019	0.017	0.19	–
11	0.648	0.621	0.015	0.013	0.14	–
12	0.703	0.661	0.011	0.011	0.17	–
13	0.605	0.598	0.022	0.046	0.16	0.19 [134]
14	0.611	0.611	0.022	0.030	0.17	0.18 [142]
15	0.586	0.586	0.021	0.041	0.21	0.20 [142]
16	0.642	0.634	0.006	0.006	0.16	–
17	0.622	0.613	0.019	0.049	0.22	–
18	0.541	0.552	0.020	0.038	0.30	–
19	0.293	0.293	0.079	0.088	–	0.38 [155]
20	0.492	0.492	0.051	0.121	–	0.30 [155]
21	0.217	0.217	0.089	0.092	–	0.42 [155]
22	0.219	0.219	0.089	0.103	–	0.44 [155]
23	0.226	0.226	0.090	0.102	0.56	0.48 [155]
24	0.108	0.108	0.062	0.090	0.44	0.39 [76]
25	0.888	0.891	0.058	0.048	0.30	0.35 [172]
26	0.900	0.680	0.029	0.025	0.28	0.24 [173]
27	0.890	0.881	0.041	0.032	0.20	0.29 [174]

Table 5.1: $\mathcal{O}$ calculated at the ground state geometry. Λ and κ^2 for all 27 molecules. κ^2_{GS} refers to the the lowest absorption band, *i.e.* where the gradient of the S_1 state at the ground state optimised geometry in performed. κ^2_{S1} corresponds to the calculation of the gradient of the S_0 state at the S_1 state optimised geometry. Theoretical and experimental FWHM are also shown.

distance between the donor and acceptor groups. Consequently, small structural changes will be responsible to large energy fluctuations and therefore a broad FWHM. It therefore follows that a significant variation in orbital overlap or CT character of the state will allow a trend with FWHM to be established. However, as can be observed in Figures 5.6a and b, for molecules exhibiting similar CT character, a trend between FWHM and either $\mathcal{O}$ or Λ is far less clear. In addition, while this analysis can be performed very quickly, it provides no insight into the normal modes responsible for the structural changes and broadening of the emission spectrum. Consequently, in the following section we move to the DHO model to establish a clearer trend and understanding.

5.3.3 Displaced HO Model to Estimate Emission Width

Fig. 5.6c (corresponding numerical data in Table 5.1) shows the κ^2_{GS} extracted from the DHO model, which as described in the section 2.3 describes the vibronic coupling within the system and can be related to the FWHM. In this first example the calculations have been performed at the ground state optimised geometry and therefore as illustrated in Fig. 5.4a, strictly corresponds to the width of the first absorption peak. In the present work we use this as a proxy for the emission FWHM and given the little configurational reorganisation between the ground and excited states for all of these molecules, it is expected to represent a good approximation. Importantly, this shows a significantly stronger correlation than observed using the CT metrics, discussed in the previous section, supported by the R^2=0.77. Fig. 5.6d shows the same trend, but in this case the gradient calculation has been performed in the electronic ground state at the S_1 optimised geometry as shown schematically in Fig. 5.4b. While this more rigorously corresponds to the emission FWHM, we observe a slightly weaker correlation with R^2=0.70. This is associated with the requirement to optimise geometries using TDDFT, which can pose problems for the CT- [52, 112] and MR-type [144] emitters.

The correlations identified illustrate a relatively easy to calculate metric which can be related to the emission FWHM. However, beyond these correlations between FWHM and κ^2, the DHO makes it possible to easily identify specific normal modes which contribute most strongly to the FWHM. As outlined in the introduction, this is most prominent for emitting states which exhibit electronic structure changes delocalised over multiple atoms, as vibrational motion will most strongly effect the excited state energy leading to a broader FWHM. This scenario is most clearly observed in the π-conjugated organic fluorophores; **25**, **26** and **27**. In these cases, as shown in Figures B.25-B.27, the density difference between the ground and excited state primarily occurs between the atoms, due to the $\pi - \pi^*$ excitations. Here the occupation of the antibonding orbitals leads to structural changes of the conjugated core, giving rise to a strong vibronic progression on the emission with peaks separated by $\sim$0.2 eV, *i.e.* the vibrational frequency of double bonded carbons.

For both the truxene-based molecules (**1-9**) and multiple-resonance emitters (**10-18**), the density difference plots shown in Figures B.1-B.18 exhibit density differences which are more localised on atomic sites, minimising their bonding/antibonding character and therefore the vibronic coupling in the excited state of the molecules. This is responsible for the narrower FWHM observed. As described above for **1**, the FWHM of the truxene-based molecules is largely controlled by hydrogen wagging and slight breathing motion of the carbon-carbon bonds in the main structure. For **2** the contribution of the carbon-carbon breathing mode is enlarged contributing to the larger FWHM. For **6**, **8** and **9** an asymmetric stretch of the central 6 membered carbon ring, as shown in Figures B.6,B.8, B.9 is responsible for the emission FWHM.

For the multi-resonance type emitters (**10-18**), the FWHM is dominated by breathing and stretching of the central B,N-core. For **17** and **18**, the extended π-system combined with the oxygen and sulphur fused into the framework leads to a non-planar structure. As shown in the density difference plots in Figures B.17 and B.18 this gives rise to some CT character and delocalisation of the density changes over the bonding regions, consequently a broader emission.

5.3.4 Excited states properties of 13, 14 and 15

Having established the correlation between emission FWHM and κ^2 in the previous section, in this final part we take a deeper look into **13**, **14** and **15**, known in the literature as DABNA-1 [134], 2PXZBN and 2PTZBN [142], respectively. As outlined in the introduction, the ISC/rISC mechanism of **13** has been widely studied in the literature [144–146] with a general consensus that spin-vibronic coupling is important [175, 176] . The focus in the present case is the influence of incorporating oxygen and sulphur into the B-N framework to enhance ISC.

Table 5.2 shows the excited state energies computed using TDDFT or CC2 for the lowest singlet and triplet states of each system. All calculations were performed at the S_1 optimised geometry. The TDDFT energetics for the S_1 state are in reasonable agreement with the CC2 calculations. However, as previously discussed in ref. [144], the singlet-triplet gap is very different due to the improved treatment of electron correlation in CC2 which is important in the MR-type emitters. Indeed, for all three molecules, the CC2 energies compare well to the fluorescence and phosphorescence spectra reported in ref. [134] and [142]. The higher lying triplet states (T_2 and T_3), which have been invoked in the spin-vibronic mechanism [145, 146] are also shown and important in this context of this mechanism is that the fusing of the O and S into the B-N framework appears to lower the energy gap between the lowest and higher lying triplets states which would lead to more effective mixing of the states. Finally, table 5.2 also shows the spin-orbit coupling between the singlet and triplet states. This clearly demonstrates inclusion of the O and S atoms increases SOC, important for ISC.

	Method	E_{S_1}	E_{T_1}	E_{T_2}	E_{T_3}	SS	λ	$E^{SOC}_{S_1-T_1}$	$E^{SOC}_{S_1-T_2}$	$E^{SOC}_{S_1-T_3}$	k^{calc}_{ISC}	k^{expt}_{ISC}
13	TDDFT	2.94	2.49	3.18	3.30	0.18	0.03	0.04	0.30	0.35	9.71×10^{2}	4.5×10^{6}
	LR-CC2	2.82	2.68	3.42	3.49	–	–	–	–	–		
14	TDDFT	2.59	2.12	2.48	2.91	0.21	0.02	0.05	0.53	0.89	8.0×10^{2}	3.27×10^{7}
	LR-CC2	2.43	2.29	2.69	3.14	–	–	–	–	–		
15	TDDFT	2.46	2.07	2.47	2.94	0.24	0.03	0.24	0.65	0.74	7.98×10^{5}	6.67×10^{7}
	LR-CC2	2.37	2.26	2.71	3.16	–	–	–	–	–		

TABLE 5.2: The excited state energies, spin-orbit coupling matrix elements of **13**, **14** and **15** at the S_1 optimised geometry. Calculation of the Stokes shift (SS) is derives from the DHO model. The reorganisation energy is the change in the energy of the final state when switching from the singlet to triplet geometry. The calculate k_{ISC} calculated using Fermi's golden rule combined with a Marcus formalism to estimate the Franck–Condon weighted density of states. The experimental rates are obtained from ref. [134, 142].

The enhanced SOC for O and S appear to support the advantages of incorporating hetero atoms in the framework to increase the ISC. To shed more insight into this, k_{ISC} was simulated using the Fermi's golden rule combined with a Marcus formalism to estimate the Franck-Condon weighted density of states:

$$k_{ISC} = \frac{2\pi}{\hbar} \sum_{f} \left| \langle \psi_f \left| \hat{\mathcal{H}}_{SO} \right| \psi_i \rangle \right|^2 \sqrt{\frac{\pi}{\lambda k_b T}} exp\left(-\frac{(\Delta E_{ST} + \lambda)^2}{4\lambda k_b T} \right) \tag{5.6}$$

Here λ corresponds to the reorganisation energy, which is the change in the energy of the final state when switching from the singlet to triplet geometry, while ΔE_{ST} is the energy gap between the two states.

Using Eq. 5.6, the calculated rate of ISC for **13** is k_{ISC}=9.71×10^{2} s^{-1}, between 3-4 orders of magnitude smaller than the experimentally determined rate of k_{ISC}=4.5×10^{6} s^{-1}. While this represents a substantial deviation, it is important to highlight that the present computational approach includes only the direct ISC mechanism. This partial agreement aligns with the findings of Kim *et al.* [146], who recently computed both the direct and spin-vibronic ISC rates for **13**. They showed that the spin-vibronic pathway dominates and, in excellent agreement with the present calculations, they reported a direct k_{ISC} of 10^{2-3} s^{-1}. This strongly suggests that our method reliably captures the direct ISC component, and the discrepancy with experimental results arises primarily due to the omission of the spin-vibronic contribution, which we plan to include in future work. Once incorporated, we expect the computed total ISC rate to align more closely with experiment. A similar situation is observed with **14**, with the calculated rate 4-5 orders of magnitude smaller than the experimentally determined rate, suggesting that the spin-vibronic mechanism dominates. This again supports the conclusion that, for molecules like 13 and 14, the spin-vibronic coupling is the dominant pathway for ISC, and its exclusion explains the quantitative mismatch with the experiment. However, the situation is somewhat different for **15**. Here, the S atoms fused into the B-N framework leads to a significant enhancement in the spin-orbit coupling between the lowest singlet and triplet states. This, combined with the smaller energy S_1-T_1 energy gap leads to a calculated direct k_{ISC}=7.98×10^5 s^{-1}. While this remains just under 2 orders of magnitude smaller than the experimentally determined rate of 6.67×10^7 s^{-1}, it suggests that the spin-vibronic mechanism has the smaller contribution compared to direct ISC in the case of **15**.

5.4 Discussion and Conclusions

Colour purity is often a core consideration when designing and optimising molecules to deliver high-resolution and energy efficient organic light emitting diodes (OLEDs), as it directly affects the sharpness and quality of the emitted light. One of the main contributors to colour purity is the emission full width at half maximum (FWHM), which defines the spectral sharpness of the emission. In this chapter, we have demonstrated how the DHO model can be used as a practical tool to predict the emission FWHM for a range of organic functional molecules exhibiting emitting states of different characteristics, including π-π^*, CT and MR which represent key classes of materials currently under investigation for OLED applications. The value of this approach lies in the fact that the key parameters required to estimate the FWHM can be obtained efficiently without any excited state optimisations which can be very time consuming and resource-intensive. Moreover, the model provides physical insight by linking spectral broadening to specific vibrational modes, allowing chemists to rationally modify molecular structures to suppress detrimental vibrational couplings. The DHO not only provides an attractive framework for interpreting excited state structural changes in terms of specific normal modes, but also by its efficiency offers new perspectives for incorporating considerations of emission FWHM into rational molecular design and high-throughput screening procedures. In addition, it is relatively straightforward to extend the DHO to include off-diagonal vibronic coupling between excited states, allowing exploration of non-Condon and non-Born-Oppenheimer effects [123, 177] that have been identified to be important for functional organic molecules, especially those exhibiting TADF [175, 176], where spin–vibronic interactions play a pivotal role in triplet-to-singlet upconversion. The DHO model can thus serve not only as a screening tool, but also helps us to understand complicated behaviour in excited-state dynamics, especially in materials where traditional Franck–Condon approaches fall short.

To complement this model, we have performed quantum chemical calculations at both TDDFT and CC2 level of theory, combined with rate calculations within the semi-classical Marcus formalism of three MR-type emitters. These calculations have shed insight into the mechanism of ISC and the role of fusing O and S atoms into the B-N framework. Although the inclusion of these hetero atoms in the case of **14** and **15** leads to a slight increase in the emission FWHM it also increases the k_{ISC} [142]. This is most significant for **15**, where the incorporation of sulfur led to a greater SOC and consequently shows a more prominent increase in the direct ISC pathway compared to the spin-vibronic mechanism. In these cases, the similarity of the character of the S_1 and T_1 states leads to a small reorganisation energy and in this regime the energy gap law, *i.e.* the rate of ISC depends exponentially on the singlte-triplet energy gap between the two states, is valid. Consequently, the smaller energy gap combined with the increased SOC leads to the increased importance of direct ISC in **15**.

This has important implications for TADF materials, as it suggests that MR emitters can achieve efficient triplet harvesting through structurally simpler mechanisms, without relying on the strong donor–acceptor interactions that make D–A molecules highly sensitive to environmental effects [80, 178–183]. The reduced environmental sensitivity of MR emitters, in conjunction with their intrinsically narrow emission profiles, makes them highly attractive candidates for OLED applications. Moreover, the insights gained here help pave the way for rational design strategies aimed at tuning emission properties and excited-state dynamics simultaneously, thus supporting the development of reliable high-throughput design rules for advanced emitter materials.

Chapter 6

Towards Accurate Simulation and Discovery of New Multi-Resonance TADF Emitters

6.1 Introduction

High triplet exciton utilisation efficiency, colour purity, and short excited state lifetimes are critical properties for high performing molecular emitters used in Organic Light Emitting Diodes (OLEDs) [71]. The efficient use of triplet states generated by electrical excitations in OLEDs can be achieved using third-row transition metal complexes that facilitate phosphorescence from the lowest triplet excited state [129, 184], as well as purely organic molecules exhibiting thermally activated delayed fluorescence (TADF) emitters [57, 58, 130] which up converts the non-emissive triplet excitons into emissive singlet states. However, both strategies primarily involve exploiting charge transfer (CT) states, which inherently produces broad emission spectra with a full width at half maximum (FWHM) of ∼70-120 nm. Consequently, while efficient, achieving the necessary colour purity, commercial OLED displays typically use colour filters and/or optical microcavity structures to narrow the emission linewidth [185]. This significantly reduces efficiency, increases power consumption, and shortens the operational lifetime, as devices are required to operate at higher brightness levels to offset the effect of the filtering.

Overcoming this challenge and achieving high performing molecules exhibiting a narrow FWHM represents a sizeable obstacle motivating a concerted research effort, a significant amount of which has focused upon multiple resonance TADF (MR-TADF) emitters [68, 186]. These compounds, first introduced by Hatakeyama *et al.* [134] aim at reducing the exchange interaction and so ΔE_{ST} by site-specific doping of electron-donating atoms (*e.g.*, nitrogen and oxygen) or withdrawing atoms/functional groups (*e.g.*, boron and ketone groups) of

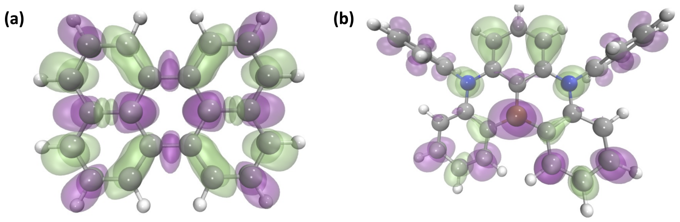

FIGURE 6.1: Density difference of associated with the S_1 excited state of perylene and **DABNA**. For the $\pi\pi^*$ excitation in perylene, even small structural changes can give rise to a broad vibronic structure on top of the emission spectrum, as excited state electron density changes are delocalised over multiple atoms and in particular in the bonding region of the molecule. In contrast, the MR-TADF emitter, **DABNA**, exhibits a density different which non-bonding in character localised predominantly on the atomic positions.

polyaromatic hydrocarbon compounds. This exploits spatial symmetry (resonance) to separate the frontier orbitals involved in the low-lying excited states and minimise their bonding/antibonding character. The resulting non-bonding molecular orbitals (MOs), see Fig. 6.1, minimises the vibronic coupling, meaning the rigid planar structures of MR-TADF tend to show very narrow emission profiles to narrow luminescence, small Stokes shifts and high photoluminescence quantum yields [81, 134, 139]. and hence can potentially bridge the gap between luminescence efficiency and colour purity in OLEDs [187], [188], [189].

Despite the promise to apply within a commercial setting, MR-TADF emitters need to overcome the typically long delayed fluorescence lifetimes due to unfavourable rISC [57, 190]. This arises primarily from the ΔE_{ST} values which are typically larger than in D-A TADF emitters due to the characteristic short range charge transfer (SRCT) mechanism that causes a larger exchange integral. In addition, these emitters tend to exhibit small spin orbit coupling matrix elements (SOCME) as the manifold of singlet and triplet states with the same character [123], therefore rISC operates strongly using the spin-vibronic mechanism requiring coupling to higher lying excited states [145, 191–194]. To overcome this some groups have sort to exploit the heavy atom effect [142, 195–198] or introduce low lying states of different character, *e.g.* CT [199] or $n \rightarrow \pi^*$ [200], to promote large SOCME and therefore increase the rate of rISC. While successful to some extent, the rate of rISC still needx to be increased and here *in silico* design is likely to play an important role in increasing the chemical space of MR-TADF emitters [201].

From the computational perspective, describing the excited state properties of MR-TADF emitters, critical for ensuring the accuracy of any *in silico* design, is challenging due to the importance of electron correlation. Indeed, linear-response time-dependent density functional theory (LR-TDDFT) is known to perform poorly in calculating the excited state properties of MR-TADF emitters. Hall *et al.* [202] demonstrated that this was due to inaccurate description of Coulomb electron correlation and any computational methodology used should include (at least partially) double excitations from the ground state reference wavefunction. The authors demonstrated methods such as spin-component scaling second-order approximate coupled cluster (SCS-CC2) gave much improved excited-state energy prediction compared to LR-TDDFT. However, while the performance is good, this comes at a cost of computational expense. Indeed, the formal scaling of coupled-cluster calculations with single and double excitations (CCSD) is $O(N^6)$, where N reflects the system size in terms of number of basis functions. While this reduces to $O(N^5)$ for CC2 as double excitations are partially included [203], it remains significantly more demanding than TDDFT based methods.

Herein, we have investigated the performance of mixed-reference spin-flip time-dependent density functional theory (MRSF-TDDFT) [204, 205] in describing the excited state properties of MR-TADF emitters. The results indicate that this approach accurately predicts the excited state properties including the crucial ΔE_{ST}. Building upon this, we adopt this method to explore the excited state properties of systems designed to enhance the coupling between singlet and triplet states by increasing the density of states.

In addition, narrow blue MR-TADF emitters are in high demand due to their potential to overcome the crucial remaining challenge in developing cost-effective, highly efficient, and stable OLEDs for display lighting applications [206]. Although notable progress has been made [207], still significant challenges persist in the development of high performing deep blue MR-TADF emitters. Achieving this requires higher energy compared to green or red emission, making it difficult to do so without causing significant energy losses and efficiency roll-off [206]. Inverse design combined with high-throughput computational screening is a powerful approach and can be used to discover novel deep blue MR-TADF emitters, which is advantageous over traditional methodologies though effective but can be time-consuming and resource-intensive [208–210], [211], [212]. Inverse design methodologies involves focus on specifying desired properties and then identifying or generating new molecular structures that meet these criteria. High-throughput virtual screening (HTVS) utilises computational power to quickly assess a vast chemical space, accelerating the quest for novel and valuable materials. However, MR

TADF is a relatively new approach, which has resulted in a limited number of documented deep blue MR TADF emitters in the literature. This scarcity of desirable data makes it more challenging to design new efficient blue emitters using high-throughput virtual screening or machine learning.

To address this problem, we employed the STONED algorithm to generate a large and diverse dataset of potential candidates, recently proposed in [213], leverages string modifications in the SELFIES (Self-Referencing Embedded Strings) molecular representation, bypassing the need for extensive datasets and lengthy training times typically required for traditional machine learning approaches. SELFIES ensures that every generated string is a valid molecule, thus significantly enhancing the efficiency of the molecule generation process. Following the generation of a comprehensive molecular dataset, we performed high-throughput screening using computational methods to evaluate key properties relevant to deep blue MR-TADF performance. Overall, we have used computational funnel approach, like the schematic shown in Fig. 6.2 systematically narrowing down the candidate pool through successive layers of increasingly stringent criteria. This multi-stage screening ensured that only the most promising candidates were retained for detailed analysis.

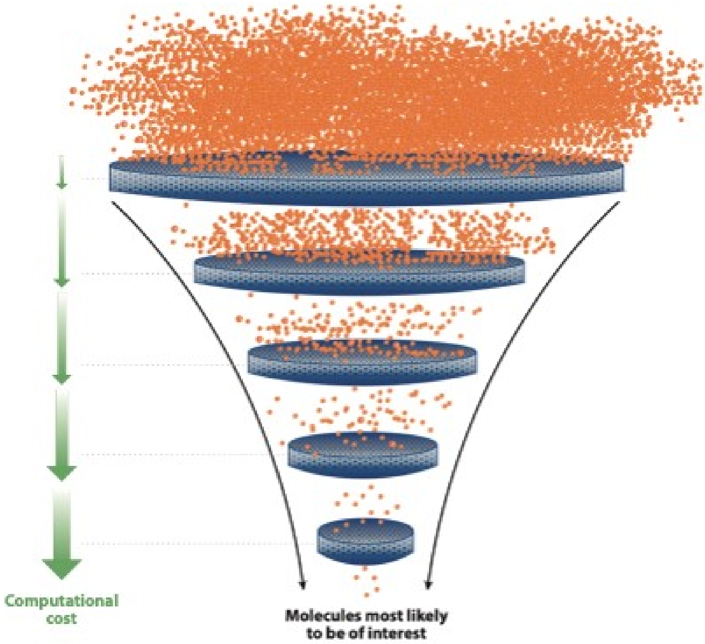

FIGURE 6.2: A computational funnel scheme: The increasingly strict rules filter out lots of unimportant molecules, leaving only the best candidates in a virtual library.

6.2 Theory and Computational details

LR-TDDFT is a popular computational method, widely used to simulate the excited states of large molecular systems. However, as discussed above it is unable to accurately capture the excited states in MR-TADF emitters as the single excitation representation used in LR-TDDFT (Fig. 6.3) fails to accurately describe the Coulomb correlation interaction. This can be circumnavigated using methods incorporating higher-order excitations, *e.g.* CC2, albeit accompanied with a significant increase in computational cost.

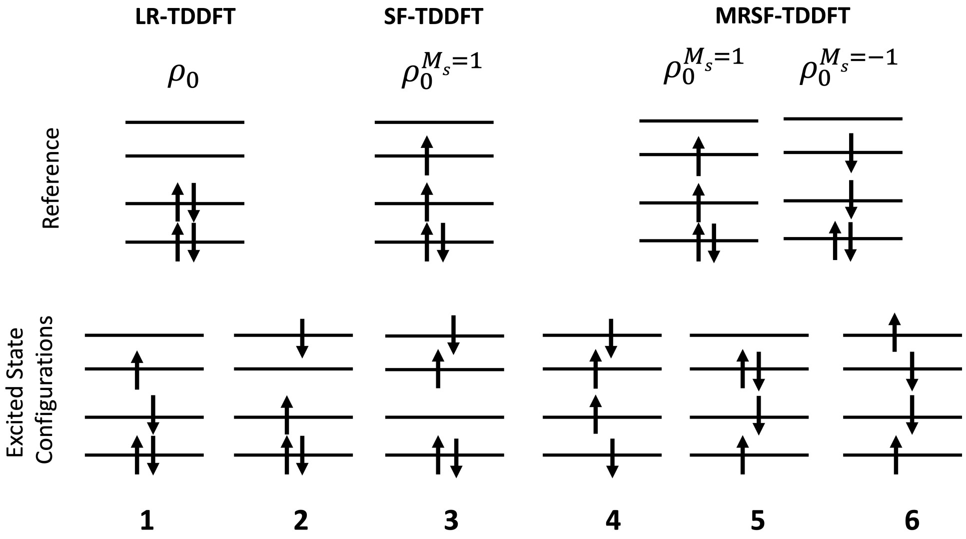

FIGURE 6.3: *Upper:* Schematic of the reference wavefunctions used in LR-TDDFT, SF-TDDFT and MRSF-TDDFT. *Lower:* Excited state electron configurations which may be important for describing the excited state. Configurations 1 and 2 represent single excitations from a ground state reference and therefore can be described in all methods. Configurations 3 and 4 are higher order and can only be described by SF-TDDFT and MRSF-TDDFT. Finally, configurations 5 and 6 are only accessible from the MRSF-TDDFT.

To overcome this, while retaining the benefits of TDDFT, *i.e.* computational efficiency, one can exploit the spin-flip (SF) *ansatz* [214, 215], which represents a less conventional approach to describe the multi-configurational electronic structure and has been shown to recover strong correlation effects [216, 217]. This method maintains the single excitation representation, but commences from a triplet reference state. Consequently, the electronic ground state appears as a negative excitation between the two singly occupied orbitals (**e.g.** LUMO→HOMO). As a result, SF-TDDFT is able to capture configurations which formally correspond to two electron excitations from the electronic ground state, *e.g.* configuration 3 and 4 in Fig. 6.3.

While SF-TDDFT offers many advantages for describing excited stats [218], the use of a single component of the reference triplet state (*e.g.* M_s=1) results in substantial spin contamination, which often impedes identification of the response excited state as a singlet or a triplet [219]. In the context of MR-TADF this is especially important given the role of higher lying triplet states *via* the spin-vibronic mechanism [72, 73, 123, 145, 191–194]. MRSF-TDDFT [204] seeks to ameliorated the spin contamination by use of both high-spin components of the triplet state, *i.e.*, M_S = +1 and M_S = -1 (Fig. 6.3), as a reference for obtaining response excited states and consequently, MRSF-TDDFT recovers almost all of the spin configurations necessary for restoring the proper total spin of the SF excited states. Since its development in 2018 [204], MRSF-TDDFT has been applied to a number of different situations and displays great promise as an accurate and computationally efficient method for describing excited states [205, 220–225]

In section 6.3.1 and 6.3.2, all structures were optimised in the ground, lowest singlet or triplet excited states using density functional theory (DFT) and linear response time-dependent density functional theory (LR-TDDFT) within the Tamm-Dancoff approximation (TDA) [226] and the PBE0 exchange and correlation functional [227] as implemented within the ORCA quantum chemistry package [109]. Multi-reference electronic structure calculations were performed using the State-average complete active space self-consistent field (SA-CASSCF) approach with the def2-TZVP basis set. Dynamic correlation was taken into account with a second-order N-electron valence perturbation theory (NEVPT2) calculation on top of the CASSCF wavefunction as implemented within ORCA [109].

All MRSF-TDDFT single point calculations were performed using the GAMESS-US program package [228]. The MRSF-TDDFT equations were solved within the approximation of the PBE0 exchange and correlation functional and a def2-TZVP basis set. All energies recorded described the solvent environment using the conductor-like polarisable continuum medium (CPCM) [114] and the properties of toluene.

Following these calculations, the radiative decay rate ($k_r(S_1 \rightarrow S_0)$) can be obtained from the Einstein spontaneous emission equation [229]:

$$k_r(S_1 \rightarrow S_0) = \frac{f \Delta E^2}{1.499} \tag{6.1}$$

where f_{osc} is the oscillator strength and ΔE is the vertical excitation energy in cm^{-1} at the S_1 geometry.

In section 6.3.3, three-stage high-throughput virtual screening (HTVS) has been done for discovering narrow blue MR-TADF emitters. Starting from 88 known molecules, successive filtering based on energy gap, oscillator strength, and emission criteria narrows the pool to 6 promising candidates, with increasing computational accuracy and cost at each stage (Fig. 6.4). We began with a carefully chosen collection of 88 narrow MR TADF molecules extracted after thoroughly reviewing the existing literature (see appendix). Employing the semi-empirical quantum chemistry method PM3 (Parametric Method 3) optimisation which provides a quick and approximate analysis, we narrowed down the selection to 82 molecules by considering those with a HOMO-LUMO gap greater than 3eV.

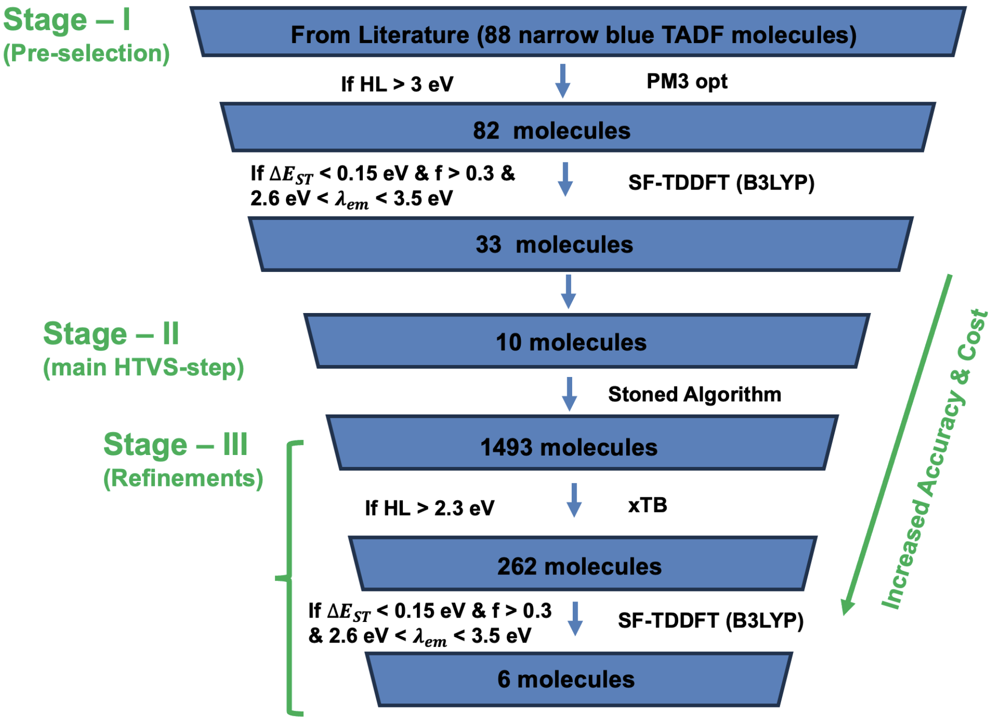

FIGURE 6.4: Methodology

Subsequently, we applied the more accurate SF-TDDFT method to these 82 molecules. We have used SF-TDDFT instead of MR-SF-TDDFT for our analysis in this case because we were focusing solely on the first triplet state. SF-TDDFT offers here a good balance between computational efficiency and accuracy, making it well-suited to our study and providing the necessary detail without the extra computational cost of MR-SF-TDDFT. We filtered the candidates further based on specific criteria, selecting molecules with a singlet-triplet gap below 0.15 eV, emission wavelengths ranging from 2.6 to 3.5 eV, and oscillator strengths exceeding 0.3. This refined our list to 33 promising molecules (see appendix). Further, we singled out the top 10 candidates (Fig. 6.9) and applied a STONED algorithm to this subset, resulting in the generation of an extensive dataset comprising 12000 molecules, starting with a SMILES structure which undergoes string reordering to generate alternative SMILES and converting it into SELFIES for robust molecular representation. Incremental changes within SELFIES allowed seamless structural modifications. Four key techniques were employed: random character changes in SELFIES for valid molecule generation, multiple representations to enhance diversity, deterministic interpolations for precise generation, and fingerprint comparisons for structural similarity. These methods constructed local chemical subspaces (Fig. 6.5), enabling the discovery of novel molecules with structural similarities to the initial seed structures through successive mutations.

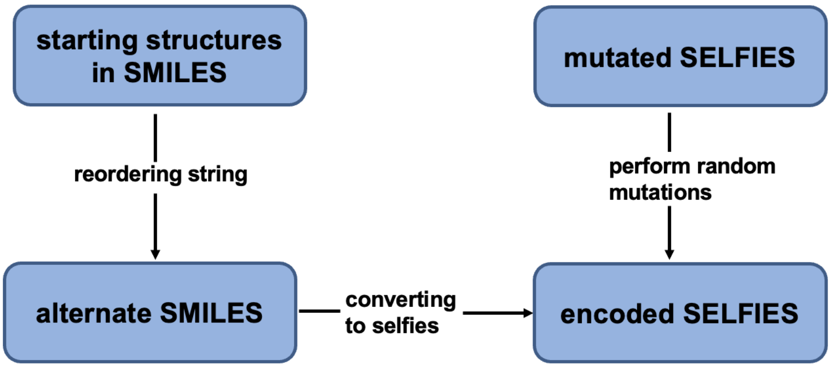

FIGURE 6.5: Formation of Local Chemical Subspace

To refine this extensive dataset, we applied a filtering criterion, ensuring that the newly generated molecules retained at least 75% similarity to the original set and comprised no less than 75% of the initial molecule count, resulting achieved a data set of 1493 structures. This refined dataset was then subjected to the xTB (extended Tight-Binding) semi-empirical method known for their speed and are commonly employed in large-scale simulations, screening studies, and exploratory calculations where a balance between accuracy and computational cost is essential. From this analysis, we identified 262 molecules based on a criterion of a HOMO-LUMO gap greater than 2.3 eV (see C.2). Furthermore, we applied again SF-TDDFT method to the subset of 262 molecules. Through this refinement, we isolated a subset of those molecules that met stringent criteria: a singlet-triplet gap less than 0.15 eV, an oscillator strength greater than 0.3, and emission wavelengths falling within the range of 2.6 to 3.5 eV. A few molecules met the criteria, while others did not. For instance, the molecule with the SMILES string "Nc1cccc2c1b1c3ccccc3n(c3ccccc3)c3cccc(c13)n2c1ccccc1" had a wavelength of 3.203 eV, a singlet-triplet gap of 0.179 eV, and an oscillator strength of 0.58. Since its singlet-triplet gap exceeded 0.15 eV, it did not meet the criteria. After filtering all 262 molecules, we ultimately identified the 6 best candidates.

All calculations were performed using the ORCA quantum chemistry package and employed the def2-SVP basis set and the B3LYP exchange-correlation functional throughout. Initially, SF-TDDFT was used to optimise and compute the excited states within the computational funnel approach. Subsequently, for the same set of 6 molecules, all structures were re-optimised in both ground and triplet states using DFT and TDDFT, followed by the computation of excited state energies. This systematic and iterative approach, combining the strengths of both semi-empirical and first-principles methods, enabled a thorough exploration and refinement to predict novel blue narrow TADF molecules.

6.3 Results

6.3.1 Benchmarking MRSF-TDDFT for MR-Emitters

Fig. 6.6a shows a correlation plot between the MRSF-TDDFT(PBE0) calculated and experimental absorption energies for the 50 MR-TADF structures considered in this work (see Figure S1-S3 and Table S1). Overall, this displays a strong correlation, although in a similar manner to that observed in ref. [202], it does not follow the $y = x$ line (grey dashed) but rather a shifted line of the form $y = 1.135x$, suggesting the error between experiment and theory increases with energy. While factors such as solvatochromism can influence the total energy, this absolute error suggests aspects of electron correlation are still lacking and this is discussed below. The r^2 value for between the data and this best fit line is 0.90, with the colour of the data points indicating the distance from this best fit line, with white being closest and red furthest away. The mean absolute deviation (MAD) between MRSF-TDDFT(PBE0) calculated and experimental absorption energies is 0.37 eV, very comparable to the performance of SCS-CC2 reported in ref. [202].

Fig. 6.6b shows the corresponding correlation plot for the MRSF-TDDFT(PBE0) calculated and experimental emission energies. In common with the observations for the absorption energies, there is strong correlation between calculated and experimental values, which follows again follows a line of best fit of the form $y = 1.135x$. Overall

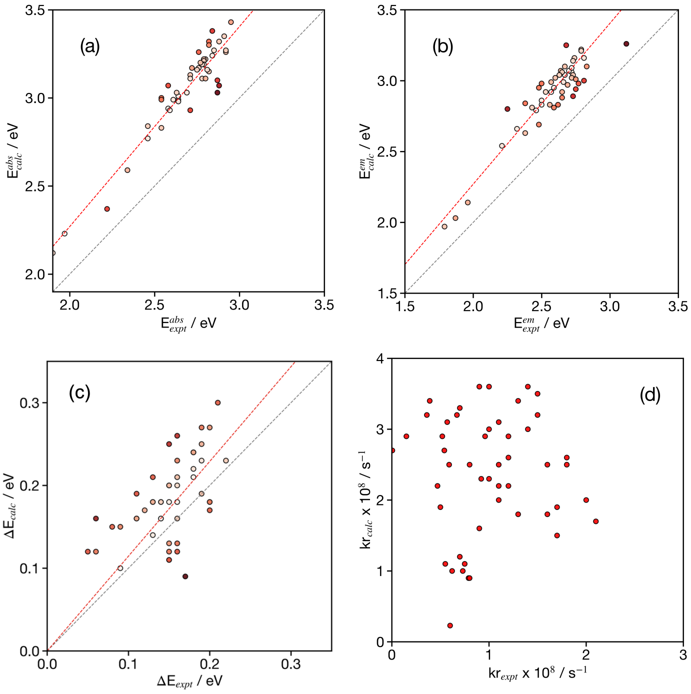

FIGURE 6.6: Experimental and MRSF-TDDFT(PBE0) calculated correlations for the (a) absorption, (b) emission, (c) ΔE_{ST} and (d) $k_r(S_1 \rightarrow S_0)$ for the 50 MR-TADF structures (see Figure S1-S3 and Table S1) considered in this work. In Figure (a)-(c) the colour of the dots represent the distance from the red line of best fit, with white being closest and red furthest away.

the MAD 0.33 eV is slighter smaller than observed for the absorption energies and comparable performance to that presented for SCS-CC2 simulations [202].

The correlation between MRSF-TDDFT(PBE0) calculated and experimental ΔE_{ST} are shown in Fig. 6.6c. In this case only a modest correlation (r^2 value of 0.35) between the experimentally determined and calculated values are determined although the dataset exhibits a MAD of 0.05 eV, in excellent agreement with the SCS-CC2 simulations presented in ref. [202]. This error is smaller than the absorption and emission energies largely due to the smaller values under consideration for this parameter. But a MAD=0.05 eV indicates that the MRSF-TDDFT(PBE0) is sufficiently accurate to understand and design MR-TADF materials. Finally, in terms of materials development, it is not only important to accurately predict the energetics, such as ΔE_{ST}, but also properties such as the radiative rate. Fig. 6.6d shows the correlation between the calculated and experimental radiative rate. Here MRSF-TDDFT(PBE0) is unable to capture the trends reported experimentally as there is little correlation between the

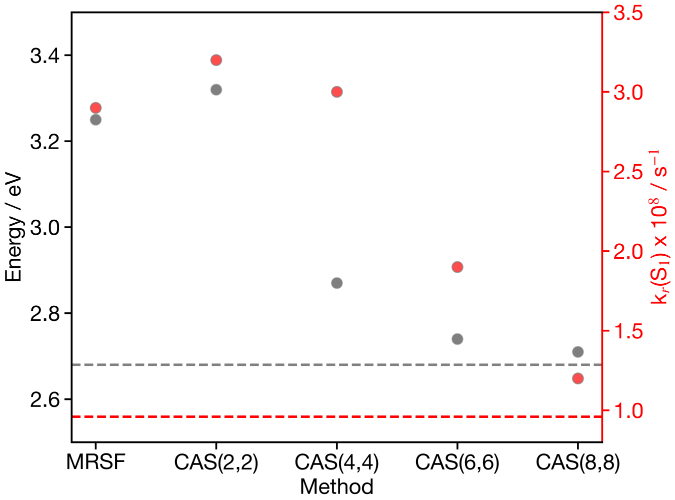

FIGURE 6.7: Emission energy and radiative rate of DABNA-1 calculated using MRSF-TDDFT(PBE0) and NEVPT2, with increasing size of active space. The dashed lines represent the experimental values extracted from ref. [134].

experiment and theory. While the calculated radiative rate neglects 2^{nd}-order Herzberg-Teller effects, the allowed nature of these transitions suggests that these effects are likely to be weak and consequently, these simualtions highlights that for such calculations care should be taken in over interpreting the calculated oscillator strengths.

While Fig. 6.6a-c show correlations between experiment and MRSF-TDDFT(PBE0) simulations, there is, as mentioned above, a consistent absolute error which is why the correlations following the shifted line of the form $y = 1.135x$, rather than the desired $y = x$. To rationalise this, Fig. 6.7 shows the energy and radiative rate of **DABNA-1** [134] calculated using MRSF-TDDFT(PBE0) and NEVPT2, with increasing size of active space. The NEVPT2(2,2) simulations incorporate the HOMO-1 and LUMO orbitals primarily responsible for the S$_1$ excited state and consequently as expected provide values which are similar (albeit slightly worse) than the MRSF-TDDFT(PBE0) calculations. Upon increasing the active space there is a clear improvement towards the experimental values, marked with the dashed lines in Fig. 6.7. Indeed, both the (6,6) and (8,8) active spaces provide values which are in close agreement to experiment, although for the radiative rate an (8,8) active space is required. This demonstrates, that while the double excitations are required to provide a consistent description between the singlet and triplet states, high order excitations are required to achieve the absolute energies and oscillator strengths. Given the lack of correlation observed in Fig. 6.6d this would appear most important for the calculated radiative rate which is typically more sensitive to the fine details of the wavefunction.

6.3.2 Increasing the Density of Coupled States: Combining CT and MR States

The density of coupled states with different characters is known to influence the rate of ISC and rISC [162]. Recently, Wu *et al.* [200] aimed to merge boron and carbonyl-based MR-TADF emitters, demonstrating improved performance. Beyond the more commonly encountered B, N- and C=O, N-doped polycyclic aromatic hydrocarbons (PAHs) using nitrogen as an electron-rich atom, Chang *et al.* [230] recently developed a boron and sulphur (B,S)-doped PAH, specifically 5,9-dithia-13b-boranaphtho[3,2,1-de]anthracene (BSS), as a nitrogen-free MR-TADF emitter. This design exploits the heavy atom effect of sulphur atoms [231] to increase the rISC rate. Building on this concept, Fig. 6.8 shows two derivatives that include acridan and carbazole groups attached to the MR BSS unit. These groups create the potential for CT states, providing a framework for regulating excited state characteristics to tune emission wavelength and FWHM. Moreover, this design generates a manifold of states with different characters, creating opportunities to increase the rISC rate. Notably, the **BSS-Ac** emitter demonstrates a much smaller roll-out in a device, suggesting a shorter delayed fluorescence lifetime due to a faster rISC rate.

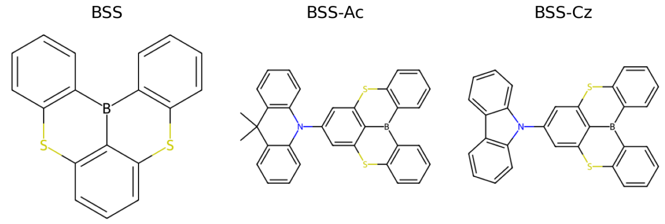

FIGURE 6.8: The sulfur (B,S)-doped PAH (5,9-dithia-13b-boranaphtho[3,2,1-de]anthracene, BSS) based molecules studied in the work. See ref. [230] for original experimental work.

Table 6.1 shows the energetics and spin orbit couplings of **BSS**, **BSS-Ac** and **BSS-Cz**. The lowest MR state occurs at 3.24, 3.17 and 3.15 eV, this is larger than the 2.85 eV reported experimentally [230], however when the calculated values are corrected for the correlations identified in Fig. 6.6 (*i.e.* divided by 1.135), values of 2.85, 2.79 and 2.78 eV arise in excellent agreement with the experiment. For **BSS-Ac**, as shown in Fig. C.4, the MR state is not the lowest, which corresponds to a CT band, with a much weaker oscillator strength. This is also observed in the S_1 geometry and is consistent with the emission spectrum reported in ref.

	Geom.	E_{S1}	E_{S2}	f_{S1}	E_{T1}	E_{T2}	SOC_{x-T_1} / cm^{-1}	SOC_{x-T_2} / cm^{-1}
BSS	GS	3.24	3.74	0.5158	3.03	3.50	S_1=0.76; S_2=1.67	S_1=0.80; S_2=0.13
	S_1	3.11	3.62	0.4593	2.92	3.39	S_1=0.92; S_2=1.59	S_1=0.30; S_2=0.72
BSS-Ac	GS	2.84	3.17	0.0492	2.74	2.98	S_1=0.72 ; S_2=3.75	S_1=2.02; S_2=5.54
	S_1	2.71	3.06	0.0125	2.68	2.95	S_1=0.94; S_2=4.36	S_1=0.44 ; S_2=6.69
BSS-Cz	GS	3.15	3.28	0.3871	3.07	3.18	S_1=0.74, S_2=3.26	S_1=1.66 S_2=2.59
	S_1	3.09	3.16	0.3564	2.97	3.02	S_1=0.89; S_2=2.70	S_1=0.95 ; S_2=1.51

TABLE 6.1: Excited state energies, oscillator strength and spin-orbit couplings for **BSS**, **BSS-Ac** and **BSS-Cz** at its ground and excited S_1 state geometry. Energies are reported in eV and spin-orbit couplings in cm^{-1}. Oscillator strengths are unitless.

[230] which exhibits dual emission with the lower being a broad band of CT character. While this is unfavourable for achieving high colour purity OLEDs, it does demonstrate the close proximity of the states of different character favourable for rISC.

Compared to BSS, the inclusion of the acridan and carbazole groups attached to the MR BSS unit displays an increase in the SOCME between the low lying state and this is largest for **BSS-Ac**. However, one could ascribe this to be the reason the OLED performance as reported in ref. [230] improves for **BSS-Ac** compared to **BSS-Cz**, the couple moments only increase the rate quadratically. Instead, the higher rISC is associated with the smaller ΔE_{ST}, **BSS-Ac** = 0.03 eV compared to **BSS-Cz** = 0.12 eV. This gap is smaller as the lowest states are predominantly CT in character (see Fig. C.4), while in contrast the MR character of the lowest states in **BSS-Cz** means it has a gap comparable to the MR base unit **BSS**. Consequently, these two emitters exhibit similar OLED performance [230, 232] and this highlights the importance of correctly aligning the CT and MR states to achieve optimal performance. In this sense, given the dipole moment of the CT states, fine tuning could be achieved by modifying the dipole moment of the host rather than changing the structure of the emitter [80, 180, 233, 234].

6.3.3 Discovering Narrow Blue MR-TADF emitters

Fig. 6.10 shows the 6 best structures filtered out from 262 molecules generated by STONED algorithm, that met stringent criteria: a singlet-triplet gap less than 0.15 eV, an oscillator strength greater than 0.3, and emission wavelengths falling within the range of 2.6 to 3.5 eV. We can see that, these structures are largely similar, lacking the diversity we anticipated. In addition, although the input molecules do not contain iodine, the algorithm introduced iodine atoms as substituents in several of the generated molecules. The appearance of iodine-substituted molecules is more likely due to the intrinsic nature of the STONED algorithm, which explores chemical space using the full SELFIES alphabet. Since iodine is part of this default token set, the algorithm may introduce it during molecular mutations, even if it was not present in the input structures.

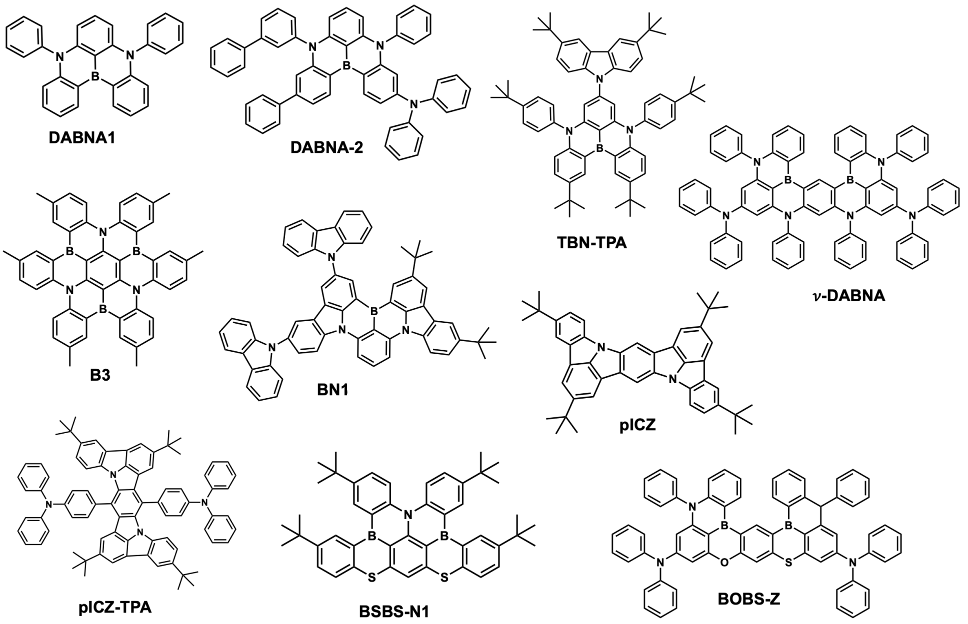

FIGURE 6.9: 10 molecules selected to develop within the STONED Algorithm

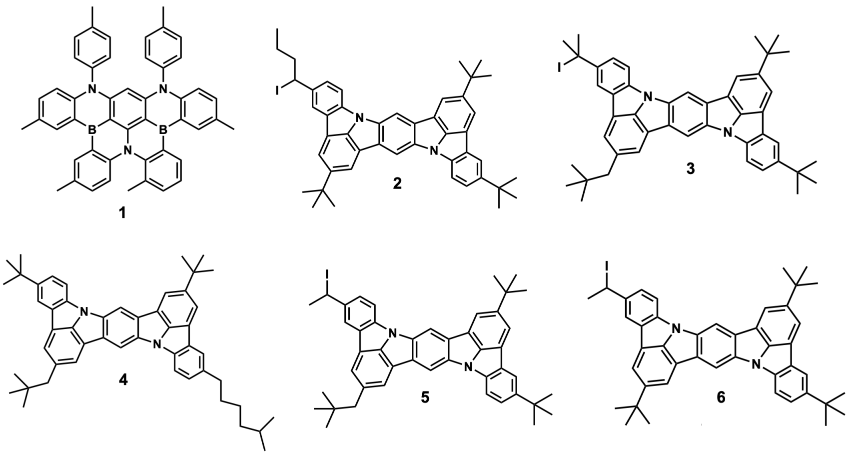

FIGURE 6.10: 6 Molecules met criteria; a singlet-triplet gap less than 0.14 eV, an oscillator strength greater than 0.3, and emission wavelengths falling within the range of 2.6 to 3.5 eV; generated with STONED Algorithm

	λ_{em} **(eV)**	ΔE_{ST} **(eV)**	f_0 **(eV)**
1	3.093	0.136	0.31
2	3.05	0.137	0.81
3	3.045	0.131	0.83
4	3.015	0.135	0.67
5	3.048	0.136	0.8
6	3.054	0.135	0.83

TABLE 6.2: Excited State Energies calculated using SF-TDDFT

	Geometry	λ_{em} **(eV)**	ΔE_{ST} **(eV)**	f_0 **(eV)**
1	S_0	3.076	0.136	0.31
	T_1	2.915	0.149	0.31
2	S_0	3.05	0.137	0.81
	T_1	2.932	0.381	1.57
3	S_0	3.045	0.131	0.83
	T_1	2.941	0.385	1.62
4	S_0	3.018	0.135	0.67
	T_1	2.917	0.363	1.63
5	S_0	3.048	0.134	0.8
	T_1	2.936	0.383	1.59
6	S_0	3.054	0.136	0.83
	T_1	2.927	0.378	1.57

TABLE 6.3: Excited State Energies computed using DFT and TDDFT at both ground and triplet states

Despite our initial hypothesis, the results obtained using the STONED algorithm did not demonstrate significant variations, which limits chemical diversity. Figures 6.9 and 6.10 reveal that the structures generated by the algorithm were largely similar. However, the calculations, as shown in Tables 6.2 and 6.3, display the excited state energies of the final 6 molecules computed using SF-TDDFT and DFT/TDDFT, respectively. The agreement between these methods underscores the accuracy of the SF-TDDFT approach. Additionally, the consistent results across all 6 molecules highlight the structural similarity among these candidates. Although the STONED algorithm was not effective in this instance, SF-TDDFT has proven to be a reliable tool for high-throughput virtual screening and holds promise for future OLED emitter studies.

6.4 Discussion and Conclusions

The MR molecular framework has emerged as extremely promising for developing 3^{rd} generation emitters within high-performing OLEDs offering high colour purity and photoluminescence quantum yield. However, they typically suffer from long delayed lifetimes due to slow rISC rates and consequently developing novel high-performing materials using *in silico* design is an important step in the design process. In this study, we addressed the limitations of LR-TDDFT in accurately modelling the excited state properties of MR molecules. Recognising the important role of double excitations, we have employed MRSF-TDDFT to provide accurate insight into the excited state properties including the crucial ΔE_{ST}, the energy difference between the lowest singlet (S_1) and triplet (T_1) excited states.

Our findings, derived from a library of 50 MR-emitters, demonstrate that MRSF-TDDFT accurately calculates excited state energetics. The performance of MRSF-TDDFT, as assessed using mean average deviations between experimental and computational results, is comparable to that of higher-level, more computationally intensive methods such as SCS-CC2 [202]. There is a strong correlation between the experimental and computational energies corresponding to the absorption and emission spectra; however, this correlation follows a shifted line of the form $y = 1.135x$ rather than the ideal $y = x$. Using NEVPT2 simulations, we demonstrate that for the prototypical emitter, **DABNA**, this shift derives from electron correlation described by higher-order excitations as the excited state properties and radiative rates converge towards experimental values as the size of the active space is increased. This improvement is most significant in estimating the radiative rate of the emitters which demonstrates no correlation between experimental and MRSF-TDDFT results for the library of 50 MR-emitters studied. Consequently, during *in silico* design, calculated oscillator strengths should be treated with care. Additionally, the MRSF-TDDFT framework has been used to explore the excited state properties of systems designed to enhance the coupling between singlet and triplet states by increasing the density of states. Finally, to address the issue of limited data on MR emitters in the literature, we implemented a sophisticated STONED algorithm to generate a diverse dataset of MR emitters and then analysed and filtered out this data through a high-throughput virtual screening approach. The goal was to discover new narrow blue TADF MR emitters . However, despite the potential value of this approach, the algorithm did not perform as expected. The generated structures show limited diversity and are largely similar. Interestingly, several molecules contain iodine substituents, despite no iodine in the input set. This likely results from the STONED algorithm's use of the full SELFIES alphabet, which includes iodine by default and allows its random insertion during mutation. So, in short instead of producing a diverse set of structures, it generated similar structures, limiting the effectiveness of our screening process. Despite the ineffectiveness of the STONED algorithm in this instance, SF-TDDFT has demonstrated its reliability for high-throughput virtual screening and holds significant potential for future OLED emitter studies.

Overall, the results presented in this work demonstrates the potential of SF-TDDFT and MRSF-TDDFT for achieving accurate and computationally efficient *in silico* development high-performing MR-TADF. Future work should focus upon understanding the excited state dynamics of these systems and towards this end, the MRSF-TDDFT approach has been successfully applied to study excited state non-adiabatic dynamics [220, 221] and therefore developing accurate potentials based upon this approach will likely provide excited new insight into the excited state dynamics controlling the functional properties of MR-TADF emitters.

Chapter 7

Conclusion and Future Works

In this thesis, we have conducted a theoretical examination of various OLED emitters by analysing their molecular and electronic characteristics through different computational methods and design techniques.

Achieving high efficiency in OLEDs is essential for their increasing use in modern technologies, both in terms of quantum efficiency and fabrication costs and sustainability. First-generation OLEDs fall short in device efficiency, while second-generation OLEDs are too costly and unsustainable for widespread use. Third-generation OLEDs based on TADF offer new opportunities by achieving 100% efficiency without expensive, unsustainable metals. However, the mechanism to achieve this efficiency is more complex, requiring a detailed understanding of competing processes to enhance the design of emitters. A typical approach for TADF emitters is the donor-acceptor (D-A) configuration, which achieves 100% efficiency but results in broad emission spectra. To address this, multiple-resonance (MR) emitters have been introduced, offering narrow emission but often resulting in a small singlet-triplet energy gap. Achieving both high efficiency and narrow emission simultaneously is critical and challenging. Additionally, ensuring a long lifetime for TADF emitters remains a significant challenge.

This thesis aims to deepen the understanding of excited state processes in organic molecules, with a focus on reverse intersystem crossing (rISC), a crucial step in the TADF mechanism. It also explores strategies to achieve narrow emission and examines how to efficiently and quickly compute and study the properties of these molecules. Through this research, the goal is to enhance the design and performance of TADF emitters, balancing efficiency, emission width, and device longevity.

Firstly, we investigated a series of donor-acceptor molecules with a B-N bond to understand how steric hindrance and non-covalent interactions influence their conformational behavior and excited state properties. The molecules exhibit three major conformers—planar, bent, and twisted. In the ground state, both unhindered and sterically hindered molecules favour planar or bent conformations, which increases communication between the donor and acceptor, thus widening the singlet-triplet energy gap and making TADF less favourable. Introducing non-covalent interactions via oxygen and sulfur atoms stabilizes the twisted conformer in the excited state, which is essential for efficient TADF. These interactions also enhance spin-orbit coupling, thereby improving the rates of intersystem crossing (ISC) and reverse intersystem crossing (rISC). Adding methoxy groups improves conformational control due to non-covalent interactions, leading to more stable and efficient TADF properties, particularly in solid-state applications. We expanded our study to donor-acceptor-donor emitters which also emerged that methoxy gives better conformational control as the structure with methoxy emerged as the most promising TADF candidate due to its structural rigidity, significant conformational changes upon excitation, and favourable singlet-triplet energy gaps.

Secondly, the demand for high-resolution and energy-efficient displays necessitates luminescent materials with narrowband emission. This study employed the DHO model to predict the emission full-width at half-maximum (FWHM) for various organic molecules. The DHO model efficiently predicts FWHM without extensive excited state optimisations, making it valuable for high-throughput screening. The model can be extended to include non-Condon and non-Born-Oppenheimer effects, crucial for molecules exhibiting TADF. Incorporating oxygen and sulfur atoms into the B-N framework slightly increases emission FWHM but significantly enhances ISC rates, simplifying triplet harvesting mechanisms.

Thirdly, multi-resonance (MR) frameworks offer high color purity and photoluminescence quantum yield, but face challenges like long delayed fluorescence lifetime due to unfavourable rISC and small spin-orbit coupling. In addition, traditional methods like LR-TDDFT perform poorly in predicting the excited state properties of MR-TADF emitters due to issues with electron correlation, advanced methods such as SCS-CC2 offers accurate predictions, but it is computationally expensive. Conversely, MRSF-TDDFT provides a more efficient yet accurate alternative, effectively describing excited state properties, closely matching experimental results and outperforming traditional LR-TDDFT methods. The method accounts for higher-order excitations, improving the estimation of radiative rates and highlighting the importance of active space size in simulations. Hence, this study utilised MRSF-TDDFT to overcome these limitations. Moreover, the MRSF-TDDFT framework has been employed to explore the excited state properties of the system designed to increase the coupling between singlet and triplet states by increasing the density of states. Additionally, the development of high-performing deep blue MR-TADF emitters is essential for advancing cost-effective, efficient, and stable OLEDs for display lighting applications. Despite progress, significant challenges remain, particularly in achieving the high energy required for deep blue emission without substantial energy losses and efficiency roll-off. Inverse design and high-throughput virtual screening (HTVS) are powerful methods to address these challenges by swiftly examining extensive chemical spaces. As, MR TADF is a relatively novel approach, leading to a limited number of documented deep blue MR TADF emitters in the literature. This lack of sufficient data poses a challenge for designing new efficient blue emitters using high-throughput virtual screening or machine learning techniques. By employing the stoned algorithm, we efficiently generated a diverse set of potential candidates, avoiding the need for large datasets and prolonged training periods. Through a computational funnel approach, we systematically filtered the candidate pool, retaining only the most promising molecules for further detailed analysis. Despite the potential benefits of this approach, the algorithm did not yield the expected results. Rather than producing a varied array of structures, it generated a set of similar ones, which constrained the effectiveness of our screening process.

While the findings of this thesis has made substantial contributions to the understanding and design of TADF emitters for OLED applications, also pave the way for several future research directions that can further enhance the performance and applicability of these materials.

The current study has successfully utilised various computational techniques to predict the properties of TADF emitters. Future research can benefit from incorporating machine learning models to predict molecular properties and performance metrics with greater accuracy and efficiency. These models can be trained on the existing datasets like ChemBL, Deep4chem, etc. for TADF molecules.

Enhanced molecular design for TADF can be achieved by further exploration of non-covalent interactions, potentially leading to TADF materials with finely tuned excited state properties and improved solid-state performance. Investigating other functional groups beyond methoxy could provide deeper insights into conformational control and emission properties. Exploring a wider variety of donor and acceptor groups, and their impact on TADF properties, could yield new insights. Systematic studies on how different substituents influence the conformational stability, singlet-triplet energy gap, and intersystem crossing rates could lead to the discovery of more efficient TADF molecules.

Expanding the application of the DHO model to a wider range of materials can significantly enhance its predictive power and utility in high-throughput molecular design. Integrating traditional quantum chemistry methods with machine learning approaches could further accelerate the discovery and optimisation of new TADF materials. Moreover, addressing the long-term stability of these materials is crucial for the practical application of OLEDs. Future research should prioritize understanding the degradation mechanisms of TADF emitters, including detailed studies of the photophysical processes that lead to their degradation. By combining these advanced modeling techniques and focusing on stability issues, we can make substantial progress in developing durable and efficient OLED emitters.

In silico design and simulation efforts should continue to refine the MRSF-TDDFT framework and explore its applications in non-adiabatic dynamics. This will deepen our understanding of excited state behaviors and guide the design of next-generation TADF emitters.

By pursuing these future directions, we can continue to improve the design and functionality of OLED emitters, paving the way for more efficient, cost-effective, and sustainable organic electronic devices.

Appendix A

Appendix

Ground State			T_1^{MIN}		S_1^{MIN}	
State	Nature	ΔE / eV	Nature	ΔE / eV	Nature	ΔE / eV
S_0	–	0.56	–	0.86	–	1.03
S_1	CT	4.13	CT	3.87	CT	3.88
S_2	CT	4.64	CT	4.56	CT	4.61
S_3	CT	4.74	CT	4.71	CT	4.79
T_1	LE(A)	3.98	CT	3.86	CT	3.87
T_2	LE(A)	4.09	LE(A)	4.19	LE(A)	4.29
T_3	CT	4.12	LE(D)	4.35	LE(D)	4.50

TABLE A.1: Electronic structure at the optimised geometry of the electronic ground and lowest S_1 and T_1 states of the twisted conformer of **1a**. All energies relative to the lowest energy conformer of the **1a** molecule (planar). CT = charge transfer, LE(A) = Local exciton on the acceptor and LE(D) = Local exciton on the donor.

Ground State			T_1^{Min}		S_1^{Min}	
State	Nature	ΔE / eV	Nature	ΔE / eV	Nature	ΔE / eV
S_0	–	0.00	–	0.44	–	0.59
S_1	CT + LE(A)	4.04	LE(A)	4.29	CT	3.70
S_2	CT	4.40	CT	4.36	CT	4.28
S_3	CT	4.44	CT + LE(A)	4.51	CT	4.55
T_1	LE(A)	3.28	LE(A)	2.85	CT + LE(A)	3.44
T_2	LE(A) + CT	3.37	LE(A)	3.77	LE(A) + CT	4.02
T_3	LE(D)	3.59	LE(D)	4.03	LE(A) + CT	4.15

TABLE A.2: Electronic structure at the optimised geometry of the electronic ground and lowest S_1 and T_1 states of the planar conformer of **1a**. All energies relative to the lowest energy conformer of the **1a** molecule (planar). CT = charge transfer, LE(A) = Local exciton on the acceptor and LE(D) = Local exciton on the donor.

Ground State			T_1^{Min}		S_1^{Min}	
State	Nature	ΔE / eV	Nature	ΔE / eV	Nature	ΔE / eV
S_0	–	0.18	–	0.64	–	0.67
S_1	CT	3.62	CT	3.31	CT	3.32
S_2	CT	4.19	CT	4.15	CT	4.15
S_3	CT	4.20	CT	4.21	CT	4.23
T_1	LE(A)	3.58	CT	3.31	CT	3.31
T_2	CT + LE(D)	3.61	LE(A)	3.89	LE(A)	3.91
T_3	LE(A)	3.68	LE(D)	4.05	LE(D)	4.08

TABLE A.3: Electronic structure at the optimised geometry of the electronic ground and lowest S_1 and T_1 states of the twisted conformer of **1b**. All energies relative to the lowest energy conformer of the **1b** molecule (bent). CT = charge transfer, LE(A) = Local exciton on the acceptor and LE(D) = Local exciton on the donor.

Ground State			T_1^{MIN}		S_1^{MIN}	
State	Nature	ΔE / eV	Nature	ΔE / eV	Nature	ΔE / eV
S_0	–	0.00	–	0.45	–	0.66
S_1	CT	4.05	LE(A)	4.28	LE(A)	3.91
S_2	CT	4.35	CT	4.35	CT	4.61
S_3	CT	4.42	CT + LE(A)	4.53	CT	4.87
T_1	LE(A)	3.27	LE(A)	2.85	LE(A)	3.19
T_2	LE(A)	3.38	LE(A)	3.74	LE(A)	3.84
T_3	LE(D)	3.84	LE(D)	3.94	LE(D)	4.51

TABLE A.4: Electronic structure at the optimised geometry of the electronic ground and lowest S_1 and T_1 states of the bent conformer of **1b**. All energies relative to the lowest energy conformer of the **1b** molecule (bent). CT = charge transfer, LE(A) = Local exciton on the acceptor and LE(D) = Local exciton on the donor.

Ground State			T_1^{Min}		S_1^{Min}	
State	Nature	ΔE / eV	Nature	ΔE / eV	Nature	ΔE / eV
S_0	–	0.00	–	0.53	–	0.56
S_1	CT	3.44	CT	3.03	CT	3.03
S_2	CT	3.89	CT	3.89	CT	3.90
S_3	LE(D)	4.30	CT	4.09	CT	4.09
T_1	LE(A)	3.37	CT	3.03	CT	3.02
T_2	CT	3.43	LE(A)	3.75	LE(A)	3.78
T_3	LE(A)	3.51	LE(D)	3.85	LE(D)	3.88

TABLE A.5: Electronic structure at the optimised geometry of the electronic ground and lowest S_1 and T_1 states of the twisted conformer of **1c**. All energies relative to the lowest energy conformer of the **1c** molecule (twisted). CT = charge transfer, LE(A) = Local exciton on the acceptor and LE(D) = Local exciton on the donor.

Ground State			T_1^{Min}		S_1^{Min}	
State	Nature	ΔE / eV	Nature	ΔE / eV	Nature	ΔE / eV
S_0	–	0.12	–	0.72	–	–
S_1	CT	3.89	CT	4.04	–	–
S_2	CT	4.25	CT + LE(A)	4.37	–	–
S_3	LE(D)	4.47	LE(A)	4.46	–	–
T_1	LE(A)	3.37	LE(A)	2.91	–	–
T_2	LE(A) + CT	3.44	LE(A)	3.87	–	–
T_3	LE(D)	3.73	CT	4.09	–	–

TABLE A.6: Electronic structure at the optimised geometry of the electronic ground and lowest S_1 and T_1 states of the bent conformer of **1c**. All energies relative to the lowest energy conformer of the **1c** molecule (twisted). CT = charge transfer, LE(A) = Local exciton on the acceptor and LE(D) = Local exciton on the donor.

Ground State			T_1^{MIN}		S_1^{MIN}	
State	Nature	ΔE / eV	Nature	ΔE / eV	Nature	ΔE / eV
S_0	–	0.00	–	0.29	–	0.37
S_1	CT	3.62	CT	2.74	CT	2.74
S_2	CT + LE(D)	3.88	CT	3.34	CT	3.39
S_3	CT	3.90	CT	3.65	CT	3.67
T_1	LE(A)	3.15	CT	2.73	CT	2.72
T_2	LE(D)	3.22	CT	3.31	CT	3.37
T_3	LE(A)	3.32	LE(D)	3.49	LE(D)	3.56

TABLE A.7: Electronic structure at the optimised geometry of the electronic ground and lowest S_1 and T_1 states of the twisted conformer of **1d**. All energies relative to the lowest energy conformer of the **1d** molecule (twisted). CT = charge transfer, LE(A) = Local exciton on the acceptor and LE(D) = Local exciton on the donor.

Ground State			T_1^{MIN}		S_1^{MIN}	
State	Nature	ΔE / eV	Nature	ΔE / eV	Nature	ΔE / eV
S_0	–	0.42	–	–	–	–
S_1	CT	4.11	–	–	–	–
S_2	CT	4.30	–	–	–	–
S_3	CT	4.44	–	–	–	–
T_1	LE(A)	3.69	–	–	–	–
T_2	LE(D)	3.76	–	–	–	–
T_3	LE(A) + CT	3.77	–	–	–	–

TABLE A.8: Electronic structure at the optimised geometry of the electronic ground and lowest S_1 and T_1 states of the bent conformer of **1d**. All energies relative to the lowest energy conformer of the **1d** molecule (twisted). CT = charge transfer, LE(A) = Local exciton on the acceptor and LE(D) = Local exciton on the donor.

Ground State			T_1^{MIN}		S_1^{MIN}	
State	Nature	ΔE / eV	Nature	ΔE / eV	Nature	ΔE / eV
S_0	–	–	–	0.63	–	0.71
S_1	–	–	CT	3.04	CT	3.01
S_2	–	–	CT	3.91	CT	3.91
S_3	–	–	LE(D)	4.65	LE(D)	4.88
T_1	–	–	CT	2.99	CT	3.00
T_2	–	–	CT	3.85	CT	3.91
T_3	–	–	LE(A)	3.92	LE(A)	3.96

TABLE A.9: Electronic structure at the optimised geometry of the electronic ground and lowest S_1 and T_1 states of the twisted conformer of **2a**. All energies relative to the lowest energy conformer of the **2a** molecule (bent). CT = charge transfer, LE(A) = Local exciton on the acceptor and LE(D) = Local exciton on the donor.

Ground State			T_1^{MIN}		S_1^{MIN}	
State	Nature	ΔE / eV	Nature	ΔE / eV	Nature	ΔE / eV
S_0	–	0.00	–	0.30	–	0.39
S_1	CT	4.01	LE(A) + CT	3.94	CT	3.21
S_2	CT	4.33	LE(A)	4.10	CT	4.03
S_3	LE(A)	4.51	LE(A) + CT	4.25	LE(A)	4.73
T_1	LE(A)	3.23	LE(A)	2.48	CT	3.00
T_2	LE(A) + CT	3.32	LE(A)	3.44	LE(A) + CT	3.70
T_3	LE(A)	3.95	LE(A)	4.02	LE(A)	3.79

TABLE A.10: Electronic structure at the optimised geometry of the electronic ground and lowest S_1 and T_1 states of the bent conformer of **2a**. All energies relative to the lowest energy conformer of the **2a** molecule (bent). CT = charge transfer, LE(A) = Local exciton on the acceptor and LE(D) = Local exciton on the donor.

Ground State			T_1^{MIN}		S_1^{MIN}	
State	Nature	ΔE / eV	Nature	ΔE / eV	Nature	ΔE / eV
S_0	–	–	–	–	–	1.18
S_1	–	–	–	–	CT	3.64
S_2	–	–	–	–	CT	4.56
S_3	–	–	–	–	CT	5.25
T_1	–	–	–	–	CT	3.63
T_2	–	–	–	–	LE(A)	4.41
T_3	–	–	–	–	CT	4.54

TABLE A.11: Electronic structure at the optimised geometry of the electronic ground and lowest S_1 and T_1 states of the twisted conformer of **2b**. All energies relative to the lowest energy conformer of the **2b** molecule (bent). CT = charge transfer, LE(A) = Local exciton on the acceptor and LE(D) = Local exciton on the donor.

Ground State			T_1^{MIN}		S_1^{MIN}	
State	Nature	ΔE / eV	Nature	ΔE / eV	Nature	ΔE / eV
S_0	–	0.00	–	0.70	–	0.83
S_1	CT + LE(A)	4.14	CT	4.46	CT	3.67
S_2	CT + LE(A)	4.47	CT	4.48	CT	4.50
S_3	LE(A)	4.50	CT	4.71	CT	4.96
T_1	LE(A)	3.24	CT	2.73	CT	3.48
T_2	LE(A)	3.63	LE(A)	3.84	CT + LE(A)	4.17
T_3	LE(A)	3.97	LE(A)	4.29	LE(A)	4.20

TABLE A.12: Electronic structure at the optimised geometry of the electronic ground and lowest S_1 and T_1 states of the bent conformer of **2b**. All energies relative to the lowest energy conformer of the **2b** molecule (bent). CT = charge transfer, LE(A) = Local exciton on the acceptor and LE(D) = Local exciton on the donor.

Ground State			T_1^{MIN}		S_1^{MIN}	
State	Nature	ΔE / eV	Nature	ΔE / eV	Nature	ΔE / eV
S_0	–	0.00	–	0.85	–	0.88
S_1	CT	3.65	CT	3.25	CT	3.09
S_2	CT	3.82	CT	3.94	CT	3.95
S_3	LE(D)	4.25	CT	4.41	CT	4.41
T_1	LE(A)	3.12	CT	3.08	CT	3.08
T_2	LE(A)	3.38	CT	3.93	CT	3.94
T_3	LE(D)	3.45	LE(A)	3.95	LE(A)	4.68

TABLE A.13: Electronic structure at the optimised geometry of the electronic ground and lowest S_1 and T_1 states of the twisted conformer of **2c**. All energies relative to the lowest energy conformer of the **2c** molecule (twisted). CT = charge transfer, LE(A) = Local exciton on the acceptor and LE(D) = Local exciton on the donor.

Ground State			T_1^{MIN}		S_1^{MIN}	
State	Nature	ΔE / eV	Nature	ΔE / eV	Nature	ΔE / eV
S_0	–	0.15	–	0.80	–	–
S_1	CT	4.08	CT	4.39	–	–
S_2	CT	4.39	LE(A)	4.54	–	–
S_3	LE(A)	4.63	LE(A) + CT	4.75	–	–
T_1	LE(A)	3.37	LE(A)	2.96	–	–
T_2	LE(A)	3.48	LE(A)	3.95	–	–
T_3	LE(D)	4.04	LE(A)	4.40	–	–

TABLE A.14: Electronic structure at the optimised geometry of the electronic ground and lowest S_1 and T_1 states of the bent conformer of **2c**. All energies relative to the lowest energy conformer of the **2c** molecule (twisted). CT = charge transfer, LE(A) = Local exciton on the acceptor and LE(D) = Local exciton on the donor.

Ground State			T_1^{MIN}		S_1^{MIN}	
State	Nature	ΔE / eV	Nature	ΔE / eV	Nature	ΔE / eV
S_0	–	0.00	–	1.08	–	0.92
S_1	CT	3.78	CT	3.30	CT	3.24
S_2	CT	3.99	CT	4.21	CT	4.08
S_3	CT	4.09	CT	4.25	CT	4.14
T_1	LE(A)	3.24	CT	3.22	CT	3.22
T_2	LE(A)	3.39	CT + LE(A)	3.99	LE(A)	3.92
T_3	CT + LE(D)	3.70	CT	4.11	LE(D)	4.04

TABLE A.15: Electronic structure at the optimised geometry of the electronic ground and lowest S_1 and T_1 states of the bent conformer of **2d**. All energies relative to the lowest energy conformer of the **2d** molecule (twisted). CT = charge transfer, LE(A) = Local exciton on the acceptor and LE(D) = Local exciton on the donor.

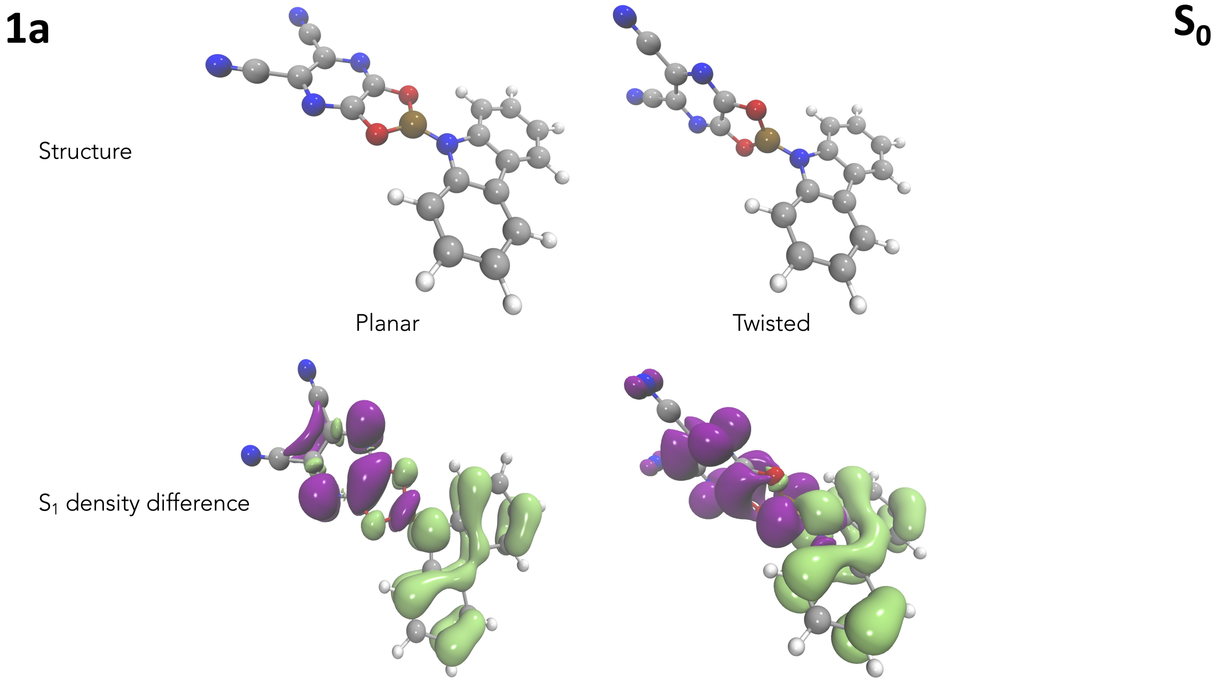

FIGURE A.1: Structure and S$_1$ density difference associated with the ground state optimised structure of **1a**.

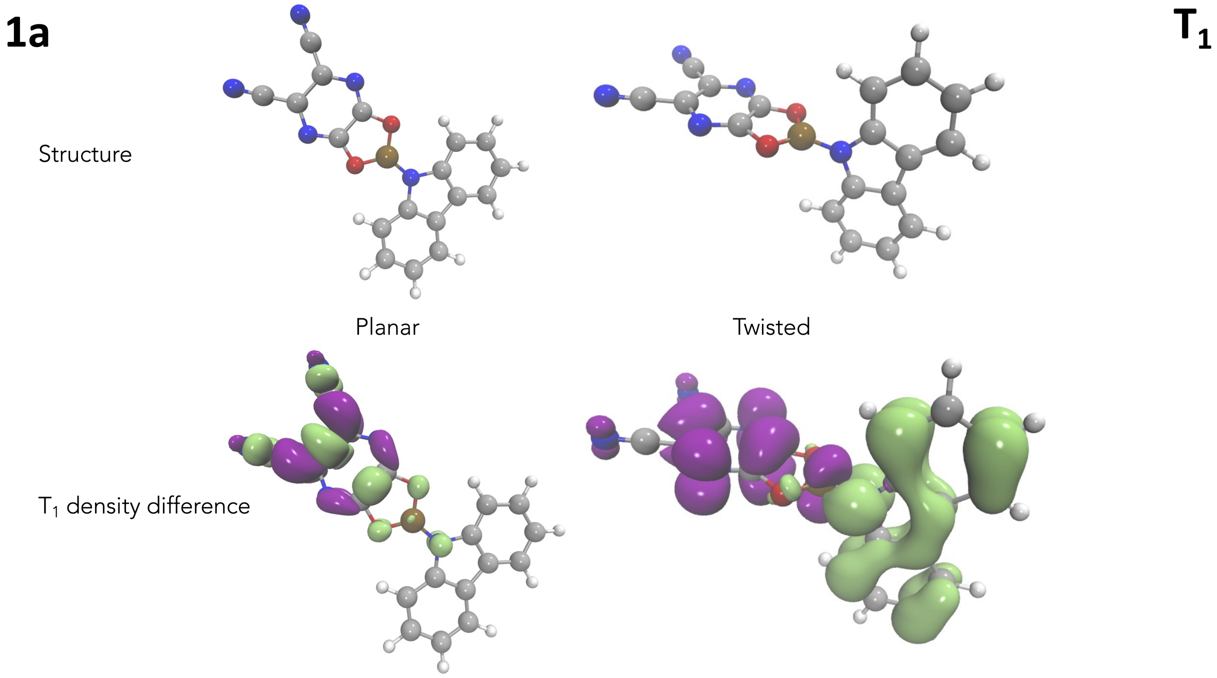

FIGURE A.2: Structure and T$_1$ density difference associated with the T$_1$ state optimised structure of **1a**.

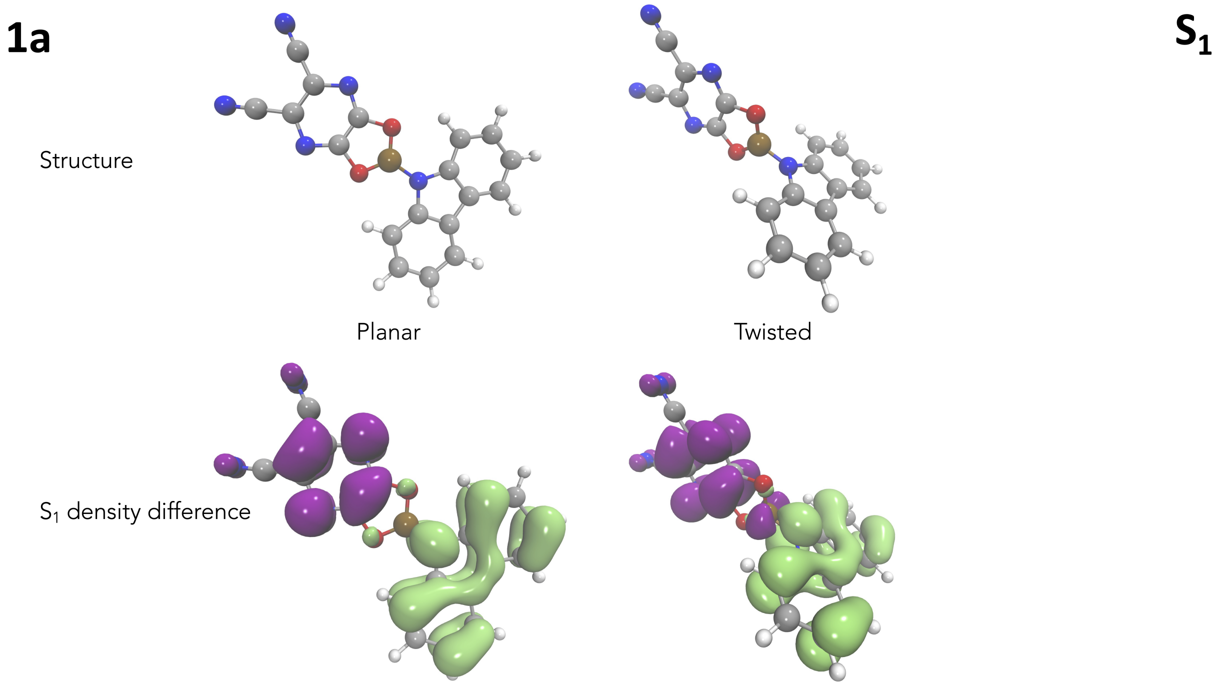

FIGURE A.3: Structure and S_1 density difference associated with the S_1 state optimised structure of **1a**.

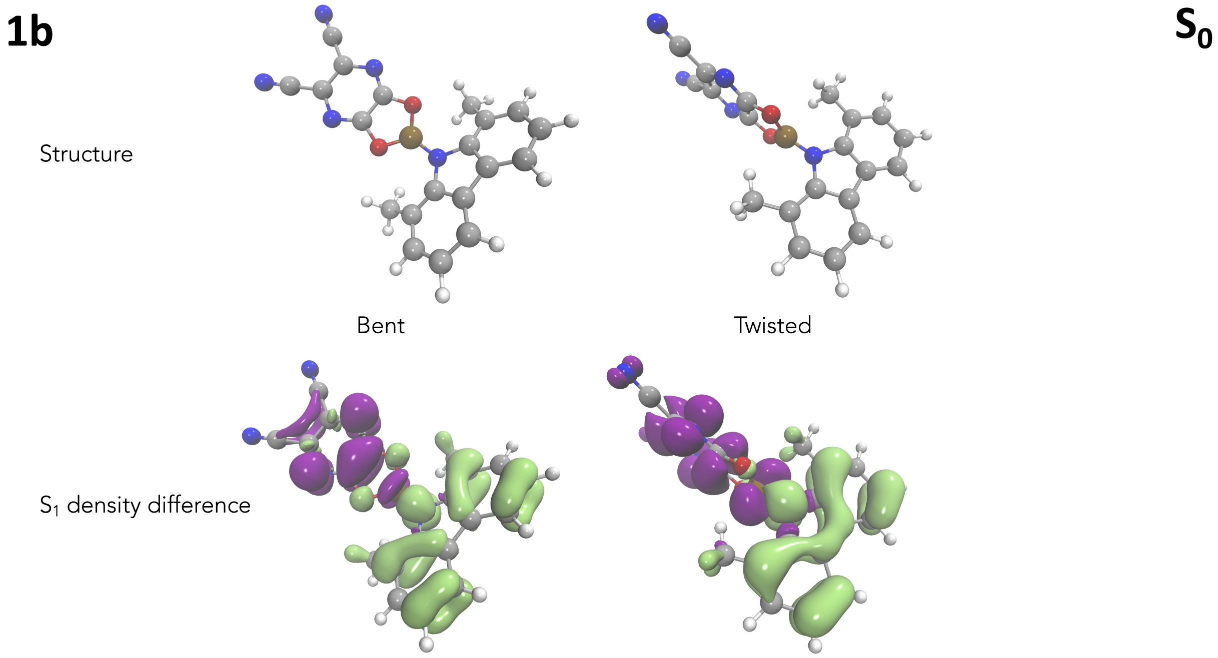

FIGURE A.4: Structure and S_1 density difference associated with the ground state optimised structure of **1b**.

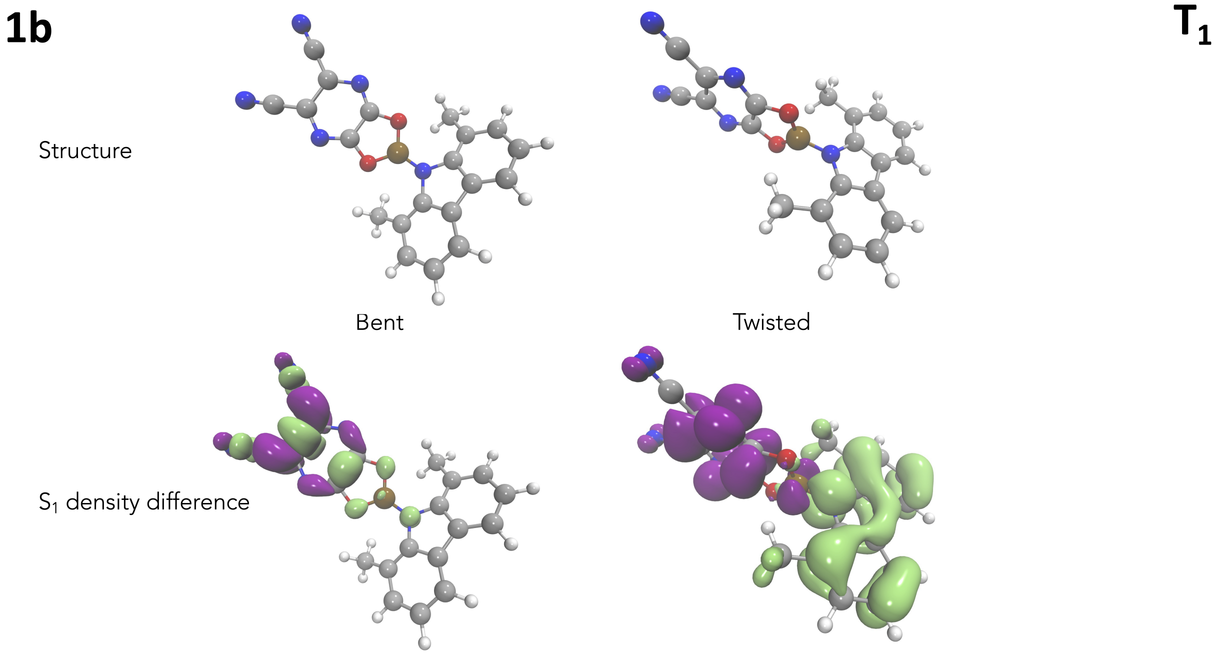

FIGURE A.5: Structure and T_1 density difference associated with the T_1 state optimised structure of **1b**.

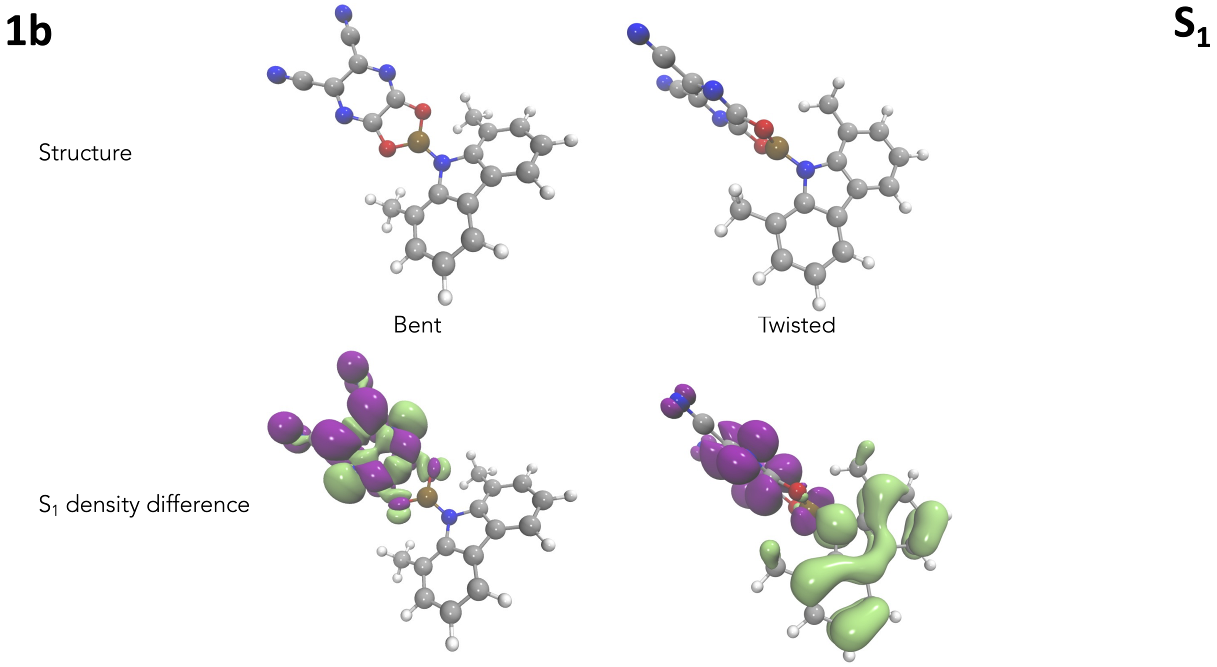

FIGURE A.6: Structure and S_1 density difference associated with the S_1 state optimised structure of **1b**.

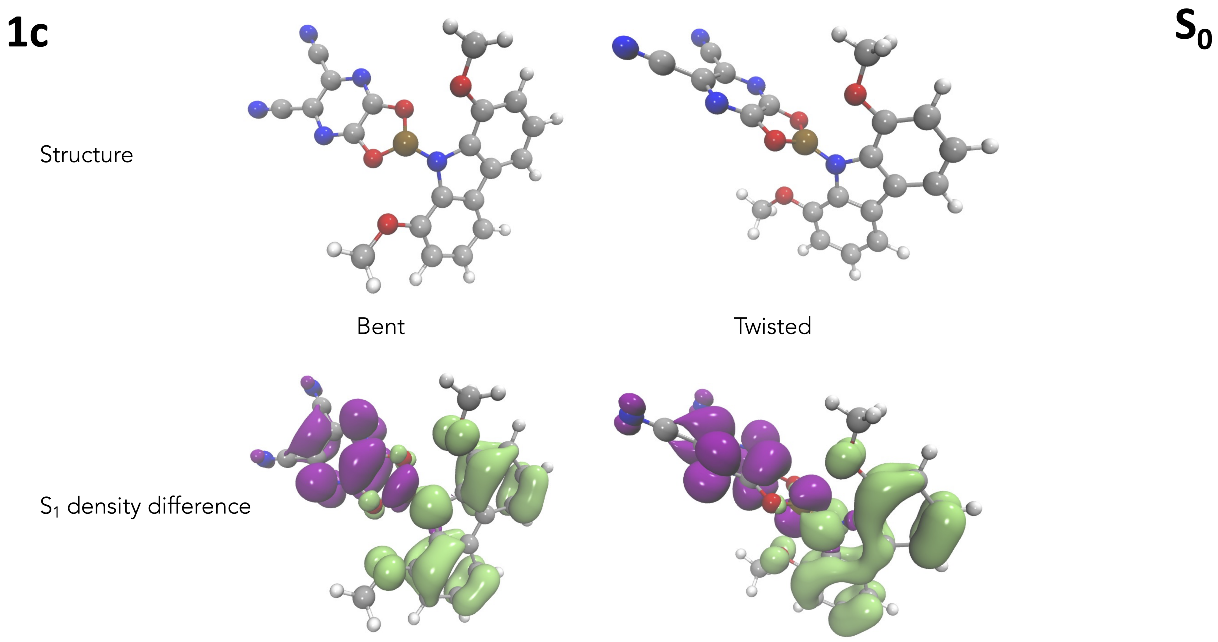

FIGURE A.7: Structure and S_1 density difference associated with the ground state optimised structure of **1c**.

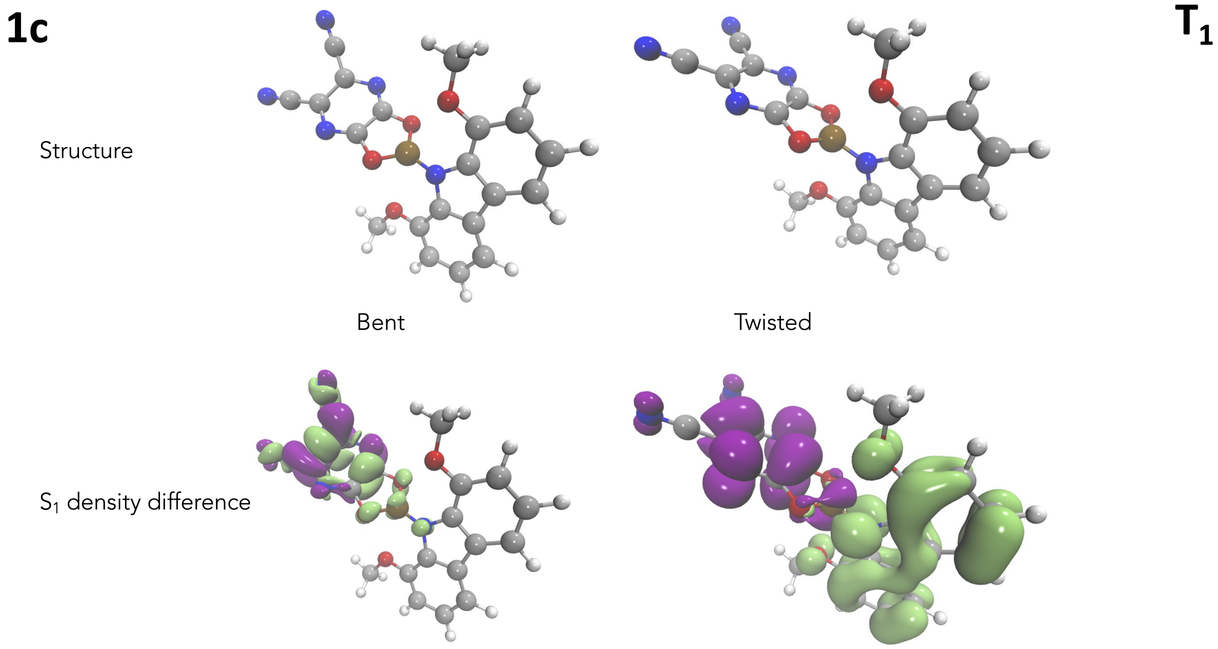

FIGURE A.8: Structure and T_1 density difference associated with the T_1 state optimised structure of **1c**.

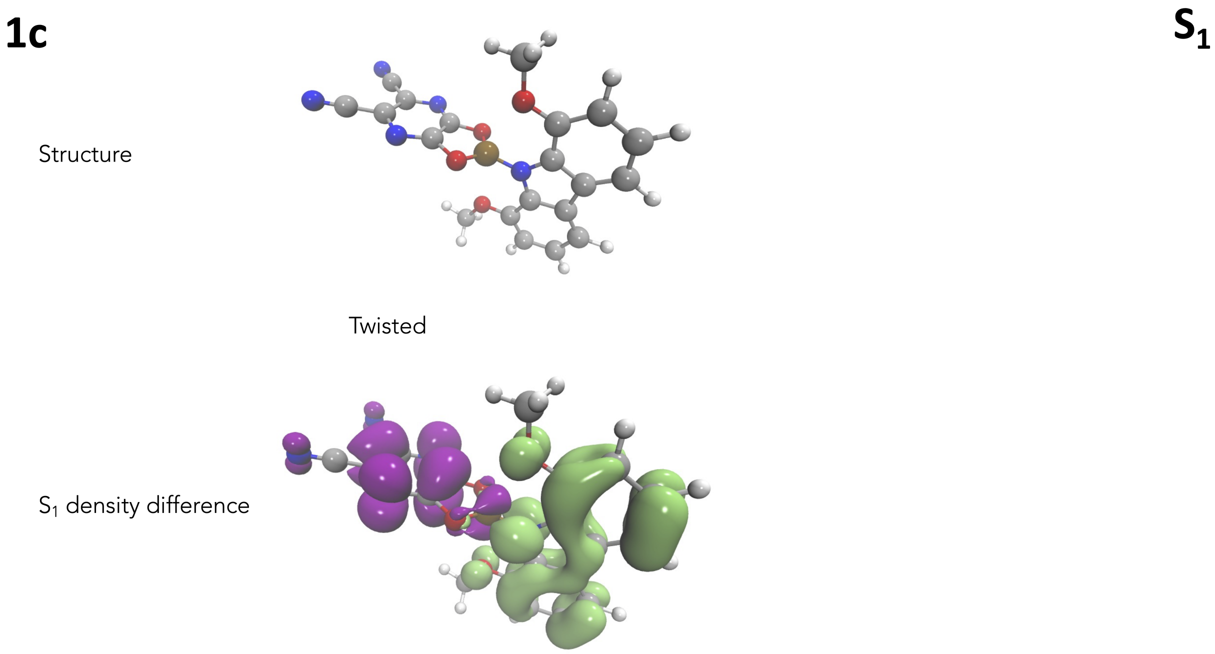

FIGURE A.9: Structure and S_1 density difference associated with the S_1 state optimised structure of **1c**.

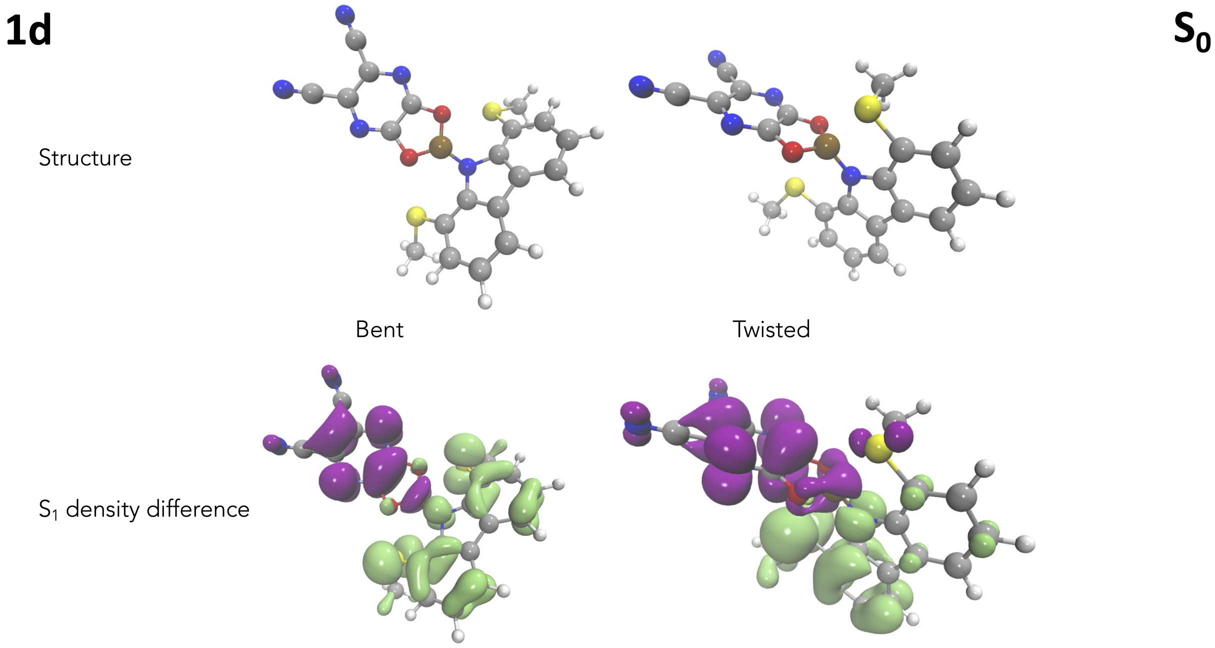

FIGURE A.10: Structure and S_1 density difference associated with the ground state optimised structure of **1d**.

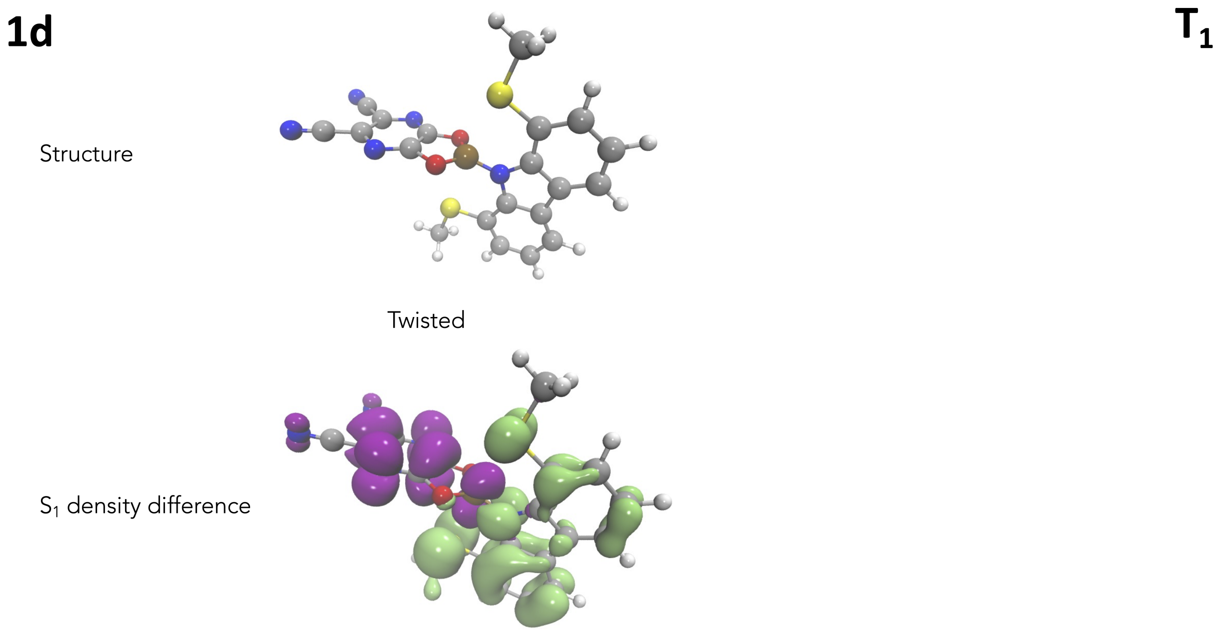

FIGURE A.11: Structure and T_1 density difference associated with the T_1 state optimised structure of **1d**.

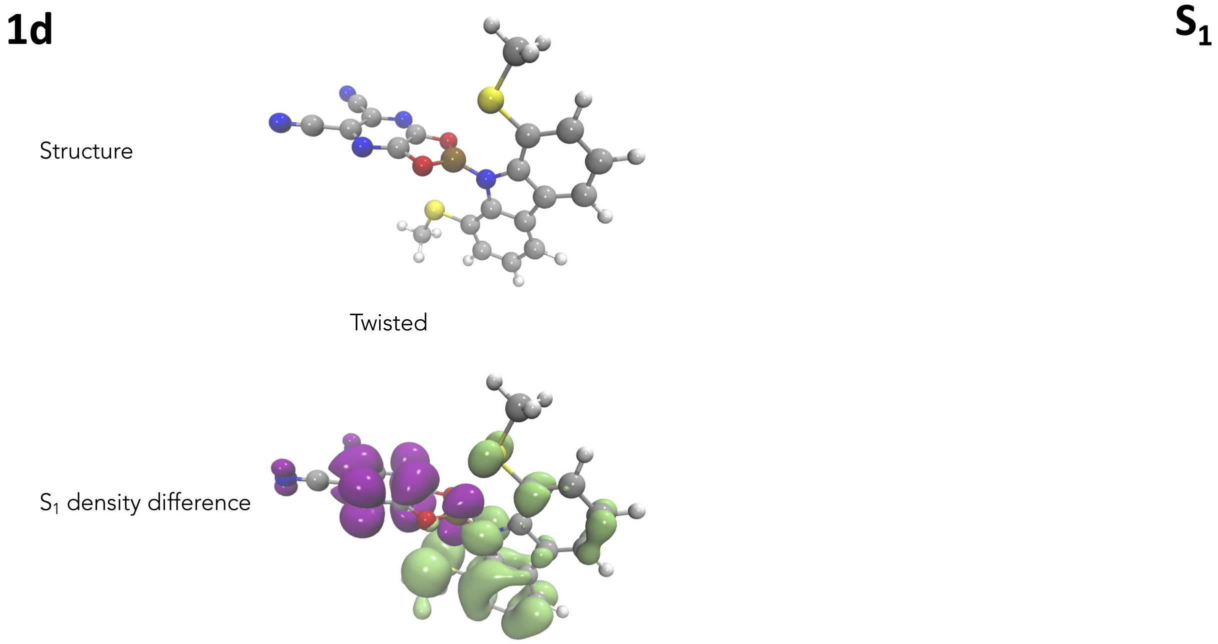

FIGURE A.12: Structure and S_1 density difference associated with the S_1 state optimised structure of **1d**.

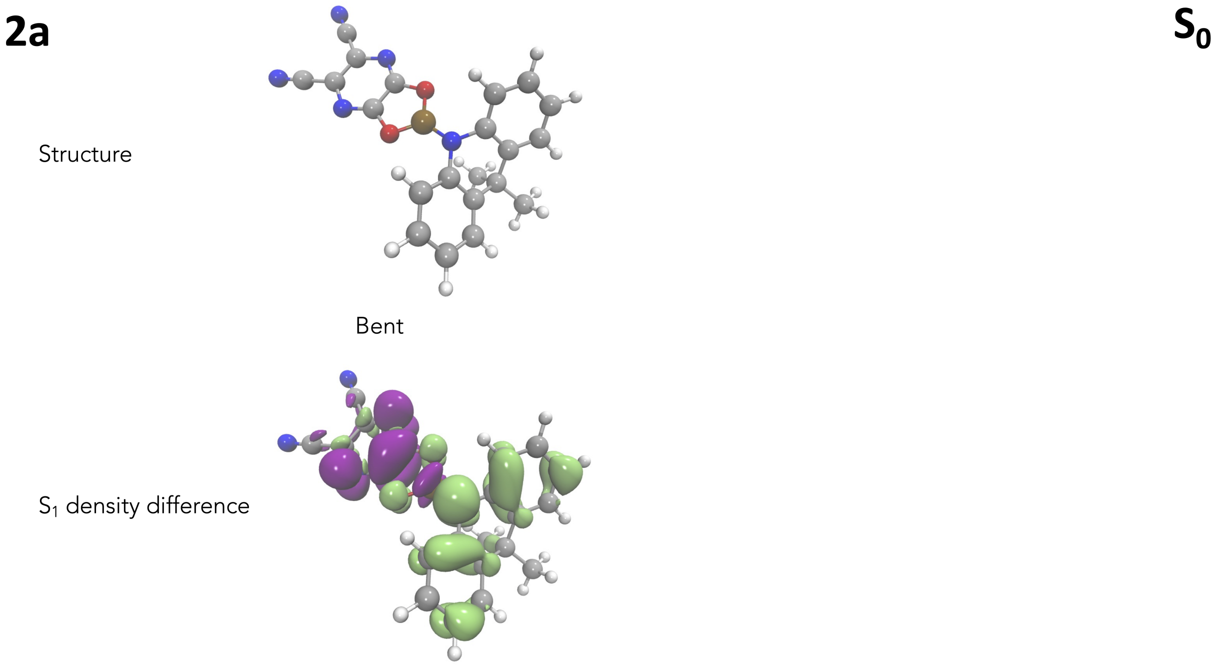

FIGURE A.13: Structure and S$_1$ density difference associated with the ground state optimised structure of **2a**.

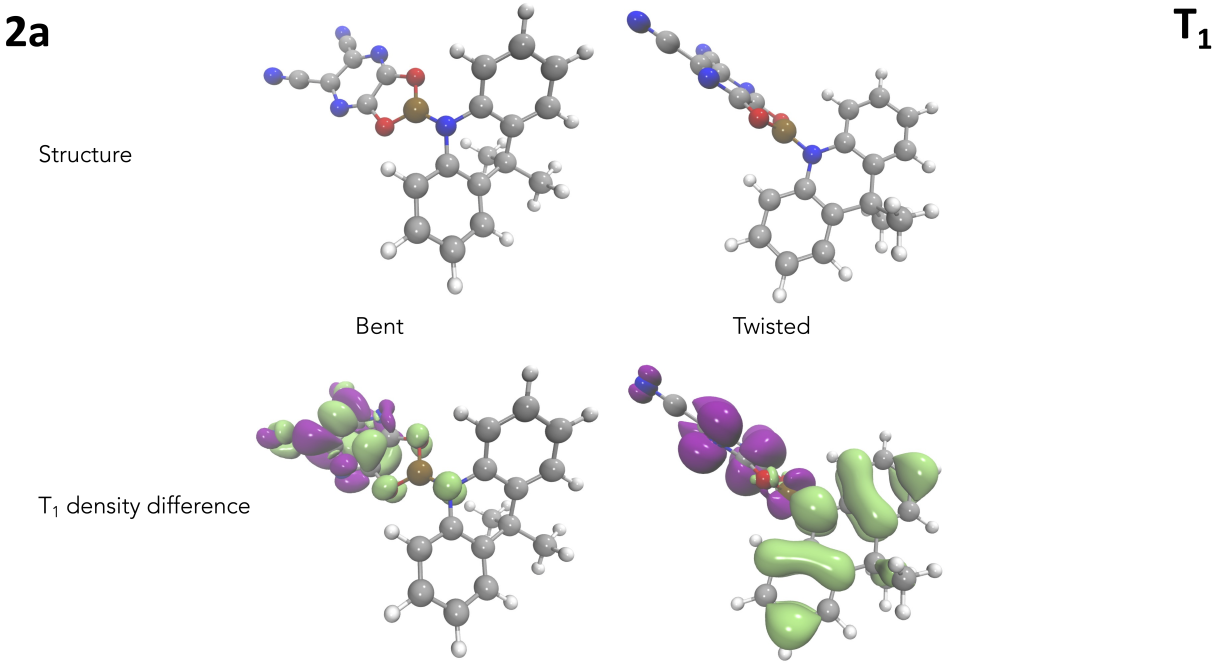

FIGURE A.14: Structure and T$_1$ density difference associated with the T$_1$ state optimised structure of **2a**.

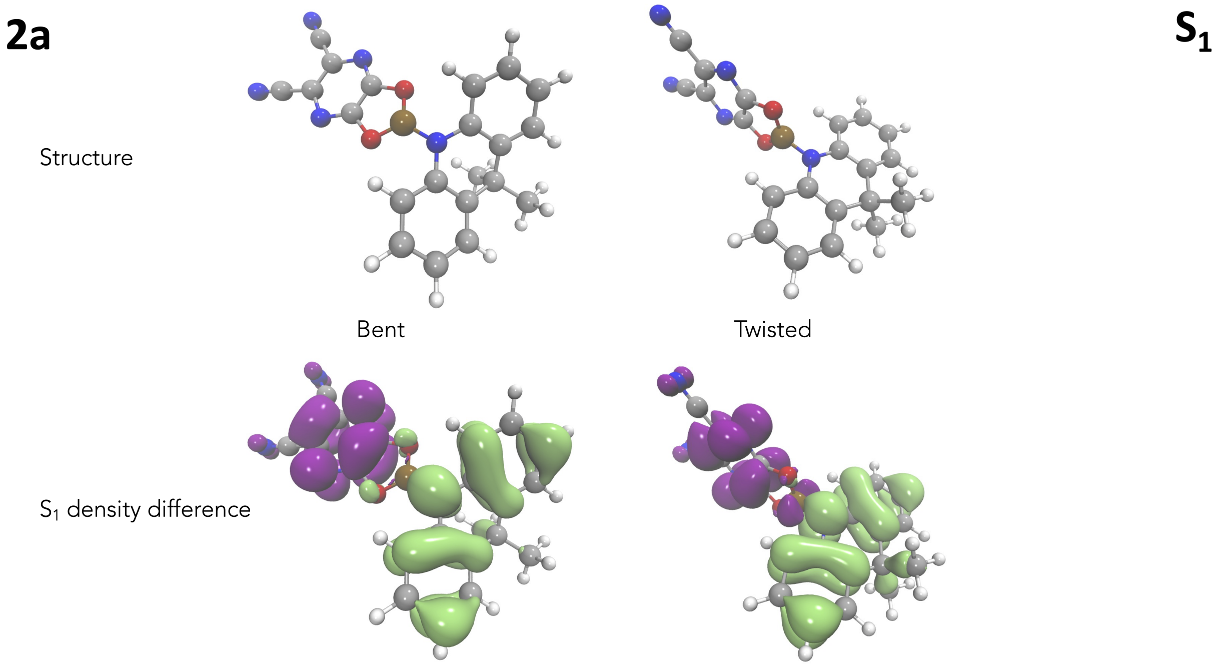

FIGURE A.15: Structure and S$_1$ density difference associated with the S$_1$ state optimised structure of **2a**.

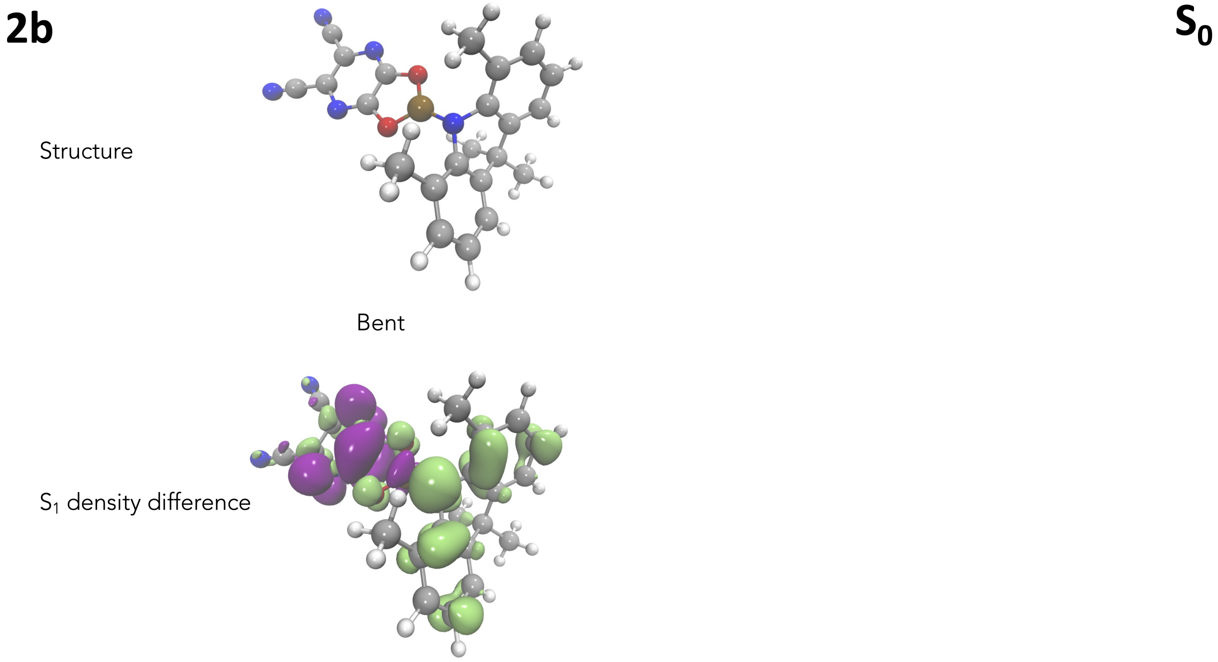

FIGURE A.16: Structure and S$_1$ density difference associated with the ground state optimised structure of **2b**.

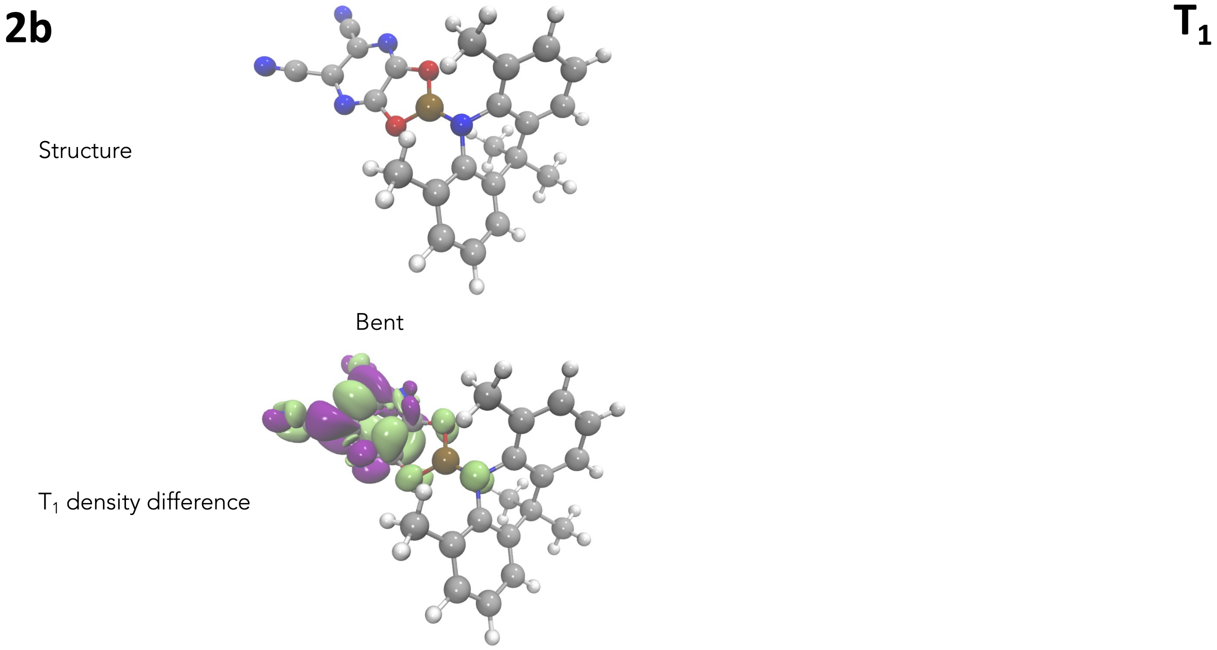

FIGURE A.17: Structure and T_1 density difference associated with the T_1 state optimised structure of **2b**.

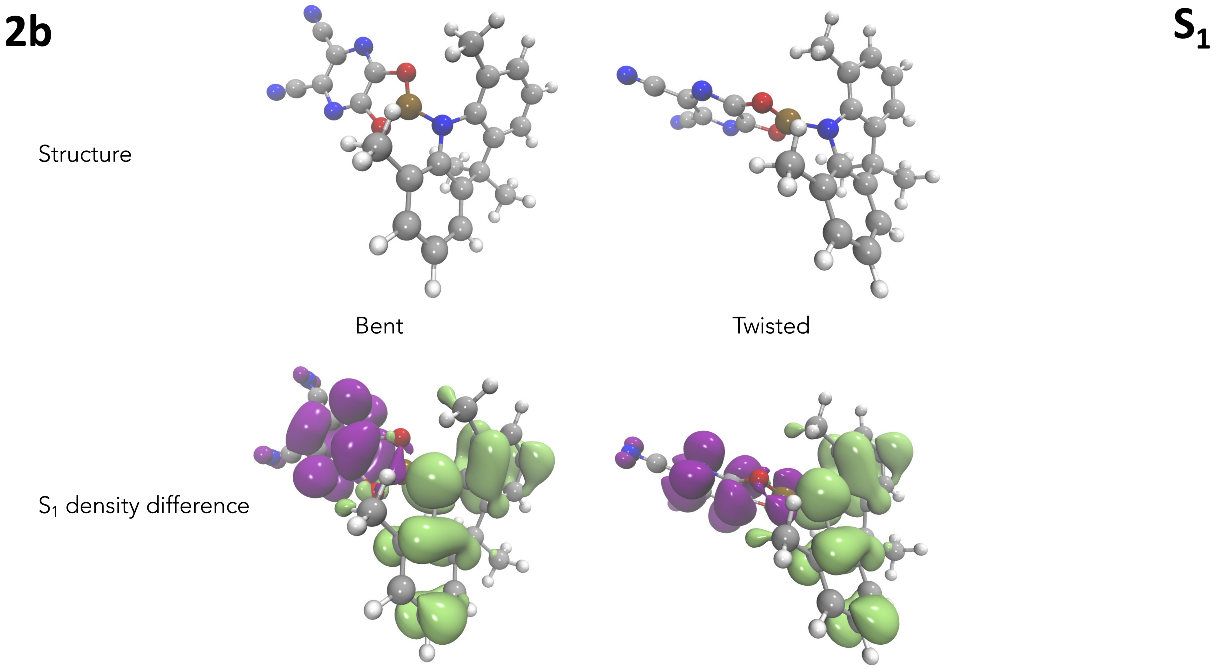

FIGURE A.18: Structure and S_1 density difference associated with the S_1 state optimised structure of **2b**.

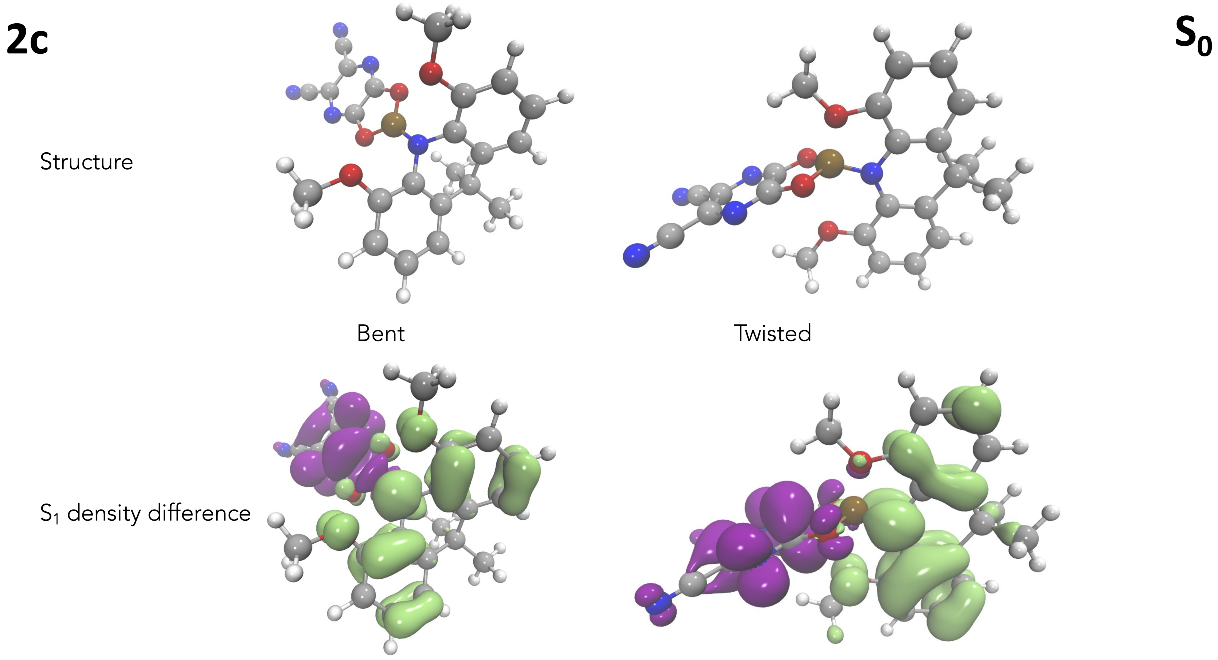

FIGURE A.19: Structure and S_1 density difference associated with the ground state optimised structure of **2c**.

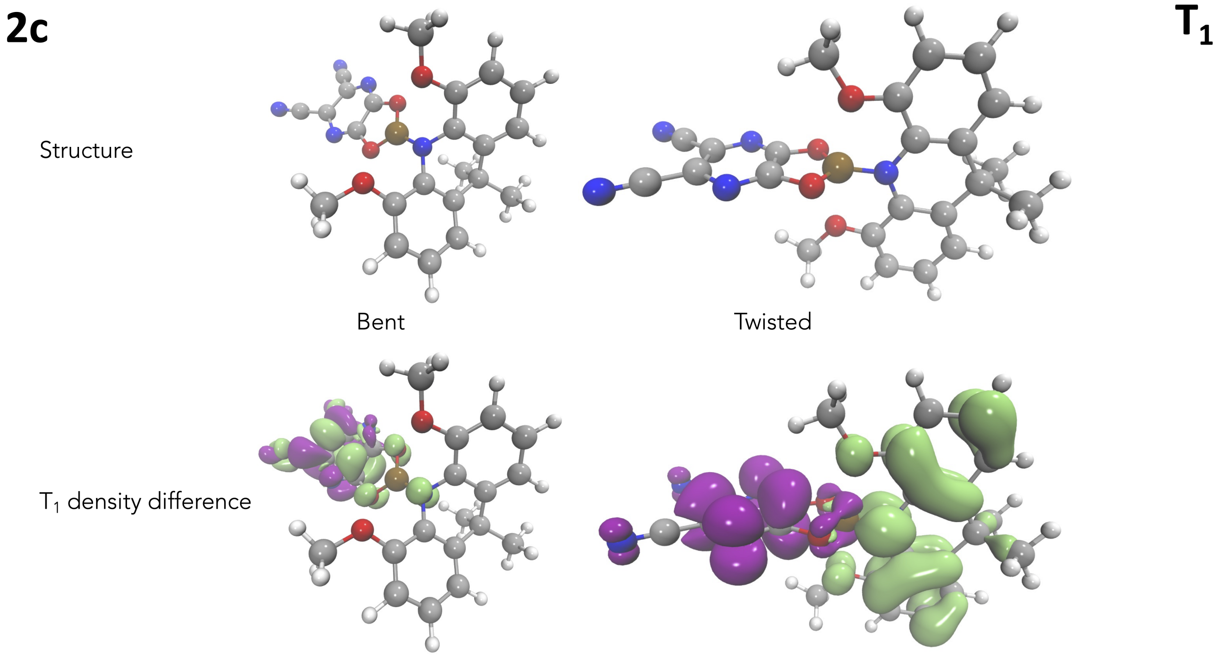

FIGURE A.20: Structure and T_1 density difference associated with the T_1 state optimised structure of **2c**.

2c **S_1**

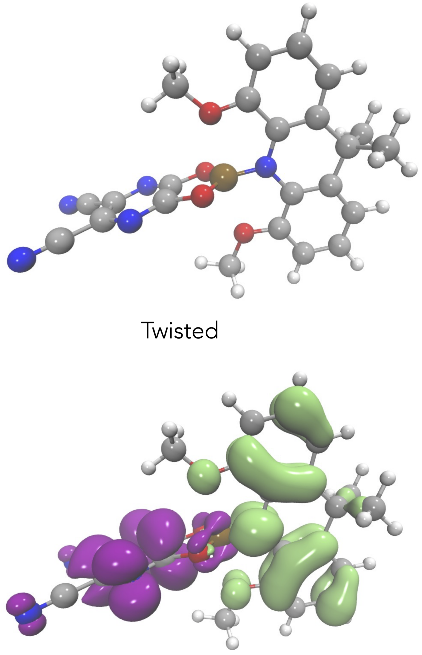

FIGURE A.21: Structure and S_1 density difference associated with the S_1 state optimised structure of **2c**.

2d **S_0**

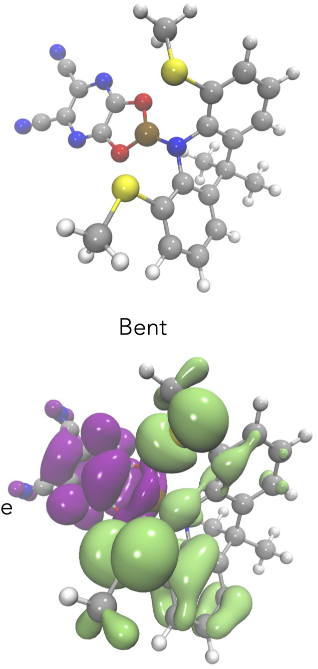

FIGURE A.22: Structure and S_1 density difference associated with the ground state optimised structure of **2d**.

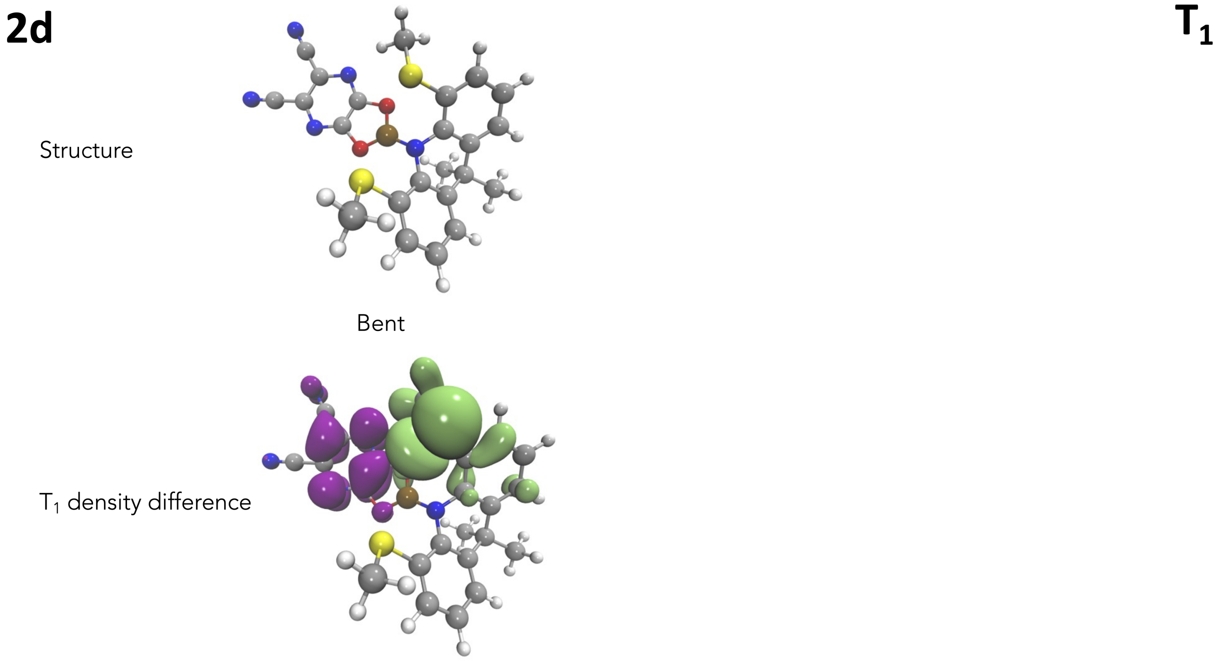

FIGURE A.23: Structure and T_1 density difference associated with the T_1 state optimised structure of **2d**.

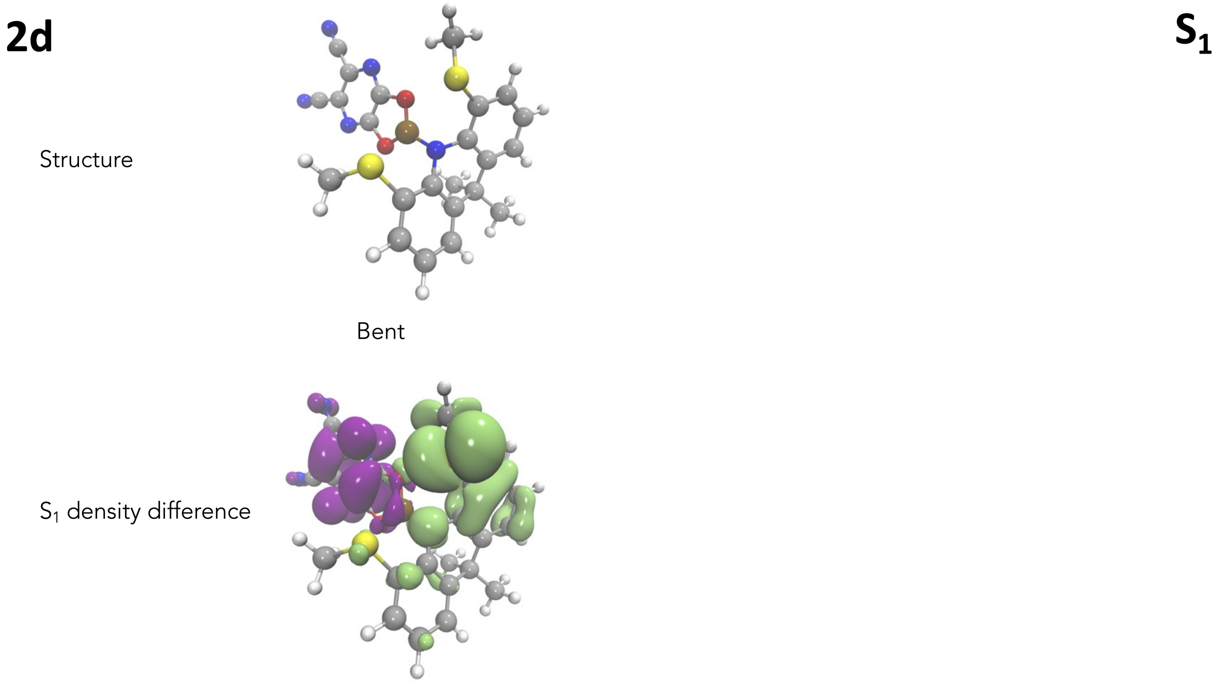

FIGURE A.24: Structure and S_1 density difference associated with the S_1 state optimised structure of **2d**.

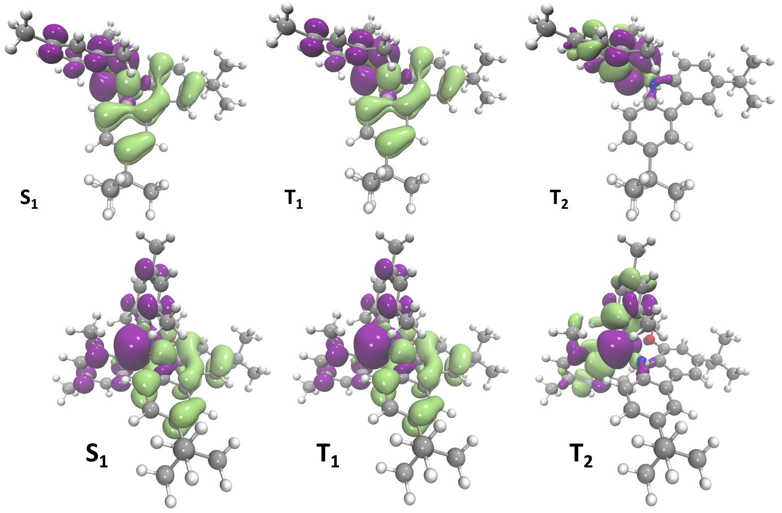

FIGURE A.25: Density differences for the low lying states of **JC258** (upper) and **JC274** (lower).

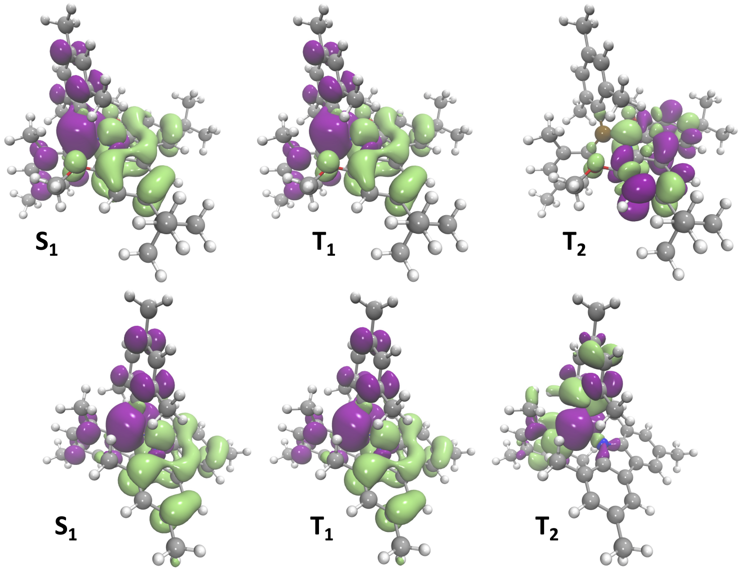

FIGURE A.26: Density differences for the low lying states of **JC257** (upper) and **JC324** (lower).

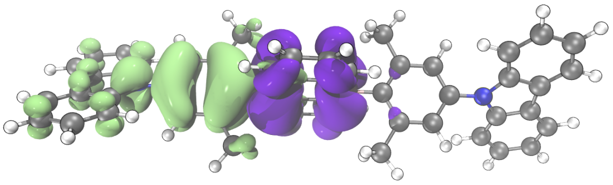

FIGURE A.27: Density differences at S_1 of **3a**

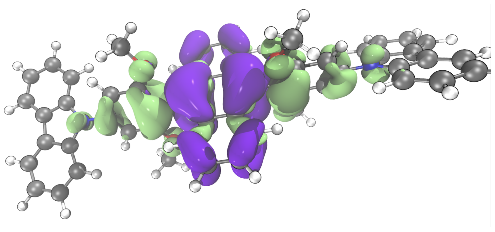

FIGURE A.28: Density differences at S_1 of **3b**

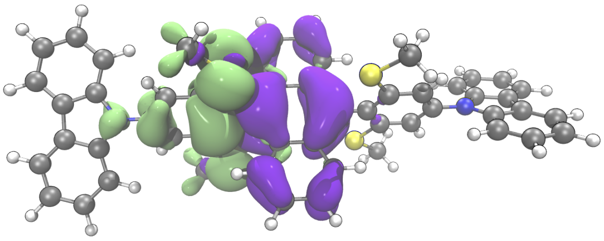

FIGURE A.29: Density differences at S_1 of **3c**

Appendix B

Appendix

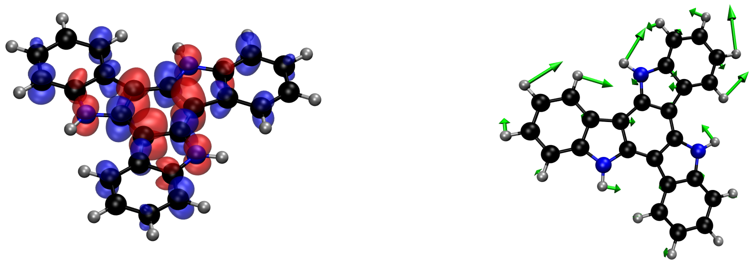

FIGURE B.1: Density difference associated with the first singlet excited state (left) & Dominant normal mode responsible for the excited state structural change (right) associated with **1**.

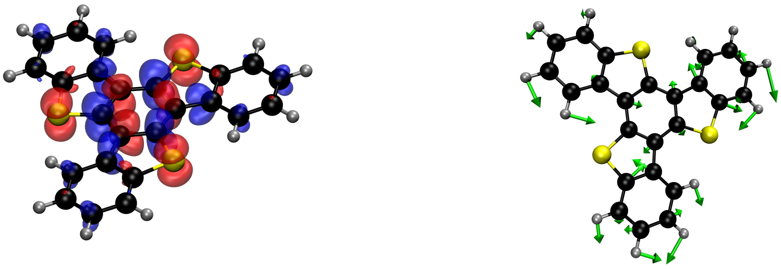

FIGURE B.2: Density difference associated with the first singlet excited state (left) & Dominant normal mode responsible for the excited state structural change (right) associated with **2**.

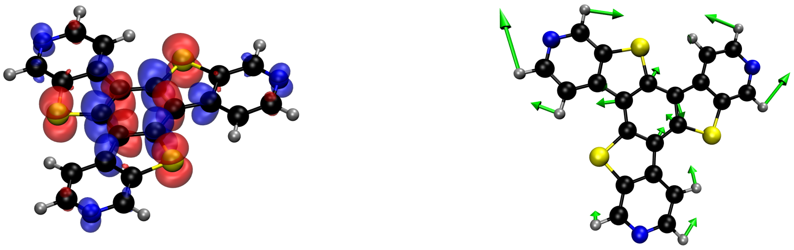

FIGURE B.3: Density difference associated with the first singlet excited state (left) & Dominant normal mode responsible for the excited state structural change (right) associated with **3**

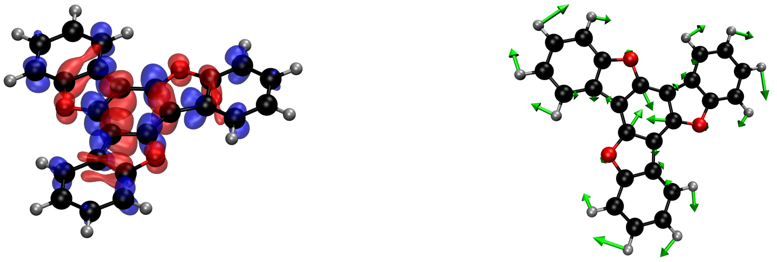

FIGURE B.4: Density difference associated with the first singlet excited state (left) & Dominant normal mode responsible for the excited state structural change (right) associated with **4**

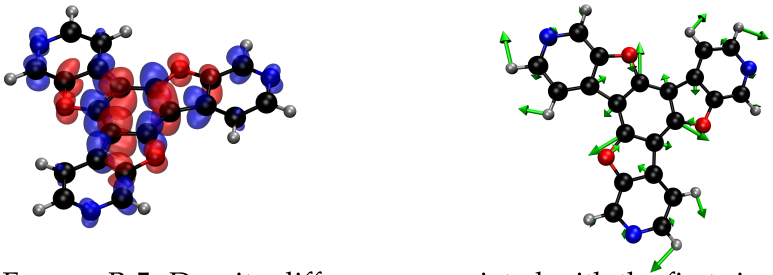

FIGURE B.5: Density difference associated with the first singlet excited state (left) & Dominant normal mode responsible for the excited state structural change (right) associated with **5**

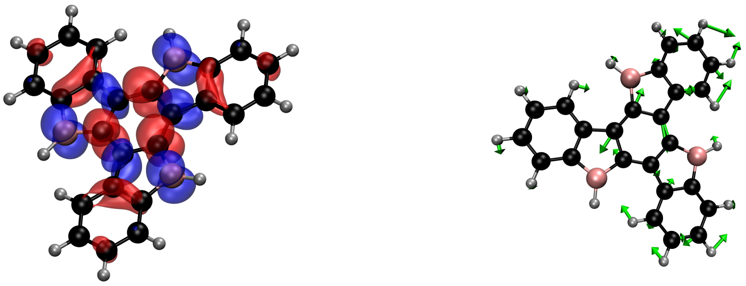

FIGURE B.6: Density difference associated with the first singlet excited state (left) & Dominant normal mode responsible for the excited state structural change (right) associated with **6**.

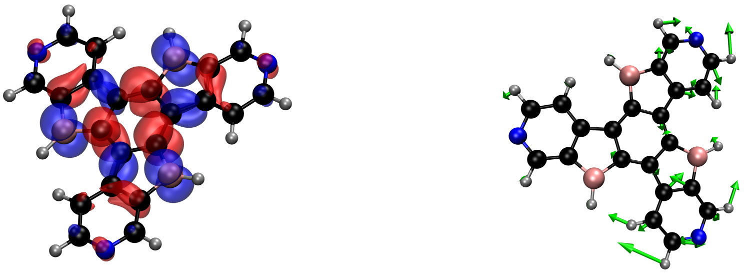

FIGURE B.7: Density difference associated with the first singlet excited state (left) & Dominant normal mode responsible for the excited state structural change (right) associated with **7**.

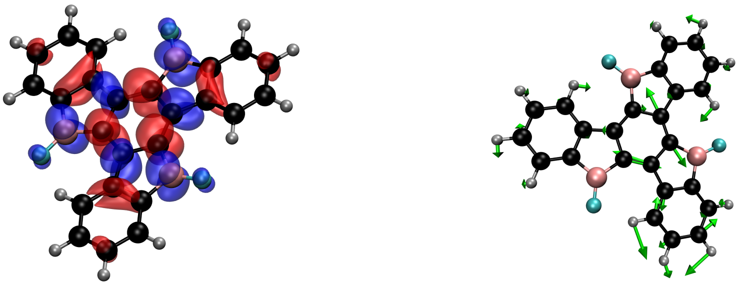

FIGURE B.8: Density difference associated with the first singlet excited state (left) & Dominant normal mode responsible for the excited state structural change (right) associated with **8**

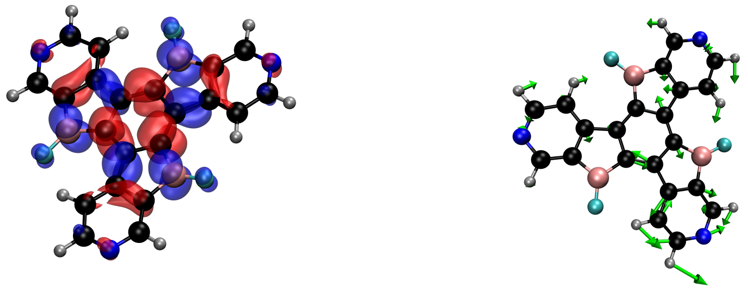

FIGURE B.9: Density difference associated with the first singlet excited state (left) & Dominant normal mode responsible for the excited state structural change (right) associated with **9**

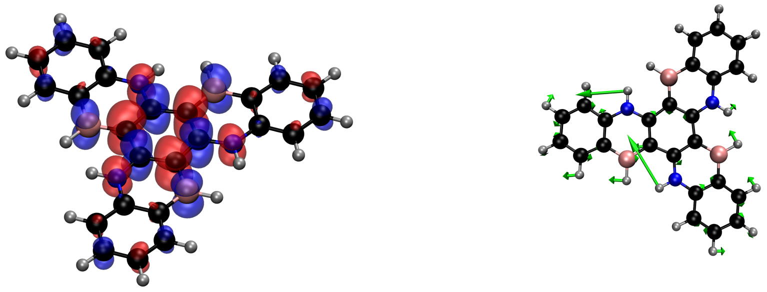

FIGURE B.10: Density difference associated with the first singlet excited state (left) & Dominant normal mode responsible for the excited state structural change (right) associated with **10**.

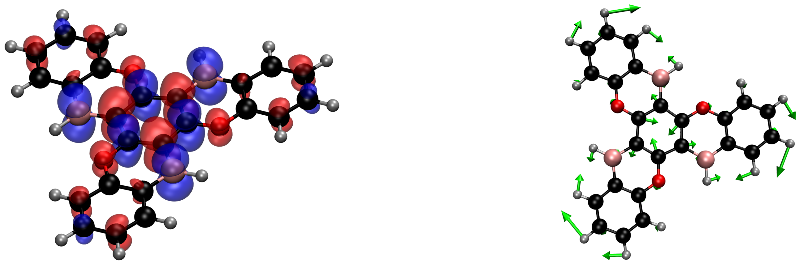

FIGURE B.11: Density difference associated with the first singlet excited state (left) & Dominant normal mode responsible for the excited state structural change (right) associated with **11**

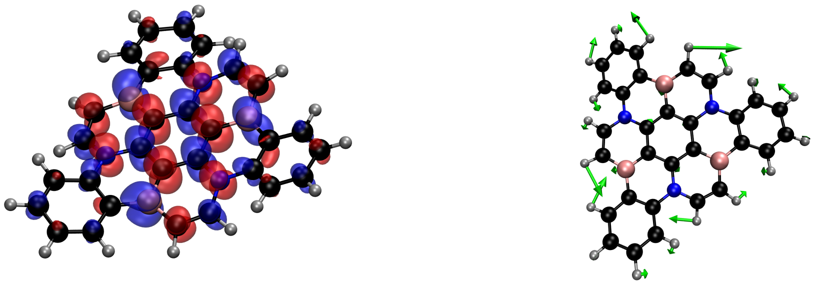

FIGURE B.12: Density difference associated with the first singlet excited state (left) & Dominant normal mode responsible for the excited state structural change (right) associated with **12**.

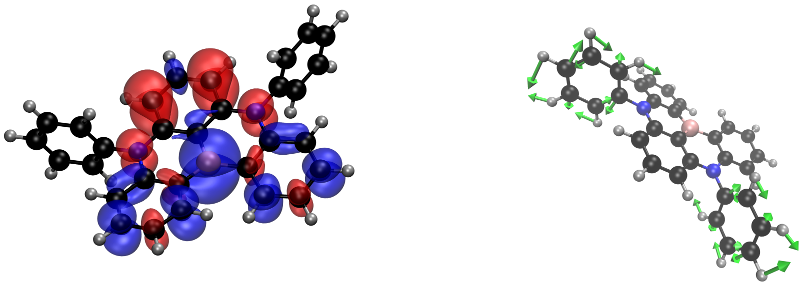

FIGURE B.13: Density difference associated with the first singlet excited state (left) & Dominant normal mode responsible for the excited state structural change (right) associated with **13**.

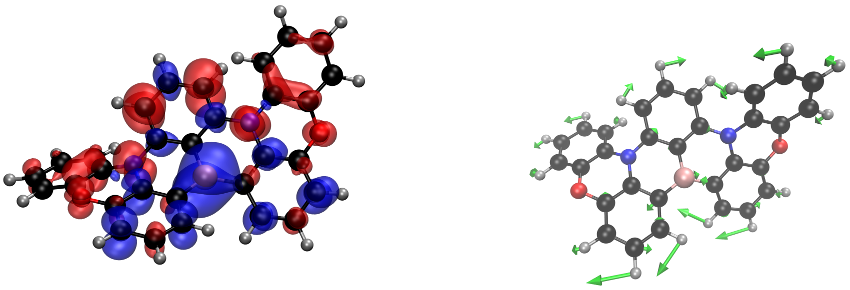

FIGURE B.14: Density difference associated with the first singlet excited state (left) & Dominant normal mode responsible for the excited state structural change (right) associated with **14**

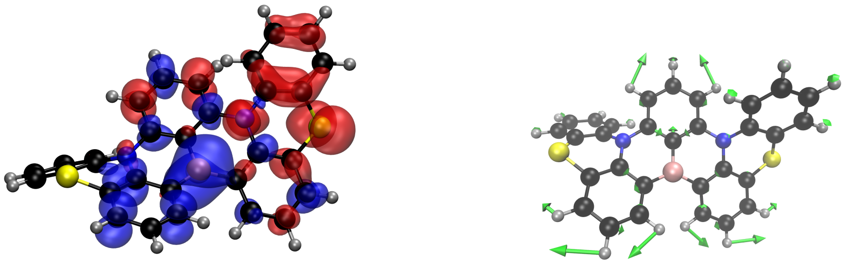

FIGURE B.15: Density difference associated with the first singlet excited state (left) & Dominant normal mode responsible for the excited state structural change (right) associated with **15**

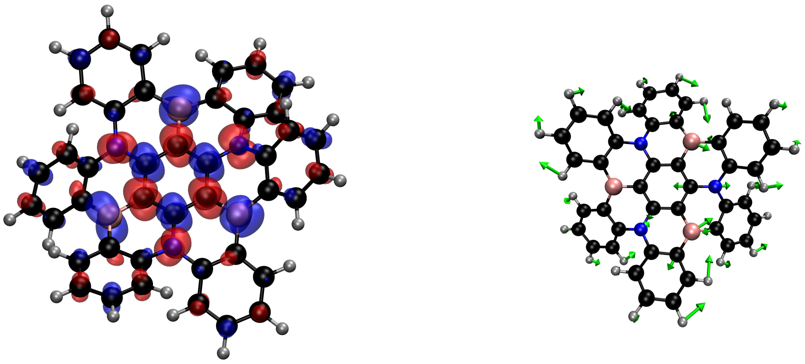

FIGURE B.16: Density difference associated with the first singlet excited state (left) & Dominant normal mode responsible for the excited state structural change (right) associated with **16**

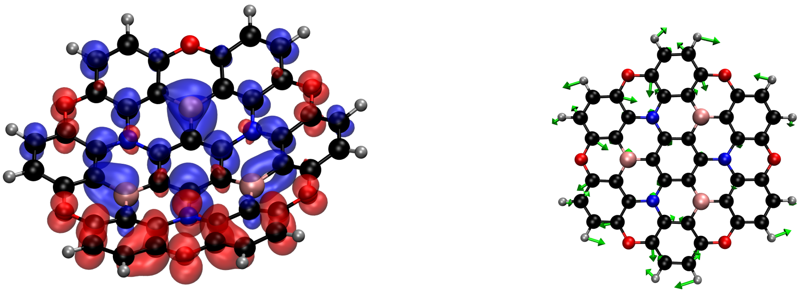

FIGURE B.17: Density difference associated with the first singlet excited state (left) & Dominant normal mode responsible for the excited state structural change (right) associated with **17**

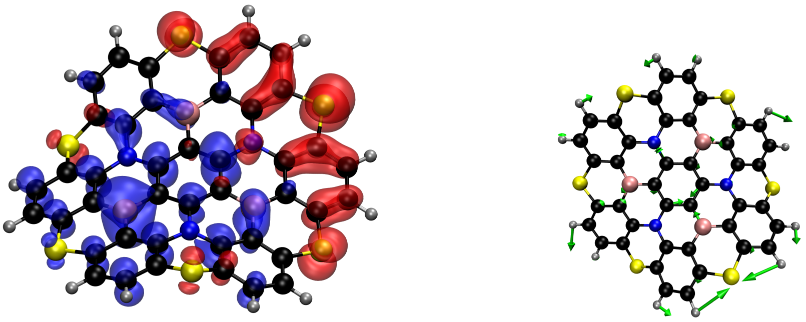

FIGURE B.18: Density difference associated with the first singlet excited state (left) & Dominant normal mode responsible for the excited state structural change (right) associated with **18**

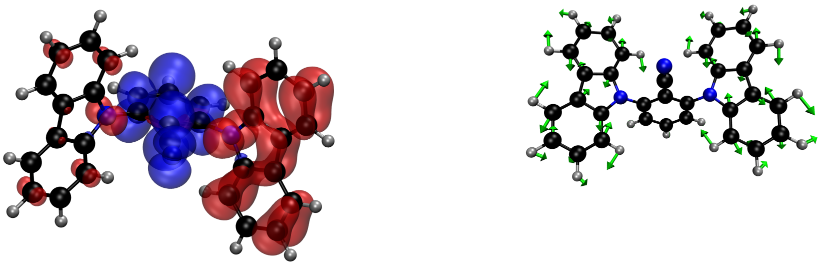

FIGURE B.19: Density difference associated with the first singlet excited state (left) & Dominant normal mode responsible for the excited state structural change (right) associated with **19**

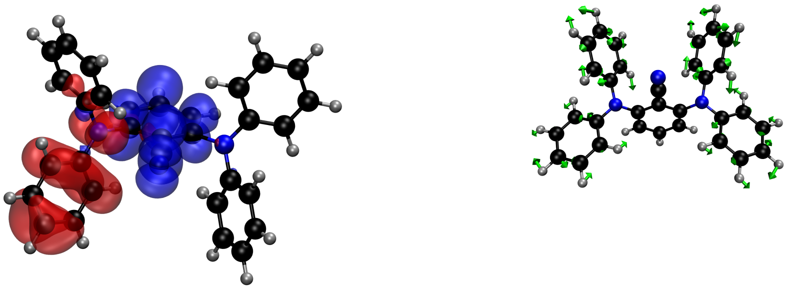

FIGURE B.20: Density difference associated with the first singlet excited state (left) & Dominant normal mode responsible for the excited state structural change (right) associated with **20**

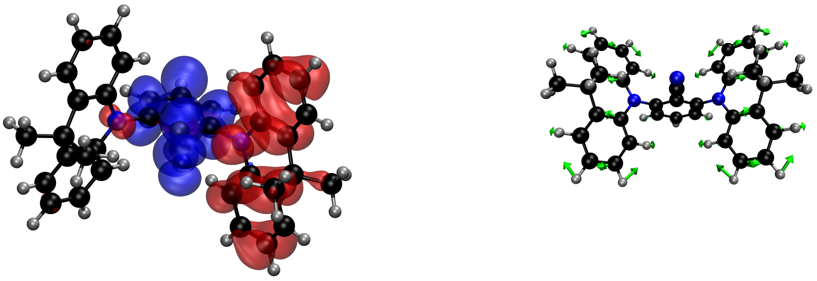

FIGURE B.21: Density difference associated with the first singlet excited state (left) & Dominant normal mode responsible for the excited state structural change (right) associated with **21**.

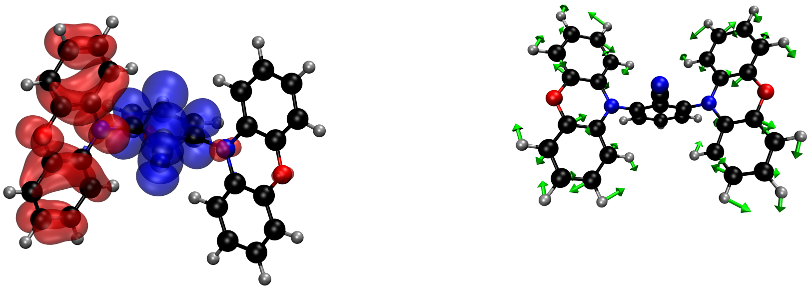

FIGURE B.22: Density difference associated with the first singlet excited state (left) & Dominant normal mode responsible for the excited state structural change (right) associated with **22**

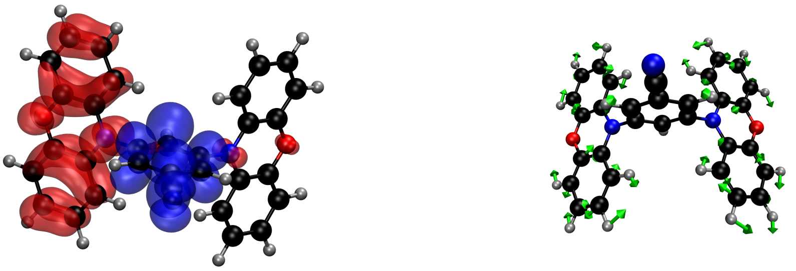

FIGURE B.23: Density difference associated with the first singlet excited state (left) & Dominant normal mode responsible for the excited state structural change (right) associated with **23**

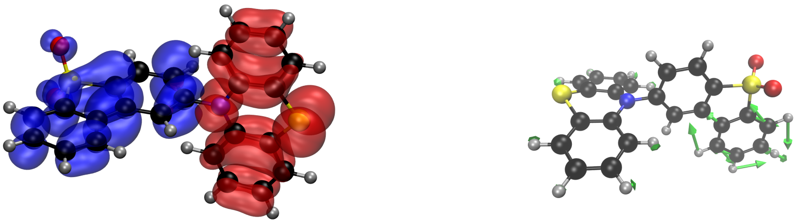

FIGURE B.24: Density difference associated with the first singlet excited state (left) & Dominant normal mode responsible for the excited state structural change (right) associated with **24**

FIGURE B.25: Density difference associated with the first singlet excited state (left) & Dominant normal mode responsible for the excited state structural change (right) associated with **25**

FIGURE B.26: Density difference associated with the first singlet excited state (left) & Dominant normal mode responsible for the excited state structural change (right) associated with **26**.

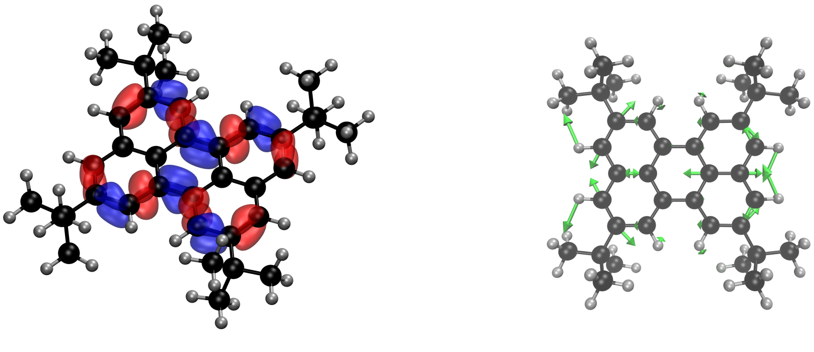

FIGURE B.27: Density difference associated with the first singlet excited state (left) & Dominant normal mode responsible for the excited state structural change (right) associated with **27**

Appendix C

Appendix

	E_{abs}	E_{em}	ΔE_{ST}	$k_r(S_1)$	Ref.	E_{abs}	E_{em}	ΔE_{ST}	$k_r(S_1)$
DABNA-1	2.84	2.68	0.18	9.6×10^7	[134]	3.38	3.25	0.24	2.9×10^8
DABNA-2	2.79	2.64	0.14	14.1×10^7	[134]	3.21	3.07	0.18	3.6×10^8
ABDNA-Me-Mes	2.71	2.56	0.20	1.0×10^8	[135]	3.13	2.99	0.23	2.3×10^8
ADBNA-Me-Tip	2.71	2.63	0.19	1.1×10^8	[135]	3.11	2.95	0.22	2.2×10^8
2F-BN	2.64	2.65	0.16	5.7×10^7	[137]	2.99	2.88	0.18	3.1×10^8
3F-BN	2.64	2.48	0.08	4.7×10^7	[137]	3.01	2.95	0.21	2.2×10^8
4F-BN	2.64	2.50	0.11	5.2×10^7	[137]	2.98	2.86	0.16	2.9×10^8
DtBuCzB	2.58	2.50	0.13	1.0×10^8	[235]	3.07	2.98	0.18	3.6×10^8
DtBuPhCzB	2.58	2.50	0.09	3.9×10^7	[235]	2.94	2.83	0.15	3.4×10^8
B3	2.88	2.81	0.15	–	[140]	3.07	3.00	0.11	2.3×10^7
B4	2.82	2.75	0.15	–	[140]	3.15	2.94	0.11	1.2×10^8
BN1	2.59	2.59	0.11	1.2×10^8	[236]	2.93	2.81	0.16	2.6×10^8
BN2	2.46	2.32	0.13	7.9×10^7	[236]	2.77	3.16	0.30	9.0×10^7
BN3	2.34	2.21	0.09	7.3×10^7	[236]	2.59	2.54	0.10	1.0×10^8
DOBNA	3.30	3.12	0.15	6.7×10^7	[106]	3.56	3.26	0.25	3.2×10^8
3-PhQAD	2.80	2.66	0.18	1.8×10^8	[82]	3.22	2.99	0.21	2.5×10^8
7-PhQAD	2.79	2.67	0.19	1.8×10^8	[82]	3.22	3.04	0.47	2.6×10^8
MeS_3DiKTa	2.76	2.65	0.21	5.4×10^7	[139]	3.26	3.06	0.30	2.7×10^8
R-BN	1.97	1.87	0.18	7.5×10^7	[237]	2.23	2.03	0.24	1.1×10^8
R-TBN	1.90	1.79	0.16	6.2×10^7	[237]	2.12	1.97	0.23	1.0×10^8
BSBS-N1	2.71	2.62	0.13	3.6×10^7	[197]	2.93	2.83	0.18	3.2×10^8
DQAO	2.82	2.67	0.19	5.9×10^7	[238]	3.32	3.10	0.34	2.5×10^8
OQAO	2.54	2.38	0.16	1.6×10^8	[238]	3.00	2.84	0.26	2.5×10^8
SQAO	2.54	2.25	0.16	1.1×10^8	[238]	2.99	2.80	0.21	2.0×10^8
AZA-BN	2.46	2.38	0.18	5.0×10^7	[239]	2.84	2.63	0.24	1.9×10^8
BN-DMAC	2.69	2.56	0.14	9.2×10^7	[240]	3.03	2.83	0.18	2.3×10^8
2PXZBN	2.61	2.46	0.19	1.6×10^8	[142]	2.99	2.79	0.19	1.8×10^8
2PTZBN	2.63	2.43	0.15	1.3×10^8	[142]	3.03	2.81	0.18	1.8×10^8

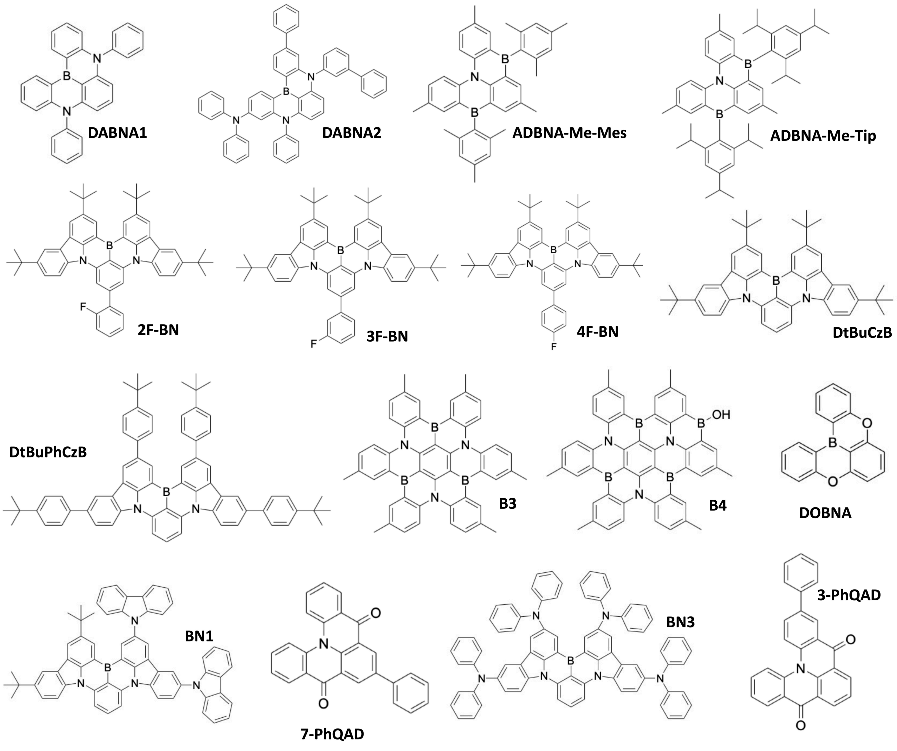

FIGURE C.1: Structures considered in this work.

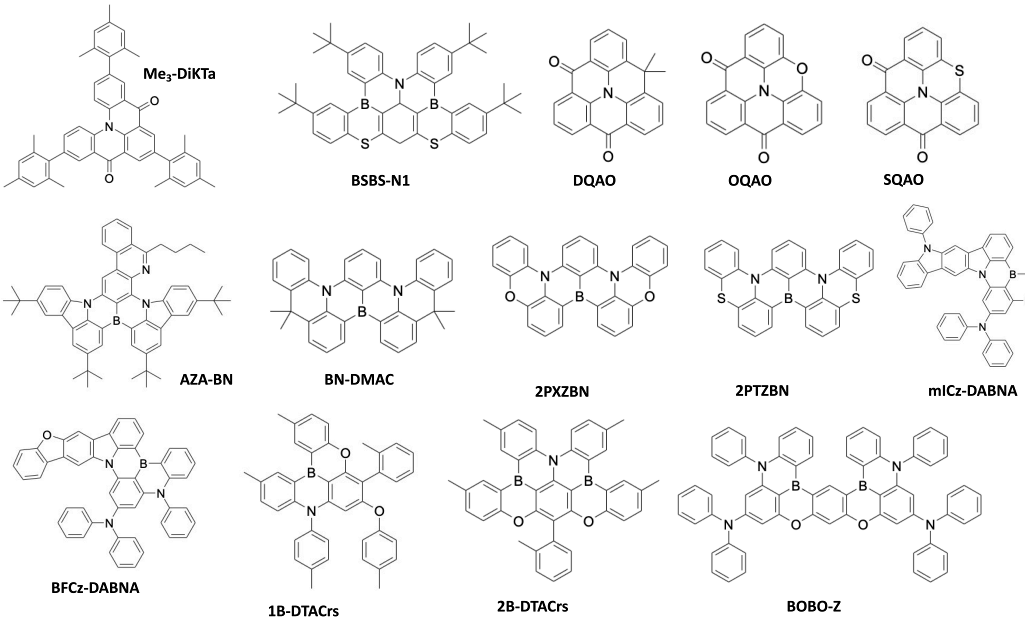

FIGURE C.2: Structures considered in this work.

	Experiment					Theory			
	E$_{abs}$	E$_{em}$	ΔE$_{ST}$	$k_r(S_1)$	Ref.	E$_{abs}$	E$_{em}$	ΔE$_{ST}$	
mICz-DABNA	2.78	2.69	0.20	1.2×10^8	[241]	3.11	2.97	0.17	2.9×10^8
BFCz-DABNA	2.81	2.72	0.20	1.1×10^8	[241]	3.16	3.06	0.18	3.1×10^8
1B-DTACrs	2.95	2.83	0.22	8.0×10^7	[242]	3.43	3.10	0.23	2.5×10^8
2B-DTACrs	2.92	2.77	0.16	1.7×10^8	[242]	3.26	2.98	0.13	1.9×10^8
BOBO-Z	2.92	2.81	0.15	1.5×10^8	[196]	3.27	3.16	0.12	3.2×10^8
BOBS-Z	2.85	2.74	0.16	9.0×10^7	[196]	3.27	3.16	0.12	3.6×10^8
BSBS-Z	2.79	2.70	0.14	7.0×10^7	[196]	3.21	3.07	0.16	3.3×10^8
BN1-2	2.82	2.73	0.20	1.3×10^8	[243]	3.30	3.14	0.18	3.4×10^8
BN2-2	2.76	2.73	0.16	1.4×10^8	[243]	3.17	3.04	0.16	3.0×10^8
BN3-2	2.79	2.72	0.15	1.7×10^8	[243]	3.19	3.09	0.13	6.8×10^8
PTZBN1	2.72	2.53	0.16	2.0×10^8	[244]	3.17	2.92	0.20	2.0×10^8
PTZBN2	2.78	2.57	0.15	2.1×10^8	[244]	3.19	2.92	0.20	1.7×10^8
PTZBN3	2.80	2.65	0.17	1.7×10^8	[244]	3.11	2.92	0.09	1.5×10^8
CzBO	2.91	2.79	0.15	1.5×10^8	[245]	3.35	3.22	0.20	3.5×10^8
CzBS	2.77	2.63	0.11	1.5×10^7	[245]	3.20	3.04	0.19	2.9×10^8
CzBSe	2.75	2.60	0.12	0.5×10^6	[245]	3.16	3.02	0.17	2.7×10^8
DBNS	2.22	1.96	0.20	5.5×10^7	[246]	2.37	2.14	0.27	1.1×10^8
BSS-PA	2.87	2.73	0.13	–	[230]	3.03	2.89	0.09	1.6×10^8
BSS-Cz	2.87	2.72	0.14	–	[230]	3.10	3.02	0.06	9.0×10^7
TPD4PA	2.88	2.79	0.05	1.2×10^8	[247]	3.32	3.21	0.17	2.2×10^8
tBu-TPD4PA	2.84	2.75	0.06	1.1×10^8	[247]	3.24	3.01	0.12	2.5×10^8
p-DiNBO	2.54	2.48	0.06	1.0×10^8	[248]	2.83	2.69	0.19	3.0×10^8

TABLE C.1: A summary of the experimental and MRSF-TDDFT(PBE0) calculated data used in this work

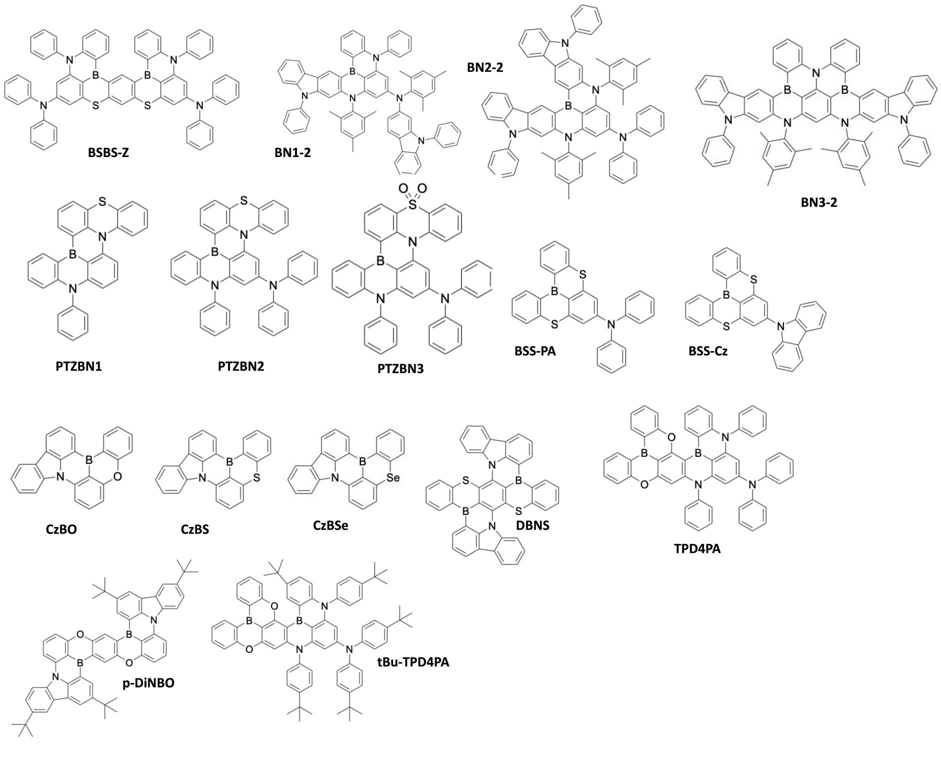

FIGURE C.3: Structures considered in this work.

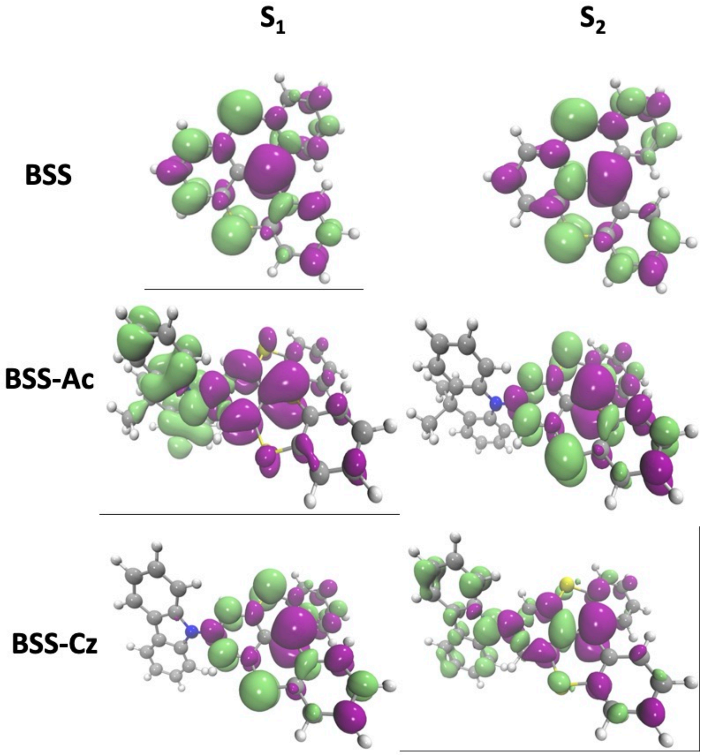

FIGURE C.4: Density differences of the S_1 and S_2 states of **BSS**, **BSS-Ac** and **BSS-Cz** at the electronic ground state geometry.

Molecules	Smiles
1	C[C@@H](CCCC(C)(C)C)c1ccc2c(c1)c1cccc3c4cc5c(cc4n2c13)c1cc(C(C)(C)C)cc2c3cc(C(C)(C)C)ccc3n5c12
2	CC(C)(C)c1ccc2c(c1)c1cc(C(C)(C)C)cc3c4cc5c(cc4n2c13)c1cc(C(C)(C)CBr)cc2c3cc(C(C)(C)C)ccc3n5c12
3	CC/N=C()/c1ccc2c(c1)c1cc(CC(C)(C)C)cc3c4cc5c(cc4n2c13)c1cc(C(C)(C)C)cc2c3cc(C(C)(C)C)ccc3n5c12
4	Cc1cc2c3cc([C@@H](C)CCCC(C)C)ccc3n3c4cc5c6cc(C(C)(C)C)cc7c8cc(C(C)(C)C)ccc8n(c5cc4c(c1)c23)c67
5	B[C@@](C)(CC)c1cc2c3cc(C(C)(C)C)ccc3n3c4cc5c6cc(C(C)(C)C)cc7c8cc(C(C)(C)C)ccc8n(c5cc4c(c1)c23)c67
6	C[C@@H](F)c1cc2c3cc(C(C)(C)C)ccc3n3c4cc5c6cc(C(C)(C)C)cc7c8cc(C(C)(C)C)ccc8n(c5cc4c(c1)c23)c67
7	CCc1ccc2c(c1)c1cc(CC(C)(C)C)cc3c4cc5c(cc4n2c13)c1cc(C(C)(C)C)cc2c3cc(C(C)(C)C)ccc3n5c12
8	CCCCCc1ccc2c(c1)c1cc(CC(C)C)cc3c4cc5c(cc4n2c13)c1cc(C(C)(C)C)cc2c3cc(C(C)(C)C)ccc3n5c12
9	CC(C)(C)Cc1cc2c3cc(Br)ccc3n3c4cc5c6cc(C(C)(C)C)cc7c8cc(C(C)(C)C)ccc8n(c5cc4c(c1)c23)c67
10	CCc1ccc2c(c1)c1cc(C(C)(C)C)cc3c4cc5c(cc4n2c13)c1cc(C(C)(C)C)cc2c3cc(C(C)(C)C)ccc3n5c12
11	CC[C@@](C)(O)c1cc2c3cc(C(C)(C)C)ccc3n3c4cc5c6cc(C(C)(C)C)cc7c8cc(C(C)(C)C)ccc8n(c5cc4c(c1)c23)c67
12	Cc1cc2c3cc(C[C@@H](C)CC(C)C)ccc3n3c4cc5c6cc(C(C)(C)C)cc7c8cc(C(C)(C)C)ccc8n(c5cc4c(c1)c23)c67
13	CCCN[C@@H](C)c1ccc2c(c1)c1cc(C(C)(C)C)cc3c4c5c6cc(C(C)(C)C)cc7c8cc(C(C)(C)C)ccc8n(c5ccc4n2c13)c67
14	CC(C)(C)c1cc2ccn3c4cc5c6cc(C(C)(C)C)cc7c8cc(C(C)(C)C)ccc8n(c5cc4c(c1)c23)c67
15	Cc1cc2cc(C(C)(C)C)cc3c4cc5c(cc4n1c23)c1cc(C(C)(C)C)cc2c3cc(C(C)(C)C)ccc3n5c12
16	CC(C)(C)c1ccc2c(c1)c1cc(C(C)(C)C)cc3c4cc5c(cc4n2c13)c1cc(C(C)(C)C)cc2c3cc(C(C)(C)Br)ccc3n5c12
17	CC(C)[C@@H](I)c1cc2c3cc(C(C)(C)C)ccc3n3c4cc5c6cc(C(C)(C)C)cc7c8cc(C(C)(C)C)ccc8n(c5cc4c(c1)c23)c67
18	CC(C)(C)c1ccc2c(c1)c1cc(C(C)(C)C)cc3c4cc5c(cc4n2c13)c1cc(C(C)(C)Cl)cc2c3cc(C(C)(C)C)ccc3n5c12
19	CC(C)(C)Cc1cc2cc(CCl)n3c4cc5c6cc(C(C)(C)C)cc7c8cc(C(C)(C)C)ccc8n(c5cc4c(c1)c23)c67
20	Oc1cccc2c1b1c3ccccc3n(c3ccccc3)c3cccc(c13)n2c1ccccc1
21	CC[C@@H](Cl)c1ccc2c(c1)c1cc(CC(C)(C)C)cc3c4cc5c(cc4n2c13)c1cc(C(C)(C)C)cc2c3cc(C(C)(C)C)ccc3n5c12
22	CC(C)(C)c1ccc2c(c1)c1cc(C(C)(C)C)cc3c4cc5c(cc4n2c13)c1cc(C(C)(C)CF)cc2c3cc(C(C)(C)C)ccc3n5c12
23	C[C@@H](I)c1cc2c3cc(C(C)(C)C)ccc3n3c4cc5c6cc(C(C)(C)C)cc7c8cc(C(C)(C)C)ccc8n(c5cc4c(c1)c23)c67
24	CC(C)(C)c1ccc2c(c1)c1cc(C(C)(C)C)cc3c4cc5c(cc4n2c13)c1cc(C(C)(C)C)cc2c3ccccc3n5c12
25	CC(C)(C)Cc1cc2cc(I)n3c4cc5c6cc(C(C)(C)C)cc7c8cc(C(C)(C)C)ccc8n(c5cc4c(c1)c23)c67
26	CCCCc1cc2c3cc(C(C)(C)C)ccc3n3c4cc5c6cc(C(C)(C)C)cc7c8cc(C(C)(C)C)ccc8n(c5cc4c(c1)c23)c67

27	CC(C)(C)Cc1cc2c3cc(CCl)ccc3n3c4cc5c6cc(C(C)(C)C)cc7c8cc(C(C)(C)C)ccc8n(c5cc4c(c1)c23)c67
28	CC(C)[C@@H](C)c1cc2c3cc(C(C)(C)C)ccc3n3c4cc5c6cc(C(C)(C)C)cc7c8cc(C(C)(C)C)ccc8n(c5cc4c(c1)c23)c67
29	Nc1cccc2c1b(c1ccccc1Nc1ccccc1)c1ccccc1n2c1ccccc1
30	CC/C(=C/c1ccc2c(c1)c1cc(CC(C)(C)C)cc3c4cc5c(cc4n2c13)c1cc(C(C)(C)C)cc2c3cc(C(C)(C)C)ccc3n5c12)/C
31	CCCO[C@@H](C)c1ccc2c(c1)c1cc(C(C)(C)C)cc3c4cc5c(cc4n2c13)c1cc(C(C)(C)C)cc2c3cc(C(C)(C)C)ccc3n5c12
32	BC(C)(C)c1ccc2c(c1)c1cc(CC(C)(C)C)cc3c4cc5c(cc4n2c13)c1cc(C(C)(C)C)cc2c3cc(C(C)(C)C)ccc3n5c12
33	CC(C)Cc1cc2c3cc(C(C)C)ccc3n3c4cc5c6cc(C(C)(C)C)cc7c8cc(C(C)(C)C)ccc8n(c5cc4c(c1)c23)c67
34	CCC[C@@H](C)c1cc2c3cc(C(C)(C)C)ccc3n3c4cc5c6cc(C(C)(C)C)cc7c8cc(C(C)(C)C)ccc8n(c5cc4c(c1)c23)c67
35	CC[C@@H](O)c1ccc2c(c1)c1cc(CC(C)(C)C)cc3c4cc5c(cc4n2c13)c1cc(C(C)(C)C)cc2c3cc(C(C)(C)C)ccc3n5c12
36	CC(C)(C)c1ccc2c(c1)c1cc(C(C)(C)C)cc3c4cc5c(cc4n2c13)c1cc(C(C)(C)C)cc2c3cc(Cl)ccc3n5c12
37	CCCB(C)Cc1cc2c3cc(C(C)(C)C)ccc3n3c4cc5c6cc(C(C)(C)C)cc7c8cc(C(C)(C)C)ccc8n(c5cc4c(c1)c23)c67
38	CC(C)[C@@H](N)c1cc2c3cc(C(C)(C)C)ccc3n3c4cc5c6cc(C(C)(C)C)cc7c8cc(C(C)(C)C)ccc8n(c5cc4c(c1)c23)c67
39	CC(C)C/N=C/c1ccc2c(c1)c1cc(C(C)(C)C)cc3c4cc5c(cc4n2c13)c1cc(C(C)(C)C)cc2c3cc(C(C)(C)C)ccc3n5c12
40	CC(C)COCc1cc2c3cc(C(C)(C)C)ccc3n3c4cc5c6cc(C(C)(C)C)cc7c8cc(C(C)(C)C)ccc8n(c5cc4c(c1)c23)c67
41	CCCC[C@@H](C)c1ccc2c(c1)c1cc(C(C)(C)C)cc3c4cc5c(cc4n2c13)c1cc(C(C)(C)C)cc2c3cc(C(C)(C)C)ccc3n5c12
42	CCCCc1ccc2c(c1)c1cc(C(C)(C)C)cc3c4cc5c(cc4n2c13)c1cc(C(C)(C)C)cc2c3cc(C(C)(C)C)ccc3n5c12
43	CC(C)(C)Cc1cc2c3cc(C(C)(C)F)ccc3n3c4cc5c6cc(C(C)(C)C)cc7c8cc(C(C)(C)C)ccc8n(c5cc4c(c1)c23)c67
44	C[C@@H](F)c1ccc2c(c1)c1cc(CC(C)(C)C)cc3c4cc5c(cc4n2c13)c1cc(C(C)(C)C)cc2c3cc(C(C)(C)C)ccc3n5c12
45	CC(C)(C)Cc1cc2cc(CI)n3c4cc5c6cc(C(C)(C)C)cc7c8cc(C(C)(C)C)ccc8n(c5cc4c(c1)c23)c67
46	C[C@@H](Cl)c1cc2c3cc(C(C)(C)C)ccc3n3c4cc5c6cc(C(C)(C)C)cc7c8cc(C(C)(C)C)ccc8n(c5cc4c(c1)c23)c67
47	CC(C)[C@@H](S)c1cc2c3cc(C(C)(C)C)ccc3n3c4cc5c6cc(C(C)(C)C)cc7c8cc(C(C)(C)C)ccc8n(c5cc4c(c1)c23)c67
48	CCC/C=C()/c1cc2c3cc(C(C)(C)C)ccc3n3c4cc5c6cc(C(C)(C)C)cc7c8cc(C(C)(C)C)ccc8n(c5cc4c(c1)c23)c67
49	CC(C)(C)Cc1cc2c3cc(C(C)(C)C)ccc3n3c4cc5c6cc(C(C)(C)C)cc7c8cc(C(C)(C)C)ccc8n(c5cc4c(c1)c23)c67
50	CPC(C)(C)c1cc2c3cc(C(C)(C)C)ccc3n3c4cc5c6cc(C(C)(C)C)cc7c8cc(C(C)(C)C)ccc8n(c5cc4c(c1)c23)c67
51	CC[C@@](C)(Br)c1cc2c3cc(C(C)(C)C)ccc3n3c4cc5c6cc(C(C)(C)C)cc7c8cc(C(C)(C)C)ccc8n(c5cc4c(c1)c23)c67
52	CC(C)CNCc1cc2c3cc(C(C)(C)C)ccc3n3c4cc5c6cc(C(C)(C)C)cc7c8cc(C(C)(C)C)ccc8n(c5cc4c(c1)c23)c67
53	CC(C)(C)c1ccc2c(c1)c1cc(C(C)(C)C)cc3c4cc5c(cc4n2c13)c1c(C(C)(C)C)ccc2c3cc(C(C)(C)C)ccc3n5c12
54	Bc1cccc2c1b1c3ccccc3n(c3ccccc3)c3cccc(c13)n2c1ccccc1

55	CC(C)(C)c1ccc2c(c1)c1cc(C(C)(C)C)cc3c4cc5c(cc4n2c13)c1cc(C(C)(C)C)cc2c3cc(C(C)(C)N)ccc3n5c12
56	CCCCc1ccc2c(c1)c1cc(CC(C)(C)C)cc3c4cc5c(cc4n2c13)c1cc(C(C)(C)C)cc2c3cc(C(C)(C)C)ccc3n5c12
57	CC(C)(C)c1ccc2c(c1)c1cc(C(C)(C)C)cc3c4cc5c(cc4n2c13)c1cc(C(C)(C)C)cc2c3cc(F)ccc3n5c12
58	CC(C)C/C=C/c1ccc2c(c1)c1cc(C(C)(C)C)cc3c4cc5c(cc4n2c13)c1cc(C(C)(C)C)cc2c3cc(C(C)(C)C)ccc3n5c12
59	Sc1cccc2c1b1c3ccccc3n(c3ccccc3)c3cccc(c13)n2c1ccccc1
60	CC(C)(C)Cc1cc2c3cc(CF)ccc3n3c4cc5c6cc(C(C)(C)C)cc7c8cc(C(C)(C)C)ccc8n(c5cc4c(c1)c23)c67
61	CCC(C)(C)c1cccc2c1c1cc(CC(C)C)cc3c4cc5c(cc4n2c13)c1cc(C(C)(C)C)cc2c3cc(C(C)(C)C)ccc3n5c12
62	CC(C)(C)c1ccc2c(c1)c1cc(C(C)(C)C)cc3c4cc5c(cc4n2c13)c1cc(C(C)(C)N)cc2c3cc(C(C)(C)C)ccc3n5c12
63	CCC[C@@H](C)c1ccc2c(c1)c1cc(C(C)(C)C)cc3c4cc5c(cc4n2c13)c1cc(C(C)(C)C)cc2c3cc(C(C)(C)C)ccc3n5c12
64	CC(C)(C)c1cc2cc(CBr)n3c4cc5c6cc(C(C)(C)C)cc7c8cc(C(C)(C)C)ccc8n(c5cc4c(c1)c23)c67
65	CC(C)(C)c1ccc2c(c1)c1cc(C(C)(C)C)cc3c4cc5c(cc4n2c13)c1cc(C(C)(C)F)cc2c3cc(C(C)(C)C)ccc3n5c12
66	CC(C)CPCc1ccc2c(c1)c1cc(C(C)(C)C)cc3c4cc5c(cc4n2c13)c1cc(C(C)(C)C)cc2c3cc(C(C)(C)C)ccc3n5c12
67	Cc1ccc2c(c1)c1cc(C(C)(C)C)cc3c4cc5c(cc4n2c13)c1cc(C(C)(C)C)cc2c3cc(C(C)(C)C)ccc3n5c12
68	CCCO[C@@H](C)c1cc2c3cc(C(C)(C)C)ccc3n3c4cc5c6cc(C(C)(C)C)cc7c8cc(C(C)(C)C)ccc8n(c5cc4c(c1)c23)c67
69	CC(C)CPCc1cc2c3cc(C(C)(C)C)ccc3n3c4cc5c6cc(C(C)(C)C)cc7c8cc(C(C)(C)C)ccc8n(c5cc4c(c1)c23)c67
70	Fc1cccc2c1b1c3ccccc3n(c3ccccc3)c3cccc(c13)n2c1ccccc1
71	CC[C@@H](F)c1ccc2c(c1)c1cc(CC(C)(C)C)cc3c4cc5c(cc4n2c13)c1cc(C(C)(C)C)cc2c3cc(C(C)(C)C)ccc3n5c12
72	CCCc1cc2c3cc(C[C@@H](C)CCC)ccc3n3c4cc5c6cc(C(C)(C)C)cc7c8cc(C(C)(C)C)ccc8n(c5cc4c(c1)c23)c67
73	CC(C)(C)c1ccc2c(c1)c1cccc3c4cc5c(cc4n2c13)c1cc(C(C)(C)C)cc2c3cc(C(C)(C)C)ccc3n5c12
74	CC(C)(C)c1ccc2c(c1)c1cc(CF)cc3c4cc5c(cc4n2c13)c1cc(C(C)(C)C)cc2c3cc(C(C)(C)C)ccc3n5c12
75	CC(C)(C)Cc1cc2c3cc(F)ccc3n3c4cc5c6cc(C(C)(C)C)cc7c8cc(C(C)(C)C)ccc8n(c5cc4c(c1)c23)c67
76	CCC/C=C()/c1ccc2c(c1)c1cc(C(C)(C)C)cc3c4cc5c(cc4n2c13)c1cc(C(C)(C)C)cc2c3cc(C(C)(C)C)ccc3n5c12
77	CC(C)(C)c1ccc2c(c1)c1cc(C(C)(C)C)cc3c4cc5c(cc4n2c13)c1cc(C(C)(C)CS)cc2c3cc(C(C)(C)C)ccc3n5c12
78	CC(C)C/N=C/c1ccc2c(c1)c1cc(C(C)(C)C)cc3c4c5c6cc(C(C)(C)C)cc7c8cc(C(C)(C)C)ccc8n(c5ccc4n2c13)c67
79	CCC/N=C/c1ccc2c(c1)c1cc(CC(C)(C)C)cc3c4cc5c(cc4n2c13)c1cc(C(C)(C)C)cc2c3cc(C(C)(C)C)ccc3n5c12
80	CC(C)(C)c1ccc2c(c1)c1cc(C(C)(C)C)cc3c4cc5c(cc4n2c13)c1cc(C(C)(C)S)cc2c3cc(C(C)(C)C)ccc3n5c12
81	Cc1cc2cc(CC(C)(C)C)cc3c4cc5c(cc4n1c23)c1cc(C(C)(C)C)cc2c3cc(C(C)(C)C)ccc3n5c12
82	CCC/N=C()/c1cc2c3cc(C(C)(C)C)ccc3n3c4cc5c6cc(C(C)(C)C)cc7c8cc(C(C)(C)C)ccc8n(c5cc4c(c1)c23)c67

83	CC(C)(C)c1ccc2c(c1)c1cc(C(C)(C)C)cc3c4c5c6cc(C(C)(C)C)cc7c8cc(C(C)(C)C)ccc8n(c5ccc4n2c13)c67
84	C[C@@H](Br)c1ccc2c(c1)c1cc(C(C)(C)C)cc3c4cc5c(cc4n2c13)c1cc(C(C)(C)C)cc2c3cc(C(C)(C)C)ccc3n5c12
85	CCC/N=C()/c1ccc2c(c1)c1cc(C(C)(C)C)cc3c4c5c6cc(C(C)(C)C)cc7c8cc(C(C)(C)C)ccc8n(c5ccc4n2c13)c67
86	CC(C)(C)Cc1cc2cc(Br)n3c4cc5c6cc(C(C)(C)C)cc7c8cc(C(C)(C)C)ccc8n(c5cc4c(c1)c23)c67
87	CC(C)[C@@H](Cl)c1cc2c3cc(C(C)(C)C)ccc3n3c4cc5c6cc(C(C)(C)C)cc7c8cc(C(C)(C)C)ccc8n(c5cc4c(c1)c23)c67
88	CC(C)c1cccc2c1c1cc(CC(C)(C)C)cc3c4cc5c(cc4n2c13)c1cc(C(C)(C)C)cc2c3cc(C(C)(C)C)ccc3n5c12
89	CC[C@@H](C)CCc1ccc2c(c1)c1cc(CC(C)C)cc3c4cc5c(cc4n2c13)c1cc(C(C)(C)C)cc2c3cc(C(C)(C)C)ccc3n5c12
90	CC(C)(C)c1ccc2c(c1)c1cc(C(C)(C)C)cc3c4cc5c(cc4n2c13)c1cc(C(C)(C)C)cc2c3cccc(C(C)(C)C)c3n5c12
91	CC(C)Cc1cc2c3cc(C(C)(C)C)ccc3n3c4cc5c6cc(C(C)(C)C)cc7c8cc(C(C)(C)C)ccc8n(c5cc4c(c1)c23)c67
92	CC(C)(C)c1ccc2c(c1)c1cc(C(C)(C)C)cc3c4cc5c(cc4n2c13)c1cc(C(C)(C)C=O)cc2c3cc(C(C)(C)C)ccc3n5c12
93	Cc1cc2c3cc(C(C)(C)CC(C)C)ccc3n3c4cc5c6cc(C(C)(C)C)cc7c8cc(C(C)(C)C)ccc8n(c5cc4c(c1)c23)c67
94	CC(C)(C)Cc1cc2cc(Cl)n3c4cc5c6cc(C(C)(C)C)cc7c8cc(C(C)(C)C)ccc8n(c5cc4c(c1)c23)c67
95	CCCN[C@@H](C)c1ccc2c(c1)c1cc(C(C)(C)C)cc3c4cc5c(cc4n2c13)c1cc(C(C)(C)C)cc2c3cc(C(C)(C)C)ccc3n5c12
96	CC(C)[C@@H](O)c1cc2c3cc(C(C)(C)C)ccc3n3c4cc5c6cc(C(C)(C)C)cc7c8cc(C(C)(C)C)ccc8n(c5cc4c(c1)c23)c67
97	CC[C@@](C)(I)c1cc2c3cc(C(C)(C)C)ccc3n3c4cc5c6cc(C(C)(C)C)cc7c8cc(C(C)(C)C)ccc8n(c5cc4c(c1)c23)c67
98	CCc1cc2c3cc(C(C)(C)C)ccc3n3c4cc5c6cc(C(C)(C)C)cc7c8cc(C(C)(C)C)ccc8n(c5cc4c(c1)c23)c67
99	CC(C)(C)CC(C)(C)c1cc2c3ccccc3n3c4cc5c6cc(C(C)(C)C)cc7c8cc(C(C)(C)C)ccc8n(c5cc4c(c1)c23)c67
100	CC(C)C/C=C/c1cc2c3cc(C(C)(C)C)ccc3n3c4cc5c6cc(C(C)(C)C)cc7c8cc(C(C)(C)C)ccc8n(c5cc4c(c1)c23)c67
101	CC(C)(C)Cc1cc2cc(F)n3c4cc5c6cc(C(C)(C)C)cc7c8cc(C(C)(C)C)ccc8n(c5cc4c(c1)c23)c67
102	CCC/C=C()/c1ccc2c(c1)c1cc(C(C)(C)C)cc3c4c5c6cc(C(C)(C)C)cc7c8cc(C(C)(C)C)ccc8n(c5ccc4n2c13)c67
103	CC(C)(C)Cc1cc2c3cc(C(C)(C)O)ccc3n3c4cc5c6cc(C(C)(C)C)cc7c8cc(C(C)(C)C)ccc8n(c5cc4c(c1)c23)c67
104	CC(C)(C)c1cc2cc(CF)n3c4cc5c6cc(C(C)(C)C)cc7c8cc(C(C)(C)C)ccc8n(c5cc4c(c1)c23)c67
105	CC(C)(C)c1ccc2c(c1)c1cc(C(C)(C)C)cc3c4cc5c(cc4n2c13)c1cc(C(C)(C)CN)cc2c3cc(C(C)(C)C)ccc3n5c12
106	CC(C)(C)Cc1cc2c3cc(Cl)ccc3n3c4cc5c6cc(C(C)(C)C)cc7c8cc(C(C)(C)C)ccc8n(c5cc4c(c1)c23)c67
107	CC[C@@](C)(P)c1cc2c3cc(C(C)(C)C)ccc3n3c4cc5c6cc(C(C)(C)C)cc7c8cc(C(C)(C)C)ccc8n(c5cc4c(c1)c23)c67
108	CC(C)(C)Pc1cc2c3cc(C(C)(C)C)ccc3n3c4cc5c6cc(C(C)(C)C)cc7c8cc(C(C)(C)C)ccc8n(c5cc4c(c1)c23)c67
109	Nc1cccc2c1b1c3ccccc3n(c3ccccc3)c3cccc(c13)n2c1ccccc1
110	CC(C)c1ccc2c(c1)c1cc(C(C)(C)C)cc3c4cc5c(cc4n2c13)c1cc(C(C)(C)C)cc2c3cc(C(C)(C)C)ccc3n5c12

111	C[C@@H](Br)c1ccc2c(c1)c1cc(CC(C)(C)C)cc3c4cc5c(cc4n2c13)c1cc(C(C)(C)C)cc2c3cc(C(C)(C)C)ccc3n5c12
112	CC(C)(C)c1cc2cc(Br)n3c4cc5c6cc(C(C)(C)C)cc7c8cc(C(C)(C)C)ccc8n(c5cc4c(c1)c23)c67
113	CC(C)(C)Cc1cc2c3ccccc3n3c4cc5c6cc(C(C)(C)C)cc7c8cc(C(C)(C)C)ccc8n(c5cc4c(c1)c23)c67
114	CC(C)(C)c1ccc2c(c1)c1cc(C(C)(C)C)cc3c4cc5c(cc4n2c13)c1cc(C(C)(C)Br)cc2c3cc(C(C)(C)C)ccc3n5c12
115	CC(C)(C)c1cc2cc(CCl)n3c4cc5c6cc(C(C)(C)C)cc7c8cc(C(C)(C)C)ccc8n(c5cc4c(c1)c23)c67
116	C[C@@H](CC(C)(C)C)c1ccc2c(c1)c1cccc3c4cc5c(cc4n2c13)c1cc(C(C)(C)C)cc2c3cc(C(C)(C)C)ccc3n5c12
117	CBC(C)(C)c1cc2c3cc(C(C)(C)C)ccc3n3c4cc5c6cc(C(C)(C)C)cc7c8cc(C(C)(C)C)ccc8n(c5cc4c(c1)c23)c67
118	CCCc1cc2c3cc(CC[C@@H](C)CCC)ccc3n3c4cc5c6cc(C(C)(C)C)cc7c8cc(C(C)(C)C)ccc8n(c5cc4c(c1)c23)c67
119	CC[C@@H](Br)c1ccc2c(c1)c1cc(CC(C)(C)C)cc3c4cc5c(cc4n2c13)c1cc(C(C)(C)C)cc2c3cc(C(C)(C)C)ccc3n5c12
120	CC(C)CNCc1ccc2c(c1)c1cc(C(C)(C)C)cc3c4cc5c(cc4n2c13)c1cc(C(C)(C)C)cc2c3cc(C(C)(C)C)ccc3n5c12
121	CC(C)(C)c1ccc2c(c1)c1cc(C(C)(C)C)cc3c4cc5c(cc4n2c13)c1cc([C@@]2(C)C=C2)cc2c3cc(C(C)(C)C)ccc3n5c12
122	CC(C)Pc1ccc2c(c1)c1cc(CC(C)(C)C)cc3c4cc5c(cc4n2c13)c1cc(C(C)(C)C)cc2c3cc(C(C)(C)C)ccc3n5c12
123	CC(C)(C)/C/1=C/[C]2[CH]N(c3c([CH][CH]1)cc(C(C)(C)C)cc3)c1c2cc2c(c1)c1cc(C(C)(C)C)cc3c4cc(C(C)(C)C)ccc4n2c13
124	CC(C)(C)c1ccc2c(c1)c1cc(C(C)(C)C)cc3c4cc5c(cc4n2c13)c1cc(C(C)(C)CI)cc2c3cc(C(C)(C)C)ccc3n5c12
125	CC[C@@H](P)c1ccc2c(c1)c1cc(CC(C)(C)C)cc3c4cc5c(cc4n2c13)c1cc(C(C)(C)C)cc2c3cc(C(C)(C)C)ccc3n5c12
126	CC(C)(C)c1ccc2c(c1)c1cc(C(C)(C)C)cc3c4cc5c(cc4n2c13)c1cc(C(C)(C)CP)cc2c3cc(C(C)(C)C)ccc3n5c12
127	CC(C)(C)c1ccc2c(c1)c1cc(C(C)(C)C)cc3c4cc5c(cc4n2c13)c1cc(C(C)(C)I)cc2c3cc(C(C)(C)C)ccc3n5c12
128	CC[C@@](C)(Cl)c1cc2c3cc(C(C)(C)C)ccc3n3c4cc5c6cc(C(C)(C)C)cc7c8cc(C(C)(C)C)ccc8n(c5cc4c(c1)c23)c67
129	CCCc1ccc2c(c1)c1cc(CC(C)(C)C)cc3c4cc5c(cc4n2c13)c1cc(C(C)(C)C)cc2c3cc(C(C)(C)C)ccc3n5c12
130	CC(C)(C)c1ccc2c(c1)c1cc(C(C)(C)C)cc3c4cc5c(cc4n2c13)c1cc(C(C)(C)CO)cc2c3cc(C(C)(C)C)ccc3n5c12
131	CCC(C)(C)c1ccc2c(c1)c1cc(CC(C)C)cc3c4cc5c(cc4n2c13)c1cc(C(C)(C)C)cc2c3cc(C(C)(C)C)ccc3n5c12
132	CC(C)(C)c1ccc2c(c1)c1cc(CI)cc3c4cc5c(cc4n2c13)c1cc(C(C)(C)C)cc2c3cc(C(C)(C)C)ccc3n5c12
133	C[C@@H](Cl)c1ccc2c(c1)c1cc(CC(C)(C)C)cc3c4cc5c(cc4n2c13)c1cc(C(C)(C)C)cc2c3cc(C(C)(C)C)ccc3n5c12
134	C[C@@H](CCC(C)(C)C)c1ccc2c(c1)c1cccc3c4cc5c(cc4n2c13)c1cc(C(C)(C)C)cc2c3cc(C(C)(C)C)ccc3n5c12
135	CC(C)[C@@H](Br)c1cc2c3cc(C(C)(C)C)ccc3n3c4cc5c6cc(C(C)(C)C)cc7c8cc(C(C)(C)C)ccc8n(c5cc4c(c1)c23)c67
136	CC(C)Cc1ccc2c(c1)c1cc(C(C)(C)C)cc3c4cc5c(cc4n2c13)c1cc(C(C)(C)C)cc2c3cc(C(C)(C)C)ccc3n5c12
137	B[C@@H](CC)c1ccc2c(c1)c1cc(CC(C)(C)C)cc3c4cc5c(cc4n2c13)c1cc(C(C)(C)C)cc2c3cc(C(C)(C)C)ccc3n5c12
138	CCCc1cc2c3cc(C(C)(C)C)ccc3n3c4cc5c6cc(C(C)(C)C)cc7c8cc(C(C)(C)C)ccc8n(c5cc4c(c1)c23)c67

139	CP(C)Cc1ccc2c(c1)c1cc(CC(C)(C)C)cc3c4cc5c(cc4n2c13)c1cc(C(C)(C)C)cc2c3cc(C(C)(C)C)ccc3n5c12
140	COC(C)(C)c1cc2c3cc(C(C)(C)C)ccc3n3c4cc5c6cc(C(C)(C)C)cc7c8cc(C(C)(C)C)ccc8n(c5cc4c(c1)c23)c67
141	CC[C@@](C)(S)c1cc2c3cc(C(C)(C)C)ccc3n3c4cc5c6cc(C(C)(C)C)cc7c8cc(C(C)(C)C)ccc8n(c5cc4c(c1)c23)c67
142	CC[C@@H](C)Cc1ccc2c(c1)c1cc(CC(C)C)cc3c4cc5c(cc4n2c13)c1cc(C(C)(C)C)cc2c3cc(C(C)(C)C)ccc3n5c12
143	CN[C@@H](C)c1ccc2c(c1)c1cc(CC(C)(C)C)cc3c4cc5c(cc4n2c13)c1cc(C(C)(C)C)cc2c3cc(C(C)(C)C)ccc3n5c12
144	Cc1cc2c3cc(C(C)(C)C)ccc3n3c4cc5c6cc(C(C)(C)C)cc7c8cc(C(C)(C)C)ccc8n(c5cc4c(c1)c23)c67
145	CC(C)CPCc1ccc2c(c1)c1cc(C(C)(C)C)cc3c4c5c6cc(C(C)(C)C)cc7c8cc(C(C)(C)C)ccc8n(c5ccc4n2c13)c67
146	CCCOCc1ccc2c(c1)c1cc(CC(C)(C)C)cc3c4cc5c(cc4n2c13)c1cc(C(C)(C)C)cc2c3cc(C(C)(C)C)ccc3n5c12
147	CCCc1ccc2c(c1)c1cc(C(C)(C)C)cc3c4cc5c(cc4n2c13)c1cc(C(C)(C)C)cc2c3cc(C(C)(C)C)ccc3n5c12
148	Cc1ccc2c(c1)c1cc(CC(C)(C)C)cc3c4cc5c(cc4n2c13)c1cc(C(C)(C)C)cc2c3cc(C(C)(C)C)ccc3n5c12
149	CC(C)(C)Cc1cc2c3cc(C(C)(C)I)ccc3n3c4cc5c6cc(C(C)(C)C)cc7c8cc(C(C)(C)C)ccc8n(c5cc4c(c1)c23)c67
150	CCCCC[C@@H](C)c1ccc2c(c1)c1cc(CCC)cc3c4cc5c(cc4n2c13)c1cc(C(C)(C)C)cc2c3cc(C(C)(C)C)ccc3n5c12
151	CC(C)(C)c1ccc2c(c1)c1cc(C(C)(C)C)cc3c4cc5c(cc4n2c13)c1cc(C(C)(C)CCl)cc2c3cc(C(C)(C)C)ccc3n5c12
152	CB(C)[C@@H](C)c1cc2c3cc(C(C)(C)C)ccc3n3c4cc5c6cc(C(C)(C)C)cc7c8cc(C(C)(C)C)ccc8n(c5cc4c(c1)c23)c67
153	CC[C@@H](C)c1ccc2c(c1)c1cc(C(C)(C)C)cc3c4cc5c(cc4n2c13)c1cc(C(C)(C)C)cc2c3cc(C(C)(C)C)ccc3n5c12
154	CC[C@@](C)(N)c1cc2c3cc(C(C)(C)C)ccc3n3c4cc5c6cc(C(C)(C)C)cc7c8cc(C(C)(C)C)ccc8n(c5cc4c(c1)c23)c67
155	CC[C@@H](S)c1ccc2c(c1)c1cc(CC(C)(C)C)cc3c4cc5c(cc4n2c13)c1cc(C(C)(C)C)cc2c3cc(C(C)(C)C)ccc3n5c12
156	CCCC[C@@H](C)c1cc2c3cc(C(C)(C)C)ccc3n3c4cc5c6cc(C(C)(C)C)cc7c8cc(C(C)(C)C)ccc8n(c5cc4c(c1)c23)c67
157	CC(C)(C)c1ccc2c(c1)c1cc(C(C)(C)C)cc3c4cc5c(cc4n2c13)c1cc(C(C)(C)C)cc2c3c(C(C)(C)C)cccc3n5c12
158	CC(C)Cc1ccc2c(c1)c1cc(CC(C)(C)C)cc3c4cc5c(cc4n2c13)c1cc(C(C)(C)C)cc2c3cc(C(C)(C)C)ccc3n5c12
159	CC[C@@](C)(F)c1cc2c3cc(C(C)(C)C)ccc3n3c4cc5c6cc(C(C)(C)C)cc7c8cc(C(C)(C)C)ccc8n(c5cc4c(c1)c23)c67
160	CC(C)(C)Cc1cc2c3cc(CBr)ccc3n3c4cc5c6cc(C(C)(C)C)cc7c8cc(C(C)(C)C)ccc8n(c5cc4c(c1)c23)c67
161	Cc1ccc(n2c3ccccc3b3c4cc(C)ccc4n4c5ccc(C)cc5b5c6cc(C)ccc6n(c6ccc(C)cc6)c6cc2c3c4c56)cc1
162	CC(C)(C)Cc1cc2c3cc(C(C)(C)Cl)ccc3n3c4cc5c6cc(C(C)(C)C)cc7c8cc(C(C)(C)C)ccc8n(c5cc4c(c1)c23)c67
163	CC(C)CCc1cc2c3cc(C(C)(C)C)ccc3n3c4cc5c6cc(C(C)(C)C)cc7c8cc(C(C)(C)C)ccc8n(c5cc4c(c1)c23)c67
164	CC(C)(C)CCCCc1ccc2c(c1)c1cccc3c4cc5c(cc4n2c13)c1cc(C(C)(C)C)cc2c3cc(C(C)(C)C)ccc3n5c12
165	CCCC[C@@H](C)c1ccc2c(c1)c1cc(CCC)cc3c4cc5c(cc4n2c13)c1cc(C(C)(C)C)cc2c3cc(C(C)(C)C)ccc3n5c12
166	Clc1cccc2c1b1c3ccccc3n(c3ccccc3)c3cccc(c13)n2c1ccccc1

167	CC(C)CCCc1ccc2c(c1)c1cc(C(C)(C)C)cc3c4cc5c(cc4n2c13)c1cc(C(C)(C)C)cc2c3cc(C(C)(C)C)ccc3n5c12
168	CC(C)(C)c1cc2cc(I)n3c4cc5c6cc(C(C)(C)C)cc7c8cc(C(C)(C)C)ccc8n(c5cc4c(c1)c23)c67
169	C=Cc1cc2cc(C(C)(C)C)cc3c4cc5c(cc4n1c23)c1cc(C(C)(C)C)cc2c3cc(C(C)(C)C)ccc3n5c12
170	C[C@@H](Cc1ccc2c(c1)c1cccc3c4cc5c(cc4n2c13)c1cc(C(C)(C)C)cc2c3cc(C(C)(C)C)ccc3n5c12)CC(C)(C)C
171	CC(C)c1ccc2c(c1)c1cc(C(C)C)cc3c4cc5c(cc4n2c13)c1cc(C(C)(C)C)cc2c3cc(C(C)(C)C)ccc3n5c12
172	CC(C)(C)c1ccc2c(c1)c1cc(C(C)(C)C)cc3c4cc5c(cc4n2c13)c1cc(C(C)(C)C)cc2c3cc(CF)ccc3n5c12
173	CC(C)(C)Cc1cc2c3cc(C(C)(C)N)ccc3n3c4cc5c6cc(C(C)(C)C)cc7c8cc(C(C)(C)C)ccc8n(c5cc4c(c1)c23)c67
174	Cc1ccc2c(c1C(C)C)c1cc(C(C)(C)C)cc3c4cc5c(cc4n2c13)c1cc(C(C)(C)C)cc2c3cc(C(C)(C)C)ccc3n5c12
175	C/C=C()/c1ccc2c(c1)c1cc(CC(C)(C)C)cc3c4cc5c(cc4n2c13)c1cc(C(C)(C)C)cc2c3cc(C(C)(C)C)ccc3n5c12
176	CC(C)(C)c1ccc2c(c1)c1cc(C(C)(C)C)cc3c4cc5c(cc4n2c13)c1cc(C(C)(C)C)cc2c3cc(C(C)(C)P)ccc3n5c12
177	CC(C)(C)c1ccc2c(c1)c1cc(C(C)(C)C)cc3c4cc5c(cc4n2c13)c1cc(C(C)(C)[CH][PH])cc2c3cc(C(C)(C)C)ccc3n5c12
178	CC(C)(C)Cc1cc2c3cc(C(C)(C)Br)ccc3n3c4cc5c6cc(C(C)(C)C)cc7c8cc(C(C)(C)C)ccc8n(c5cc4c(c1)c23)c67
179	CC(C)(C)c1ccc2c(c1)c1cc(CCl)cc3c4cc5c(cc4n2c13)c1cc(C(C)(C)C)cc2c3cc(C(C)(C)C)ccc3n5c12
180	Pc1cccc2c1b1c3ccccc3n(c3ccccc3)c3cccc(c13)n2c1ccccc1
181	CCO[C@@H](C)c1ccc2c(c1)c1cc(CC(C)(C)C)cc3c4cc5c(cc4n2c13)c1cc(C(C)(C)C)cc2c3cc(C(C)(C)C)ccc3n5c12
182	CC(C)(C)c1cc2cc(Cl)n3c4cc5c6cc(C(C)(C)C)cc7c8cc(C(C)(C)C)ccc8n(c5cc4c(c1)c23)c67
183	CC(C)CBCc1cc2c3cc(C(C)(C)C)ccc3n3c4cc5c6cc(C(C)(C)C)cc7c8cc(C(C)(C)C)ccc8n(c5cc4c(c1)c23)c67
184	Cc1ccc2c(c1)c1cc(C[C@@H](C)CC(C)(C)C)cc3c4cc5c(cc4n2c13)c1cc(C(C)(C)C)cc2c3cc(C(C)(C)C)ccc3n5c12
185	CC(C)(C)Bc1cc2c3cc(C(C)(C)C)ccc3n3c4cc5c6cc(C(C)(C)C)cc7c8cc(C(C)(C)C)ccc8n(c5cc4c(c1)c23)c67
186	CC(C)(C)Cc1cc2c3cc(I)ccc3n3c4cc5c6cc(C(C)(C)C)cc7c8cc(C(C)(C)C)ccc8n(c5cc4c(c1)c23)c67
187	CCCP[C@@H](C)c1ccc2c(c1)c1cc(C(C)(C)C)cc3c4c5c6cc(C(C)(C)C)cc7c8cc(C(C)(C)C)ccc8n(c5ccc4n2c13)c67
188	C[C@@H](F)c1ccc2c(c1)c1cc(C(C)(C)C)cc3c4cc5c(cc4n2c13)c1cc(C(C)(C)C)cc2c3cc(C(C)(C)C)ccc3n5c12
189	C[C@@H](Br)c1cc2c3cc(C(C)(C)C)ccc3n3c4cc5c6cc(C(C)(C)C)cc7c8cc(C(C)(C)C)ccc8n(c5cc4c(c1)c23)c67
190	CC(C)(C)c1ccc2c(c1)c1cc(C(C)(C)C)cc3c4cc5c(cc4n2c13)c1cc(C(C)(C)C)cc2c3cc(C(C)(C)Cl)ccc3n5c12
191	CC(C)(C)Cc1cc2ccn3c4cc5c6cc(C(C)(C)C)cc7c8cc(C(C)(C)C)ccc8n(c5cc4c(c1)c23)c67
192	C[C@@H](Cl)c1ccc2c(c1)c1cc(C(C)(C)C)cc3c4cc5c(cc4n2c13)c1cc(C(C)(C)C)cc2c3cc(C(C)(C)C)ccc3n5c12
193	CC(C)(C)c1ccc2c(c1)c1cc(C(C)(C)C)cc3c4cc5c(cc4n2c13)c1cc(C(C)(C)C)cc2c3cc(CBr)ccc3n5c12
194	CC(C)[C@@H](P)c1cc2c3cc(C(C)(C)C)ccc3n3c4cc5c6cc(C(C)(C)C)cc7c8cc(C(C)(C)C)ccc8n(c5cc4c(c1)c23)c67

195	CC(C)CCCc1ccc2c(c1)c1cc(C(C)(C)C)cc3c4c5c6cc(C(C)(C)C)cc7c8cc(C(C)(C)C)ccc8n(c5ccc4n2c13)c67
196	CC(C)(C)c1ccc2c(c1)c1cc(C(C)(C)C)cc3c4cc5c(cc4n2c13)c1cc(C(C)(C)C=N)cc2c3cc(C(C)(C)C)ccc3n5c12
197	CC(C)(C)c1ccc2c(c1)c1cc(C(C)(C)C)cc3c4cc5c(cc4n2c13)c1cc(C(C)(C)C)cc2c3cc(CCl)ccc3n5c12
198	CC(C)c1cc2c3cc(C(C)(C)C)ccc3n3c4cc5c6cc(C(C)(C)C)cc7c8cc(C(C)(C)C)ccc8n(c5cc4c(c1)c23)c67
199	CCB(C)Cc1ccc2c(c1)c1cc(CC(C)(C)C)cc3c4cc5c(cc4n2c13)c1cc(C(C)(C)C)cc2c3cc(C(C)(C)C)ccc3n5c12
200	C[C@@H](CCc1ccc2c(c1)c1cccc3c4cc5c(cc4n2c13)c1cc(C(C)(C)C)cc2c3cc(C(C)(C)C)ccc3n5c12)CC(C)(C)C
201	CC(C)(C)c1ccc2c(c1)c1cc(C(C)(C)C)cc3c4cc5c(cc4n2c13)c1cc(C(C)(C)C)cc2c3cc(Br)ccc3n5c12
202	B[C@@H](c1cc2c3cc(C(C)(C)C)ccc3n3c4cc5c6cc(C(C)(C)C)cc7c8cc(C(C)(C)C)ccc8n(c5cc4c(c1)c23)c67)C(C)C
203	CB[C@@H](C)c1ccc2c(c1)c1cc(CC(C)(C)C)cc3c4cc5c(cc4n2c13)c1cc(C(C)(C)C)cc2c3cc(C(C)(C)C)ccc3n5c12
204	CCc1ccc2c(c1)c1cc(CCCC(C)(C)C)cc3c4cc5c(cc4n2c13)c1cc(C(C)(C)C)cc2c3cc(C(C)(C)C)ccc3n5c12
205	CC(C)COCc1ccc2c(c1)c1cc(C(C)(C)C)cc3c4cc5c(cc4n2c13)c1cc(C(C)(C)C)cc2c3cc(C(C)(C)C)ccc3n5c12
206	CC[C@@H](I)c1ccc2c(c1)c1cc(CC(C)(C)C)cc3c4cc5c(cc4n2c13)c1cc(C(C)(C)C)cc2c3cc(C(C)(C)C)ccc3n5c12
207	BC(C)(C)c1cc2c3cc(C(C)(C)C)ccc3n3c4cc5c6cc(C(C)(C)C)cc7c8cc(C(C)(C)C)ccc8n(c5cc4c(c1)c23)c67
208	Cc1ccc(n2c3ccc(C)cc3b3c4cc(C)ccc4n4c5c(C)cccc5b5c6cc(C)ccc6n(c6ccc(C)cc6)c6cc2c3c4c56)cc1
209	CC(C)(C)c1ccc2c(c1)c1cc(C(C)(C)C)cc3c4cc5c(cc4n2c13)c1cc(C(C)(C)C)cc2c3cc(C(C)(C)F)ccc3n5c12
210	CC[C@@H](C)c1ccc2c(c1)c1cc(CC(C)(C)C)cc3c4cc5c(cc4n2c13)c1cc(C(C)(C)C)cc2c3cc(C(C)(C)C)ccc3n5c12
211	CC(C)(C)c1cc2cc(CI)n3c4cc5c6cc(C(C)(C)C)cc7c8cc(C(C)(C)C)ccc8n(c5cc4c(c1)c23)c67
212	CC(C)C/C=C/c1ccc2c(c1)c1cc(C(C)(C)C)cc3c4c5c6cc(C(C)(C)C)cc7c8cc(C(C)(C)C)ccc8n(c5ccc4n2c13)c67
213	CCCB[C@@H](C)c1cc2c3cc(C(C)(C)C)ccc3n3c4cc5c6cc(C(C)(C)C)cc7c8cc(C(C)(C)C)ccc8n(c5cc4c(c1)c23)c67
214	Cc1cc2c3cc([C@@H](C)CCC(C)C)ccc3n3c4cc5c6cc(C(C)(C)C)cc7c8cc(C(C)(C)C)ccc8n(c5cc4c(c1)c23)c67
215	CC(C)(C)Cc1cc2c3cc(C(C)(C)S)ccc3n3c4cc5c6cc(C(C)(C)C)cc7c8cc(C(C)(C)C)ccc8n(c5cc4c(c1)c23)c67
216	CC(C)(C)Cc1cc2cc(CBr)n3c4cc5c6cc(C(C)(C)C)cc7c8cc(C(C)(C)C)ccc8n(c5cc4c(c1)c23)c67
217	CCC(C)(C)c1cc2c3cc(C(C)(C)C)ccc3n3c4cc5c6cc(C(C)(C)C)cc7c8cc(C(C)(C)C)ccc8n(c5cc4c(c1)c23)c67
218	CC(C)(C)c1ccc2c(c1)c1cc(C(C)(C)C)cc3c4cc5c(cc4n2c13)c1cc(C(C)(C)C)cc2c3cc(C(C)(C)O)ccc3n5c12
219	CCC[C@@H](C)c1ccc2c(c1)c1cc(CC(C)C)cc3c4cc5c(cc4n2c13)c1cc(C(C)(C)C)cc2c3cc(C(C)(C)C)ccc3n5c12
220	CC(=O)c1cc2c3cc(C(C)(C)C)ccc3n3c4cc5c6cc(C(C)(C)C)cc7c8cc(C(C)(C)C)ccc8n(c5cc4c(c1)c23)c67
221	CCCP[C@@H](C)c1ccc2c(c1)c1cc(C(C)(C)C)cc3c4cc5c(cc4n2c13)c1cc(C(C)(C)C)cc2c3cc(C(C)(C)C)ccc3n5c12
222	CC(C)(C)Cc1cc2c3cc(C(C)(C)P)ccc3n3c4cc5c6cc(C(C)(C)C)cc7c8cc(C(C)(C)C)ccc8n(c5cc4c(c1)c23)c67

223	CC[C@@H](C)c1cc2c3cc(C(C)(C)C)ccc3n3c4cc5c6cc(C(C)(C)C)cc7c8cc(C(C)(C)C)ccc8n(c5cc4c(c1)c23)c67
224	CC(C)(C)c1ccc2c(c1)c1cc(C(C)(C)C)cc3c4cc5c(cc4n2c13)c1cc(C(C)(C)C)cc2c3cc(C(C)(C)C)ccc3n5c12
225	CC(C)(C)c1ccc2c(c1)c1cc(CBr)cc3c4cc5c(cc4n2c13)c1cc(C(C)(C)C)cc2c3cc(C(C)(C)C)ccc3n5c12
226	Cc1cc(C(C)C)c2c(c1)c1cc(C(C)(C)C)cc3c4cc5c(cc4n2c13)c1cc(C(C)(C)C)cc2c3cc(C(C)(C)C)ccc3n5c12
227	CC(=C(C)c1cc2c3cc(C(C)(C)C)ccc3n3c4cc5c6cc(C(C)(C)C)cc7c8cc(C(C)(C)C)ccc8n(c5cc4c(c1)c23)c67)C
228	CCCO[C@@H](C)c1ccc2c(c1)c1cc(C(C)(C)C)cc3c4c5c6cc(C(C)(C)C)cc7c8cc(C(C)(C)C)ccc8n(c5ccc4n2c13)c67
229	C=CC(C)(C)c1cc2c3cc(C(C)(C)C)ccc3n3c4cc5c6cc(C(C)(C)C)cc7c8cc(C(C)(C)C)ccc8n(c5cc4c(c1)c23)c67
230	CC(C)(C)CC(C)(C)c1ccc2c(c1)c1cccc3c4cc5c(cc4n2c13)c1cc(C(C)(C)C)cc2c3cc(C(C)(C)C)ccc3n5c12
231	CCCc1cc2c3cc(C(C)(C)CCC)ccc3n3c4cc5c6cc(C(C)(C)C)cc7c8cc(C(C)(C)C)ccc8n(c5cc4c(c1)c23)c67
232	CC(C)(C)Cc1cc2c3cc(CI)ccc3n3c4cc5c6cc(C(C)(C)C)cc7c8cc(C(C)(C)C)ccc8n(c5cc4c(c1)c23)c67
233	BCC(C)(C)c1cc2c3cc(C(C)(C)C)ccc3n3c4cc5c6cc(C(C)(C)C)cc7c8cc(C(C)(C)C)ccc8n(c5cc4c(c1)c23)c67
234	CC(C)(C)c1ccc2c(c1)c1cc(C(C)(C)C)cc3c4cc5c(cc4n2c13)c1cc(C(C)(C)C)cc2c3cc(CI)ccc3n5c12
235	CC(C)(C)c1ccc2c(c1)c1cc(C(C)(C)C)cc3c4cc5c(cc4n2c13)c1cc(C(C)(C)C)cc2c3cc(C(C)(C)S)ccc3n5c12
236	CC(C)(C)c1ccc2c(c1)c1cc(C(C)(C)C)cc3c4cc5c(cc4n2c13)c1cc(C(C)(C)C)cc2c3cc(I)ccc3n5c12
237	CC(C)CCCc1cc2c3cc(C(C)(C)C)ccc3n3c4cc5c6cc(C(C)(C)C)cc7c8cc(C(C)(C)C)ccc8n(c5cc4c(c1)c23)c67
238	CC[C@@H](N)c1ccc2c(c1)c1cc(CC(C)(C)C)cc3c4cc5c(cc4n2c13)c1cc(C(C)(C)C)cc2c3cc(C(C)(C)C)ccc3n5c12
239	Cc1cc2c3cc(C(C)(C)C)ccc3n3c4cc5c6cc(C(C)(C)C)cc7c8cc(C(C)(C)C)ccc8n(c5cc4c(c1C(C)C)c23)c67
240	CCC/N=C()/c1ccc2c(c1)c1cc(C(C)(C)C)cc3c4cc5c(cc4n2c13)c1cc(C(C)(C)C)cc2c3cc(C(C)(C)C)ccc3n5c12
241	CC(C)(C)c1ccc2c(c1)c1cc(C(C)(C)C)cc3c4cc5c(cc4n2c13)c1cc(C(C)(C)O)cc2c3cc(C(C)(C)C)ccc3n5c12
242	CC(C)(C)c1ccc2c(c1)c1cc(C(C)(C)C)cc3c4ccc5c6cc(C(C)(C)C)cc7c8cc(C(C)(C)C)ccc8n(c67)c5c4n2c13
243	CCCC[C@@H](C)c1ccc2c(c1)c1cc(CC(C)C)cc3c4cc5c(cc4n2c13)c1cc(C(C)(C)C)cc2c3cc(C(C)(C)C)ccc3n5c12
244	CP[C@@H](C)c1ccc2c(c1)c1cc(CC(C)(C)C)cc3c4cc5c(cc4n2c13)c1cc(C(C)(C)C)cc2c3cc(C(C)(C)C)ccc3n5c12
245	Cc1cccc2c1b1c3ccccc3n(c3ccccc3)c3cccc(c13)n2c1ccccc1
246	CCCP[C@@H](C)c1cc2c3cc(C(C)(C)C)ccc3n3c4cc5c6cc(C(C)(C)C)cc7c8cc(C(C)(C)C)ccc8n(c5cc4c(c1)c23)c67
247	CCCN[C@@H](C)c1cc2c3cc(C(C)(C)C)ccc3n3c4cc5c6cc(C(C)(C)C)cc7c8cc(C(C)(C)C)ccc8n(c5cc4c(c1)c23)c67
248	CC(C)(C)/C/1=C/[C]2[CH]N3c4cc5c6cc(C(C)(C)C)cc7c8cc(C(C)(C)C)c(cc8n(c5cc24)c67)[C]([CH]1)c1cc(C(C)(C)C)ccc31
249	Cc1c(CC(C)C)ccc2c1c1cc(C(C)(C)C)cc3c4cc5c(cc4n2c13)c1cc(C(C)(C)C)cc2c3cc(C(C)(C)C)ccc3n5c12
250	BC(C)(C)c1ccc2c(c1)c1cc(C(C)(C)C)cc3c4cc5c(cc4n2c13)c1cc(C(C)(C)C)cc2c3cc(C(C)(C)C)ccc3n5c12

251	CC(C)(C)c1ccc2c(c1)c1cc(C(C)(C)C)cc3c4cc5c(cc4n2c13)c1cc(C(C)(C)P)cc2c3cc(C(C)(C)C)ccc3n5c12
252	C[C@@H](I)c1ccc2c(c1)c1cc(C(C)(C)C)cc3c4cc5c(cc4n2c13)c1cc(C(C)(C)C)cc2c3cc(C(C)(C)C)ccc3n5c12
253	C[C@@H](c1cc2c3cc(C(C)(C)C)ccc3n3c4cc5c6cc(C(C)(C)C)cc7c8cc(C(C)(C)C)ccc8n(c5cc4c(c1)c23)c67)P(C)C
254	CC(C)C/N=C/c1cc2c3cc(C(C)(C)C)ccc3n3c4cc5c6cc(C(C)(C)C)cc7c8cc(C(C)(C)C)ccc8n(c5cc4c(c1)c23)c67
255	CC(C)CCc1ccc2c(c1)c1cc(C(C)(C)C)cc3c4cc5c(cc4n2c13)c1cc(C(C)(C)C)cc2c3cc(C(C)(C)C)ccc3n5c12
256	CC(C)COCc1ccc2c(c1)c1cc(C(C)(C)C)cc3c4c5c6cc(C(C)(C)C)cc7c8cc(C(C)(C)C)ccc8n(c5ccc4n2c13)c67
257	CC(C)(C)c1ccc2c(c1)c1cc(C(C)(C)C)cc3c4cc5c(cc4n2c13)c1cc(C2(C)CC2)cc2c3cc(C(C)(C)C)ccc3n5c12
258	CC(C)(C)c1cc2cc(F)n3c4cc5c6cc(C(C)(C)C)cc7c8cc(C(C)(C)C)ccc8n(c5cc4c(c1)c23)c67
259	C[C@@H](I)c1ccc2c(c1)c1cc(CC(C)(C)C)cc3c4cc5c(cc4n2c13)c1cc(C(C)(C)C)cc2c3cc(C(C)(C)C)ccc3n5c12
260	CC(C)c1ccc2c(c1)c1cc(CC(C)(C)C)cc3c4cc5c(cc4n2c13)c1cc(C(C)(C)C)cc2c3cc(C(C)(C)C)ccc3n5c12
261	Cc1cc2c3cc(CC[C@@H](C)CC(C)C)ccc3n3c4cc5c6cc(C(C)(C)C)cc7c8cc(C(C)(C)C)ccc8n(c5cc4c(c1)c23)c67
262	CC(C)CNCc1ccc2c(c1)c1cc(C(C)(C)C)cc3c4c5c6cc(C(C)(C)C)cc7c8cc(C(C)(C)C)ccc8n(c5ccc4n2c13)c67

TABLE C.2: Smile strings of 262 structures generated using STONED Algorithm

Bibliography

(1) Hong, G.; Gan, X.; Leonhardt, C.; Zhang, Z.; Seibert, J.; Busch, J. M.; Bräse, S. "A Brief History of OLEDs—Emitter Development and Industry Milestones", *Advanced Materials* **2021**, *33*, 2005630.

(2) Bernanose, A.; Comte, M.; Vouaux, P. "Sur un nouveau mode d'émission lumineuse chez certains composés organiques", *Journal de Chimie Physique* **1953**, *50*, Publisher: EDP Sciences, 64–68.

(3) Tang, C. W.; VanSlyke, S. A. "Organic electroluminescent diodes", *Applied physics letters* **1987**, *51*, 913–915.

(4) Wakimoto, R. M. T.; Nagayama, K.; Okuda, Y.; Nakada, H.; Tohma, T. In *SPIE, San Diego*, 1996.

(5) Baldo, M. A.; O'Brien, D. F.; You, Y.; Shoustikov, A.; Sibley, S.; Thompson, M. E.; Forrest, S. R. "Highly efficient phosphorescent emission from organic electroluminescent devices", *Nature* **1998**, *395*, Publisher: Nature Publishing Group, 151–154.

(6) "Recent Progress of OLED", *Advanced Display* **2007**.

(7) Dawson, R. M. A.; Kane, M. G. "24.1: Invited Paper: Pursuit of Active Matrix Organic Light Emitting Diode Displays", *SID Symposium Digest of Technical Papers* **2001**, *32*, 372–375.

(8) New startup to commercialize Kyushu's TADF emitters, OLED Info, 2015.

(9) Rauenbühler, N. CYNORA introduces fluorescent blue emitter that gives OLED devices a substantial efficiency boost, `https://cynora.com/cynora-introduces-fluorescent-blue-emitter-that-gives-oled-devices-a-substantial-efficiency-boost/`, 2020.

(10) Visser, P. "OLED technology: also the ultimate lighting solution?", *Optik & Photonik* **2008**, *3*, 27–29.

(11) Miller, M. E. In *Color in Electronic Display Systems: Advantages of Multi-primary Displays*, Miller, M. E., Ed.; Springer International Publishing: 2019, pp 107–133.

(12) Honda, K., *Photochemical Processes in Organized Molecular Systems*; Elsevier: 2012.

(13) Baryshnikov, G.; Minaev, B.; Ågren, H. "Theory and calculation of the phosphorescence phenomenon", *Chemical reviews* **2017**, *117*, 6500–6537.

(14) Endo, A.; Ogasawara, M.; Takahashi, A.; Yokoyama, D.; Kato, Y.; Adachi, C. "Thermally activated delayed fluorescence from Sn4+–porphyrin complexes and their application to organic light emitting diodes—A novel mechanism for electroluminescence", *Advanced Materials* **2009**, *21*, 4802–4806.

(15) Endo, A.; Sato, K.; Yoshimura, K.; Kai, T.; Kawada, A.; Miyazaki, H.; Adachi, C. "Efficient up-conversion of triplet excitons into a singlet state and its application for organic light emitting diodes", *Applied Physics Letters* **2011**, *98*, 42.

(16) Delorme, R.; Perrin, F. "Durées de fluorescence des sels d'uranyle solides et de leurs solutions", *Journal de Physique et le Radium* **1929**, *10*, 177–186.

(17) Lewis, G. N.; Lipkin, D.; Magel, T. T. "Reversible photochemical processes in rigid media. A study of the phosphorescent state", *Journal of the American Chemical Society* **1941**, *63*, 3005–3018.

(18) Parker, C.; Hatchard, C. "Triplet-singlet emission in fluid solutions. Phosphorescence of eosin", *Transactions of the Faraday Society* **1961**, *57*, 1894–1904.

(19) Nakanotani, H.; Higuchi, T.; Furukawa, T.; Masui, K.; Morimoto, K.; Numata, M.; Tanaka, H.; Sagara, Y.; Yasuda, T.; Adachi, C. "High-efficiency organic light-emitting diodes with fluorescent emitters", *Nature communications* **2014**, *5*, 1–7.

(20) Dias, F. B.; Penfold, T. J.; Monkman, A. P. "Photophysics of thermally activated delayed fluorescence molecules", *Methods and applications in fluorescence* **2017**, *5*, 012001.

(21) Wong, M. Y.; Zysman-Colman, E. "Purely Organic Thermally Activated Delayed Fluorescence Materials for Organic Light-Emitting Diodes", *Advanced Materials* **2017**, *29*, 1605444.

(22) Ward, J. S.; Nobuyasu, R. S.; Batsanov, A. S.; Data, P.; Monkman, A. P.; Dias, F. B.; Bryce, M. R. "The interplay of thermally activated delayed fluorescence (TADF) and room temperature organic phosphorescence in sterically-constrained donor–acceptor charge-transfer molecules", *Chem. Commun.* **2016**, *52*, 2612–2615.

(23) Penfold, T.; Dias, F.; Monkman, A. P. "The theory of thermally activated delayed fluorescence for organic light emitting diodes", *Chemical communications* **2018**, *54*, 3926–3935.

(24) Uoyama, H.; Goushi, K.; Shizu, K.; Nomura, H.; Adachi, C. "Highly efficient organic light-emitting diodes from delayed fluorescence", *Nature* **2012**, *492*, 234–238.

(25) Etherington, M. K.; Gibson, J.; Higginbotham, H. F.; Penfold, T. J.; Monkman, A. P. "Revealing the spin–vibronic coupling mechanism of thermally activated delayed fluorescence", *Nature communications* **2016**, *7*, 1–7.

(26) Tao, Y.; Yuan, K.; Chen, T.; Xu, P.; Li, H.; Chen, R.; Zheng, C.; Zhang, L.; Huang, W. "Thermally activated delayed fluorescence materials towards the breakthrough of organoelectronics", *Advanced Materials (Deerfield Beach, Fla.)* **2014**, *26*, 7931–7958.

(27) Zysman-Colman, E. "Molecular designs offer fast exciton conversion", *Nature Photonics* **2020**, *14*, 593–594.

(28) Noda, H.; Nakanotani, H.; Adachi, C. "Excited state engineering for efficient reverse intersystem crossing", *Science Advances* **2018**, *4*, eaao6910.

(29) Hosokai, T.; Matsuzaki, H.; Nakanotani, H.; Tokumaru, K.; Tsutsui, T.; Furube, A.; Nasu, K.; Nomura, H.; Yahiro, M.; Adachi, C. "Evidence and mechanism of efficient thermally activated delayed fluorescence promoted by delocalized excited states", *Science Advances* **2017**, *3*, e1603282.

(30) Dias, F. B. "Kinetics of thermal-assisted delayed fluorescence in blue organic emitters with large singlet–triplet energy gap", *Philosophical Transactions of the Royal Society A: Mathematical, Physical and Engineering Sciences* **2015**, *373*, 20140447.

(31) Dias, F. B.; Bourdakos, K. N.; Jankus, V.; Moss, K. C.; Kamtekar, K. T.; Bhalla, V.; Santos, J.; Bryce, M. R.; Monkman, A. P. "Triplet harvesting with 100% efficiency by way of thermally activated delayed fluorescence in charge transfer OLED emitters", *Advanced Materials* **2013**, *25*, 3707–3714.

(32) Dias, F. B.; Santos, J.; Graves, D. R.; Data, P.; Nobuyasu, R. S.; Fox, M. A.; Batsanov, A. S.; Palmeira, T.; Berberan-Santos, M. N.; Bryce, M. R., et al. "The role of local triplet excited states and D-A relative orientation in thermally activated delayed fluorescence: photophysics and devices", *Advanced Science* **2016**, *3*, 1600080.

(33) Hatakeyama, T.; Shiren, K.; Nakajima, K.; Nomura, S.; Nakatsuka, S.; Kinoshita, K.; Ni, J.; Ono, Y.; Ikuta, T. "Ultrapure blue thermally activated delayed fluorescence molecules: efficient HOMO–LUMO separation by the multiple resonance effect", *Advanced Materials* **2016**, *28*, 2777–2781.

(34) Kondo, Y.; Yoshiura, K.; Kitera, S.; Nishi, H.; Oda, S.; Gotoh, H.; Sasada, Y.; Yanai, M.; Hatakeyama, T. “Narrowband deep-blue organic light-emitting diode featuring an organoboron-based emitter”, *Nature Photonics* **2019**, *13*, 678–682.

(35) Sperger, T.; Sanhueza, I. A.; Schoenebeck, F. “Computation and Experiment: A Powerful Combination to Understand and Predict Reactivities”, *Accounts of Chemical Research* **2016**, *49*, 1311–1319.

(36) Guido, C. A.; Cortona, P.; Mennucci, B.; Adamo, C. “On the Metric of Charge Transfer Molecular Excitations: A Simple Chemical Descriptor”, *Journal of Chemical Theory and Computation* **2013**, *9*, 3118–3126.

(37) Neese, F. “Software update: The The ORCA program system—Version 5.0”, *WIREs Computational Molecular Science* **2022**, *12*, e1606.

(38) TURBOMOLE V7.5.1 2021, a development of University of Karlsruhe and Forschungszentrum Karlsruhe GmbH, 1989-2007, TURBOMOLE GmbH, since 2007; available from \ \tt https://www.turbomole.org.

(39) Szabo, A.; Ostlund, N., *Modern Quantum Chemistry: Introduction to Advanced Electronic Structure Theory*; Dover Books on Chemistry; Dover Publications: 1996.

(40) Roothaan, C. C. J. “New Developments in Molecular Orbital Theory”, *Rev. Mod. Phys.* **1951**, *23*, 69–89.

(41) In *A Chemist’s Guide to Density Functional Theory*; John Wiley & Sons, Ltd: 2001, pp 265–293.

(42) Burke, K.; Perdew, J. P.; Ernzerhof, M. “Why the generalized gradient approximation works and how to go beyond it”, *International Journal of Quantum Chemistry* **1997**, *61*, 287–293.

(43) Lee, C.; Yang, W.; Parr, R. G. “Development of the Colle-Salvetti correlation-energy formula into a functional of the electron density”, *Phys. Rev. B* **1988**, *37*, 785–789.

(44) Perdew, J. P.; Burke, K.; Ernzerhof, M. “Generalized Gradient Approximation Made Simple”, *Phys. Rev. Lett.* **1996**, *77*, 3865–3868.

(45) Becke, A. D. “Becke’s three parameter hybrid method using the LYP correlation functional”, *J. Chem. Phys* **1993**, *98*, 5648–5652.

(46) Adamo, C.; Barone, V. “Toward reliable density functional methods without adjustable parameters: The PBE0 model”, *The Journal of Chemical Physics* **1999**, *110*, 6158–6170.

(47) Santra, G.; Calinsky, R.; Martin, J. M. L. "Benefits of Range-Separated Hybrid and Double-Hybrid Functionals for a Large and Diverse Data Set of Reaction Energies and Barrier Heights", *The Journal of Physical Chemistry A* **2022**, *126*, 5492–5505.

(48) Vydrov, O. A.; Scuseria, G. E. "Assessment of a long-range corrected hybrid functional", *The Journal of Chemical Physics* **2006**, *125*, 234109.

(49) Yanai, T.; Tew, D.; Handy, N. "A new hybrid exchange-correlation functional using the Coulomb-Attenuating Method (CAM-B3LYP)", *Chemical Physics Letters* **2004**, *393*, 51–57.

(50) Sun, H.; Zhong, C.; Brédas, J.-L. "Reliable Prediction with Tuned Range-Separated Functionals of the Singlet–Triplet Gap in Organic Emitters for Thermally Activated Delayed Fluorescence", *Journal of Chemical Theory and Computation* **2015**, *11*, 3851–3858.

(51) Livshits, E.; Baer, R. "A well-tempered density functional theory of electrons in molecules", *Physical Chemistry Chemical Physics* **2007**, *9*, 2932.

(52) Penfold, T. J. "On predicting the excited-state properties of thermally activated delayed fluorescence emitters", *The Journal of Physical Chemistry C* **2015**, *119*, 13535–13544.

(53) Runge, E.; Gross, E. K. U. "Density-Functional Theory for Time-Dependent Systems", *Phys. Rev. Lett.* **1984**, *52*, 997–1000.

(54) Dreuw, A.; Head-Gordon, M. "Single-Reference ab Initio Methods for the Calculation of Excited States of Large Molecules", *Chemical Reviews* **2005**, *105*, 4009–4037.

(55) Marques, M.; Gross, E. "Time-Dependent Density Functional Theory", *Annu. Rev. Phys. Chem.* **2004**, *55*, DOI: `10.1146/annurev.physchem.55.091602.094449`.

(56) Weigend, F.; Ahlrichs, R. "Balanced basis sets of split valence, triple zeta valence and quadruple zeta valence quality for H to Rn: Design and assessment of accuracy", *Phys. Chem. Chem. Phys.* **2005**, *7*, 3297–3305.

(57) Liu, Y.; Li, C.; Ren, Z.; Yan, S.; Bryce, M. R. "All-organic thermally activated delayed fluorescence materials for organic light-emitting diodes", *Nature Reviews Materials* **2018**, *3*, 1–20.

(58) Wong, M. Y.; Zysman-Colman, E. "Purely organic thermally activated delayed fluorescence materials for organic light-emitting diodes", *Advanced Materials* **2017**, *29*, 1605444.

(59) Zieger, S. E.; Steinegger, A.; Klimant, I.; Borisov, S. M. “TADF-Emitting Zn (II)-Benzoporphyrin: An indicator for simultaneous sensing of oxygen and temperature”, *ACS sensors* **2020**, *5*, 1020–1027.

(60) Ni, F.; Li, N.; Zhan, L.; Yang, C. “Organic thermally activated delayed fluorescence materials for time-resolved luminescence imaging and sensing”, *Advanced Optical Materials* **2020**, *8*, 1902187.

(61) Bryden, M. A.; Zysman-Colman, E. “Organic thermally activated delayed fluorescence (TADF) compounds used in photocatalysis”, *Chemical Society Reviews* **2021**, *50*, 7587–7680.

(62) Wang, Y.; Gao, X.-W.; Li, J.; Chao, D. “Merging an organic TADF photosensitizer and a simple terpyridine–Fe (iii) complex for photocatalytic CO 2 reduction”, *Chemical Communications* **2020**, *56*, 12170–12173.

(63) Crucho, C. I.; Avó, J.; Nobuyasu, R.; Pinto, S. N.; Fernandes, F.; Lima, J. C.; Berberan-Santos, M. N.; Dias, F. B. “Silica nanoparticles with thermally activated delayed fluorescence for live cell imaging”, *Materials Science and Engineering: C* **2020**, *109*, 110528.

(64) Li, T.; Yang, D.; Zhai, L.; Wang, S.; Zhao, B.; Fu, N.; Wang, L.; Tao, Y.; Huang, W. “Thermally Activated Delayed Fluorescence Organic Dots (TADF Odots) for Time-Resolved and Confocal Fluorescence Imaging in Living Cells and In Vivo”, *Advanced Science* **2017**, *4*, 1600166.

(65) Qiu, H.; Wang, W.; Cheng, H.; Lu, Y.; Li, M.; Chen, H.; Fang, X.; Jiang, C.; Zheng, Y. “Triple Optically Modulated and Enzymatically Responsive Organic Afterglow Materials for Dynamic Anti-counterfeiting”, *Materials Chemistry Frontiers* **2022**.

(66) Yang, J.-C.; Ho, Y.-C.; Chan, Y.-H. “Ultrabright fluorescent polymer dots with thermochromic characteristics for full-color security marking”, *ACS applied materials & interfaces* **2019**, *11*, 29341–29349.

(67) Naveen, K. R.; Yang, H. I.; Kwon, J. H. “Double boron-embedded multiresonant thermally activated delayed fluorescent materials for organic light-emitting diodes”, *Communications Chemistry* **2022**, *5*, 1–14.

(68) Madayanad Suresh, S.; Hall, D.; Beljonne, D.; Olivier, Y.; Zysman-Colman, E. “Multiresonant thermally activated delayed fluorescence emitters based on heteroatom-doped nanographenes: recent advances and prospects for organic light-emitting diodes”, *Advanced Functional Materials* **2020**, *30*, 1908677.

(69) Dias, F. B.; Penfold, T. J.; Monkman, A. P. "Photophysics of thermally activated delayed fluorescence molecules", *Methods and applications in fluorescence* **2017**, *5*, 012001.

(70) Eng, J.; Penfold, T. J. "Open questions on the photophysics of thermally activated delayed fluorescence", *Communications Chemistry* **2021**, *4*, 1–4.

(71) Eng, J.; Penfold, T. J. "Understanding and designing thermally activated delayed fluorescence emitters: beyond the energy gap approximation", *The Chemical Record* **2020**, *20*, 831–856.

(72) Etherington, M. K.; Gibson, J.; Higginbotham, H. F.; Penfold, T. J.; Monkman, A. P. "Revealing the spin–vibronic coupling mechanism of thermally activated delayed fluorescence", *Nature communications* **2016**, *7*, 1–7.

(73) Gibson, J.; Monkman, A. P.; Penfold, T. J. "The importance of vibronic coupling for efficient reverse intersystem crossing in thermally activated delayed fluorescence molecules", *ChemPhysChem* **2016**, *17*, 2956.

(74) Evans, E. W.; Olivier, Y.; Puttisong, Y.; Myers, W. K.; Hele, T. J.; Menke, S. M.; Thomas, T. H.; Credgington, D.; Beljonne, D.; Friend, R. H., et al. "Vibrationally assisted intersystem crossing in benchmark thermally activated delayed fluorescence molecules", *The Journal of Physical Chemistry Letters* **2018**, *9*, 4053–4058.

(75) Drummond, B. H.; Aizawa, N.; Zhang, Y.; Myers, W. K.; Xiong, Y.; Cooper, M. W.; Barlow, S.; Gu, Q.; Weiss, L. R.; Gillett, A. J., et al. "Electron spin resonance resolves intermediate triplet states in delayed fluorescence", *Nature Communications* **2021**, *12*, 1–11.

(76) Ward, J. S.; Nobuyasu, R. S.; Batsanov, A. S.; Data, P.; Monkman, A. P.; Dias, F. B.; Bryce, M. R. "The interplay of thermally activated delayed fluorescence (TADF) and room temperature organic phosphorescence in sterically-constrained donor–acceptor charge-transfer molecules", *Chemical Communications* **2016**, *52*, 2612–2615.

(77) Nobuyasu, R. S.; Ward, J. S.; Gibson, J.; Laidlaw, B. A.; Ren, Z.; Data, P.; Batsanov, A. S.; Penfold, T. J.; Bryce, M. R.; Dias, F. B. "The influence of molecular geometry on the efficiency of thermally activated delayed fluorescence", *Journal of Materials Chemistry C* **2019**, *7*, 6672–6684.

(78) Serevičius, T.; Bučiūnas, T.; Bucevičius, J.; Dodonova, J.; Tumkevičius, S.; Kazlauskas, K.; Juršėnas, S. "Room temperature phosphorescence vs. thermally activated delayed fluorescence in carbazole–pyrimidine cored compounds", *Journal of Materials Chemistry C* **2018**, *6*, 11128–11136.

(79) Serevičius, T.; Skaisgiris, R.; Fiodorova, I.; Kreiza, G.; Banevičius, D.; Kazlauskas, K.; Tumkevičius, S.; Juršėnas, S. “Single-exponential solid-state delayed fluorescence decay in TADF compounds with minimized conformational disorder”, *Journal of Materials Chemistry C* **2021**, *9*, 836–841.

(80) Northey, T.; Stacey, J.; Penfold, T. J. “The role of solid state solvation on the charge transfer state of a thermally activated delayed fluorescence emitter”, *Journal of Materials Chemistry C* **2017**, *5*, 11001–11009.

(81) Ahmad, S. A.; Eng, J.; Penfold, T. J. “Rapid predictions of the colour purity of luminescent organic molecules”, *Journal of Materials Chemistry C* **2022**, *10*, 4785–4794.

(82) Li, X.; Shi, Y.-Z.; Wang, K.; Zhang, M.; Zheng, C.-J.; Sun, D.-M.; Dai, G.-L.; Fan, X.-C.; Wang, D.-Q.; Liu, W., et al. “Thermally activated delayed fluorescence carbonyl derivatives for organic light-emitting diodes with extremely narrow full width at half-maximum”, *ACS applied materials & interfaces* **2019**, *11*, 13472–13480.

(83) Cho, Y. J.; Jeon, S. K.; Lee, S.-S.; Yu, E.; Lee, J. Y. “Donor interlocked molecular design for fluorescence-like narrow emission in deep blue thermally activated delayed fluorescent emitters”, *Chemistry of Materials* **2016**, *28*, 5400–5405.

(84) Franca, L. G.; Danos, A.; Monkman, A. “Spiro donor–acceptor TADF emitters: naked TADF free from inhomogeneity caused by donor acceptor bridge bond disorder. Fast rISC and invariant photophysics in solid state hosts”, *Journal of Materials Chemistry C* **2022**, *10*, 1313–1325.

(85) Lee, I.; Lee, J. Y. “Molecular design of deep blue fluorescent emitters with 20% external quantum efficiency and narrow emission spectrum”, *Organic Electronics* **2016**, *29*, 160–164.

(86) Pander, P.; Swist, A.; Motyka, R.; Soloducho, J.; Dias, F. B.; Data, P. “Thermally activated delayed fluorescence with a narrow emission spectrum and organic room temperature phosphorescence by controlling spin–orbit coupling and phosphorescence lifetime of metal-free organic molecules”, *Journal of Materials Chemistry C* **2018**, *6*, 5434–5443.

(87) Sem, S.; Jenatsch, S.; Stavrou, K.; Danos, A.; Monkman, A. P.; Ruhstaller, B. “Determining non-radiative decay rates in TADF compounds using coupled transient and steady state optical data”, *Journal of Materials Chemistry C* **2022**, *10*, 4878–4885.

(88) Liu, J.; Li, Z.; Hu, T.; Gao, T.; Yi, Y.; Wang, P.; Wang, Y. "Modulating Non-Radiative Deactivation via Acceptor Reconstruction to Expand High-Efficient Red Thermally Activated Delayed Fluorescent Emitters", *Advanced Optical Materials* **2022**, *10*, 2102558.

(89) Penfold, T. J.; Eng, J. "Tailoring Donor-Acceptor Emitters to Minimise Localisation Induced Quenching of Thermally Activated Delayed Fluorescence", *ChemPhotoChem* **2022**.

(90) Wang, K.; Liu, W.; Zheng, C.-J.; Shi, Y.-Z.; Liang, K.; Zhang, M.; Ou, X.-M.; Zhang, X.-H. "A comparative study of carbazole-based thermally activated delayed fluorescence emitters with different steric hindrance", *Journal of Materials Chemistry C* **2017**, *5*, 4797–4803.

(91) Tu, C.; Liang, W. "NB-Type Electronic Asymmetric Compounds as Potential Blue-Color TADF Emitters: Steric Hindrance, Substitution Effect, and Electronic Characteristics", *ACS omega* **2017**, *2*, 3098–3109.

(92) Sommer, G. A.; Mataranga-Popa, L. N.; Czerwieniec, R.; Hofbeck, T.; Homeier, H. H.; Müller, T. J.; Yersin, H. "Design of conformationally distorted donor–acceptor dyads showing efficient thermally activated delayed fluorescence", *The Journal of Physical Chemistry Letters* **2018**, *9*, 3692–3697.

(93) Wang, K.; Zheng, C.-J.; Liu, W.; Liang, K.; Shi, Y.-Z.; Tao, S.-L.; Lee, C.-S.; Ou, X.-M.; Zhang, X.-H. "Avoiding energy loss on TADF emitters: controlling the dual conformations of D–A structure molecules based on the pseudoplanar segments", *Advanced Materials* **2017**, *29*, 1701476.

(94) Etherington, M. K.; Franchello, F.; Gibson, J.; Northey, T.; Santos, J.; Ward, J. S.; Higginbotham, H. F.; Data, P.; Kurowska, A.; Dos Santos, P. L., et al. "Regio-and conformational isomerization critical to design of efficient thermally-activated delayed fluorescence emitters", *Nature communications* **2017**, *8*, 1–11.

(95) Rajamalli, P.; Senthilkumar, N.; Huang, P.-Y.; Ren-Wu, C.-C.; Lin, H.-W.; Cheng, C.-H. "New molecular design concurrently providing superior pure blue, thermally activated delayed fluorescence and optical out-coupling efficiencies", *Journal of the American Chemical Society* **2017**, *139*, 10948–10951.

(96) Chen, X.-K.; Tsuchiya, Y.; Ishikawa, Y.; Zhong, C.; Adachi, C.; Brédas, J.-L. "A new design strategy for efficient thermally activated delayed fluorescence organic emitters: from twisted to planar structures", *Advanced Materials* **2017**, *29*, 1702767.

(97) He, X.; Lou, J.; Li, B.; Wang, H.; Peng, X.; Li, G.; Liu, L.; Huang, Y.; Zheng, N.; Xing, L., et al. "An ultraviolet fluorophore with narrowed emission via coplanar molecular strategy", *Angewandte Chemie International Edition* **2022**, *61*, e202209425.

(98) Shimoda, Y.; Miyata, K.; Saigo, M.; Tsuchiya, Y.; Adachi, C.; Onda, K. "Intramolecular-rotation driven triplet-to-singlet upconversion and fluctuation induced fluorescence activation in linearly connected donor–acceptor molecules", *The Journal of Chemical Physics* **2020**, *153*.

(99) Hempe, M.; Kukhta, N. A.; Danos, A.; Batsanov, A. S.; Monkman, A. P.; Bryce, M. R. "Intramolecular Hydrogen Bonding in Thermally Activated Delayed Fluorescence Emitters: Is There Evidence Beyond Reasonable Doubt?", *The Journal of Physical Chemistry Letters* **2022**, *13*, 8221–8227.

(100) Bergmann, K.; Hojo, R.; Hudson, Z. M. "Uncovering the Mechanism of Thermally Activated Delayed Fluorescence in Coplanar Emitters Using Potential Energy Surface Analysis", *The Journal of Physical Chemistry Letters* **2023**, *14*, 310–317.

(101) Spuling, E.; Sharma, N.; Samuel, I. D.; Zysman-Colman, E.; Bräse, S. "(Deep) blue through-space conjugated TADF emitters based on [2.2] paracyclophanes", *Chemical Communications* **2018**, *54*, 9278–9281.

(102) Lee, Y. H.; Park, S.; Oh, J.; Shin, J. W.; Jung, J.; Yoo, S.; Lee, M. H. "Rigidity-induced delayed fluorescence by ortho donor-appended triarylboron compounds: record-high efficiency in pure blue fluorescent organic light-emitting diodes", *ACS applied materials & interfaces* **2017**, *9*, 24035–24042.

(103) Conboy, G.; Spencer, H. J.; Angioni, E.; Kanibolotsky, A. L.; Findlay, N. J.; Coles, S. J.; Wilson, C.; Pitak, M. B.; Risko, C.; Coropceanu, V.; Brédas, J.-L.; Skabara, P. J. "To bend or not to bend – are heteroatom interactions within conjugated molecules effective in dictating conformation and planarity?", *Mater. Horiz.* **2016**, *3*, 333–339.

(104) Kharandiuk, T.; Hussien, E. J.; Cameron, J.; Petrina, R.; Findlay, N. J.; Naumov, R.; Klooster, W. T.; Coles, S. J.; Ai, Q.; Goodlett, S.; Risko, C.; Skabara, P. J. "Noncovalent Close Contacts in Fluorinated Thiophene–Phenylene–Thiophene Conjugated Units: Understanding the Nature and Dominance of O···H versus S···F and O···F Interactions with Respect to the Control of Polymer Conformation", *Chemistry of Materials* **2019**, *31*, 7070–7079.

(105) Wu, T.-L.; Huang, M.-J.; Lin, C.-C.; Huang, P.-Y.; Chou, T.-Y.; Chen-Cheng, R.-W.; Lin, H.-W.; Liu, R.-S.; Cheng, C.-H. "Diboron compound-based organic light-emitting diodes with high efficiency and reduced efficiency roll-off", *Nature Photonics* **2018**, *12*, 235–240.

(106) Hirai, H.; Nakajima, K.; Nakatsuka, S.; Shiren, K.; Ni, J.; Nomura, S.; Ikuta, T.; Hatakeyama, T. "One-step borylation of 1, 3-diaryloxybenzenes towards efficient materials for organic light-emitting diodes", *Angewandte Chemie* **2015**, *127*, 13785–13789.

(107) Suzuki, K.; Kubo, S.; Shizu, K.; Fukushima, T.; Wakamiya, A.; Murata, Y.; Adachi, C.; Kaji, H. "Triarylboron-Based Fluorescent Organic Light-Emitting Diodes with External Quantum Efficiencies Exceeding 20%", *Angewandte Chemie* **2015**, *127*, 15446–15450.

(108) Ji, L.; Griesbeck, S.; Marder, T. B. "Recent developments in and perspectives on three-coordinate boron materials: a bright future", *Chemical Science* **2017**, *8*, 846–863.

(109) Neese, F. "The ORCA program system", *Wiley Interdisciplinary Reviews: Computational Molecular Science* **2012**, *2*, 73–78.

(110) Hirata, S.; Head-Gordon, M. "Time-dependent density functional theory within the Tamm–Dancoff approximation", *Chemical Physics Letters* **1999**, *314*, 291–299.

(111) Iikura, H.; Tsuneda, T.; Yanai, T.; Hirao, K. "A long-range correction scheme for generalized-gradient-approximation exchange functionals", *The Journal of Chemical Physics* **2001**, *115*, 3540–3544.

(112) Eng, J.; Laidlaw, B. A.; Penfold, T. J. "On the geometry dependence of tuned-range separated hybrid functionals", *Journal of computational chemistry* **2019**, *40*, 2191–2199.

(113) Weigend, F. "Accurate Coulomb-fitting basis sets for H to Rn", *Phys. Chem. Chem. Phys.* **2006**, *8*, 1057–1065.

(114) Klamt, A.; Schüürmann, G. "COSMO: a new approach to dielectric screening in solvents with explicit expressions for the screening energy and its gradient", *Journal of the Chemical Society, Perkin Transactions 2* **1993**, 799–805.

(115) Perdew, J. P.; Burke, K.; Ernzerhof, M. "Generalized Gradient Approximation Made Simple", *Physical Review Letters* **1996**, *77*, 3865–3868.

(116) Adamo, C.; Barone, V. "Toward reliable density functional methods without adjustable parameters: The PBE0 model", *The Journal of Chemical Physics* **1999**, *110*, 6158–6170.

(117) Weigend, F.; Ahlrichs, R. "Balanced basis sets of split valence, triple zeta valence and quadruple zeta valence quality for H to Rn: Design and assessment of accuracy", *Physical Chemistry Chemical Physics* **2005**, *7*, 3297–3305.

(118) Yang, L.; Horton, J. T.; Payne, M. C.; Penfold, T. J.; Cole, D. J. "Modeling Molecular Emitters in Organic Light-Emitting Diodes with the Quantum Mechanical Bespoke Force Field", *Journal of Chemical Theory and Computation* **2021**, *17*, 5021–5033.

(119) Cozzolino, A. F.; Vargas-Baca, I.; Mansour, S.; Mahmoudkhani, A. H. "The nature of the supramolecular association of 1, 2, 5-chalcogenadiazoles", *Journal of the American Chemical Society* **2005**, *127*, 3184–3190.

(120) Chaudret, R.; De Courcy, B.; Contreras-Garcia, J.; Gloaguen, E.; Zehnacker-Rentien, A.; Mons, M.; Piquemal, J.-P. "Unraveling non-covalent interactions within flexible biomolecules: from electron density topology to gas phase spectroscopy", *Physical Chemistry Chemical Physics* **2014**, *16*, 9876–9891.

(121) Contreras-Garcıa, J.; Johnson, E. R.; Keinan, S.; Chaudret, R.; Piquemal, J.-P.; Beratan, D. N.; Yang, W. "NCIPLOT: a program for plotting noncovalent interaction regions", *Journal of chemical theory and computation* **2011**, *7*, 625–632.

(122) Johnson, E. R.; Keinan, S.; Mori-Sánchez, P.; Contreras-Garcıa, J.; Cohen, A. J.; Yang, W. "Revealing noncovalent interactions", *Journal of the American Chemical Society* **2010**, *132*, 6498–6506.

(123) Penfold, T. J.; Gindensperger, E.; Daniel, C.; Marian, C. M. "Spin-vibronic mechanism for intersystem crossing", *Chemical reviews* **2018**, *118*, 6975–7025.

(124) Anne, O. "Rigid and planar -conjugated molecules leading to long-lived intramolecular charge-transfer states exhibiting thermally activated delayed fluorescence", *Necronomicon* **2019**, *7*, 6672–6684.

(125) Miranda-Salinas, H.; Rodriguez-Serrano, A.; Kaminski, J. M.; Dinkelbach, F.; Hiromichi, N.; Kusakabe, Y.; Kaji, H.; Marian, C. M.; Monkman, A. P. "Conformational, Host, and Vibrational Effects Giving Rise to Dynamic TADF Behavior in the Through-Space Charge Transfer, Triptycene Bridged Acridine-Triazine Donor Acceptor TADF Molecule TpAT-tFFO", *The Journal of Physical Chemistry C* **2023**, *127*, 8607–8617.

(126) Park, S.-I.; Xiong, Y.; Kim, R.-H.; Elvikis, P.; Meitl, M.; Kim, D.-H.; Wu, J.; Yoon, J.; Yu, C.-J.; Liu, Z., et al. "Printed assemblies of inorganic light-emitting diodes for deformable and semitransparent displays", *science* **2009**, *325*, 977–981.

(127) Yang, Y.; Zheng, Y.; Cao, W.; Titov, A.; Hyvonen, J.; Manders, J. R.; Xue, J.; Holloway, P. H.; Qian, L. "High-efficiency light-emitting devices based on quantum dots with tailored nanostructures", *Nature Photonics* **2015**, *9*, 259–266.

(128) Holmes, M. J.; Zhu, T.; Massabuau, F. C.-P.; Jarman, J.; Oliver, R. A.; Arakawa, Y. "Pure single-photon emission from an InGaN/GaN quantum dot", *APL Materials* **2021**, *9*, 061106.

(129) Yersin, H., *Highly efficient OLEDs with phosphorescent materials*; Wiley Online Library: 2008.

(130) Yersin, H., *Highly efficient OLEDs: Materials based on thermally activated delayed fluorescence*; John Wiley & Sons: 2019.

(131) Takada, N.; Tsutsui, T.; Saito, S. "Control of emission characteristics in organic thin-film electroluminescent diodes using an optical-microcavity structure", *Applied physics letters* **1993**, *63*, 2032–2034.

(132) Spindler, J. P.; Hatwar, T. K.; Miller, M. E.; Arnold, A. D.; Murdoch, M. J.; Kane, P. J.; Ludwicki, J. E.; Alessi, P. J.; Van Slyke, S. A. "System considerations for RGBW OLED displays", *Journal of the Society for Information Display* **2006**, *14*, 37–48.

(133) Kondo, Y.; Yoshiura, K.; Kitera, S.; Nishi, H.; Oda, S.; Gotoh, H.; Sasada, Y.; Yanai, M.; Hatakeyama, T. "Narrowband deep-blue organic light-emitting diode featuring an organoboron-based emitter", *Nature Photonics* **2019**, *13*, 678–682.

(134) Hatakeyama, T.; Shiren, K.; Nakajima, K.; Nomura, S.; Nakatsuka, S.; Kinoshita, K.; Ni, J.; Ono, Y.; Ikuta, T. "Ultrapure blue thermally activated delayed fluorescence molecules: efficient HOMO–LUMO separation by the multiple resonance effect", *Advanced Materials* **2016**, *28*, 2777–2781.

(135) Oda, S.; Kawakami, B.; Kawasumi, R.; Okita, R.; Hatakeyama, T. "Multiple resonance effect-induced sky-blue thermally activated delayed fluorescence with a narrow emission band", *Organic letters* **2019**, *21*, 9311–9314.

(136) Sun, D.; Suresh, S. M.; Hall, D.; Zhang, M.; Si, C.; Cordes, D. B.; Slawin, A. M.; Olivier, Y.; Zhang, X.; Zysman-Colman, E. "The design of an extended multiple resonance TADF emitter based on a polycyclic amine/carbonyl system", *Materials Chemistry Frontiers* **2020**, *4*, 2018–2022.

(137) Zhang, Y.; Zhang, D.; Wei, J.; Liu, Z.; Lu, Y.; Duan, L. "Multi-resonance induced thermally activated delayed fluorophores for narrowband green OLEDs", *Angewandte Chemie* **2019**, *131*, 17068–17073.

(138) Liang, X.; Yan, Z.-P.; Han, H.-B.; Wu, Z.-G.; Zheng, Y.-X.; Meng, H.; Zuo, J.-L.; Huang, W. “Peripheral amplification of multi-resonance induced thermally activated delayed fluorescence for highly efficient OLEDs”, *Angewandte Chemie International Edition* **2018**, *57*, 11316–11320.

(139) Hall, D.; Suresh, S. M.; dos Santos, P. L.; Duda, E.; Bagnich, S.; Pershin, A.; Rajamalli, P.; Cordes, D. B.; Slawin, A. M.; Beljonne, D., et al. “Improving Processability and Efficiency of Resonant TADF Emitters: A Design Strategy”, *Advanced Optical Materials* **2020**, *8*, 1901627.

(140) Matsui, K.; Oda, S.; Yoshiura, K.; Nakajima, K.; Yasuda, N.; Hatakeyama, T. “One-shot multiple borylation toward BN-doped nanographenes”, *Journal of the American Chemical Society* **2018**, *140*, 1195–1198.

(141) Oda, S.; Kumano, W.; Hama, T.; Kawasumi, R.; Yoshiura, K.; Hatakeyama, T. “Carbazole-Based DABNA Analogues as Highly Efficient Thermally Activated Delayed Fluorescence Materials for Narrowband Organic Light-Emitting Diodes”, *Angewandte Chemie* **2021**, *133*, 2918–2922.

(142) Hua, T.; Zhan, L.; Li, N.; Huang, Z.; Cao, X.; Xiao, Z.; Gong, S.; Zhou, C.; Zhong, C.; Yang, C. “Heavy-Atom Effect Promotes Multi-Resonance Thermally Activated Delayed Fluorescence”, **2021**.

(143) Tanaka, H.; Oda, S.; Ricci, G.; Gotoh, H.; Tabata, K.; Kawasumi, R.; Beljonne, D.; Olivier, Y.; Hatakeyama, T. “Hypsochromic Shift of Multiple-Resonance-Induced Thermally Activated Delayed Fluorescence by Oxygen Atom Incorporation”, *Angewandte Chemie International Edition* **2021**.

(144) Pershin, A.; Hall, D.; Lemaur, V.; Sancho-Garcia, J.-C.; Muccioli, L.; Zysman-Colman, E.; Beljonne, D.; Olivier, Y. “Highly emissive excitons with reduced exchange energy in thermally activated delayed fluorescent molecules”, *Nature communications* **2019**, *10*, 1–5.

(145) Northey, T.; Penfold, T. “The intersystem crossing mechanism of an ultrapure blue organoboron emitter”, *Organic Electronics* **2018**, *59*, 45–48.

(146) Kim, I.; Cho, K. H.; Jeon, S. O.; Son, W.-J.; Kim, D.; Rhee, Y. M.; Jang, I.; Choi, H.; Kim, D. S. “Three-state-involving vibronic resonance is a key to enhancing reverse intersystem crossing dynamics of organoboron-based ultrapure blue emitters”, **2020**.

(147) Chan, C.-Y.; Tanaka, M.; Lee, Y.-T.; Wong, Y.-W.; Nakanotani, H.; Hatakeyama, T.; Adachi, C. “Stable pure-blue hyperfluorescence organic light-emitting diodes with high-efficiency and narrow emission”, *Nature Photonics* **2021**, *15*, 203–207.

(148) Cao, Y.; Eng, J.; Penfold, T. “Excited State Intramolecular Proton Transfer Dynamics for Triplet Harvesting in Organic Molecules”, *The Journal of Physical Chemistry A* **2019**, *123*, 2640–2649.

(149) Cai, W.; Ren, K.; Zhao, A.; Wu, X.; He, R.; Li, M.; Shen, W. “The study of intramolecular decay and intermolecular energy transfer for phosphorescent organic light-emitting devices”, *Physical Chemistry Chemical Physics* **2021**, *23*, 7495–7503.

(150) Ferrer, F. J. A.; Santoro, F. “Comparison of vertical and adiabatic harmonic approaches for the calculation of the vibrational structure of electronic spectra”, *Physical Chemistry Chemical Physics* **2012**, *14*, 13549–13563.

(151) Baiardi, A.; Bloino, J.; Barone, V. “General time dependent approach to vibronic spectroscopy including Franck–Condon, Herzberg–Teller, and Duschinsky effects”, *Journal of chemical theory and computation* **2013**, *9*, 4097–4115.

(152) De Souza, B.; Neese, F.; Izsák, R. “On the theoretical prediction of fluorescence rates from first principles using the path integral approach”, *The Journal of chemical physics* **2018**, *148*, 034104.

(153) Gómez-Bombarelli, R.; Aguilera-Iparraguirre, J.; Hirzel, T. D.; Duvenaud, D.; Maclaurin, D.; Blood-Forsythe, M. A.; Chae, H. S.; Einzinger, M.; Ha, D.-G.; Wu, T., et al. “Design of efficient molecular organic light-emitting diodes by a high-throughput virtual screening and experimental approach”, *Nature materials* **2016**, *15*, 1120–1127.

(154) Zhao, K.; Omar, Ö. H.; Nematiaram, T.; Padula, D.; Troisi, A. “Novel thermally activated delayed fluorescence materials by high-throughput virtual screening: going beyond donor–acceptor design”, *Journal of Materials Chemistry C* **2021**, *9*, 3324–3333.

(155) Ansari, R.; Shao, W.; Yoon, S.-J.; Kim, J.; Kieffer, J. “Charge Transfer as the Key Parameter Affecting the Color Purity of Thermally Activated Delayed Fluorescence Emitters”, *ACS Applied Materials & Interfaces* **2021**.

(156) De Silva, P.; Kim, C. A.; Zhu, T.; Van Voorhis, T. “Extracting design principles for efficient thermally activated delayed fluorescence (TADF) from a simple four-state model”, *Chemistry of materials* **2019**, *31*, 6995–7006.

(157) Wislicenus, W. “Ueber die vereinigung verschiedener ester durch natrium”, *Berichte der deutschen chemischen Gesellschaft* **1887**, *20*, 589–595.

(158) Maciejczyk, M. R.; Williams, J. G.; Robertson, N.; Pietraszkiewicz, M. “Monothiatruxene: a new versatile core for functional materials”, *RSC advances* **2017**, *7*, 49532–49535.

(159) Goubard, F.; Dumur, F. “Truxene: a promising scaffold for future materials”, *RSC advances* **2015**, *5*, 3521–3551.

(160) Zhang, G.; Rominger, F.; Mastalerz, M. “Fused π-Extended Truxenes via a Threefold Borylation as the Key Step”, *Chemistry–A European Journal* **2016**, *22*, 3084–3093.

(161) Dos Santos, P. L.; Ward, J. S.; Congrave, D. G.; Batsanov, A. S.; Eng, J.; Stacey, J. E.; Penfold, T. J.; Monkman, A. P.; Bryce, M. R. “Triazatruxene: A Rigid Central Donor Unit for a D–A3 Thermally Activated Delayed Fluorescence Material Exhibiting Sub-Microsecond Reverse Intersystem Crossing and Unity Quantum Yield via Multiple Singlet–Triplet State Pairs”, *Advanced Science* **2018**, *5*, 1700989.

(162) Eng, J.; Hagon, J.; Penfold, T. J. “D–A 3 TADF emitters: the role of the density of states for achieving faster triplet harvesting rates”, *Journal of Materials Chemistry C* **2019**, *7*, 12942–12952.

(163) Górski, K.; Noworyta, K.; Mech-Piskorz, J. “Influence of the heteroatom introduction on the physicochemical properties of 5-heterotruxenes containing nitrogen, oxygen and sulfur atom”, *RSC Advances* **2020**, *10*, 42363–42377.

(164) Górski, K.; Mech-Piskorz, J.; Noworyta, K.; Leśniewska, B.; Pietraszkiewicz, M. “Efficient synthesis of 5-oxatruxene and the unusual influence of oxygen heteroatom on its physico-chemical properties”, *New Journal of Chemistry* **2018**, *42*, 5844–5852.

(165) Becke, A. D. “Becke’s three parameter hybrid method using the LYP correlation functional”, *J. Chem. Phys* **1993**, *98*, 5648–5652.

(166) Lee, C.; Yang, W.; Parr, R. “Density-functional exchange-energy approximation with correct asymptotic behaviour”, *Phys. Rev. B* **1988**, *37*, 785–789.

(167) Vosko, S. H.; Wilk, L.; Nusair, M. “Accurate spin-dependent electron liquid correlation energies for local spin density calculations: a critical analysis”, *Canadian Journal of physics* **1980**, *58*, 1200–1211.

(168) Stephens, P. J.; Devlin, F. J.; Chabalowski, C. F.; Frisch, M. J. "Ab initio calculation of vibrational absorption and circular dichroism spectra using density functional force fields", *The Journal of physical chemistry* **1994**, *98*, 11623–11627.

(169) TURBOMOLE V7.5.1 2021, a development of University of Karlsruhe and Forschungszentrum Karlsruhe GmbH, 1989-2007, TURBOMOLE GmbH, since 2007; available from `https://www.turbomole.org`.

(170) Peach, M. J. G.; Benfield, P.; Helgaker, T.; Tozer, D. J. "Excitation energies in density functional theory: An evaluation and a diagnostic test", *The Journal of Chemical Physics* **2008**, *128*, 044118.

(171) Smith, L. D.; Dijkstra, A. G. "Quantum dissipative systems beyond the standard harmonic model: Features of linear absorption and dynamics", *The Journal of chemical physics* **2019**, *151*, 164109.

(172) Ahn, T.-S.; Müller, A. M.; Al-Kaysi, R. O.; Spano, F. C.; Norton, J. E.; Beljonne, D.; Brédas, J.-L.; Bardeen, C. J. "Experimental and theoretical study of temperature dependent exciton delocalization and relaxation in anthracene thin films", *The Journal of chemical physics* **2008**, *128*, 054505.

(173) Parker, C.; Hatchard, C. "Delayed fluorescence of pyrene in ethanol", *Transactions of the Faraday Society* **1963**, *59*, 284–295.

(174) HoáLee, I.; YeobáLee, J., et al. "High efficiency blue fluorescent organic light-emitting diodes using a conventional blue fluorescent emitter", *Journal of Materials Chemistry C* **2015**, *3*, 8834–8838.

(175) Gibson, J.; Penfold, T. "Nonadiabatic coupling reduces the activation energy in thermally activated delayed fluorescence", *Physical Chemistry Chemical Physics* **2017**, *19*, 8428–8434.

(176) Penfold, T.; Dias, F.; Monkman, A. P. "The theory of thermally activated delayed fluorescence for organic light emitting diodes", *Chemical communications* **2018**, *54*, 3926–3935.

(177) Stanton, J. F. "An unusually large nonadiabatic error in the BNB molecule", *The Journal of chemical physics* **2010**, *133*, 174309.

(178) Yang, L.; Horton, J. T.; Payne, M. C.; Penfold, T. J.; Cole, D. J. "Modeling Molecular Emitters in Organic Light-Emitting Diodes with the Quantum Mechanical Bespoke Force Field", *Journal of Chemical Theory and Computation* **2021**, *17*, 5021–5033.

(179) Dhali, R.; Huu, D. A. P.; Bertocchi, F.; Sissa, C.; Terenziani, F.; Painelli, A. "Understanding TADF: a joint experimental and theoretical study of DMAC-TRZ", *Physical Chemistry Chemical Physics* **2021**, *23*, 378–387.

(180) Stavrou, K.; Franca, L. G.; Monkman, A. P. "Photophysics of TADF Guest–Host Systems: Introducing the Idea of Hosting Potential", *ACS applied electronic materials* **2020**, *2*, 2868–2881.

(181) Dos Santos, P. L.; Ward, J. S.; Bryce, M. R.; Monkman, A. P. "Using guest–host interactions to optimize the efficiency of TADF OLEDs", *The journal of physical chemistry letters* **2016**, *7*, 3341–3346.

(182) Ishimatsu, R.; Matsunami, S.; Shizu, K.; Adachi, C.; Nakano, K.; Imato, T. "Solvent effect on thermally activated delayed fluorescence by 1, 2, 3, 5-tetrakis (carbazol-9-yl)-4, 6-dicyanobenzene", *The Journal of Physical Chemistry A* **2013**, *117*, 5607–5612.

(183) Méhes, G.; Goushi, K.; Potscavage Jr, W. J.; Adachi, C. "Influence of host matrix on thermally-activated delayed fluorescence: Effects on emission lifetime, photoluminescence quantum yield, and device performance", *Organic Electronics* **2014**, *15*, 2027–2037.

(184) Chang, C.-F.; Cheng, Y.-M.; Chi, Y.; Chiu, Y.-C.; Lin, C.-C.; Lee, G.-H.; Chou, P.-T.; Chen, C.-C.; Chang, C.-H.; Wu, C.-C. "Highly efficient blue-emitting iridium (III) carbene complexes and phosphorescent OLEDs", *Angewandte Chemie International Edition* **2008**, *47*, 4542–4545.

(185) Cho, T.-Y.; Lin, C.-L.; Wu, C.-C. "Microcavity two-unit tandem organic light-emitting devices having a high efficiency", *Applied physics letters* **2006**, *88*.

(186) Luo, X.-F.; Xiao, X.; Zheng, Y.-X. "Recent progress of multi-resonance thermally activated delayed fluorescence emitters with efficient reverse intersystem crossing process", *Chemical Communications* **2024**.

(187) Wu, T.-L.; Huang, M.-J.; Lin, C.-C.; Huang, P.-Y.; Chou, T.-Y.; Chen-Cheng, R.-W.; Lin, H.-W.; Liu, R.-S.; Cheng, C.-H. "Diboron compound-based organic light-emitting diodes with high efficiency and reduced efficiency roll-off", *Nature Photonics* **2018**, *12*, 235–240.

(188) Xue, Q.; Xie, G. "Thermally Activated Delayed Fluorescence beyond Through-Bond Charge Transfer for High-Performance OLEDs", *Advanced Optical Materials* **2021**, *9*, 2002204.

(189) Jiang, H.; Jin, J.; Wong, W.-Y. "High-Performance Multi-Resonance Thermally Activated Delayed Fluorescence Emitters for Narrowband Organic Light-Emitting Diodes", *Advanced Functional Materials* **2023**, *33*, 2306880.

(190) Wang, J.; Li, N.; Zhong, C.; Miao, J.; Huang, Z.; Yu, M.; Hu, Y. X.; Luo, S.; Zou, Y.; Li, K., et al. "Metal-Perturbed Multiresonance TADF Emitter Enables High-Efficiency and Ultralow Efficiency Roll-Off Nonsensitized OLEDs with Pure Green Gamut", *Advanced Materials* **2023**, *35*, 2208378.

(191) Lee, H. L.; Jeon, S. O.; Kim, I.; Kim, S. C.; Lim, J.; Kim, J.; Park, S.; Chwae, J.; Son, W.-J.; Choi, H., et al. "Multiple-Resonance Extension and Spin-Vibronic-Coupling-Based Narrowband Blue Organic Fluorescence Emitters with Over 30% Quantum Efficiency", *Advanced Materials* **2022**, *34*, 2202464.

(192) Patil, V. V.; Lee, H. L.; Kim, I.; Lee, K. H.; Chung, W. J.; Kim, J.; Park, S.; Choi, H.; Son, W.-J.; Jeon, S. O., et al. "Purely spin-vibronic coupling assisted triplet to singlet up-conversion for real deep blue organic light-emitting diodes with over 20% efficiency and y color coordinate of 0.05", *Advanced Science* **2021**, *8*, 2101137.

(193) Kim, I.; Cho, K. H.; Jeon, S. O.; Son, W.-J.; Kim, D.; Rhee, Y. M.; Jang, I.; Choi, H.; Kim, D. S. "Three states involving vibronic resonance is a key to enhancing reverse intersystem crossing dynamics of an organoboron-based ultrapure blue emitter", *Jacs Au* **2021**, *1*, 987–997.

(194) Hagai, M.; Inai, N.; Yasuda, T.; Fujimoto, K. J.; Yanai, T. "Extended theoretical modeling of reverse intersystem crossing for thermally activated delayed fluorescence materials", *Science Advances* **2024**, *10*, eadk3219.

(195) Hu, Y. X.; Miao, J.; Hua, T.; Huang, Z.; Qi, Y.; Zou, Y.; Qiu, Y.; Xia, H.; Liu, H.; Cao, X., et al. "Efficient selenium-integrated TADF OLEDs with reduced roll-off", *Nature Photonics* **2022**, *16*, 803–810.

(196) Park, I. S.; Yang, M.; Shibata, H.; Amanokura, N.; Yasuda, T. "Achieving Ultimate Narrowband and Ultrapure Blue Organic Light-Emitting Diodes Based on Polycyclo-Heteraborin Multi-Resonance Delayed-Fluorescence Emitters", *Advanced Materials* **2022**, *34*, 2107951.

(197) Nagata, M.; Min, H.; Watanabe, E.; Fukumoto, H.; Mizuhata, Y.; Tokitoh, N.; Agou, T.; Yasuda, T. "Fused-Nonacyclic Multi-Resonance Delayed Fluorescence Emitter Based on Ladder-Thiaborin Exhibiting Narrowband Sky-Blue Emission with Accelerated Reverse Intersystem Crossing", *Angewandte Chemie International Edition* **2021**, *60*, 20280–20285.

(198) Park, I. S.; Min, H.; Yasuda, T. "Ultrafast Triplet–Singlet Exciton Interconversion in Narrowband Blue Organoboron Emitters Doped with Heavy Chalcogens", *Angewandte Chemie International Edition* **2022**, *61*, e202205684.

(199) Xu, Y.; Li, C.; Li, Z.; Wang, Q.; Cai, X.; Wei, J.; Wang, Y. "Constructing charge-transfer excited states based on frontier molecular orbital engineering: narrowband green electroluminescence with high color purity and efficiency", *Angewandte Chemie International Edition* **2020**, *59*, 17442–17446.

(200) Wu, S.; Zhang, L.; Wang, J.; Kumar Gupta, A.; Samuel, I. D.; Zysman-Colman, E. "Merging Boron and Carbonyl based MR-TADF Emitter Designs to Achieve High Performance Pure Blue OLEDs", *Angewandte Chemie International Edition* **2023**, *62*, e202305182.

(201) Cai, W.; Zhong, C.; Ma, Z.-W.; Cai, Z.-Y.; Qiu, Y.; Sajid, Z.; Wu, D.-Y. "Machine-learning-assisted performance improvements for multi-resonance thermally activated delayed fluorescence molecules", *Physical Chemistry Chemical Physics* **2024**, *26*, 144–152.

(202) Hall, D.; Sancho-Garcıa, J. C.; Pershin, A.; Ricci, G.; Beljonne, D.; Zysman-Colman, E.; Olivier, Y. "Modeling of multiresonant thermally activated delayed fluorescence emitters properly accounting for electron correlation is key!", *Journal of Chemical Theory and Computation* **2022**, *18*, 4903–4918.

(203) Christiansen, O.; Koch, H.; Jørgensen, P. "The second-order approximate coupled cluster singles and doubles model CC2", *Chemical Physics Letters* **1995**, *243*, 409–418.

(204) Lee, S.; Filatov, M.; Lee, S.; Choi, C. H. "Eliminating spin-contamination of spin-flip time dependent density functional theory within linear response formalism by the use of zeroth-order mixed-reference (MR) reduced density matrix", *The Journal of chemical physics* **2018**, *149*.

(205) Horbatenko, Y.; Lee, S.; Filatov, M.; Choi, C. H. "Performance analysis and optimization of mixed-reference spin-flip time-dependent density functional theory (MRSF-TDDFT) for vertical excitation energies and singlet–triplet energy gaps", *The Journal of Physical Chemistry A* **2019**, *123*, 7991–8000.

(206) Gao, Y.; Wu, S.; Shan, G.; Cheng, G. "Recent Progress in Blue Thermally Activated Delayed Fluorescence Emitters and Their Applications in OLEDs: Beyond Pure Organic Molecules with Twist D--A Structures", *Micromachines* **2022**, *13*, 2150.

(207) Lee, H.; Karthik, D.; Lampande, R.; Ryu, J. H.; Kwon, J. H. "Recent Advancement in Boron-Based Efficient and Pure Blue Thermally Activated Delayed Fluorescence Materials for Organic Light-Emitting Diodes", *Frontiers in Chemistry* **2020**, *8*, 373.

(208) Curtarolo, S.; Hart, G. L. W.; Nardelli, M. B.; Mingo, N.; Sanvito, S.; Levy, O. "The high-throughput highway to computational materials design", *Nature Materials* **2013**, *12*, 191–201.

(209) Shoichet, B. K. "Virtual screening of chemical libraries", *Nature* **2004**, *432*, 862–865.

(210) Pyzer-Knapp, E. O.; Li, K.; Aspuru-Guzik, A. "Learning from the Harvard Clean Energy Project: The Use of Neural Networks to Accelerate Materials Discovery", *Advanced Functional Materials* **2015**, *25*, 6495–6502.

(211) Gómez-Bombarelli, R.; Aguilera-Iparraguirre, J.; Hirzel, T. D.; Duvenaud, D.; Maclaurin, D.; Blood-Forsythe, M. A.; Chae, H. S.; Einzinger, M.; Ha, D.-G.; Wu, T., et al. "Design of efficient molecular organic light-emitting diodes by a high-throughput virtual screening and experimental approach", *Nature materials* **2016**, *15*, 1120–1127.

(212) Lu, S.-Y.; Mukhopadhyay, S.; Froese, R.; Zimmerman, P. M. "Virtual Screening of Hole Transport, Electron Transport, and Host Layers for Effective OLED Design", *Journal of Chemical Information and Modeling* **2018**, *58*, 2440–2449.

(213) Nigam, A.; Pollice, R.; Krenn, M.; Gomes, G. d. P.; Aspuru-Guzik, A. "Beyond generative models: superfast traversal, optimization, novelty, exploration and discovery (STONED) algorithm for molecules using SELFIES", *Chemical Science* **2021**, *12*, 7079–7090.

(214) Krylov, A. I. "Spin-flip configuration interaction: an electronic structure model that is both variational and size-consistent", *Chemical Physics Letters* **2001**, *350*, 522–530.

(215) Krylov, A. I. "Size-consistent wave functions for bond-breaking: The equation-of-motion spin-flip model", *Chemical Physics Letters* **2001**, *338*, 375–384.

(216) Krylov, A. I. "Spin-flip equation-of-motion coupled-cluster electronic structure method for a description of excited states, bond breaking, diradicals, and triradicals", *Accounts of chemical research* **2006**, *39*, 83–91.

(217) Casanova, D.; Krylov, A. I. "Spin-flip methods in quantum chemistry", *Physical Chemistry Chemical Physics* **2020**, *22*, 4326–4342.

(218) Herbert, J. M.; Mandal, A. In *Time-dependent density functional theory*; Jenny Stanford Publishing: 2022, pp 361–404.

(219) Sears, J. S.; Sherrill, C. D.; Krylov, A. I. “A spin-complete version of the spin-flip approach to bond breaking: What is the impact of obtaining spin eigenfunctions?”, *The Journal of chemical physics* **2003**, *118*, 9084–9094.

(220) Lee, S.; Park, W.; Nakata, H.; Filatov, M.; Choi, C. H. In *Time-Dependent Density Functional Theory*; Jenny Stanford Publishing: 2022, pp 101–139.

(221) Park, W.; Lee, S.; Huix-Rotllant, M.; Filatov, M.; Choi, C. H. “Impact of the dynamic electron correlation on the unusually long excited-state lifetime of thymine”, *The Journal of Physical Chemistry Letters* **2021**, *12*, 4339–4346.

(222) Horbatenko, Y.; Sadiq, S.; Lee, S.; Filatov, M.; Choi, C. H. “Mixed-reference spin-flip time-dependent density functional theory (MRSF-TDDFT) as a simple yet accurate method for diradicals and diradicaloids”, *Journal of Chemical Theory and Computation* **2021**, *17*, 848–859.

(223) Komarov, K.; Park, W.; Lee, S.; Zeng, T.; Choi, C.-H. “Accurate Spin-Orbit Coupling and Intersystem Crossing by Relativistic Mixed-Reference Spin-Flip (MRSF)-TDDFT”, **2022**.

(224) Park, W.; Alıas-Rodrıguez, M.; Cho, D.; Lee, S.; Huix-Rotllant, M.; Choi, C. H. “Mixed-reference spin-flip time-dependent density functional theory for accurate x-ray absorption spectroscopy”, *Journal of Chemical Theory and Computation* **2022**, *18*, 6240–6250.

(225) Baek, Y. S.; Lee, S.; Filatov, M.; Choi, C. H. “Optimization of three state conical intersections by adaptive penalty function algorithm in connection with the mixed-reference spin-flip time-dependent density functional theory method (MRSF-TDDFT)”, *The Journal of Physical Chemistry A* **2021**, *125*, 1994–2006.

(226) Hirata, S.; Head-Gordon, M.; Bartlett, R. J. “Configuration interaction singles, time-dependent Hartree–Fock, and time-dependent density functional theory for the electronic excited states of extended systems”, *The Journal of Chemical Physics* **1999**, *111*, 10774–10786.

(227) Adamo, C.; Scuseria, G. E.; Barone, V. “Accurate excitation energies from time-dependent density functional theory: Assessing the PBE0 model”, *The Journal of chemical physics* **1999**, *111*, 2889–2899.

(228) Zahariev, F.; Xu, P.; Westheimer, B. M.; Webb, S.; Galvez Vallejo, J.; Tiwari, A.; Sundriyal, V.; Sosonkina, M.; Shen, J.; Schoendorff, G., et al. "The General Atomic and Molecular Electronic Structure System (GAMESS): Novel Methods on Novel Architectures", *Journal of Chemical Theory and Computation* **2023**, *19*, 7031–7055.

(229) Hilborn, R. C. "Einstein coefficients, cross sections, f values, dipole moments, and all that", *American Journal of Physics* **1982**, *50*, 982–986.

(230) Chang, Y.; Wu, Y.; Wang, X.; Li, W.; Yang, Q.; Wang, S.; Shao, S.; Wang, L. "Boron, sulfur-doped polycyclic aromatic hydrocarbon emitters with multiple-resonance-dominated lowest excited states for efficient narrowband deep-blue emission", *Chemical Engineering Journal* **2023**, *451*, 138545.

(231) Li, Q.; Wu, Y.; Wang, X.; Yang, Q.; Hu, J.; Zhong, R.; Shao, S.; Wang, L. "Boron-, Sulfur-and Nitrogen-Doped Polycyclic Aromatic Hydrocarbon Multiple Resonance Emitters for Narrow-Band Blue Emission", *Chemistry–A European Journal* **2022**, *28*, e202104214.

(232) Chen, F.; Zhao, L.; Wang, X.; Yang, Q.; Li, W.; Tian, H.; Shao, S.; Wang, L.; Jing, X.; Wang, F. "Novel boron-and sulfur-doped polycyclic aromatic hydrocarbon as multiple resonance emitter for ultrapure blue thermally activated delayed fluorescence polymers", *Science China Chemistry* **2021**, *64*, 547–551.

(233) Wang, C.; Zhang, Q. "Understanding solid-state solvation-enhanced thermally activated delayed fluorescence using a descriptor-tuned screened range-separated functional", *The Journal of Physical Chemistry C* **2018**, *123*, 4407–4416.

(234) Sun, H.; Hu, Z.; Zhong, C.; Chen, X.; Sun, Z.; Brédas, J.-L. "Impact of dielectric constant on the singlet–triplet gap in thermally activated delayed fluorescence materials", *The journal of physical chemistry letters* **2017**, *8*, 2393–2398.

(235) Xu, Y.; Cheng, Z.; Li, Z.; Liang, B.; Wang, J.; Wei, J.; Zhang, Z.; Wang, Y. "Molecular-structure and device-configuration optimizations toward highly efficient green electroluminescence with narrowband emission and high color purity", *Advanced Optical Materials* **2020**, *8*, 1902142.

(236) Qi, Y.; Ning, W.; Zou, Y.; Cao, X.; Gong, S.; Yang, C. "Peripheral decoration of multi-resonance molecules as a versatile approach for simultaneous long-wavelength and narrowband emission", *Advanced Functional Materials* **2021**, *31*, 2102017.

(237) Zhang, Y.; Zhang, D.; Huang, T.; Gillett, A. J.; Liu, Y.; Hu, D.; Cui, L.; Bin, Z.; Li, G.; Wei, J., et al. "Multi-Resonance Deep-Red Emitters with Shallow Potential-Energy Surfaces to Surpass Energy-Gap Law", *Angewandte Chemie International Edition* **2021**, *60*, 20498–20503.

(238) Zou, S.-N.; Peng, C.-C.; Yang, S.-Y.; Qu, Y.-K.; Yu, Y.-J.; Chen, X.; Jiang, Z.-Q.; Liao, L.-S. "Fully Bridged Triphenylamine Derivatives as Color-Tunable Thermally Activated Delayed Fluorescence Emitters", *Organic Letters* **2021**, *23*, 958–962.

(239) Zhang, Y.; Zhang, D.; Wei, J.; Hong, X.; Lu, Y.; Hu, D.; Li, G.; Liu, Z.; Chen, Y.; Duan, L. "Achieving pure green electroluminescence with CIEy of 0.69 and EQE of 28.2% from an aza-fused multi-resonance emitter", *Angewandte Chemie* **2020**, *132*, 17652–17656.

(240) Jiang, P.; Zhan, L.; Cao, X.; Lv, X.; Gong, S.; Chen, Z.; Zhou, C.; Huang, Z.; Ni, F.; Zou, Y., et al. "Simple Acridan-Based Multi-Resonance Structures Enable Highly Efficient Narrowband Green TADF Electroluminescence", *Advanced Optical Materials* **2021**, *9*, 2100825.

(241) Lee, H.; Braveenth, R.; Park, J. D.; Jeon, C. Y.; Lee, H. S.; Kwon, J. H. "Manipulating Spectral Width and Emission Wavelength towards Highly Efficient Blue Asymmetric Carbazole Fused Multi-Resonance Emitters", *ACS Applied Materials & Interfaces* **2022**, *14*, 36927–36935.

(242) Chan, C.-Y.; Suresh, S. M.; Lee, Y.-T.; Tsuchiya, Y.; Matulaitis, T.; Hall, D.; Slawin, A. M.; Warriner, S.; Beljonne, D.; Olivier, Y., et al. "Two boron atoms versus one: high-performance deep-blue multi-resonance thermally activated delayed fluorescence emitters", *Chemical Communications* **2022**, *58*, 9377–9380.

(243) Lv, X.; Miao, J.; Liu, M.; Peng, Q.; Zhong, C.; Hu, Y.; Cao, X.; Wu, H.; Yang, Y.; Zhou, C., et al. "Extending the π-Skeleton of Multi-Resonance TADF Materials towards High-Efficiency Narrowband Deep-Blue Emission", *Angewandte Chemie* **2022**.

(244) Hua, T.; Miao, J.; Xia, H.; Huang, Z.; Cao, X.; Li, N.; Yang, C. "Sulfone-Incorporated Multi-Resonance TADF Emitter for High-Performance Narrowband Blue OLEDs with EQE of 32%", *Advanced Functional Materials* **2022**, 2201032.

(245) Park, I. S.; Min, H.; Yasuda, T. "Ultrafast Triplet–Singlet Exciton Interconversion in Narrowband Blue Organoboron Emitters Doped with Heavy Chalcogens", *Angewandte Chemie International Edition* **2022**, *61*, e202205684.

(246) Wang, Y.; Zhang, K.; Chen, F.; Wang, X.; Yang, Q.; Wang, S.; Shao, S.; Wang, L. "Boron-, Sulfur- and Nitrogen-Doped Tridecacyclic Aromatic Emitters with Multiple Resonance Effect for Narrowband Red Emission†", *Chinese Journal of Chemistry*, *n/a*, DOI: `https://doi.org/10.1002/cjoc.202200356`.

(247) Naveen, K. R.; Lee, H.; Seung, L. H.; Jung, Y. H.; Keshavananda Prabhu, C.; Muruganantham, S.; Kwon, J. H. "Modular design for constructing narrowband deep-blue multiresonant thermally activated delayed fluorescent emitters for efficient organic light emitting diodes", *Chemical Engineering Journal* **2023**, *451*, 138498.

(248) Liu, G.; Sasabe, H.; Kumada, K.; Arai, H.; Kido, J. "Nonbonding/Bonding Molecular Orbital Regulation of Nitrogen-Boron-Oxygen-embedded Blue/Green Multiresonant TADF Emitters with High Efficiency and Color Purity", *Chemistry – A European Journal* **2022**, *28*, e202201605.